Boundary Layer Instabilities Due to Surface Irregularities: A Harmonic Navier-Stokes Approach

Submitted in partial fulfilment of the requirements for the degree of Doctor of Philosophy of Imperial College London and the Diploma of Imperial College London by

Thibaut Appel

Imperial College London

Department of Mathematics

March 2021

To my family.

– Declaration of Originality –

I declare herewith that the intellectual content of this thesis is entirely the product of my own work, except where otherwise indicated. It does not contain material which has been submitted, either partially or in full, for the award of any other qualification at any other educational institution. Any ideas or quotations from the work of other sources, published or otherwise, are explicitly acknowledged in accordance with the standard referencing practices. I confirm that some fragments of this work have been published as

- Peer-reviewed proceedings

  Appel, T., Cooke, E., Mughal, S. & Ashworth, R. (2021) BiGlobal stability analysis of swept-wing boundary layers with forward and backward facing steps. In: Sherwin, S., Schmid, P. & Wu, X. (eds.), *Laminar-Turbulent Transition: 9th IUTAM Symposium, London, UK, September 2–6, 2019*. IUTAM, 38. Cham, Switzerland, Springer. DOI: 10.1007/978-3-030-67902-6_30.

- Conference papers

  Appel, T., Mughal, S. & Ashworth, R. (2019) Global stability analysis of a boundary layer with surface indentations. In: *2019 AIAA Aviation Forum, Fluid Dynamics Conference, 17–21 June 2019, Dallas, TX*. AIAA Paper 2019-3537. DOI: 10.2514/6.2019-3537.

Thibaut Appel

24th March 2021

– Copyright Statement –

– Abstract –

Maintaining laminar flow and delaying transition to turbulence on aircraft wings reduces friction drag and hence fuel consumption for an improved ecological footprint. Nonetheless, widespread models of disturbance growth in boundary layers discard important transition stages and are inadequate to incorporate the effect of surface irregularities causing rapid variations in the underlying steady flow. This thesis applies global or Harmonic Navier-Stokes (HNS) methods to quantify the growth of instabilities in shear flows with two inhomogeneous spatial directions. Such methods deliver greater fidelity than the standard Parabolised Stability Equations (PSE). This work presents an efficient parallel computational framework to solve linear and non-linear HNS problems. We use BiGlobal analysis to investigate the existence of temporally unstable modes on a flat plate with smooth indentations featuring laminar separation bubbles (LSBs). Then, for the first time, it is applied to a swept-wing boundary layer featuring Backward- and Forward-Facing Steps (BFSs and FFSs). Localised unstable modes are identified for step heights exceeding the local boundary-layer displacement thickness of the clean geometry. BFSs are found to be more destabilising than equivalent FFSs, especially in the presence of the LSB formed behind the infinite-swept BFS. Next, we introduce the non-linear HNS method as an improvement over the non-linear PSE, able to model receptivity and non-linear mode interaction at a fraction of the cost of Direct Numerical Simulation. The method can model flow destabilisation scenarios on swept wings exhibiting surface features and holds the potential for accurate transition prediction. Its performance is assessed in the case of a Tollmien-Schlichting wave interacting with a cylindrical roughness located on a nearly flat aerofoil section. Finally, we consider crossflow disturbances generated by placing Discrete Roughness Elements (DRE) at the leading edge of a swept wing and follow their non-linear development up to a strongly saturated state. Non-linear receptivity effects are found to arise with increasing DRE heights.

– Acknowledgements –

I would like to express my sincere gratitude to the European Union and Airbus for their support of this research work at such a pivotal time for the aeronautical industry. In particular, I am indebted to Dr Stephen Rolston for his warm welcome and for providing an amiable, balanced environment to nurture my research approach. I shall express my gratitude to Dr Shahid Mughal for his support and technical advice throughout the research journey. I also thank Dr Richard Ashworth for his trust and his industrial insight. Furthermore, I would like to warmly thank my PhD examiners, Prof Peter Schmid and Docent Ardeshir Hanifi, for the enjoyable viva and their stimulating feedback.

It has been a long road full of obstacles and there are so many amazing souls who should be mentioned, without whom writing this piece of work would have been much more difficult.

Arthur, as two PhD students we have been in the same boat since the beginning, and I am so grateful to have met you. Your humour as well as your world-renowned zest for life were instrumental in the completion of this thesis. I am happy you saw the light at the end of the tunnel and hope we can embark on the surf trip we always cherished. Paul, you have equally contributed to contain my frenzy and I am sending positive waves for your PhD research. It is impossible not to mention Julien, Guillaume and Hugo. Whenever we spent holidays or silly moments all together, my research issues would fall into oblivion; our banter embodied my leitmotiv, that is working seriously without taking ourselves seriously.

A number of London visits punctuated the last four years. I am immensely grateful to Helena, Julia and Jamie, my 'British family', for welcoming me to the River House, a real haven of rest. Thank you for all the enjoyable evenings we had. For the same reasons, I thank Sarah and Mike for their generosity and all the geeky aviation discussions. I cannot possibly forget Annika. Our catch-ups were scarce yet were always quality time.

Huzafa, from the outset your presence in the office was a breath of fresh air. I admired your dedication and strong work ethics. In addition, I will reminisce about our fluid mechanics discussions, our latte & mocha breaks and most importantly our shared LaTeX fetish. Attending your wedding ceremony in Scotland was a true privilege. I would also like to pay my regards to Francesco, the laid-back Milanese, for all our discussions and his short-but-intense Bristol visit.

Taking my thoughts across the Atlantic, every time I chatted with Tal I could feel I was soaking up the Californian sun. Thank you for being a great friend. Silvia, your support in the early stages of the PhD was incredible, and I will never forget it. Without a doubt, I can say I have been the luckiest tenant in Bristol, even arguably in the United Kingdom. I always say, John, that you have been a friend rather than just a landlord. Life at 587 will be dearly missed as well as our wild tennis matches on Court 1.

Laura, there are not enough words to describe how valuable your support was. Your unconditional patience and your understanding proved monumental towards the completion of this thesis. I look up to your simplicity and your empathy. For all our travel adventures that allowed us escaping, I am wholeheartedly thankful—and obviously excited for the many others still to come. I can already hear African elephants growling and trumpeting.

Finally, I must express my deepest gratitude to my parents. You have been supporting me no matter the circumstances and have instilled precious values in me, such as the taste for hard work and diligence. You have always been attached to my freedom and have ensured I could make my own way. I could have never achieved this without you. Lucie, I must say it has been frustrating to be separated by the English Channel. Our reunions were seldom, but I am confident the future holds something different. Thank you for your support.

I would also like to thank the incredible artists who accompanied this research and the intensive months of writing this thesis. They created entire worlds in which my conceptual and numerical thoughts could blossom, besides bringing me joy and resilience during the hard moments. A non-exhaustive list includes Richie Hawtin, Palms Trax, Ricardo Villalobos, F.U.S.E., Alva Noto, Henrik Schwarz, Pete Namlook, Plastikman, Manuel Göttsching, Daft Punk, Arnaud Rebotini, Jean-Michel Jarre, Kraftwerk, Laurent Garnier, Bonobo, From Within, Raresh, Tale of Us, New Order, Hunee, Dubfire, David Morales, Petar Dundov, Issa Bagayogo, TM404, Aphex Twin. . .

– Contents –

– List of Figures –

– List of Tables –

– List of Acronyms –

2D	Two-dimensional
2.5D	Two-and-a-half-dimensional
3D	Three-dimensional
AMG	Algebraic Multigrid
BGK	Bhatnagar-Gross-Krook
BFS	Backward-Facing Step
CF	Crossflow
CFD	Computational Fluid Dynamics
CFS	Complex-Frequency-Shifted
CPU	Central Processing Unit
DAE	Differential Algebraic Equation
DFT	Discrete Fourier Transform
DNS	Direct Numerical Simulation
FSC	Falkner-Skan-Cooke
FDM	Finite Difference Method
FFS	Forward-Facing Step
HLFC	Hybrid Laminar Flow Control
HNS	Harmonic Navier-Stokes
HPC	High-Performance Computing
GEVP	Generalised Eigenvalue Problem
IBVP	Initial Boundary Value Problem

LES Large Eddy Simulation

LHNS Linearised Harmonic Navier-Stokes

LPPE Linearised Pressure Poisson Equation

LSB Laminar Separation Bubble

LST Linear Stability Theory

LU Lower-Upper

MFD Mean Flow Distortion

MPI Message Passing Interface

MUMPS MUltifrontal Massively Parallel Solver

NLF Natural Laminar Flow

NLHNS Non-Linear Harmonic Navier-Stokes

NLPSE Non-Linear Parabolised Stability Equations

ODE Ordinary Differential Equation

PDE Partial Differential Equation

PC Pressure Compatibility

PETSc Portable, Extensible Toolkit For Scientific Computation

PML Perfectly Matched Layer

PPE Pressure Poisson Equation

PSE Parabolised Stability Equations

RAM Random-Access Memory

RANS Reynolds-Averaged Navier-Stokes

RMS Root Mean Square

SLEPc Scalable Library For Eigenvalue Problem Computations

TS Tollmien-Schlichting

– List of Symbols –

Subscripts

- $\bullet_{\infty}$ free-stream value
- $\bullet_{crit}$ critical value
- $\bullet_{e}$ edge value
- $\bullet_{i}$ imaginary part
- $\bullet_{lam}$ laminar value
- $\bullet_{r}$ real part
- $\bullet_{rms}$ root-mean-square value
- $\bullet_{tr}$ transitional value
- $\bullet_{w}$ wall value

Superscripts

- $\tilde{\bullet}$ perturbation quantity
- $\bar{\bullet}$ mean quantity
- $\hat{\bullet}$ amplitude quantity
- $\breve{\bullet}$ complex continued quantity
- $\bullet^{*}$ dimensional quantity
- $\bullet^{\dagger}$ complex conjugate
- $\bullet^{H}$ Hermitian transpose
- $\bullet^{T}$ Transpose

Greek symbols

- Γ pressure gradient parameter
- $\boldsymbol{\Delta}$ vector Laplace operator
- Δ Laplace operator
- Λ sweep angle
- Ξ computational domain

Ω physical control volume

α streamwise wavenumber

β spanwise wavenumber

γ growth rate

δ boundary layer thickness

δ^* displacement thickness

δ_{ij} Kronecker delta

ε infinitesimal quantity

ζ complex frequency shift

θ momentum thickness

κ grid compression factor

λ roughness width or radius

μ dynamic (shear) viscosity

ν kinematic viscosity

ρ density

σ damping profile

σ_{ij} Cauchy stress tensor

τ under-relaxation coefficient

ω angular frequency

Latin symbols

A wave amplitude

AoA angle of attack

$\mathbb{C}$ set of complex numbers

E total disturbance energy

F reduced frequency

H shape factor

L length scale

M number of spanwise harmonics

Ma Mach number

N N-factor; number of temporal harmonics

$\mathbb{R}$ set of real numbers

R_c reflection coefficient

Re Reynolds number

U streamwise velocity scale

$\mathbb{V}$ set of molecular velocities

W spanwise velocity scale

$\mathbf{c}$ microscopic velocity vector

c microscopic velocity; phase velocity; wing chord

c_f skin-friction coefficient

c_p pressure coefficient

d ordinary derivative

f frequency

h roughness height

i imaginary unit

ℓ Blasius boundary layer thickness

n number of grid nodes

n_p number of MPI processes

p pressure

$\mathbf{q}$ vector of flow variables

q finite-difference order

s curvilinear streamwise coordinate

t time coordinate

$\mathbf{u}$ velocity vector

u streamwise velocity

v wall-normal velocity

w spanwise velocity

$\mathbf{x}$ coordinate vector

x streamwise coordinate

y wall-normal coordinate

z spanwise coordinate

Other symbols

∂ partial derivative

∇ del operator

Chapter 1

Introduction

1.1 The challenge of laminar flow in aviation

Commercial aviation is at a pivotal moment of its eventful history. Most economic indicators of the industry have been positive since the end of the 20th century. For instance, the world annual traffic has been continuously increasing and doubling every 15 years since 1988, while displaying robustness to exogenous and world-changing crises such as oil shocks or the 2007–2008 financial crisis (Airbus, 2019). According to the International Air Transport Association (IATA), in 2019 alone approximately 4.54 billion passengers worldwide were scheduled on commercial flights.

The prospects of a rise in world population by the middle of the 21st century imply an increasing demand for air travel, potentially leading to a further doubling of the worldwide passenger traffic (Airbus, 2019). Nevertheless, several short- to medium-term challenges are expected to foster a transformation of aviation. Besides the uncertainties of trade wars and protectionist policies, decarbonisation is currently a pressing issue for the aviation sector with respect to curbing climate change. The popularity of the 'flygskam' (flight shame) movement in Sweden is likely to resonate and cascade over stakeholders, putting pressure to reduce the carbon footprint of the industry.

Although the average fuel consumption of commercial aircraft has undergone a 45% decrease from 1968 to 2014 (Kharina & Rutherford, 2015), the carbon dioxide (CO_2) emissions from aviation in 2019 still totalled 950 Mt or roughly 2.6% of the global CO_2 emissions (IEA, 2020). The other emissions of an aircraft, including nitrogen oxides (NO_x), water vapour, soot particles or sulphate particles also have a non-negligible impact on climate. Based on data from 2005, Lee et al.

(2009) estimated that total aviation emissions accounted for 4.9% of the total anthropogenic radiative forcing[1]. Such metric was predicted to triple or quadruple by 2050 compared to its 2000 value (Lee et al., 2009). These figures further highlight the room for manoeuvre that aviation has along its greener pathway.

In an effort to tackle environment challenges head-on, the FlightPath 2050 initiative from the Advisory Council for Aviation Research and innovation in Europe wants to reach a reduction of 75% in CO_2 emissions per passenger-kilometre as well as a 90% reduction in NO_x emissions by the 2050 horizon, compared to the generation of aircraft from 2000 (European Commission, 2012). There is still some way to go before the emergence of zero-emission flight with alternative propulsion systems, whether it is in the form of a solar-powered aircraft, a fully electric aircraft or a variant powered with hydrogen fuel cells. Several actors are currently shaping hybrid-electric aircraft demonstrators. However, there is a significant reduction in fuel consumption and CO_2 emissions to be gained with numerous new technology concepts with relatively high technology readiness levels. These include new engine architectures, the improvement of propulsion efficiency, the further exploitation of biomimicry, or disruptive airframe configurations.

Amongst other potential improvements in aerodynamics also leading to fuel savings, many efforts are devoted to aircraft drag reduction. As Kroo (2001, p. 587) amusingly pointed,

> 'transportation is fundamentally 0% efficient as it involves moving mass from rest at one point to rest at another point, so that the energy of the system is unchanged. That it does take energy to accomplish this objective is due to the presence of drag [. . .]'

In the case of a subsonic commercial aircraft flying in cruise conditions, the sources of drag are clearly identified. Figure 1.1 tells that skin-friction drag accounts for almost half of the total drag. While lift-induced drag still represents around 37% of the total drag, the overall effect of other components remains marginal and equals approximately 15%[2]. The after-body drag is due to the vortex shedding and flow separation in the rear part of the fuselage, whereas wave drag arises due to compressibility effects in the transonic regime. Finally, the intersection of several aerodynamic surfaces mostly results in an increased total drag compared to their distinct contribution and is known as interference drag. The skin-friction drag is

[1] the balance between incoming solar radiation energy and energy radiated back to space.

[2] Such an aircraft drag breakdown shall not be seen as carved in stone; the drag component terminology varies in the literature and the overall drag budget remains unique for each type of aircraft and complex to predict accurately.

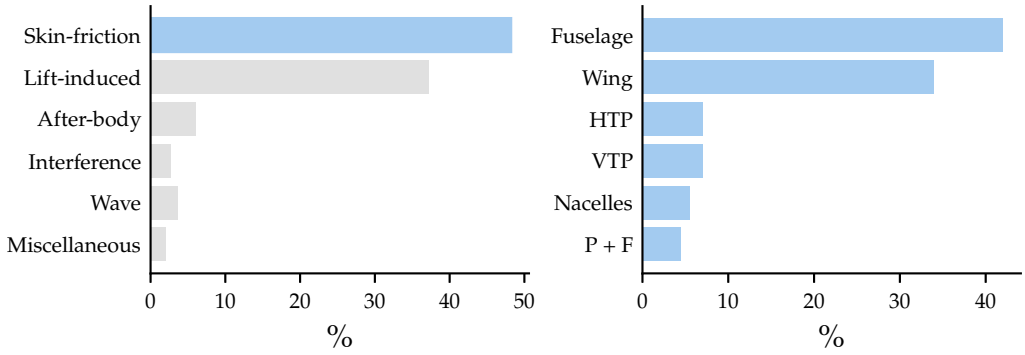

Figure 1.1: Total drag breakdown of a typical commercial aircraft at cruise conditions (*left*) and respective contributions of aircraft surfaces to skin-friction drag (*right*). Data respectively given in Marec (2001) and Schrauf (2005).

mostly engendered by the flow on the fuselage and on the wings as indicated by Fig. 1.1.

It seems natural to target skin-friction drag on the fuselage and on the wings, in view of its significant impact on the total aircraft drag. From a physical viewpoint, the major culprit for a consequential rise in skin-friction drag is the occurrence of turbulent flow, as opposed to laminar flow. Therefore, the pursuit of maintaining laminar flow on aircraft surfaces is a potential game changer. Schrauf (2005) evaluated that the total drag would be reduced by approximately 16%, should laminar flow be maintained on 40% of the wings, the horizontal tailplane (HTP), the vertical tailplane (VTP), the nacelles as well as the pylons and fairings (P + F). Maintaining laminar flow on the fuselage is indeed hopeless on account of the very large Reynolds numbers[3] reached there (Schrauf, 2005), yet maximising the extent of laminar flow past the leading edge of wings holds the potential for considerable fuel savings.

These are the objectives of the techniques of Natural Laminar Flow (NLF) and Hybrid Laminar Flow Control (HLFC). The former endeavours to devise a suitable geometry-induced pressure gradient distribution along the wing in order to stabilise disturbances leading to the transition to turbulence. As its name implies, HLFC relies on the combination of a flow control technique, typically near the leading edge, with NLF commonly applied on the aft part of the wing; such a control technique can be *active* and may involve suction, cooling or blowing. On the other hand, a *passive* solution, not necessitating an external energy source, may be employed with the example of micron-sized roughness elements placed close to the leading edge. These favourably modify the flow by generating co-rotating vortices. These so-called 'killer' disturbances can dampen the most dangerous naturally

[3] introduced on Page 35.

Figure 1.2: Wing extremity of the Airbus A340 used in the BLADE project. The bottom part shows the multitude of natural surface excrescences occurring on a commercial aircraft wing. The mounted NLF wing extension is visible on the upper part and contained step-like and cylinder-like roughness features. © 2017 Airbus. Photograph by P. Pigeyre.

occurring vortical disturbances which might otherwise grow and ultimately lead to turbulent breakdown.

The feasibility of HLFC with transport aeroplanes was ascertained at the very end of the 20th century, as Boeing and the National Aeronautics and Space Administration (NASA) performed a flight demonstration with a suction system mounted alongside a porous leading-edge panel on a Boeing B757 (Boeing, 1999). Moreover, Airbus measured a fuel consumption reduction over the course of a flight test with a suction system installed on the vertical tailplane of an Airbus A320 (Henke, 1999). The Boeing B787-9 began commercial service in 2014 and marked the first use of HLFC in commercial aviation. It is reported to employ passive suction on the vertical tailplane. The B787-10 variant that entered service in 2018 is also fitted with the same system.

Obtaining NLF is notoriously more difficult, however a few success stories have emerged over the years. Partial NLF was reached on the engine nacelles of the Boeing B787. As part of the Clean Sky European research programme, Airbus and various industrial partners undertook a project entitled Breakthrough Laminar Aircraft Demonstrator in Europe (BLADE) that was carried out in 2017 and 2018 with several flight tests using a modified Airbus A340. That demonstrator was

the first ever mounted with an NLF wing section, visible in Fig. 1.2. The laminar outer wing section was nine-meters long with an integrated leading edge and upper-wing surface, the latter made of carbon fibre reinforced plastic. Flight tests demonstrated that a stable laminar flow was sustained from Mach 0.78 to Mach 0.75 (Gubisch, 2018) which is a typical range of cruise speeds for A320-family aircraft. The laminar flow stability during wing flexion and wing twisting was also assessed. Further tests involving surface roughness were carried out, which are pertinent to the work performed in this thesis.

It is believed that HLFC implemented on wings as well as on the horizontal and vertical tailplanes could engender a reduction of fuel consumption of 10% (Gubisch, 2019). As opposed to a turbulent-flow wing, Airbus estimates that for an 800 NM (1,480 km) journey at Mach 0.75, NLF may lead aircraft drag to decrease by 8%, or equivalently save 4.6% of fuel. As promising as these prospects of improvement may seem, there are nonetheless a few remaining hurdles before such technologies can be routinely used on an industrial scale for the next generation of aircraft. One of these is the successful modelling of the transition from laminar flow to turbulent flow.

1.2 Towards improved transition modelling

The phenomenon of turbulence has been scrutinised for decades, if not centuries. In his groundbreaking experiment on the motion of water in pipes, Reynolds (1883) observed with coloured water the laminar and turbulent regimes, which he respectively referred to as 'direct' and 'sinuous'. He argued that the critical velocity reached before the breakdown to turbulence is clearly dependent upon the initial level of disturbance in the inflow. Furthermore, he conjectured the importance of a non-dimensional parameter for the 'birth of eddies',

$$\mathrm{Re} = \frac{\rho U L}{\mu} \tag{1.1}$$

which is famously known as the Reynolds number Re. It involves a length scale L, a velocity scale U, the dynamic viscosity μ and the density of the fluid ρ. The Reynolds number remains the paramount measure in a fluid system to characterise its laminarity or its turbulence.

There has been a consensus that the laminar-turbulent transition strongly pertains to the concept of *boundary layer*, which was described for the first time by Prandtl (1905) in his seminal contribution. The boundary layer denotes the thin flow region adjacent to a solid surface where friction and viscosity effects are predominant.

It separates the solid surface of zero relative flow velocity and the inviscid outer flow with 'free-stream' velocity, which necessarily implies a high velocity gradient within it. Prandtl's boundary layer theory has bridged the gap between the Euler equations, describing the dynamics of inviscid flows and the Navier-Stokes equations describing the evolution of a viscous fluid. By emphasising the role of viscosity via boundary-layer theory, Prandtl indeed contributed to addressing the deficiencies of the inviscid theory revealed in experiments.

To this day, the Navier-Stokes equations still hold mysteries related to their mathematical properties. Analytical solutions can only be derived via simplifying assumptions, while the existence and smoothness of general solutions to the three-dimensional (3D) equations remain an open problem. In 2013, Oterbayev published what he thought was a proof of the said problem before realising he had committed a mistake. Later, Tao (2016) even demonstrated that smooth solutions to averaged Navier-Stokes equations with unbounded energy in a finite time can be constructed, which might have scuppered the hopes of respectable mathematicians to solve the renowned problem in a not too distant future.

In spite of an irrefutable mathematical bedrock, the Navier-Stokes equations have been solved numerically. With the advent of Computational Fluid Dynamics (CFD), digital mock-ups have indeed replaced drawing boards which contributed to change design processes in aviation in the last few decades. By offering a 'numerical wind-tunnel', CFD has contributed to the successful modelling and prediction of complex flow phenomena. It thus supported the design of modern fluid systems including, of course, transport aircraft. However, the laminar-turbulent transition is such a complex physical phenomenon with high sensitivity to environmental conditions that its numerical modelling remains a major challenge. This thesis endeavours to address some aspects of boundary-layer instabilities leading to transition, specifically in presence of surface irregularities.

1.3 Motivation and objectives

The various facets of transition, with mechanisms pertaining to swept wings and the impact of surface irregularities, give rise to an important modelling complexity. There is no denying that such complexity is not currently captured by state-of-the-art industrial tools for wing design, and that there remains a significant capability gap between high-fidelity CFD and low-fidelity transition modelling.

Contemporary transition prediction tools are decades old, based on a near-conical flow assumption for tapered wing geometries with a smooth surface. They are

furthermore heavily relying on *local* theories together with a semi-empirical method known as the e^N method in order to estimate the transition location. It may be argued that these are appropriate to model the variety of subsonic, swept-wing boundary-layer transition mechanisms which have become commonplace from a design viewpoint. However, the impact of surface roughness is neglected by the current capabilities, leaving key physics out of the scope. This consequently forces aircraft manufacturers to over-conservatively design natural-laminar-flow wings, which induces a loss of aerodynamic efficiency. Hence, there is an essential need for higher-fidelity modelling capabilities able to seamlessly incorporate surface imperfection effects on flow disturbance evolution.

Global theories form the basis of this thesis, with relaxed assumptions on the flow field physics. As such, these are excellent candidates to fill the gap between the current modelling methods and the complexity required by scientists and engineers to devise HLFC techniques. They enable replication of a well-known free-stream environment or a state of roughness on the surface, thereby reproducing transition mechanisms accurately for the ultimate purpose of improved transition prediction. In particular, global methodologies are fit to numerically handle real-world, swept-wing boundary layers with surface roughness for which literature contributions remain scarce. Nonetheless, the local and non-local methods do not necessitate significant computational power whereas an additional computational effort is required with global methods, whilst not reaching the overwhelming cost of Direct Numerical Simulation (DNS).

In this thesis, we develop a single computational code that encompasses global methodologies, and we then demonstrate its ability to comprehensively capture the effect of surface roughness on swept-wing boundary layers. On the one hand, we use the so-called *temporal BiGlobal* analysis, aimed at recovering self-sustained instabilities that are amplified in time in the form of eigenvalues. It is applied to boundary layers in the presence of Laminar Separation Bubbles (LSBs), and to our best knowledge, for the first time on swept-wing boundary layers featuring backward- and forward-facing steps. On the other hand, we also exploit the Harmonic Navier-Stokes (HNS) method devised for the spatial stability of boundary layers. We introduce its non-linear variant and demonstrate its legitimacy for investigating the non-linear growth of instabilities generated by a roughness element, in both flat-plate and swept-wing boundary-layer flows. Both Linearised Harmonic Navier-Stokes (LHNS) and Non-Linear Harmonic Navier-Stokes (NLHNS) are amplitude-based methods rather than amplification-based. Should their capability for accurate transition prediction be established, the added value of modelling would contribute to further reducing manufacturing tolerances

for NLF wings. Finally, the code heavily relies on parallel computing in order to obtain rapid computation times while maintaining a significant level of accuracy.

1.4 Outline

This thesis is structured as follows.

Chapter 2 provides a review of the laminar-turbulent transition processes and of its mechanisms pertaining to swept wings. It is followed by developments about the current state of transition modelling and transition prediction, where local, non-local and global methods are thoroughly presented. This background chapter finally reviews the state-of-the-art on surface-induced transition.

Chapter 3 introduces the governing equations of this thesis and mathematically develops the stability theories presented in Chapter 2 with a focus on the global approaches: BiGlobal, LHNS and NLHNS. Prior to their numerical application, the chapter also discusses the boundary treatment and in particular the Perfectly Matched Layer (PML) method applied for the first time in the current flow stability framework.

Chapter 4 describes the numerical implementation of the stability theories within the computational tool that has been developed in this work. The adopted discretisation methods, the code structure as well as the underlying algorithms are presented. Its parallel efficiency and its limitations with respect to treating fully 3D problems are further discussed.

Chapter 5 focuses on the linear instability of boundary layers incorporating surface irregularities. After verifying the computational tool against two selected cases, BiGlobal and LHNS stability analyses are undertaken on a two-dimensional (2D), flat-plate boundary layer with indentations of increasing height. The first application of BiGlobal analysis on a swept-wing boundary layer with surface features, namely backward- and forward-facing steps of varying height, is also presented.

Chapter 6 presents the verification and validation of the NLHNS approach that has been developed on three previously documented cases. The method is then applied to investigate the non-linear growth of instabilities in the wake of a cylindrical roughness element, firstly on a flat-plate boundary layer and then on a swept-wing boundary layer generated from experimental data.

Chapter 7 recapitulates the findings of this thesis, provides final remarks and suggests several perspectives on future lines of research.

Chapter 2

Transition and Stability

Just point yourself in the direction of your dreams, find your strength in the sound, and make your transition

—Underground Resistance, *Transition*, *2002*

This background chapter establishes the laminar-turbulent transition context of the thesis. We review the various stages involved in the process as well as the specific transition mechanisms occurring in swept-wing boundary layers. This includes Tollmien-Schlichting and crossflow instabilities. Subsequently, we present the different computational strategies able to model transition, with an emphasis on stability theory. The local and non-local theories are discussed ahead of presenting global theories and the harmonic Navier-Stokes approach. We discuss the existing transition prediction strategies before laying out literature background on transition due to surface irregularities, in line with the modelling objectives of the current work.

2.1 A tale of laminar-turbulent transition

2.1.1 The road from laminar flow to turbulent flow

The transition process of a laminar boundary layer is multifaceted, highly non-linear and to a considerable extent dependent upon many environmental conditions. For most flow configurations, the succession of stages and scenarios described by Morkovin, Reshotko and Herbert (1994) and presented in Fig. 2.1 serves as a rather empirical reference. By itself, turbulence is described as a very

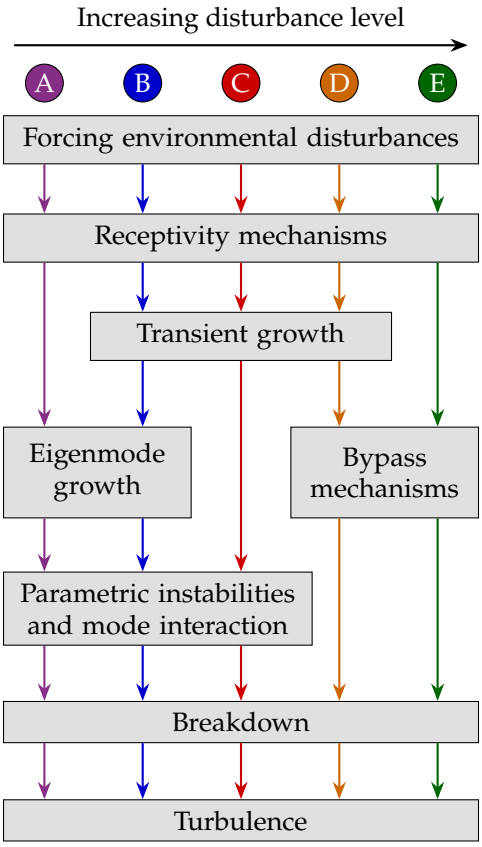

Figure 2.1: A simplified depiction of the paths from laminar to turbulent for a boundary layer, according to Morkovin, Reshotko and Herbert (1994)

dissipative process following the Richardson-Kolmogorov energy cascade, where the unstable, largest eddies break up into smaller eddies until at the smallest scales, structures are dissipated into internal energy. Transition rather conceptually appears as a reverse of the said cascade, since small-scale disturbances lead to larger-scale distortions until turbulence flares.

Laminar-turbulent transition is essentially an initial value problem, determined by the forcing environmental disturbances penetrating the boundary layer as spatial and/or temporal fluctuations. Disturbances may be of an acoustic (pressure), kinematic (vorticity) or of an entropic (temperature) nature. Surface roughness or vibration, free-stream turbulence or the external imposition of heating, cooling, suction or blowing on the boundary layer are examples of what may cause them. From an experimental or numerical point of view, minute disturbances are not directly measurable but only observed further downstream as they grow. Different paths to the breakdown of the boundary layer to a turbulent state are then conceivable according to the characteristics of disturbances (amplitude level, spectral content) but also of the surrounding environment: Reynolds and Mach

numbers, surface curvature, state of roughness or for an aircraft wing the sweep angle.

Transition is systematically initiated by how disturbances impose their signature and are internalised within the boundary layer. The term *receptivity* was picked by Morkovin (1969a) to denote such a mechanism. From that point onwards, the die is cast; via receptivity, the signature of disturbances determines the initial conditions to the process, namely their level of amplitude, phase and frequency. Disturbances are then ready to be converted into further transition mechanisms. Kerschen (1989) distinguished between *natural* receptivity and *forced* receptivity. The concept of natural receptivity pertains to the interaction between a naturally occurring acoustic, vortical or entropic disturbance and the leading edge of a wing or a roughness element. Since the generated instability wave typically has a much smaller wavelength compared to the natural disturbance, a wavelength conversion process must occur to transfer energy (Kerschen, 1989). Goldstein (1985) highlighted that sudden surface deformations are sites where such a conversion occurs. Conversely, forced receptivity does not involve any interaction, however it involves an external, unsteady forcing source whose frequency is tailored to trigger an instability wave within the boundary layer. The role of receptivity was identified long before the contribution of Morkovin, for example by Schubauer and Skramstad (1947) who demonstrated the receptivity of a flat-plate boundary layer to a vibrating ribbon to produce instability waves. Receptivity usually remains the most difficult stage to reproduce in transition prediction models for flows of practical interest (Schmid & Henningson, 2001).

In Figs. 2.1 and 2.2, path Ⓐ corresponds to a setting with very low disturbance amplitude that typically matches that of a subsonic flight with a smooth surface. In that case, receptivity is directly followed by the exponential growth of instability waves through linear mechanisms for an unstable boundary layer. The *primary*, most unstable instabilities correspond to exponentially growing eigenmodes of the boundary layer. Initially, the instabilities have an infinitesimal magnitude with respect to the flow field. Their subsequent evolution is modulated by pressure or temperature gradients, or surface mass flux. Once they reach a certain threshold of amplitude, the primary modes interact between each other and with the mean flow in a non-linear fashion before the onset of secondary (or parametric) instabilities. The non-linear interaction may lead to the saturation of disturbance amplitude, and consequently to a steady or quasi-steady modified boundary-layer flow. It is in that sense that one denotes the process as *secondary* instability of the new flow. While the primary instabilities are typically amplified on a long streamwise distance, secondary instabilities are triggered and rapidly amplified over a much

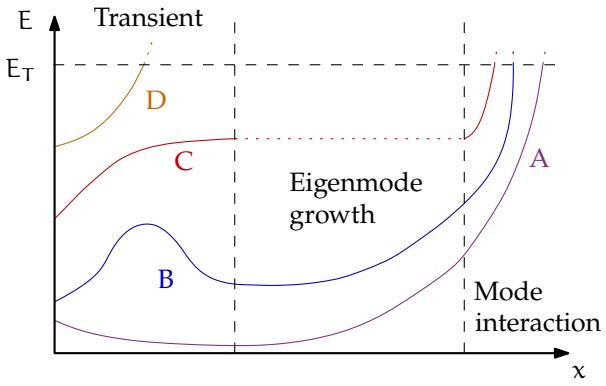

Figure 2.2: Idealised, qualitative disturbance energy evolution of one purely unstable component, according to each transition path of Fig. 2.1 except for pure bypass transition. Above E_T, breakdown to turbulence is triggered.

shorter streamwise extent (Saric, 1985). At this stage, streamwise vortices are generated and for a flat-plate flow the transition fundamentally becomes 3D.

For higher-yet-moderate disturbance amplitudes in paths B and C, the instabilities entering the boundary layer undergo transient growth. Its usual signature is through the superposition of two exponentially decaying perturbations which may exhibit an algebraic, or *transient* growth, followed by its eventual exponential decay if the disturbance amplitude remains moderate. Transient growth is explained mathematically by the non-normality, or equivalently the non-orthogonal character of eigenfunctions of the operator governing the evolution of the flow instabilities. The first study involving transient growth was offered by Ellingsen and Palm (1975) who demonstrated that a 3D fluctuation introduced in a bounded shear layer can lead to a non-modal linear amplification in time, unrelated to an unstable eigenvalue. This corresponds to the so-called *lift-up* effect labelled by Landahl (1975), observed beforehand in experiments and further explained by Landahl (1980) when he investigated algebraic instability with an arbitrary 3D disturbance. The lift-up mechanism usually leads to strong transient growth of instability streaks in otherwise linearly stable flows. Until approximately the 1990s, laminar-turbulent transition was however vastly scrutinised through the narrow prism of path A. Transient growth in time was notably developed by Hultgren and Håkan Gustavsson (1981), and Trefethen et al. (1993) who related it to the important concept of a pseudospectrum in hydrodynamic stability. Later extensions to transient growth in space followed with the work of Schmid, Lundbladh and Henningson (1994) and, for example by the contribution of Reshotko (2001). These works helped to explain why, in a few experiments, transition occurred for subcritical values of Re predicted with linear growth theory. Further transition paths were then considered, including transient growth as a candidate mechanism. According to

the magnitude of transient growth, whether it is a non-modal response to external forcing or the non-modal growth of optimal disturbances (Schmid & Henningson, 2001), the instabilities are likely to provide a higher amplitude to kick-off a linear exponential instability (path B) or short-circuit modal growth to directly kick-off secondary or non-linear instabilities (path C).

Paths A, B and C correspond to what could be called *natural* transition, as opposed to *bypass* transition occurring in paths D and E. The term was introduced by Morkovin (1969b), even though at the time transition was extensively studied through A. Any mechanism involving anything other than an unstable linear mode was by default catalogued as part of bypass transition.[1] Its definition could now include transient growth, which has offered the explanation of bypass mechanisms in various situations (Reshotko, 2001). Here, bypass transition is seen as a process emanating solely from non-modal growth mechanisms (Schmid & Henningson, 2001). Bypass transition typically occurs with a high surrounding free-stream turbulence level, or in the presence of large surface roughness. Path D describes the situation in which the action of strong transient growth results in a weakly turbulent disturbance spectrum, with high-frequency content (Reshotko, 2001). The fluctuations then force the laminar boundary layer to break down without secondary instability or mode interactions. In the presence of an even higher disturbance level, the laminar-turbulent transition completely bypasses any linear amplification mechanism following path E. Bypass mechanisms are typically characterised by the spatially and temporally random emergence of streamwise elongated streaks within the boundary layer, with alternating positive and negative streamwise disturbance velocities (Schlatter et al., 2008). With hindsight, the concept of transition may not be applied in the case of path E as there is no sufficient spatial and temporal extent for a laminar region to develop and the boundary layer instantly trips to turbulence. Some recent investigations even lead to the belief that bypass transition is not necessarily preceded by receptivity mechanisms, suggesting a possible path 'F'.

Regardless of the path followed to laminar-turbulent transition, the boundary-layer breakdown is usually more rapid than previous stages. It involves a multitude of different scales and frequencies emanating from non-linearity and breaks any symmetry present in the instability fields (Schmid & Henningson, 2001), which results in the occurrence of a few localised turbulent spots. These then grow and coalesce to form the final, turbulent boundary layer. Turbulent spots were first described by Emmons (1951) on a flat-plate flow and are represented in the

[1] A recurrent joke was that laminar-turbulent transition even bypassed the knowledge of the scientific community.

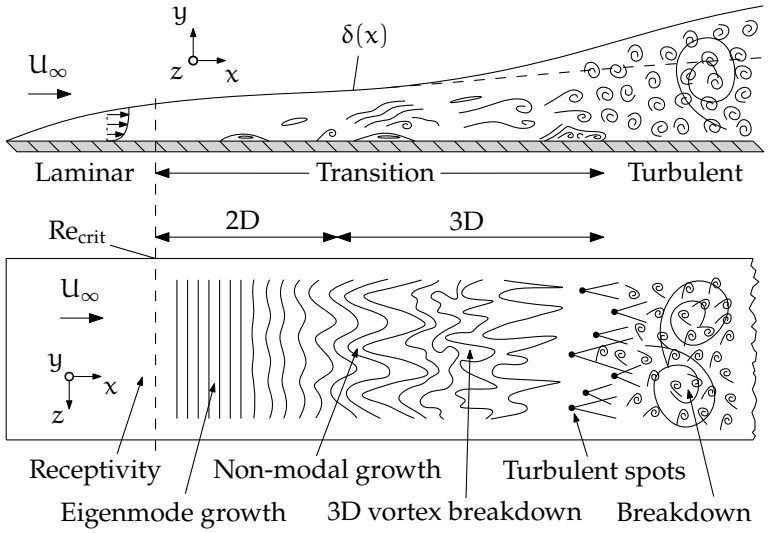

Figure 2.3: Idealised depiction of the laminar-turbulent transition process in a boundary layer developing on a flat plate, adapted from White (2006). δ denotes the thickness of the boundary layer.

idealised transition sketch in Fig. 2.3. In light of the previous descriptions it should be noted that the succession of these various paths and stages depicts laminar-turbulent transition in a rather idealised fashion as they might not always occur distinctly in nature.

The difficulty of modelling transition on an aircraft wing lies in the uncertainty on the path taken by the flow to become turbulent. As previously mentioned, a boundary layer on a smooth wing surface would typically undergo transition via path (A). However, what happens in the presence of a relatively 'small' or 'large' surface roughness? Isolated roughness elements are likely to trigger bypass transition following paths (D) and (E). Nonetheless, their location, height and streamwise extent will naturally impact the mechanisms of the transition of the boundary layer downstream. Before alluding to surface-induced transition, the typical transition mechanisms on swept wings are discussed.

2.1.2 Transition mechanisms on swept wings

Swept wings are commonly found on subsonic aircraft by virtue of their ability to delay and weaken shock waves, to increase the critical Mach number and hence to reduce wave drag at high subsonic speeds. However, their use comes at the expense of laminar-turbulent transition triggered at a more upstream position compared to an unswept wing, as Gray (1952) observed for the first time in flight tests. The boundary layer developing on a swept wing is subjected to several identified transition mechanisms, which are for the most part well understood for subsonic flights with a smooth wing surface assumption.

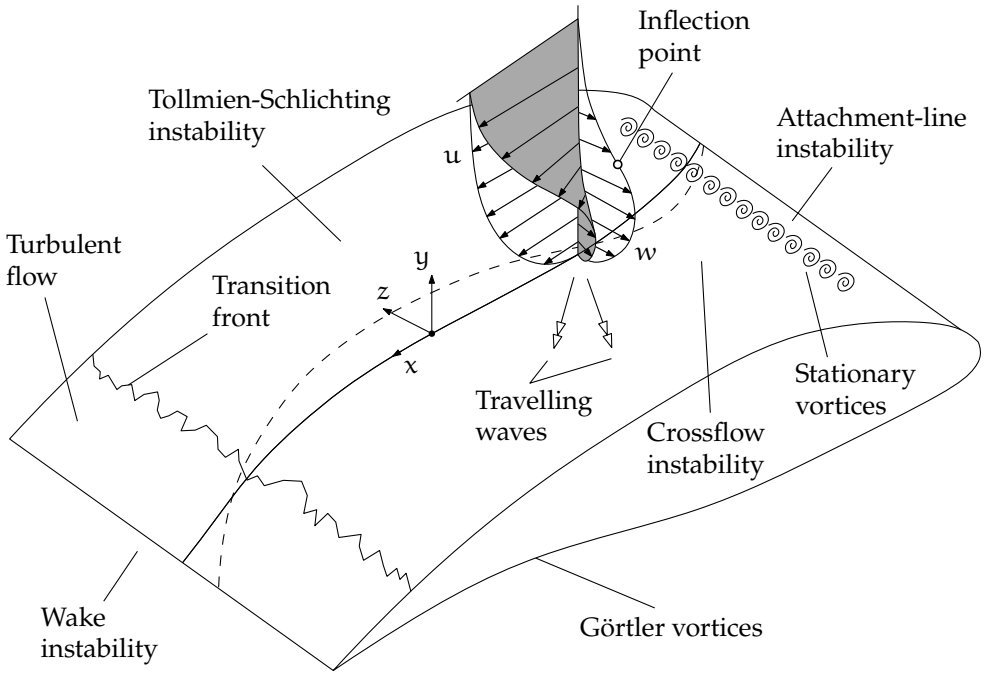

Figure 2.4: Illustration of a swept-wing boundary layer with streamwise (u) and crossflow (w) velocity profiles and associated transition mechanisms. Streamline at the edge of the boundary layer (**—**) and wall streamline (**- -**).

A taxonomy of typical transition mechanisms for 3D boundary layers appearing on swept wings is presented in Fig. 2.4. As the flow reaches the leading edge, it diverges on either side of the attachment line, resulting in a thin boundary layer formed along the upper and lower surfaces of the wing. The flow field is unaligned with the direction of the pressure gradient due to the sweep angle. Therefore, the boundary layer is 3D and the inviscid streamline at its edge is curved. From the edge of the boundary layer towards the surface, the streamwise velocity diminishes until it completely vanishes. The imbalance between the constant pressure gradient and the centripetal force is then compensated by a spanwise velocity component perpendicular to the local inviscid streamline, or *crossflow* (CF) component. This is the source of three-dimensionality of the boundary layer, represented in an exaggerated manner in Fig. 2.4. On the upper surface, the CF velocity is directed inboard as the flow is accelerating near the leading edge. Further downstream, past the pressure minimum in a decelerating flow, it is directed outboard.

A first physical hurdle that must be overcome to maintain and maximise the streamwise extent of laminarity on a wing is preventing leading-edge contamination and attachment-line instability. If turbulent flow has already been initiated by such mechanisms and relaminarisation does not occur, it is then futile to optimise the laminar wing further downstream. For a swept wing, leading-edge contamination occurs when perturbations emanate from the wing-root junction, or via the often

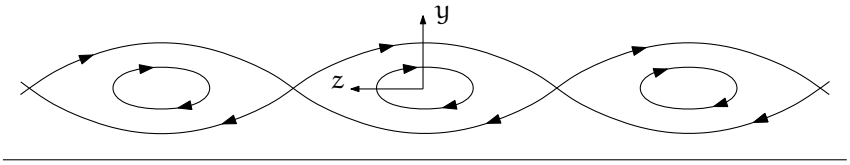

Figure 2.5: Crossflow vortices

turbulent boundary layer that has developed on the fuselage. These disturbances are rapidly propagated along the attachment line due to the dominant CF velocity component in that region, and typically trigger bypass transition. The experimental investigations of Pfenninger (1965) and Gaster (1967) showed that keeping the attachment-line Reynolds number based on momentum thickness Re_θ below 90 to 100 is necessary to avoid leading-edge contamination extending to the entire wing chord extent. This criterion remains valid to this day. Should the flow be maintained laminar in the vicinity of the attachment line via flow control or a 'Gaster' bump (Gaster, 1965), the boundary layer will be from that point onwards subjected to attachment-line instability. In this case, low-amplitude disturbances may grow along the chord via viscous mechanisms similarly encountered on a flat plate. Hall et al. (1984) uncovered a class of travelling wave disturbances later entitled 'Görtler-Hämmerlin' that play a role in attachment-line instability. Reasonable agreements with the wind-tunnel experiments from Pfenninger and Bacon (1969) led to a consensus about the critical value of Re_θ, estimated within the range 230 to 240. Therefore, clear design guidance exists to control leading-edge contamination and attachment-line instabilities. This can be achieved by adjusting the sweep angle, the leading-edge ellipticity ratio or the leading-edge radius.

Instabilities that are not induced by the leading edge are now addressed. As previously discussed, a swept-wing boundary layer has a zero CF velocity component both at the solid surface and at the edge of the boundary layer. The CF profile consequently features an inflection point, which according to Rayleigh (1880) is a necessary condition for instability. Conditions are then met for a 3D inflectional instability of inviscid type, named CF instability. It arises in regions where CF velocity varies significantly in the streamwise direction, that is in favourable pressure gradient regions (Saric, Reed & White, 2003) for a small distance downstream of the attachment line. The first experimental evidence of CF instability on swept wings is attributed to Gray (1952) before additional experiments with flow over a rotating disk were reported by Gregory, Stuart and Walker (1955), who also formalised a theoretical framework for the linear instability of 3D boundary layers. They appear in the form of spanwise-periodic vortices whose axes are nearly aligned with the local inviscid streamlines. Seen from the streamwise direction, such CF

Figure 2.6: Stationary crossflow vortices and transition front on a 45° swept wing visualised with naphthalene at $\mathrm{Re} = 2.19 \times 10^6$ (based on chord) from Dagenhart and Saric (1999)

vortices have a 'cat's eye' structure displayed in Fig. 2.5. Considering the instability alone, the vortices are counter-rotating as opposed to co-rotating when these are superimposed on the mean flow (McLean, 2012). Experimentally, their location can be marked using chemicals that are volatile to friction. Since CF vortices induce high wall shear, they leave a trail of ridges as can be seen on Fig. 2.6 in which the saw-toothed transition front pattern is also visible.

CF waves are either stationary (zero frequency) or travelling, with wavelengths of the order of three to four times the boundary layer thickness. Although both types may coexist in a swept-wing boundary layer, transition ensues from one type only (Saric et al., 2003); stationary CF waves tend to dominate in low-disturbance environments in the presence of surface roughness, minimal as it may be, whereas the impact of travelling CF is evident in high-disturbance environments with non-negligible free-stream turbulence and a smooth surface (Deyhle & Bippes, 1996). The maximum CF velocity component is typically 3% of the boundary layer edge velocity (Reed & Saric, 1989), and stationary CF disturbances are weak in the plane of Fig. 2.5. However, these are able to strongly distort the streamwise velocity profile, resulting in inflected profiles that are fertile ground for high-frequency secondary instabilities and non-linear interactions (White & Saric, 2005).

Further aft on the wing, the streamlines are more oriented towards the local streamwise direction. An adverse pressure gradient develops and the boundary layer risks destabilisation to *Tollmien-Schlichting* (TS) waves. Named after Tollmien (1929) and Schlichting (1933) who highlighted their existence theoretically by

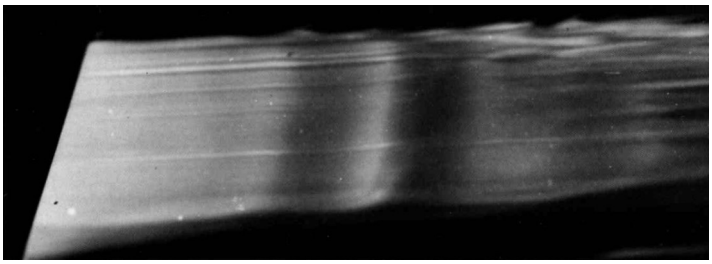

Figure 2.7: Tollmien-Schlichting waves developing in a flat-plate boundary layer at $\mathrm{Re} = 10^6$ (based on plate length) made visible with coloured fluid. © 1980 ONERA. Photograph by H. Werlé.

studying the most amplified disturbances in a flat-plate flow, this kind of instability is predominant in unswept flat-plate flows. Its observability in nature was first confirmed by the experiment of Schubauer and Skramstad (1947). Unlike CF instability which can be stationary, TS waves are travelling disturbances only, most amplified in the streamwise direction and reaching wavelengths of about 10 times the boundary layer thickness. As reflected by Fig. 2.7, they are generally 2D. Oblique TS waves may also exist in the incompressible regime but tend to be less amplified than 2D waves (Mack, 1984). However, oblique TS waves tend to be the most amplified in boundary layers where large compressibility effects arise, or naturally in 3D boundary layers. In the latter case, the most amplified wavenumber direction is tilted. Another difference with the CF mechanism is that TS instabilities solely originate from viscosity and are destabilised by adverse pressure gradients.

On a swept wing, TS and CF instabilities usually coexist. Their control then consists of a trade-off due to competing flow destabilisation effects arising from favourable pressure gradient and adverse pressure gradient regions. While the former destabilises CF and stabilises TS, the latter destabilises TS and stabilises CF. The sweep angle of the wing is also a paramount parameter. It is thought that the TS mechanism dominates transition for sweep angles between 0° and 25°, whereas CF instability is predominant in the transition process for sweep angles greater than 30° to 35° (Joslin, 1998). Both mechanisms are able to amplify and break down laminarity between these ranges (Joslin, 1998). Narrow-body aircraft wings are usually swept by 25° whereas larger wide-body aircraft use sweep angles between 32° and 38°.

The fourth mechanism involved in laminar-turbulent transition on swept wings is the so-called Görtler instability, arising when the boundary layer extends over a concave surface. The inviscid stability criterion involving the centrifugal forces exerted on a flow was described by Rayleigh (1917). Görtler (1941) revisited the

concept with laminar boundary layers and demonstrated that the solutions to the disturbance equations feature counter-rotating vortices, entitled Görtler vortices, whose axes are aligned with the streamwise direction. Additionally, these are prone to a secondary instability that originates from the distortion of the mean flow and its saturation (Saric, 1994), leading to a turbulent breakdown. The same distortion in the spanwise direction is also destabilising for TS waves (Saric, 1994). Nevertheless, the control of Görtler-type instabilities is tractable from an NLF point of view since it is sufficient to avoid concave sections along the wing. However, concavity is typically present on the lower surface of supercritical aerofoils to maximise lift in compensation to the flat upper surface designed to delay boundary layer separation induced by shock waves.

The boundary-layer instabilities involved in this thesis are mostly of the TS and CF types. While Görtler instabilities fall beyond the scope of current work, existing results on attachment-line instabilities are used as part of a verification case. As Reed and Saric (2008) pointed out, further factors have an impact on swept-wing transition. The corner flows in wing-fuselage junctions or wing-pylon junctions hold the potential to destabilise laminar flow in neighbouring regions. In addition, even at subsonic or transonic cruise speeds, the upper wing surface may display local regions of low supersonic flows involving their own transition mechanisms, falling out of the scope of this thesis. Most importantly, surface irregularities located on the wing have a significant impact on the transition process, for which a review is given in Section 2.4.

2.2 Transition modelling

CFD has proven its worth in providing reliable models with which to solve fully turbulent flows. However, modelling laminar-turbulent transition and obtaining its numerical solution remain daunting challenges given the complexity of the process previously described. Nonetheless, the relationship of CFD with laminar-turbulent transition could be deemed as dichotomous. On the one hand, it comprises methodologies for the fully resolved simulation of transition with impractical computational costs for routine use, with severe usability limitations for design engineers that explore thousands of parameters. On the other hand, it relies on methodologies based on statistical and simplistic physical models which typically fail to account for the critical mechanisms described in Section 2.1.2.

2.2.1 DNS, LES and RANS

The two methods which fall in the first category are Direct Numerical Simulation (DNS) and Large Eddy Simulation (LES). DNS solves the full, unsteady Navier-Stokes equations without any turbulence model with a grid sufficiently fine to capture the so-called Kolmogorov scales, corresponding to the smallest turbulent motions and structures. It thus allows for the accurate simulation of isolated transition mechanisms, including bypass mechanisms and breakdown, as demonstrated for example by Durbin, Jacobs and Wu (2002). Unfortunately, DNS is still limited to low Reynolds numbers as the number of degrees of freedom required for sufficient resolution scales as $O(Re^{9/4})$ and the Central Processing Unit (CPU) time scales as $O(Re^3)$. The method also necessitates high-order discretisation methods in order to minimise numerical dissipation and numerical dispersion. Nonetheless, such methods struggle to adapt well to complex geometries. Despite the continuous improvement of computing resources that has followed Moore's law, the growth rate of computational power has clearly diminished in the 2010s. Therefore, short of a quantum computing or biological computing breakthrough, it renders DNS not applicable for routine transition modelling at least in the next century for the aeronautical field (Spalart & Venkatakrishnan, 2016).

In an LES, the more energetic, larger-scale turbulent motions or *eddies* are solved while the small-scale (*sub-grid*) motions are modelled via an eddy-viscosity approach (Smagorinsky, 1963) which is essentially a low-pass filtering of the Navier-Stokes equations. Such treatment allows a coarser resolution, with a weaker dependence on Re; nonetheless the computation cost remains prohibitively high. Unless wall-layer models are used, a DNS-like resolution is indeed still needed in the vicinity of a solid wall as the assumption of isotropic small scales made by most LES models has to be discarded. Furthermore, the underlying assumption behind LES states that energy cascades from large-scale structures to small-scale structures. The principles of LES thus conceptually seem to conflict with the very essence of transition physical characteristics. In addition to this critical drawback, the transition onset predicted with LES is sensitive to the choice of the Smagorinsky constant used in the interaction model between the unfiltered scales and the filtered scales (Germano et al., 1991). The sensitivity to the sub-grid model makes LES case-dependent, since its impact may alter the determinism of early transition stages (Fasel, Meitz & Bachman, 1997) and hence lead to the relaminarisation of transitional flows. Therefore, it may be argued that LES is not sufficiently equipped to model laminar-turbulent transition. Regardless of modelling aspects, much like DNS it has also fallen victim of 'false prophecies' claiming that overnight runs of

$O(10)$ hours would become routine by now, whereas in pure computing terms industrial-scale LES is still not reached (Löhner, 2019).

The second category consists of statistical methods for transition modelling, all based on Reynolds-Averaged Navier-Stokes (RANS) equations. These are obtained by averaging the Navier-Stokes equations over time or over a set of realisations, and by incorporating additional transport equations. These are needed to retrieve the information lost by the averaging process and to close the system. The high level of turbulence modelling suppresses the need for a fine computation grid. For this reason, the RANS approach yields a more reasonable computation time. At best, the low-Re models that were developed may reproduce the features of bypass transition, yet their ability to predict transition can be questioned (Menter, Langtry & Völker, 2006). Intermittency transport methods with empirical correlations or laminar fluctuation energy methods were also proposed. According to Menter et al. (2006), two general shortcomings are of note. In general-purpose CFD codes that incorporate RANS models, computing the required boundary-layer integral quantities is not usually convenient, especially in the case of unstructured grids. Moreover, the averaging process eliminates the effects of linear disturbance growth, a salient mechanism in transition. These aspects pinpoint the impracticality of RANS for the purpose of transition modelling.

2.2.2 Stability theory: from local LST to global HNS

The methods in the category of stability theory are the ones considered in this thesis, and belong to what could be entitled *natural transition prediction*, since they are able to quantify the evolution of infinitesimal disturbances introduced in a boundary layer. Considering the framework of Lyapunov stability of dynamical systems, a finite-amplitude laminar boundary layer is seen as a point of equilibrium of the Navier-Stokes system; this is what has been referred to as the mean flow, or *base* flow[2] and is denoted $\bar{\mathbf{q}}$ from this point onwards. If the system is perturbed near the point of equilibrium with a disturbance $\tilde{\mathbf{q}}$, the system is deemed Lyapunov-stable if for a given position x and for any future time $t \geqslant 0$,

$$\forall \varepsilon > 0,\ \exists \gamma > 0 \mid \|\bar{\mathbf{q}}(x,0) - \tilde{\mathbf{q}}(x,0)\| < \gamma \Rightarrow \|\bar{\mathbf{q}}(x,t) - \tilde{\mathbf{q}}(x,t)\| < \varepsilon. \tag{2.1}$$

Otherwise expressed, if it is possible to restrain the initial perturbation near the point of equilibrium then the perturbation will decay to an arbitrarily small value at future times. The interest here is more towards stability at an infinite time horizon,

[2] Strictly speaking, the mean flow denotes a time-averaged flow field and the base flow denotes a stationary flow field. These two concepts are often conflated in the literature.

or asymptotic instability. In such case, if the equilibrium state is Lyapunov-stable then it is asymptotically stable if

$$\exists \gamma > 0 \mid \|\bar{\mathbf{q}}(x,0) - \tilde{\mathbf{q}}(x,0)\| < \gamma \Rightarrow \lim_{t\to\infty} \|\bar{\mathbf{q}}(x,t) - \tilde{\mathbf{q}}(x,t)\| = 0 \tag{2.2}$$

that is, the disturbance vanishes at an infinite time horizon below a certain threshold in the initial perturbation of the system. Otherwise, the equilibrium state is asymptotically unstable. It is in this particular setting that a laminar boundary layer is described as stable or unstable. It may be noted in passing that stability can be defined in an alternative way, for example via the kinetic energy of disturbances as suggested by Joseph (1976).

The concepts described above pertain to temporal stability analysis, which is bound to the asymptotic behaviour at large times for perturbations with real spatial wavenumbers. Conversely, spatial stability analysis[3] focuses on the boundary layer response to time-harmonic forcing in order to determine whether perturbations grow, or decay in space. The concept of spatial stability is then equally important for boundary layers in the presence of isolated roughness elements.

Naturally, disturbances arising in boundary layers may generally grow both in time and space, requiring an adjusted mathematical arsenal. At this stage, the framework is the linear response of a dynamical system to a spatially and temporally localised impulse at $(x,t) = (0,0)$. In what follows, the definitions are for the most part borrowed from the review article of Huerre and Monkewitz (1990). The evolution of the resulting wave packet, or impulse response is determined by the Green's function $G(x,t)$ which satisfies the relation

$$D\left(-i\frac{\partial}{\partial x}, i\frac{\partial}{\partial t}\right) G(x,t) = \delta(x)\delta(t) \tag{2.3}$$

where δ is the Dirac delta function, and D is the operator defining the general dispersion relation,

$$D(k,\omega) = 0. \tag{2.4}$$

Equation (2.4) characterises the coupling between spatial behaviour and temporal behaviour, respectively expressed by the wave number k and the frequency ω. The dispersion relation dictates which waves are 'permitted' in the wave packet, and governs the spatio-temporal dynamics of the system. This allows linear stability to

[3] It is also known as the 'signalling problem'.

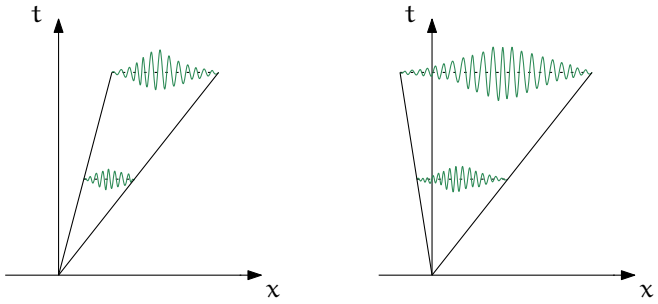

Figure 2.8: Convective (*left*) and absolute (*right*) instabilities

be defined in terms of the x-t plane. The flow is said to be linearly stable if

$$\lim_{t\to\infty} G(x,t) = 0 \quad \text{along all rays} \quad \frac{x}{t} = \text{constant} \tag{2.5}$$

and linearly unstable if

$$\lim_{t\to\infty} G(x,t) = \infty \quad \text{along at least one ray} \quad \frac{x}{t} = \text{constant.} \tag{2.6}$$

Then for linearly unstable flows, it is possible to distinguish between *convectively unstable* flows, satisfying

$$\lim_{t\to\infty} G(x,t) = 0 \quad \text{along the ray} \quad \frac{x}{t} = 0 \tag{2.7}$$

and *absolutely unstable* flows for which

$$\lim_{t\to\infty} G(x,t) = \infty \quad \text{along the ray} \quad \frac{x}{t} = 0. \tag{2.8}$$

These definitions of convective and absolute instability concepts are illustrated in Fig. 2.8. At asymptotically large times, the wave component with zero group velocity in the impulse persists at the origin. If the given wave is amplified while convected downstream away from the source and decaying at the initial location at large times, eventually leaving the flow undisturbed, the instability is convective. On the other hand, if the wave packet maintains an unbounded growth at large times at the point of impulse, propagating both downstream and upstream, the instability is absolute. The convective/absolute nature of the flow determines whether it is an *oscillator*, or a *noise amplifier* (Huerre & Monkewitz, 1990). Boundary layers tend to act as noise amplifiers, that are accompanied almost everywhere by regions of convective instability where perturbations are amplified locally and convected downstream. Noise amplifiers are rather dominated by extrinsic dynamics, where the stability is governed by the spectral content of the incoming perturbation. In contrast, oscillators display intrinsic dynamics and tend to exhibit

a characteristic frequency and a large region of absolute instability that dominates the flow.

This is an opportunity to stress the important distinction between absolute and global instability. The notions of convective and absolute instabilities are sensible only in a purely local framework, where the stability is scrutinised at a certain streamwise location. This goes hand in hand with a parallel flow assumption, considering equilibrium states that are invariant in the streamwise direction. In contrast, many boundary-layer flows of interest are non-parallel, with a strict non-uniformity in the streamwise direction especially in the presence of surface irregularities. Global instability then refers to the whole flow field, with eigenmodes featuring an unknown x-dependence. Using the concept of Green's function, the flow is *globally unstable* if

$$\lim_{t\to\infty} G(x,t) = \infty \quad \text{for some } x. \tag{2.9}$$

For base flows varying slowly in the streamwise direction, a necessary condition for global instability is the existence of a finite region of absolute instability (Schmid & Henningson, 2001).

Although beyond the scope of this thesis, it shall be highlighted that the concept of stability in transient growth analysis requires setting aside the Lyapunov stability framework, since an asymptotic point of view hinders the observation of finite-time processes. Stability is then redefined as the amplification of an initial perturbation energy over a prescribed time interval (Schmid, 2007). In such a finite internal, one may define the gain as the ratio between final disturbance energy and initial disturbance energy. In particular, Farrell (1988) denoted the initial flow disturbances producing the maximum gain as *optimal perturbations*, while the transient growth related to the maximum gain is referred to as *optimal growth*.

Deploying stability theory in practice requires the computation of the laminar base flow. Semi-analytical flows for simple or synthetic solutions are relatively straightforward to solve, whereas the use of CFD is necessary for more complex geometries. A well-known constraint is that only low Reynolds numbers yield steady laminar solutions. However, computing stable (or unstable) steady solutions past the threshold of critical Reynolds numbers has been facilitated by the development of stabilisation techniques, including the Recursive Projection Method (Shroff & Keller, 1993), the selective frequency damping approach (Åkervik et al., 2006) or the 'BoostConv' algorithm (Citro et al., 2017).

This thesis focuses on the application and the development of stability theory methodologies based on an Harmonic Navier-Stokes (HNS) formulation, where the time coordinate and the spanwise coordinate are treated in Fourier space. The aim is to have at disposal a linear framework, where global instabilities arising from linear mechanisms and likely to trigger bypass transition can be modelled—and a non-linear framework, modelling the linear growth of instabilities and ultimately the non-linear growth of instabilities. In the latter case, mode interaction and secondary instabilities are incorporated, which renders the method potentially able to model the stages occurring just before the breakdown to turbulence. The following sections review the stability theory methodologies, whose mathematical description is further given in Section 3.2.

Local approach

At one end of the spectrum, *local* approaches based on the parallel-flow or quasi-parallel-flow assumptions have dominated research on laminar-turbulent transition for a vast majority of the 20th century. The approximation of the base flow and of the disturbance field to be dependent only upon the wall-normal direction, where the effects of viscosity are most palpable, yields a tractable framework commonly referred to as Linear Stability Theory (LST). Although there is a clear overlap in the designation with respect to 'stability theory' methods, such a terminology was logical a few decades ago, when the lack of computational power dictated the use of such mathematical simplifications. The associated incompressible LST equations can be recast as the Orr-Sommerfeld equation, named after the work of Orr (1907) and Sommerfeld (1909). Seen as a one-dimensional eigenvalue problem, the TS modes are the well known, most unstable solutions to the Orr-Sommerfeld equation. Excellent reviews of LST are provided by Mack (1984) and by Schlichting and Gersten (2017). By virtue of its inexpensive computational cost, LST has been used jointly with the e^N method for transition prediction, discussed in Section 2.3.

LST constitutes a practical tool for primary investigations. For example, absolute instability regions can be detected by sweeping along the whole streamwise domain of the base flow. However, its modelling simplifications result in inherent deficiencies due to several physical effects ignored by the method, namely the streamwise history of the disturbance (from the assumption of weak variation compared to the wall-normal direction), the wall-normal velocity of the mean flow (from the assumption of negligible magnitude compared to the streamwise mean flow) and non-linear mode interactions for large disturbance amplitudes. Inhomogeneity is present only in the direction normal to wavefronts. Despite those features, as mentioned in Section 2.4 the local character of LST has not hindered its

application to investigation of the effect of roughness. Although qualitative criteria were derived, the strong non-parallelism of the base flows when either surface roughness or surface curvature are present in the streamwise direction inevitably leads to quantitative discrepancies between local methods and a method based on a non-local theory.

Non-local approach

Theoretical contributions explained the discrepancies of the critical Reynolds number and disturbance growth rates between the LST and the experiment of Schubauer and Skramstad (1947). Bouthier (1972), Bouthier (1973) and Saric and Nayfeh (1975) applied perturbation theory and the method of multiple scales, while Gaster (1974) devised an asymptotic series in terms of $Re^{1/2}$ as a correction to parallel-flow theory. Furthermore, Hall (1983) investigated the development of Görtler vortices via a set of parabolic equations, whereas Itoh (1986) also derived, independently, parabolic equations to investigate the spatial instability of travelling waves in a non-linear fashion. It is in that spirit that Herbert and Bertolotti (1987) recognised the importance of equations obtained at an intermediate step from the aforementioned contributions, named Parabolised Stability Equations (PSE), which also denotes the name given to the methodology. Simen (1992) also devised independently a similar framework to model convective instabilities in 3D and compressible non-uniform flows.

The underlying assumption of the PSE is a slow evolution of the base flow in the streamwise direction, allowing the method to incorporate the effects of mild base flow gradients, or mild body curvature. Due to their near-parabolic character, the PSE account for not only the local flow conditions, but also the upstream history of the disturbance and for this reason they are often associated with a *non-local* terminology. They are hence suited for the analysis of convective instabilities in boundary layers, for either exponential or transient growth. Their computational cost is low, due to the parabolised nature of the equations which can be solved simply by marching forward in space.

The PSE also bear the advantage that they can be easily extended to model the interaction of modes and their evolution in a weakly non-linear fashion, an approach referred to as Non-Linear Parabolised Stability Equations (NLPSE). The latter thus allows non-linear disturbance evolution and interactions to be modelled up to almost the final breakdown stages. In particular, in the non-linear modelling of CF disturbances the method progresses up to where the primary disturbances saturate. From that point onwards, the analysis of the saturated

state superimposed on the base flow is undertaken using secondary instability theory. There are a significant number of studies demonstrating the practicality of linear PSE for numerous shear flows of interest; these have ascertained its maturity, embodied by the state-of-the-art NOLOT code (Hein et al., 1994). In addition, the method has also been considerably associated with the e^N method for transition prediction purposes as a significant improvement compared to the conventional LST. A comprehensive review of linear PSE and of its non-linear extension is given by Herbert (1997), while Pralits et al. (2000) demonstrated its applicability to sensitivity analysis by means of an adjoint formulation.

The very nature of the PSE yields a fundamental drawback; absolute or global instability regions display ellipticity, which is discarded by the parabolic approach. A related, essential concern is whether they provide an appropriate framework to incorporate the effect of surface irregularities. Depending upon their height and shape, these might not constitute a 'slow' streamwise evolution for the base flow by inducing locally stronger gradients. Therefore, there should be a certain threshold of roughness geometry characteristics above which the PSE approach inaccurately predicts the disturbance evolution downstream of the said roughness element. This is specifically questionable in boundary layers with surface irregularities generating LSBs, characterised by regions of local reversed flow. Although applying the PSE method in such regions is questionable due to its near-parabolic character, Hein (2000) successfully applied PSE for pressure-induced LSBs on a flat plate. Park and Park (2013) managed to compute PSE solutions for boundary layers over 2D humps, featuring reversed flow regions. However, the authors reported NLPSE results only without reversed flow, which suggests their non-linear approach was most likely unstable in the presence of large geometrically-induced LSBs. Thomas, Mughal and Ashworth (2017) also described PSE calculations with LSBs generated by waviness on an unswept wing and suggested the reversed flow regions were not strong enough to trigger disturbances propagating upstream.

Another pitfall, from a numerical point of view, is that the PSE suffer from numerical instability when the streamwise step size is too small (Li & Malik, 1995). Hence, base flow gradients appearing in short spatial scales, or surface roughness of minute width are not successfully resolved by the method where a greater number of discrete points would be necessary, consequently violating the step-size restriction. Andersson, Henningson and Hanifi (1998) suggested the addition of a term in the equations to alleviate the step-size restriction and allowing finer streamwise discretisation. Furthermore, the PSE is unable to model the generation of boundary-layer instabilities or receptivity. For the NLPSE, initial disturbance

amplitudes at the first streamwise station must be provided by another method or often via a trial-and-error process.

Global, or harmonic Navier-Stokes approach

With the improvement of computing resources and algorithms for the numerical solutions of problems governed by Partial Differential Equations (PDEs), the local LST and non-local PSE theories have been broadened to a setting incorporating the instability of flows with less symmetry, namely with at least two inhomogeneous spatial directions. As typically considered in this thesis, a boundary-layer flow developing on an infinite swept wing presents inhomogeneity in the streamwise and wall-normal directions as opposed to the homogeneous spanwise direction, whereas a 3D roughness element induces a fully 3D flow field. With respect to stability theory, the slow streamwise evolution assumption of the PSE method is therefore lifted and analysis pertaining to that class of flows is commonly referred to as *global* stability analysis (Theofilis, 2003). Such 'global' stability terminology should not be confused with the 'global' instability described by Huerre and Monkewitz (1990).

Theofilis (2003) associates the name of global instability to an eigenvalue-based approach, where the stability analysis consists of numerically uncovering unstable eigenmodes belonging to the discrete spectra of the governing equations. More accurately, the terms 'TriGlobal' and 'BiGlobal' were proposed to respectively denote eigenvalue-based analyses of 3D base flows and two-and-a-half-dimensional (2.5D) (or 2D) base flows. Although the grounds of this terminology are more than questionable and confusing,[4] this thesis adopts the same lexicon to denote eigenvalue-based analyses in accordance with the literature.

In the global approach, the time coordinate is treated harmonically. For 2.5D base flows, the spanwise coordinate is also handled in frequency space. Therefore, for global, spatial instability analyses we also refer to the methodology as HNS. The HNS method can be seen as a linearised 'DNS' for stability analysis; besides the time and/or spanwise Fourier expansion, there is no further modelling assumption with full ellipticity in space and full retention of base flow terms. For that reason, the HNS methodology is able to resolve all short scales or account for the rapid variations of the base flow. Furthermore, the process of receptivity is also incorporated into the model, which is also able to detect both regions of absolute and convective instabilities, a clear improvement compared to the capabilities of PSE and most importantly LST. However, its computational cost is higher relative

[4] BiGlobal and TriGlobal should essentially be called 2.5D and 3D eigenvalue problems.

to the PSE approach but much less than undertaking a DNS. In this thesis, an efficient computational tool is introduced to reduce the cost of the approach.

Since the receptivity stage is directly incorporated and directly provides the evolution of a disturbance as the response to some external forcing, the LHNS embodies amplitude-based modelling compared to amplification-based modelling offered by LST or PSE. In the same vein as the PSE, the LHNS can be extended to a finite-amplitude approach where non-linear mode interactions are captured. Such an NLHNS approach has the potential for significantly accurate modelling of several transition stages from receptivity to the secondary instability of the boundary layer.

Unless sophisticated matrix-free techniques such as time-stepping (Eriksson & Rizzi, 1985; Edwards et al., 1994) are used for its numerical application, the TriGlobal problem is prohibitively expensive to solve in a matrix-forming approach. This is due to the treatment of three inhomogeneous spatial directions coupled with the application of an eigenvalue algorithm. However, the computational tool introduced by this thesis yields a short turnaround time for the usually also expensive BiGlobal analysis, able to retrieve global linear instabilities potentially leading to bypass transition. However, the BiGlobal approach is purely amplification-based. The information about growth (or decay) for a linear mode is solely encapsulated in the growth rate of the corresponding eigenvalue, while the eigenfunction gives the spatial description of the mode. Nonetheless, BiGlobal stability analysis remains a powerful tool to unravel self-sustained linear mechanisms and the associated dynamics in a given 2.5D base flow.

Reviews on BiGlobal (and TriGlobal) analyses are offered by Theofilis (2003) and Theofilis (2011), while a thorough mathematical description has been given by Groot (2018) with a level of hindsight which was certainly lacking in the field. This thesis considers BiGlobal application cases with surface irregularities that are inhomogeneous in the streamwise direction, a framework in which the analysis is known to be significantly sensitive numerically and to yield convergence of the global spectrum with some difficulty. It may furthermore be mooted that such an eigenvalue-based analysis requires significant effort to provide further insight into the physical mechanisms associated with the instability modes. Furthermore, there are restrictions in performing the analysis in Fourier space, since considering discrete modes leaves the 'return' to physical space not straightforward.

2.3 Transition prediction

While a laminar boundary layer possesses intrinsic characteristics, a specific transition Reynolds number simply does not exist. Unfortunately, the 'many faces of transition' (Morkovin, 1969b) described in Fig. 2.1 exacerbate the difficulty of accurately predicting the location of laminar-turbulent transition, since the process is heavily dependent upon the level of environmental disturbances. Even the environmental settings themselves are tedious to correlate; a low-turbulence in-flight environment typically differs from a high-turbulence wind-tunnel environment. Besides, the variety of transition mechanisms arising on a swept wing potentially competing with each other and the complications of in-flight characterisation of surface roughness have compounded the task of accurate transition prediction. The latter was however identified as a key area of development in the NASA's CFD Vision 2030 study, on the basis of the tremendous gap between the capabilities of transition modelling and the CFD state of the art. This matter was highlighted by Slotnick et al. (2014, p. 25), stating that

> '[...] [A]n additional research thrust must be devoted toward the development of reliable and practical transition models that can be incorporated in the turbulence models being matured along each of the development tracks. The transition prediction method should be fully automatic, and be able to account for transition occurring from various mechanisms such as Tollmien-Schlichting waves, cross-flow instabilities, Görtler vortices, and non-linear interactions associated with bypass transition.'

Aircraft design, and in particular the scaling process from wind-tunnel tests to flight, are currently impacted by the lack of a robust transition prediction capability. Most CFD tools based on Navier-Stokes equations are consequently run with a fully turbulent state assumption (Slotnick et al., 2014). In the transition community, the lack of a universal description of transition prompted the introduction of both purely empirical approaches, and semi-empirical approaches coupled with local and non-local stability theories. This section briefly reviews these widespread, existing methods.

The first category of correlation that appeared was based on boundary layer integral quantities. Michel (1951) devised a correlation based on experimental data with the momentum thickness Reynolds number. Owen and Randall (1952) introduced a criterion based on a CF Reynolds number. A further method was provided by Granville (1953) with the momentum thickness Reynolds number expressed as a function of the so-called Pohlhausen parameter. Later, Pfenninger

(1977) linked the CF Reynolds number with the CF shape factor for the design of supercritical aerofoils. Some of these old correlations were further extended in the following decades. Such empirical criteria are straightforward to implement and yet tend to have a limited domain of application, while they totally discard the modelling of transition mechanisms.

Motivated by exploiting boundary layer profiles directly rather than indirectly via integral quantities, van Ingen (1956) and Smith and Gamberoni (1956) introduced independently the e^N method. It is based on the linear growth of instabilities, following the hypothesis that the non-linear mode interactions and breakdown stages extend over a small spatial extent, with a rapid 'burst' to turbulence. Therefore, the transition onset is assumed to be triggered when the wave amplitude A is e^N times the wave amplitude A_0 at the beginning of amplification. For a 2D boundary layer, a disturbance is entirely determined by its frequency f and the N-factor is defined as the envelope of the amplification curves as

$$N(x) = \max_f \left\{ \ln \left(\frac{A(x)}{A_0} \right) \right\}. \tag{2.10}$$

The e^N method is semi-empirical to the extent that the calculated N-factor needs to be experimentally correlated for determining the critical value of N at the transition onset. Naturally, for a given streamwise location, higher critical N-factors are reached with lower turbulence levels, whereas the presence of roughness or high free-stream turbulence decreases the critical N-factors. In a low-turbulence environment and 2D boundary layers, the critical value $N = 9$ was assumed to be valid for a certain period of time[5] whereas it is now accepted that the transition onset occurs when the N-factor reaches values ranging from 7 to 10 (Arnal & Casalis, 2000) meaning the disturbance has been amplified up to roughly 1,100 to 22,000 times compared to its initial amplitude.

Worthy of note is that 3D boundary layers, typical of swept wings complicate the application of the method. How should we deal efficiently with different mechanisms involved in the transition process and different directions of propagation? The reviews of Arnal (1994) and Arnal and Casalis (2000) discuss the scope of the method as well as the interrelated considerations when 3D boundary layers are involved. It is possible to compute an N-factor via the envelope of several envelope curves, while situations with simultaneous TS and CF mechanisms have motivated the introduction of distinct N-factors, respectively N_{TS} and N_{CF} with differing critical values. A further ambiguity concerns along which path should

[5] The method was originally called e^9-method for that specific reason.

the amplification be computed, whether it is along the chord direction, along the group velocity direction or along the potential flow direction.

The e^N-method has been the prevalent transition prediction method in the aeronautical industry, associated with the application of LST or PSE. For 3D flows, it nonetheless suffers from several pitfalls. There is an important scatter of the N values given by the various computation strategies, and the method produces pathological cases when TS and CF instability coexist (Arnal & Casalis, 2000). These pitfalls could have been expected due to the simplicity of the method discarding important transition stages; it does not account for the perturbation amplitude upstream of the first neutral point, implying that the receptivity mechanism is completely neglected. As explained, it also discards non-linear interactions as the growth rate is integrated only along a linear amplification path. Consequently, its ability to absorb the effect of surface irregularities involving more complex physics may be questioned.

A related approach introduced to simplify the computation of growth rates or N-factors is to use a database. Exact linear stability theory results are generated *a priori* for a wide range of parameters such as integral quantities, velocity peaks or local Reynolds numbers and usually for self-similar boundary layers. In this way, the parameters necessary for the application of the e^N-method on an unknown boundary layer are determined via interpolation from tabulated values or analytical relationship from the database. These database methods were proposed by Arnal (1989), Stock and Degenhart (1989), Gaster and Jiang (1994) and Drela (2003) in the case of TS waves. For CF instabilities, databases were designed by Dagenhart (1981) and Casalis and Arnal (1996). Later, van Ingen (2008) developed a database with stability diagrams characterised by the shape factor of velocity profiles. An analogous, albeit more sophisticated approach consists in applying neural networks, for which the pioneers were Fuller, Saunders and Vandsburger (1997) who managed to compute disturbance growth rates associated with jet flows. Crouch, Crouch and Ng (2002) also used neural networks to determine TS and CF N-factors for low-speed swept-wings.

However, in view of the importance of the receptivity process, a need to shift from an amplification-based prediction to an amplitude-based prediction has been identified. This led to further methodologies that are presented briefly below. In line with experiments where the transition location was closer to the leading edge with higher levels of free-stream turbulence, Mack (1977) suggested an empirical correlation between the N-factor and the turbulent intensity Tu for

the amplification of 2D TS waves,

$$N = -8.43 - 2.34 \ln(Tu) \tag{2.11}$$

valid for $0.1\% < Tu < 2\%$ and calibrated to fit wind-tunnel experiments without pressure gradients. This was a first example of a linear amplitude-based method expressed via a variable N-factor relationship. Later, Crouch and Ng (2000) formally introduced the variable N-factor method, accounting for the effects of surface roughness and the level of turbulent intensity for 3D boundary layers. The method combines a receptivity model, linear growth and an amplitude correlation, and yielded fine agreement with experimental data for CF instabilities in low-to-moderate disturbance levels (Crouch & Ng, 2000).

Finally, transition prediction capability may make a leap forward with the consideration of non-linear amplitude methods. Including the effects of non-linear mode interaction to describe breakdown has the potential to trace the onset of transition via monitoring of the averaged wall shear, which has been demonstrated experimentally. That is what Chang and Malik (1994) performed by means of NLPSE on supersonic boundary layers, as they highlighted the sudden rise in average skin-friction. Malik et al. (1999) also employed NLPSE computations and suggested an N-factor correlation based on secondary instability modes which turned out to be more robust in matching experimental values compared to an amplitude-based criterion.

Crouch (1997) insisted that '[g]iven sufficient information about the free-stream environment and the aircraft geometry and surface finish, a non-linear amplitude-based prediction method can be expected to yield the best estimates of the transition location.' It should be highlighted that receptivity is incorporated in the NLPSE approach solely by the 'manual' prescription of initial disturbance amplitudes for individual modes involved in the transition. Therefore, those must be tailored to match a given experimental setting or a given disturbance environment which often proves out to be dependent upon a trial-and-error approach. An alternative is to provide an appropriate receptivity model. For example, Chang and Choudhari (2005) used adjoint PSE to determine receptivity efficiency functions and predicted accurately the inflow disturbance environment for the NLPSE computations on a supersonic swept wing. In the same vein, adjoint methodologies were also employed to compute receptivity-based input for NLPSE applied to stationary CF vortices (Hanifi, 2015).

The NLHNS concept introduced in this thesis has potential to encompass detailed spectral content of the disturbance for critical modes without relying on a manual prescription of their amplitude or on a receptivity model.

2.4 State of the art on surface-induced transition

Understanding and quantifying the sensitive impact of surface imperfections on transition is essential for the practical application of flow control aiming at maintaining laminarity and for sustaining its benefits. On an aircraft wing, sources of surface roughness include maintenance damage due to scratches or impacts, hail dents, insect contamination, residuals of grease or liquids, or ice accretion. There are also rivet heads, or natural excrescences formed by junctions between detachable components located on the leading edge and on the wing box. These are all visible in the lower part of Fig. 1.2.

Surface roughness generally acts as a receptivity site which leads to modulations of the base flow. These interact with free-stream disturbances or pre-existing boundary-layer instabilities and typically generate streamwise or spanwise vorticity, thus impacting upon local disturbance growth and convection. Roughness may be an amplifier (or an attenuator) of convective instabilities, or may induce regions of absolute instabilities. There is a multitude of parameters involved in the roughness interaction with the boundary layer such as its shape, size and location; although literature contributions are numerous, accounting for all these aspects along with the flow parameters and surface curvature in a globalised fashion is simply impossible. In addition to that, a distinction must be made between 2D roughness in 2D boundary layers, 2D roughness in 3D boundary layers or 3D roughness in 3D boundary layers.

The height of the roughness relative to the local boundary-layer displacement thickness h/δ^* is naturally an important guide to gauge its ability to trigger an early transition. Above a certain threshold, flow separation may occur, which engenders reversed flow prone to instabilities. However, such a unique height measure is not linked with the flow dynamics and cannot fully describe transition characteristics. Among the first experimental studies focusing on surface-induced transition on either flat plates (Tani, Hama & Mituisi, 1940) or aerofoils (Fage, 1943), a quantity of interest was the roughness Reynolds number Re_{hh}[6] which is defined as

$$Re_{hh} = \frac{U(h)h}{\nu} \tag{2.12}$$

[6] also commonly encountered in the form Re_h, Re_k or Re_{kk}.

where $U(h)$ is the unperturbed streamwise velocity at the roughness height, h. Another roughness Reynolds number, though this time based on the free-stream velocity, has also been utilised as an alternative (Nenni & Gluyas, 1966),

$$Re_{h\infty} = \frac{U_\infty h}{\nu}. \tag{2.13}$$

Experiments in the 1950s employed correlations based on the critical roughness Reynolds number $Re_{hh,crit}$ below which transition location remains unaffected and above which the transition location starts to shift upstream. Such a correlation based on $Re_{hh,crit}$ does not encompass the whole complexity of the transition in the presence of a roughness element.

In broad terms, low roughness elements ($h/\delta^* \approx 10\%$) distort only slightly the base flow and do not induce wake regions of non-negligible vorticity. They tend to act as a linear amplifier of incoming disturbances. When investigating the receptivity of a 2D roughness to sound, Saric, Hoos and Radeztsky (1991) found that the TS amplitude evolved linearly with roughness height for Re_{hh} in the 0.5 to 5 range. Medium roughness element heights cause the receptivity to become non-linear (Saric et al., 1991), while distorting the base flow sufficiently to yield vortical structures just behind the roughness and velocity streaks further downstream (Gaster, Grosch & Jackson, 1994). However, the rapid stabilisation of the base flow in the streamwise direction typically overcomes the unsteady disturbance growth, hence these tend to decay and a laminar state of the boundary layer can be maintained (Ergin & White, 2006). Finally, high roughness elements ($h \approx \delta^*$ or above) yield a significant mean flow distortion and complex flow patterns in their wake where the effects of non-linearity may cause transition abruptly just downstream of the roughness location via a bypass mechanism. It should however be highlighted that specific roughness arrangements act as passive laminar flow control devices and delay transition, as demonstrated for example with the stabilisation of TS waves by longitudinal streaks (Cossu & Brandt, 2004; Fransson et al., 2005), or with the suppression of the most linearly unstable CF disturbance by discrete roughness elements (Saric, Carrillo & Reibert, 1998).

2.4.1 Roughness in 2D boundary layers

Naturally, the impact of roughness in 2D flows has been a first building block and numerous authors undertook theoretical or experimental studies.

Humps

Fage (1943) examined with wind tunnel experiments the effect of various surface irregularities, namely humps, indentations and ridges on a flat plate with a small favourable pressure gradient and on an aerofoil. Several investigations (Nayfeh, Ragab & Al-Maaitah, 1988; Cebeci & Egan, 1989; Masad & Iyer, 1994) applied LST and the e^N-method to the case of a 2D flat-plate hump and found qualitative agreement with the experiment of Fage (1943). Masad and Iyer (1994) observed a gradual upstream shift of the predicted transition onset location as the height of the hump is increased, until the latter reaches a critical value inducing a rapid shift. However, beyond that threshold, the transition location remains unaffected. Increasing the width of the hump moves the transition location further downstream. Wörner, Rist and Wagner (2003) applied DNS to confirm the destabilisation effect of a 2D hump on TS waves. Their amplification varied linearly with the height of the hump roughly up to $h/\delta^* = 0.5$ and to vary non-linearly for $h/\delta^* \approx 1$. A rectangular hump was found to be more destabilising than a rounded hump, while as revealed in previous studies the effect of its width is less than that of its height.

Park and Park (2013) applied PSE and NLPSE to ascertain the influence of 2D humps on TS waves, computing the base flows with DNS. Non-linear effects were apparent when amplitudes of the incoming waves reached above 1% of the free-stream velocity. Even with a low disturbance amplitude, the hump induced a strong amplification and its presence shifted the location of breakdown upstream. A subharmonic mode was found to be unstable over a wide range of spanwise wavenumbers, while the growth of the secondary waves was mostly affected by the amplitude of the primary wave. Franco Sumariva, Hein and Valero (2020) focused on the effect of humps on TS waves by means of an adaptive method where PSE is applied in near-parallel flow regions and LHNS is applied in the region of the hump. The authors computed the base flow solutions with RANS without turbulence modelling. Relative to the local boundary-layer displacement thickness, they distinguished three groups of height; for small and medium humps, the transition location based on the N-factor moved only slightly upstream for smooth humps whereas it was severely impacted when the humps had a rectangular shape. High rectangular humps promoted transition immediately downstream of the hump, while the TS amplification behaviour of large rounded humps depended greatly on their length. 3D TS waves were also found to be less amplified than 2D TS waves.

Worthy of note is also the contribution of de Paula et al. (2017), who carried out measurements of the scattering of a 2D TS wave by a cylindrical element placed

in a zero-pressure-gradient region of an aerofoil section. The wave scattering was linear up to heights equalling approximately 8% of the local displacement thickness and quadratic for heights as large as 20%.

Indentations

Thomas et al. (2018) analysed the effect of small, smooth Gaussian-shaped indentations located on an unswept aerofoil on the amplification of TS waves using PSE and LHNS. Their base flow solutions were obtained using RANS and setting the transition location far downstream in the chordwise direction. TS disturbances were found to be significantly amplified by deeper and wider gaps, and a correlation between the N-factor variation and the indentation geometry was suggested.

Waviness

2D waviness imposed on a boundary layer was studied by Lessen and Gangwani (1976) who found that Re_{crit} decreased by 10% when a waviness amplitude of only 1% of the boundary layer thickness was imposed. Later, Holmes et al. (1985) experimented with waviness on an unswept wing, but with the orientation of the waviness set at some angle to the leading edge. It triggered a large adverse pressure gradient that drove TS destabilisation. Thomas et al. (2016) focused on 2D surface waviness on an unswept, infinite wing section. They found that waviness promoted TS growth, especially for smaller wavelength and larger amplitude surface variations as the N-factor scaled with h^2/λ where λ is the wavelength, consistently with Wie and Malik (1998) who performed their analysis on a flat plate. The phase of the waviness was also found to be a TS modifier. However, unlike in the analysis of Wie and Malik (1998), longer wavelength deformations were found to damp TS waves by creating a more intense favourable pressure gradient section compared to a smooth surface.

Steps

A general trend observed in the literature is that 2D Forward-Facing Steps (FFSs) seem less detrimental in promoting transition compared to 2D Backward-Facing Steps (BFSs). In the case of 2D steps, experiments conducted by Nenni and Gluyas (1966) led the authors to suggest an empirical criterion based on $Re_{h\infty}$. They associated critical values above which the transition location moves significantly, namely $Re_{h\infty,crit} = 900$ for a BFS and $Re_{h\infty,crit} = 1{,}800$ for an FFS. In an analogous manner, the experiments of Holmes et al. (1985) confirmed that the critical step

height was larger for an FFS than for a BFS. Perraud and Séraudie (2000) also confirmed with LST the validity of the said criterion, and noted that the upstream shift of the transition front was rather rapid for FFSs and more gradual for BFSs as the step height increased. However, this was tempered by the experiments of Drake et al. (2010) who reported a gradual forward movement of transition location with FFSs, although still less gradual than corresponding BFSs. Their contribution as well as a previous series of experiments (Drake, Bender & Westphal, 2008) also suggested that a favourable pressure gradient increased the maximum attainable height for which transition location does not move forward, for both kinds of steps.

Further experiments on a flat plate (Wang & Gaster, 2005) suggested that, under similar free-stream parameters and absolute step height, the forward movement of transition is larger for a BFS than for an FFS, and that the decrease in the transition N-factor correlated with the relative step height. Similar conclusions were reached in another flat-plate experiment (Crouch, Kosorygin & Ng, 2006) where the transition N-factor was found to vary linearly with h/δ^*. For equal step heights, the N-factor reduction was greater for BFSs compared to FFSs which correlates with previously mentioned contributions. Crouch and Kosorygin (2020) extended that work and showed that the variable N-factor method on a TS-dominated flat-plate boundary layer reproduces well the effect of a rectangular protrusion modelled by a linear combination of an FFS and a BFS. Nonetheless, it was found that the effect of the protrusion could be mostly attributed to the BFS, with less impact from the FFS further downstream. This seems to confirm the more destabilising role of BFSs; 2D FFSs can even have a stabilising effect on the boundary layer (Wörner et al., 2003). Crouch and Kosorygin (2020) also stated that the method overestimates the effects of steps when these are well upstream of the instability neutral point, suggesting the steps affect TS growth rather than receptivity.

Xu, Lombard and Sherwin (2017a) also considered the effect of 2D FFSs whose height ranged from 4% to 30% of the local boundary layer thickness, and with varying shape. They concluded that TS growth rates were similar between smooth steps and a flat surface, provided that the step height remained small and that the frequency remained large. For larger steps, destabilisation was more evident and even clearer for sharp steps since they induce the formation of an LSB, which mitigates previous observations. The topic of LSBs is further developed in Section 2.4.3. These features are in agreement with the experiments of Holmes et al. (1985), who emphasised the importance of the FFS shape with respect to its critical step height and reported that $Re_{h\infty,crit}$ increased from 1,800 to 2,700 when the FFS was adjusted from sharp to rounded. Hildebrand, Choudhari and

Paredes (2020) computationally reproduced the experimental conditions of Wang and Gaster (2005) and used a combination of PSE and LHNS to assess transition prediction in the presence of BFSs of varying heights. These yielded a strong destabilisation, especially for high frequencies, immediately behind the step before a weak stabilisation until the growth rates returned to their roughness-free values. Their excellent agreement with measured transition locations was attributed to the BFS-induced destabilisation rather than the TS amplitude variation due to additional receptivity in the vicinity of the step.

2.4.2 Roughness in 3D boundary layers

There are still many areas to explore with 3D boundary layers. It has been explained that TS instability may be easily controlled by prescribing a favourable pressure gradient but to the detriment of the stability of CF. Therefore, there is a critical need for gaining further insight into the interaction between surface excrescences and CF instability, and into the mechanisms it engenders. Theoretical or experimental studies of roughness elements in swept-wing flows remain scarce.[7] Ashworth and Mughal (2015) analysed the effect of a shallow 3D indentation on an NLF wing section with PSE-3D and demonstrated that stationary CF modes with high wavenumber are highly destabilised and amplified in the indentation wake where stationary CF would normally be stabilised.

In the case of steps, Perraud and Séraudie (2000) conducted swept-wing experiments with varying step heights, sweep angles and angles of attack. Swept-wing steps displayed similar qualitative behaviour as flat-plate steps in that the move of transition front was sudden for FFSs, as opposed to more gradual for BFSs. The authors also confirmed that $Re_{h\infty,crit}$ for BFSs was approximately half of that for FFSs, but they found a noticeable sensitivity of $Re_{h\infty,crit}$ in the CF-dominated boundary layer.

Research on more detailed mechanisms associated with steps, beyond correlation of height with transition location, has recently gained more traction. In contrast to the qualitative step behaviour in 2D boundary layers with respect to TS instabilities, the experiments of Duncan et al. (2014) indicated that the FFS led to a larger CF N-factor increase than the BFS. Saeed, Mughal and Morrison (2016) later performed experiments to analyse the impact of sharp steps on CF on a swept wing. They observed that excrescences near the neutral point induce the greatest value dispersion of stationary CF amplitude. Steps placed further downstream

[7] except with arrays of discrete roughness elements used for laminar flow control, not considered in this thesis.

and of greater height seemed to promote earlier transition. Signs of travelling CF instabilities were captured in their data acquisition; the authors attributed the earlier transition to the interaction between the more developed stationary CF and the travelling disturbance. Above a threshold height, the excrescence did not impact the boundary layer development.

Further insight into the physics associated with steps in a swept-wing flow was gained thanks to Tufts et al. (2017). Their computations suggested a physics-based correlation between the critical FFS height and the height of the core of the incoming stationary CF vortex interacting with the helical flow region downstream of the step. That critical height was associated with a sharp amplification of stationary CF modes as well as an upstream movement of the transition front towards the step. No stationary mode amplification was identified in the presence of BFSs. Rius Vidales et al. (2018) carried out a parametric, experimental study on a swept wing and distinguished three regimes in terms of transition location and transition front pattern with an FFS. They emphasised that their boundary between sub-critical and critical regimes agreed reasonably well with the criterion provided by Tufts et al. (2017).

Eppink et al. (2018) performed measurements in the wake of a BFS of nearly half the local unperturbed boundary-layer thickness placed on a swept flat plate with an imposed pressure gradient to promote the growth of stationary CF vortices. The step caused an increase of stationary CF amplitude and an upstream shift of the transition front, yet she found that travelling CF, a TS wave and shear-layer instability all persisting after the reattachment region most likely contributed significantly to transition. Subsequently, Eppink (2020) dedicated herself to studying experimentally the FFS-induced mechanisms associated with CF instability growth and breakdown on a swept flat plate. Besides revealing a correlation between critical step height and initial amplitude of CF vortices, two regions of growth were identified for steps above critical height; the first one was linear whereas the second one ensued from the high-intensity modulation of the shear layer by the stationary CF vortices. A vortex-shedding mechanism was related to the unsteady transition mechanisms, occurring downstream of reattachment regions.

Concerning TS and CF instabilities on swept wings with surface features, there exists a clear gap between the growing variety of experimental studies and the sparsity of numerical investigations supporting these experiments. Such surface irregularities in 3D boundary layers may trigger 3D LSBs and hence boundary-layer destabilisation mechanisms that interact with each other.

2.4.3 Laminar separation bubbles

Localised surface irregularities can indeed induce a strong adverse pressure gradient in the streamwise direction and separate the boundary layer from the surface on which it is developing. This creates a separation or recirculation bubble if the flow reattaches further downstream. Although such an LSB might be stable due to limited energy exchange with the outer flow, these are prone to shear layer instabilities. Rodríguez, Gennaro and Juniper (2013) argue that 2D LSBs not only act as amplifiers, but also as oscillators if there exists a spatial region in the underlying base flow that sustains upstream-propagating waves.

Watmuff (1999) generated an LSB on a flat plate by means of an adverse pressure gradient region. The generated wave packet underwent an increase in its spectral content and was dispersive. Contrary to previous literature studies that referred to a TS mechanism, the author attributed the dispersion to a Kelvin-Helmholtz mechanism. Downstream of the region of separated flow, the mechanism was found to amplify the wave amplitude and the behaviour became non-linear as the formation of roll-ups led to a vortex loop in the reattachment region. Later, Diwan and Ramesh (2009) also studied experimentally and via Orr-Sommerfeld theory LSBs generated by an adverse pressure gradient. In similar observations to Watmuff (1999), the primary instability mechanism in the LSB associated with the separated shear layer was inviscid and inflectional in nature, yet most importantly originating from the region upstream of separation. Furthermore, they claimed the classical Kelvin-Helmholtz instability mechanism contributed to the origin of the inviscid instability only if the separated shear layer was significantly away from the wall. Xu et al. (2017b) computed boundary layer flows convecting over localised 3D surface indentations. LSBs arose within them and transformed pre-existing 2D TS waves into 3D TS waves. These were rapidly destabilised, which led to breakdown further downstream even at low Reynolds numbers. Moreover, they identified an inflectional instability of the separated shear layer as the cause of TS destabilisation.

On the other hand, there are further mechanisms involved in the instabilities of LSBs. Hammond and Redekopp (1998) analysed the instability of Falkner-Skan-Cooke (FSC) boundary-layer profiles with increasing magnitude of the reversed flow and suggested that an absolutely unstable behaviour ensues if the peak reversed flow velocity surpasses about 30%. The DNS computations of Alam and Sandham (2000) led them to state a peak reversed flow of 15% to 20% is required for the onset of absolute instability. The authors also concluded that the primary

instability of 3D LSBs with peak reversed flow velocity of less than 8% is of a convective nature.

From a global instability perspective, Theofilis, Hein and Dallmann (2000) investigated via BiGlobal analysis the existence of spanwise-periodic stationary and travelling global modes. Only the stationary mode was found to be linearly unstable, yet the authors conjectured both kinds of modes may become unstable for different parameters. They argued that these global mode findings corroborated previous topological arguments stating that an LSB in a 2D boundary layer leads to the onset of three-dimensionality, flow unsteadiness and vortex shedding. Rodríguez and Theofilis (2010) applied BiGlobal analysis in an LSB flow and stated that the threshold for the 3D centrifugal instability was as low as 7% of peak reversed velocity in the base flow. Their adjoint analysis enabled them to localise the mechanism responsible for the self-excited global mode in the vicinity of the recirculation region. Furthermore, the existence of two global linear mechanisms was further refined by Rodríguez et al. (2013), unveiling a centrifugal instability leading to the steady three-dimensionalisation of the LSB as well as a global oscillator dependent upon regions of absolute inflectional instability. After investigating a variety of LSBs, they confirmed the 7% threshold of peak reversed flow velocity for the existence of the centrifugal mode, and added that the global oscillator does not become active below 12%. Their findings were against the trend of previous literature, which generally assumed that the global oscillator resulting in self-sustained 2D vortex shedding was the primary instability.

Chapter 3

Mathematical Formulation

> Young man, in mathematics you don't understand things. You just get used to them.
>
> —John von Neumann

This chapter lays the mathematical foundations for the stability of boundary layers further analysed in this work. After deriving the incompressible Navier-Stokes equations from the kinetic theory of gases, we present the linear and non-linear stability analysis frameworks based on the time-harmonic and spanwise-periodic counterpart of the equations. We eventually discuss the boundary conditions and precisely the absorbing treatments implemented, which encompass the perfectly matched layer. For most future developments of this chapter, we adopt tensor form notation with the del operator ∇ used to apply the gradient, the divergence or curl of a scalar or vector field.

3.1 The Navier-Stokes equations

For the last few decades, CFD and laminar-turbulent transition modelling have employed a formalism based on the Navier-Stokes equations, which govern the motion of viscous fluids at a macroscopic scale. Although these equations were first obtained in a continuum mechanics framework, it is also possible to derive them using the kinetic theory of gases, which is set at the mesoscopic level. This theory is able to describe the motion of a fluid seen as a set of molecules whose size is significantly smaller than the average distance separating them.

3.1.1 From molecular description to macroscopic dynamics

Consider a phase space formed of possible positions $\mathbf{x} \in \mathbb{R}^3$ and momenta $p = m\mathbf{c}$ where m is the molecular mass and $\mathbf{c} \in \mathbb{V}^3$ the molecular (microscopic) velocity. Let t denote the time coordinate. The fundamental object in the kinetic approach is the distribution function $f(\mathbf{x}, \mathbf{c}, t)$ representing the density of molecules in both physical and velocity 3D spaces, as a mesoscopic description. It is defined such that $f(\mathbf{x}, \mathbf{c}, t)d\mathbf{x}d\mathbf{c}$ can be interpreted as the mass of the molecules positioned within the volume delimited by $\mathbf{x}$ and $\mathbf{x} + d\mathbf{x}$ and whose velocity lies between $\mathbf{c}$ and $\mathbf{c} + d\mathbf{c}$ at a time $t \geqslant 0$. The macroscopic variables are linked to their microscopic counterparts via the moments of the distribution function. Integrating over all possible velocities, the macroscopic density ρ is the zeroth moment,

$$\rho(\mathbf{x}, t) = \int_{\mathbb{V}^3} f(\mathbf{x}, \mathbf{c}, t)\, d\mathbf{c} \tag{3.1}$$

and the macroscopic velocity $\mathbf{u}$ is retrieved from the first moment of f such that

$$\rho(\mathbf{x}, t)\mathbf{u}(\mathbf{x}, t) = \int_{\mathbb{V}^3} \mathbf{c} f(\mathbf{x}, \mathbf{c}, t)\, d\mathbf{c}. \tag{3.2}$$

The spatial and temporal evolution of the distribution function f is determined by the Boltzmann equation which, in the absence of any external forces affecting the velocity of the molecules, can be written as

$$\frac{\partial f}{\partial t} + (\mathbf{c} \cdot \nabla) f = \mathcal{C}(f). \tag{3.3}$$

The distribution function is thus advected with the velocity of its molecules and redistributed in velocity space by the source term $\mathcal{C}(f)$ due to collisions. The source term is therefore coined as the collision operator. Bhatnagar, Gross and Krook (1954) modelled the term by a simple relaxation force term,

$$\mathcal{C}(f) = -\frac{1}{\tau}(f - f_{eq}) \tag{3.4}$$

meaning the distribution function tends towards an equilibrium distribution f_{eq} with a relaxation time τ. It can be interpreted as an average time between successive collisions. This is known as the Bhatnagar-Gross-Krook (BGK) approximation. If the gas (fluid) is assumed to remain in thermal equilibrium, the equilibrium distribution is the Maxwell-Boltzmann distribution,

$$f_{eq} = \rho \left(\frac{1}{2\pi RT}\right)^{3/2} \exp\left(-\frac{|\mathbf{c} - \mathbf{u}|^2}{2RT}\right) \tag{3.5}$$

where $R = k_B/m$ is the specific gas constant linked to the Boltzmann constant k_B, while T is the temperature. Furthermore, molecular collisions have the property of conserving mass and momentum. This can be expressed in terms of moments of the collision operator as

$$\int_{\mathbb{V}^3} \mathcal{C}(f)\, d\mathbf{c} = 0, \quad \int_{\mathbb{V}^3} \mathbf{c}\mathcal{C}(f)\, d\mathbf{c} = \mathbf{0}. \tag{3.6}$$

At this point, the macroscopic equations of fluid mechanics can be derived by considering the moments of the Boltzmann equation (3.3). Taking the integral of the equation over the velocity space, applying the divergence identity $(\mathbf{c}\cdot\nabla)f = \mathbf{c}\cdot\nabla f = \nabla\cdot(f\mathbf{c}) - f(\nabla\cdot\mathbf{c})$ and exploiting the mass conservation property of the collision operator yields

$$\int_{\mathbb{V}^3} \frac{\partial f}{\partial t}\, d\mathbf{c} + \int_{\mathbb{V}^3} \nabla\cdot(f\mathbf{c})\, d\mathbf{c} - \int_{\mathbb{V}^3} f(\nabla\cdot\mathbf{c})\, d\mathbf{c} = 0. \tag{3.7}$$

As independent variables, the time derivative and the velocity space integral can be permuted. Likewise, the divergence in the second derivative which pertains to spatial coordinates is independent of microscopic velocities and permutes with the integral. The third integral vanishes for the same reason. Using Eqs. (3.1) and (3.2) immediately gives the continuity equation:

$$\frac{\partial \rho}{\partial t} + \nabla\cdot(\rho\mathbf{u}) = 0. \tag{3.8}$$

In order to retrieve the momentum conservation equation, the first moment of the Boltzmann equation is calculated. The treatment of the advection term is more straightforward in a Cartesian reference frame with coordinates $\mathbf{x} = \{x_i\}_{i\in\{1,2,3\}}$. For any i and using Einstein summation convention,

$$\begin{aligned}\int_{\mathbb{V}^3} [\mathbf{c}(\mathbf{c}\cdot\nabla)f]_i\, d\mathbf{c} &= \int_{\mathbb{V}^3} c_i c_j \frac{\partial f}{\partial x_j}\, d\mathbf{c} = \frac{\partial}{\partial x_j}\int_{\mathbb{V}^3} c_i c_j f\, d\mathbf{c} \\ &= \underbrace{\frac{\partial}{\partial x_j}\int_{\mathbb{V}^3} (c_i - u_i)(c_j - u_j) f\, d\mathbf{c}}_{-\frac{\partial \sigma_{ij}}{\partial x_j}} + \underbrace{\frac{\partial}{\partial x_j}\int_{\mathbb{V}^3} (c_i u_j + c_j u_i - u_i u_j)\, d\mathbf{c}}_{\frac{\partial(\rho u_i u_j)}{\partial x_j}}.\end{aligned} \tag{3.9}$$

Using similar permutation arguments as with the continuity equation and by applying the momentum conservation of the collision operator together with Eq. (3.9), the momentum conservation equation reads

$$\frac{\partial(\rho u_i)}{\partial t} + \frac{\partial(\rho u_i u_j)}{\partial x_j} - \frac{\partial \sigma_{ij}}{\partial x_j} = 0 \tag{3.10}$$

where the momentum flux tensor was split following $\pi_{ij} = \rho u_i u_j - \sigma_{ij}$.

The closure of Eq. (3.10) requires finding an explicit expression for the Cauchy stress tensor σ_{ij} with assumptions for the distribution function f. This is achieved by the so-called Chapman-Enskog analysis, which allows recovery of the value of σ_{ij} as equal to its value in the continuum mechanics framework with a Newtonian fluid assumption.[1] Such analysis reasons in terms of the Knudsen number $Kn = L_{mfp}/L$, ratio of the molecular mean free path and a characteristic macroscopic length scale. The domain of validity of the fluid mechanics equations is for $Kn \ll 1$, when the gas can be seen as a continuum, molecular collisions are predominant and the molecular distribution is nearly at equilibrium. In the procedure, the distribution function is expressed as a Taylor series around its equilibrium value such that

$$f = f_{eq} + \varepsilon f^{(1)} + \varepsilon^2 f^{(2)} + \dots \tag{3.11}$$

where the parameter ε is associated with the Knudsen number. Retaining a zeroth-order expansion $f \simeq f_{eq}$ allows to recover the Euler equations which describe inviscid flows. A first-order perturbation, $f \simeq f_{eq} + \varepsilon f^{(1)}$ combined with the use of the BGK approximation yields an explicit expression for $f^{(1)}$ and eventually the following expression for the Cauchy stress tensor,

$$\sigma_{ij} = \mu \left(\frac{\partial u_i}{\partial x_j} + \frac{\partial u_j}{\partial x_i} \right) + \zeta \delta_{ij} \frac{\partial u_k}{\partial x_k} - \delta_{ij} p \tag{3.12}$$

specifying the normal and shear stresses at any point. δ_{ij} is the Kronecker delta defined as $\delta_{ij} = 1$ if $i = j$ and $\delta_{ij} = 0$ otherwise. The thermodynamic pressure p was introduced and is found, via Chapman-Enskog analysis to be linked with the first coefficient of viscosity, or shear viscosity[2] μ as $\mu = p\tau = \rho R T \tau$ which is associated with the transport of momentum between layers in a shear flow. The second coefficient of viscosity, or volume viscosity ζ may be decomposed in two distinct parts following

$$\mu_B = \zeta + \frac{2}{3}\mu \tag{3.13}$$

where μ_B is the bulk viscosity[3]. It characterises the resistance of the fluid to small compression or dilatation, which translates into the irreversible transform of kinetic energy to internal energy. Equation (3.13) separates the viscous contribution of the stress tensor into a trace-free shear stress tensor part as well as a normal stress tensor part.

[1] A fluid is Newtonian if at every point the flow viscous stresses depend linearly upon the strain rate, that is the rate of change of its deformation.
[2] also found under the name of dynamic viscosity.
[3] The term is often erroneously used to denote ζ itself rather than the sum.

The Chapman-Enskog analysis finds that μ_B is zero for dilute monatomic gases (Chapman & Cowling, 1970). This is consistent with the controversial Stokes hypothesis, which states that viscosity is not involved in changes of volume. An immediate consequence is that the thermodynamic pressure is equal to the mechanical pressure. The bulk viscosity may indeed have a non-negligible impact on sound-wave absorption or attenuation as well as for shock wave problems, yet does not significantly affect compressible boundary layer flows where normal stresses of viscous nature are negligible (White, 2006). For further details about the Chapman-Enskog analysis, the reader is referred to Succi (2001). Plugging Eq. (3.12) into Eq. (3.10) and using Eq. (3.8) to rearrange the time derivative and the advection term, the momentum conservation principle reads

$$\frac{\partial u_i}{\partial t} + u_j \frac{\partial u_i}{\partial x_j} + \frac{1}{\rho}\delta_{ij}\frac{\partial p}{\partial x_j} - \frac{1}{\rho}\frac{\partial}{\partial x_j}\left(\mu\left[\frac{\partial u_i}{\partial x_j} + \frac{\partial u_j}{\partial x_i} - \frac{2}{3}\delta_{ij}\frac{\partial u_k}{\partial x_k}\right]\right) = 0. \tag{3.14}$$

Now, assume an incompressible flow where the density ρ is constant in space and time, and where the viscosity depends only on the temperature, $\mu = \mu(T)$. Equation (3.8) reduces to $\nabla \cdot \mathbf{u} = \partial u_k/\partial x_k = 0$. This sweeps away the aforementioned consideration about the bulk viscosity. The momentum conservation equation is then simplified to

$$\frac{\partial u_i}{\partial t} + u_j \frac{\partial u_i}{\partial x_j} + \frac{1}{\rho}\delta_{ij}\frac{\partial p}{\partial x_j} - \nu\frac{\partial^2 u_i}{\partial x_j^2} = 0 \tag{3.15}$$

where $\nu = \mu/\rho$ is the kinematic viscosity. Denoting dimensional variables with an asterisk superscript,[4] the incompressible Navier-Stokes equations read in tensor form

$$\nabla^* \cdot \mathbf{u}^* = 0 \tag{3.16a}$$

$$\frac{\partial \mathbf{u}^*}{\partial t^*} + (\mathbf{u}^* \cdot \nabla^*)\mathbf{u}^* + \frac{1}{\rho^*}\nabla^* p^* - \nu^* \boldsymbol{\Delta}^* \mathbf{u}^* = \mathbf{0} \tag{3.16b}$$

where $\boldsymbol{\Delta} = \nabla^2$ is the vector Laplace operator.

3.1.2 Non-dimensionalisation

It is more mathematically and numerically convenient to handle dimensionless equations. Consider a length scale L^* (m), a velocity scale U^* (m s^{-1}) and a time scale L^*/U^* (s). Should inertial effects in the flow be dominant, an appropriate pressure scale is $\rho^* U^{*2}$ (kg m^{-1} s^{-1}), with the density ρ^* being constant. The non-dimensionalisation procedure on the different variables and operators involving

[4] In the following of the thesis, this notation is used sparingly and only to disambiguate when necessary.

spatial derivatives implies

$$t = \frac{U^*}{L^*} t^*, \quad \mathbf{u} = \frac{\mathbf{u}^*}{U^*}, \quad \nabla = L^* \nabla^*, \quad p = \frac{p^*}{\rho^* U^{*2}}, \quad \boldsymbol{\Delta} = L^{*2} \boldsymbol{\Delta}^*. \tag{3.17}$$

Substituting Eq. (3.17) into Eq. (3.16) gives the dimensionless, incompressible Navier-Stokes equations,

$$\nabla \cdot \mathbf{u} = 0 \tag{3.18a}$$

$$\frac{\partial \mathbf{u}}{\partial t} + (\mathbf{u} \cdot \nabla)\mathbf{u} + \nabla p - \frac{1}{Re} \boldsymbol{\Delta} \mathbf{u} = \mathbf{0}. \tag{3.18b}$$

The dimensionless factor of the viscous term is famously known as the Reynolds number

$$Re = \frac{U^* L^*}{\nu^*} \tag{3.19}$$

which holds significant importance in the laminar-turbulent transition process. It is often misguidedly described as 'the ratio of inertial forces to viscous forces'. As judiciously reminded by McLean (2012), the Reynolds number rather quantifies the rate at which momentum is diffused by viscosity in the wall-normal direction, relative to the flow velocity; the higher Re, the thinner the resulting boundary layer becomes relative to the dimensions of the body. It is then more accurate to describe the Reynolds number as a relative measure of the impact of 'global' viscous effects.

The incompressible flow regime is valid for a Mach number $Ma < 0.3$ defined as the ratio of the flow velocity to the speed of sound. In a 3D space, the incompressible Navier-Stokes equations are a system of four equations and four unknowns, namely the pressure p as well as the three velocity components $\mathbf{u} = (u, v, w)$. These equations fall into the class of convection-diffusion equations and are non-linear due to the presence of the advection term $(\mathbf{u} \cdot \nabla)\mathbf{u}$. The latter term together with the time derivative represent the rate of change of momentum of a fluid particle moving with velocity $\mathbf{u}$. Viscosity acts as a diffusion of the momentum as embodied by the $\boldsymbol{\Delta}\mathbf{u}/Re$ term. Finally, the effect of pressure forces enters as a source term in the equation.

3.1.3 Pressure Poisson equation formulation

The pressure plays a peculiar role in the incompressible Navier-Stokes equations as there is no coupling between the continuity equation and the momentum conservation equation. It appears solely in the latter through its gradient, which is a force per unit volume. However, it is not a thermodynamic quantity and as such does not satisfy an equation of state. From the viewpoint of optimisation and minimising a certain energy functional, the pressure can rather be seen as an

implicit variable or as a Lagrange multiplier which enforces that the velocity field is divergence-free following Eq. (3.18a). In time-dependent flows, the pressure waves propagate with infinite speed to maintain the incompressibility condition at every space point and at all times.

Let Ω be a physical domain subset of $\mathbb{R}^2$ or $\mathbb{R}^3$ with its boundary denoted by $\partial\Omega$, assumed piecewise smooth. The set of positions is spanned by an orthogonal coordinate system $\mathbf{x} = (x, y, z)$, allowing $\mathbf{q} = (p, u, v, w)$ to be a compact representation of the instantaneous flow quantities where p is the pressure, u the streamwise velocity, v the wall-normal velocity and w the spanwise velocity. Assume Eq. (3.18) is supplemented by the boundary conditions and initial conditions

$$\mathbf{q}(\mathbf{x}, t) = \mathbf{g}(\mathbf{x}, t) \qquad \mathbf{x} \in \partial\Omega\,, t > 0 \tag{3.20a}$$

$$\mathbf{q}(\mathbf{x}, 0) = \mathbf{h}(\mathbf{x}) \qquad \mathbf{x} \in \Omega\,, t = 0. \tag{3.20b}$$

Equations (3.18) and (3.20) are commonly referred to as the primitive formulation of the incompressible Navier-Stokes equations.

It may be solved numerically on collocated grids employing techniques such as the artificial compressibility method of Chorin (1967) or the projection method also suggested by Chorin (1968). On a staggered grid, the marker-and-cell method developed by Harlow and Welch (1965) has also been successful. However, without these approaches, it should be highlighted that applying a centred Finite Difference Method (FDM) to spatially discretise the primitive formulation on a collocated grid may lead to a non-physical pressure field satisfying the incompressible Navier-Stokes equations, also known as *checkerboard instability*.[5] Since the FDM is the numerical method used on collocated grids in this thesis, as described in Section 4.1.1, this point is further developed.

Figure 3.1 is a one-dimensional illustration of non-physical pressure field resulting from a checkerboard instability. Its derivative is zero at discrete nodes since the coupling is only between nodes separated by a distance of $2\Delta x$. The 'lack' of pressure information in the incompressible Navier-Stokes equations leads the numerical scheme to see a uniform pressure distribution, although it is formed of sawtooth patterns. More formally, the instability results from the fact that, seen as a system of Differential Algebraic Equations (DAEs), the primitive formulation of Eq. (3.18) is of strangeness index one (Weickert, 1996). The latter

[5] The checkerboard instability does not only pertain to the use of an FDM as it can also arise with a finite volume or finite element approach. In that latter framework, the checkerboard instability is induced by the violation of the famous Ladyzhenskaya-Babuška-Brezzi condition for the well-posedness of a saddle point problem.

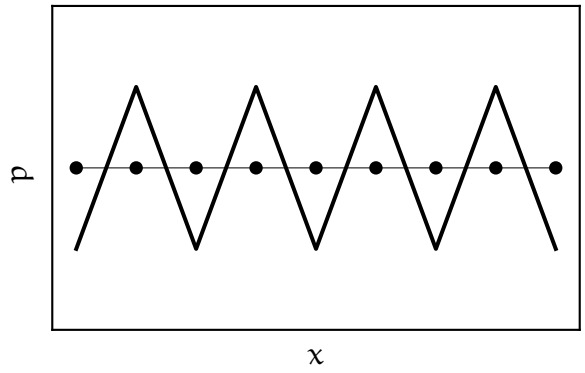

Figure 3.1: One-dimensional example of a checkerboard instability. At every grid node (●) a centred finite difference scheme reports a value $dp/dx = 0$ in spite of the function p rapidly varying.

essentially quantifies the number of transformations required with respect to the time coordinate to obtain a system of Ordinary Differential Equation (ODE). It can also be interpreted as a measure of stiffness to solve a system numerically.

The checkerboard instability can be prevented by substituting the original continuity equation by a Pressure Poisson Equation (PPE) to obtain a strangeness-free DAE system (Weickert, 1996). Taking the divergence of Eq. (3.18b), exchanging the time derivative and the divergence operator which are independent, and using the identity $\nabla \cdot (\Delta \mathbf{u}) = \nabla \cdot (\nabla(\nabla \cdot \mathbf{u}) - \nabla \times (\nabla \times \mathbf{u})) = \mathbf{0}$ with the continuity equation yields an explicit, elliptic Poisson equation for the pressure,

$$\Delta p + \nabla \cdot [(\mathbf{u} \cdot \nabla)\mathbf{u}] = 0. \tag{3.21}$$

When Eq. (3.21) substitutes Eq. (3.18a), the following equations

$$\Delta p + \nabla \cdot [(\mathbf{u} \cdot \nabla)\mathbf{u}] = 0 \qquad \mathbf{x} \in \Omega\,, t > 0 \tag{3.22a}$$

$$\frac{\partial \mathbf{u}}{\partial t} + (\mathbf{u} \cdot \nabla)\mathbf{u} + \nabla p - \frac{1}{Re}\Delta \mathbf{u} = \mathbf{0} \qquad \mathbf{x} \in \Omega\,, t > 0 \tag{3.22b}$$

together with the boundary conditions and initial conditions

$$\mathbf{q}(\mathbf{x}, t) = \mathbf{g}(\mathbf{x}, t) \qquad \mathbf{x} \in \partial\Omega\,, t > 0 \tag{3.23a}$$

$$\mathbf{q}(\mathbf{x}, 0) = \mathbf{h}(\mathbf{x}) \qquad \mathbf{x} \in \Omega\,, t = 0 \tag{3.23b}$$

$$\nabla \cdot \mathbf{u} = 0 \qquad \mathbf{x} \in \partial\Omega\,, t > 0 \tag{3.23c}$$

form what is denoted as the PPE formulation of the incompressible Navier-Stokes equations. The question is then, are the primitive and PPE formulations completely equivalent? With careful attention to the boundary conditions, they are. Although it is obvious that the primitive formulation mathematically implies

the PPE formulation, the converse is not necessarily established. Several notable contributions have discussed the equivalence between the primitive and PPE formulations, namely Gresho and Sani (1987), Johnston and Liu (2004), Rempfer (2006) and Shirokoff and Rosales (2011). It is the fulfilment of the condition in Eq. (3.23c) which essentially guarantees the equivalence. The divergence-free velocity condition must be met everywhere in Ω as well as on $\partial\Omega$. This matter is directly related to the boundary conditions imposed on $\partial\Omega$ for the flow variables, which is further developed in Section 3.3.2.

The equations governing the dynamics of fluid motion have been derived under the assumptions of an incompressible flow which behaves as an ideal gas, and as a Newtonian fluid. Moreover, the PPE formulation has been introduced. From this point, the mathematical aspects of the stability theory can be developed.

3.2 Stability theory of fluid flows

3.2.1 Perturbation equations

As mentioned in Chapter 2, linear stability theory describes the evolution of perturbations superimposed on a steady-state equilibrium $\bar{\mathbf{q}}(\mathbf{x})$, called the base flow. Following the broad definition of stability for dynamical systems, if the flow settles back to its base state after perturbation, it is considered stable. If it diverges, it is deemed unstable. A natural requirement is that $\bar{\mathbf{q}}(\mathbf{x})$ needs to be a solution of the steady Navier-Stokes equations (3.18). The assumption of a steady base flow could be relaxed to a time-periodic base flow, which could be treated by the Floquet theory. This, however, falls out of the scope of this thesis. The instantaneous flow quantities can be decomposed into a steady-state part and an infinitesimal disturbance part such that, for $\varepsilon \ll 1$,

$$\mathbf{q}(\mathbf{x}, t) = \bar{\mathbf{q}}(\mathbf{x}) + \varepsilon\tilde{\mathbf{q}}(\mathbf{x}, t). \tag{3.24}$$

Introducing the decomposition (3.24) in Eq. (3.18) and exploiting the fact that $\bar{\mathbf{q}}(\mathbf{x})$ is a steady-state solution gives the perturbation equations

$$\nabla \cdot \tilde{\mathbf{u}} = 0 \tag{3.25a}$$

$$\frac{\partial\tilde{\mathbf{u}}}{\partial t} + (\bar{\mathbf{u}} \cdot \nabla)\tilde{\mathbf{u}} + (\tilde{\mathbf{u}} \cdot \nabla)\bar{\mathbf{u}} + \nabla\tilde{p} - \frac{1}{Re}\Delta\tilde{\mathbf{u}} = -(\tilde{\mathbf{u}} \cdot \nabla)\tilde{\mathbf{u}}. \tag{3.25b}$$

Thinking of the base flow terms as space-dependent coefficients, the perturbation equations are PDEs describing the non-linear, temporal and 3D spatial evolution

of incompressible perturbations. However, to leading order $O(\varepsilon)$ and with the infinitesimal assumption the perturbation equations become linear if the quadratic term $\varepsilon^2(\tilde{\mathbf{u}} \cdot \nabla)\tilde{\mathbf{u}}$ is neglected. This leads to the so-called LHNS equations that are written as

$$\nabla \cdot \tilde{\mathbf{u}} = 0 \tag{3.26a}$$

$$\frac{\partial \tilde{\mathbf{u}}}{\partial t} + (\bar{\mathbf{u}} \cdot \nabla)\tilde{\mathbf{u}} + (\tilde{\mathbf{u}} \cdot \nabla)\bar{\mathbf{u}} + \nabla \tilde{p} - \frac{1}{Re}\Delta \tilde{\mathbf{u}} = \mathbf{0}. \tag{3.26b}$$

In the same vein as in Section 3.1.3, a Poisson equation from the pressure can be derived from Eq. (3.26). Its linearised counterpart is entitled Linearised Pressure Poisson Equation (LPPE), and the corresponding formulation of the LHNS equations reads

$$\Delta \tilde{p} + \nabla \cdot [(\bar{\mathbf{u}} \cdot \nabla)\tilde{\mathbf{u}}] + \nabla \cdot [(\tilde{\mathbf{u}} \cdot \nabla)\bar{\mathbf{u}}] = 0 \qquad \mathbf{x} \in \Omega\,, t > 0 \tag{3.27a}$$

$$\frac{\partial \tilde{\mathbf{u}}}{\partial t} + (\bar{\mathbf{u}} \cdot \nabla)\tilde{\mathbf{u}} + (\tilde{\mathbf{u}} \cdot \nabla)\bar{\mathbf{u}} + \nabla \tilde{p} - \frac{1}{Re}\Delta \tilde{\mathbf{u}} = \mathbf{0} \qquad \mathbf{x} \in \Omega\,, t > 0 \tag{3.27b}$$

which is supplemented with the boundary and initial conditions

$$\tilde{\mathbf{q}}(\mathbf{x}, t) = \mathbf{g}(\mathbf{x}, t) \qquad \mathbf{x} \in \partial\Omega\,, t > 0 \tag{3.28a}$$

$$\tilde{\mathbf{q}}(\mathbf{x}, 0) = \mathbf{h}(\mathbf{x}) \qquad \mathbf{x} \in \Omega\,, t = 0 \tag{3.28b}$$

$$\nabla \cdot \tilde{\mathbf{u}} = 0 \qquad \mathbf{x} \in \partial\Omega\,, t > 0. \tag{3.28c}$$

Just as with DNS, integrating the Initial Boundary Value Problem (IBVP) stated in Eq. (3.27) and Eq. (3.28) would require colossal computing resources and a time-marching scheme, solving for all spatial directions. Nonetheless, numerous laminar base flows of interest tend to depend upon only two spatial directions, which leads to simplifications in the perturbation equations. Perturbation functions have accordingly been sought with dimensionality reduction techniques, such as the consideration of a wave-like form with a normal mode expansion.

3.2.2 Linear harmonic Navier-Stokes approach

Normal mode assumption and discrete wave ansatzes

The Eq. (3.26) can be written in a compact form $\mathcal{L}(\tilde{\mathbf{q}}(\mathbf{x}, t)) = \mathbf{0}$, where the LHNS operator $\mathcal{L}$ depends on the base flow $\bar{\mathbf{q}}$ and Re, which are coefficients of the PDEs. These are functions of space only, while the perturbation is dependent upon both spatial and temporal coordinates. Due to this separability between time and space,

the perturbation $\tilde{\mathbf{q}}$ may be decomposed as a sum of normal modes, such as

$$\tilde{\mathbf{q}}(\mathbf{x}, t) = \frac{1}{2\pi} \int_{\mathcal{C}_\omega} \hat{\mathbf{q}}(\mathbf{x}, \omega) e^{-i\omega t} \, d\omega + \text{c.c.} \tag{3.29}$$

where the amplitude function $\hat{\mathbf{q}}$ is complex and the angular frequency ω is also complex. $\hat{\mathbf{q}}(\mathbf{x}, \omega)$ is the Fourier-Laplace transform of $\tilde{\mathbf{q}}(\mathbf{x}, t)$ which exists only if the path of integration $\mathcal{C}_\omega$ in the complex plane ensures that $\tilde{\mathbf{q}}$ is locally integrable on the interval $[0, +\infty[$. The notation 'c.c.' means 'complex conjugate' and is added due to the fact that the perturbation $\tilde{\mathbf{q}}$ is a real quantity. Plugging Eq. (3.29) in the LHNS system gives

$$\begin{aligned} \mathcal{L}(\tilde{\mathbf{q}}(\mathbf{x}, t)) &= \frac{1}{2\pi} \int_{\mathcal{C}_\omega} \mathcal{L}(\hat{\mathbf{q}}(\mathbf{x}, \omega) e^{-i\omega t}) \, d\omega + \text{c.c.} \\ &= \frac{1}{2\pi} \int_{\mathcal{C}_\omega} \mathcal{L}_\omega(\hat{\mathbf{q}}(\mathbf{x}, \omega)) e^{-i\omega t} \, d\omega + \text{c.c.} = \mathbf{0} \end{aligned} \tag{3.30}$$

where $\mathcal{L}_\omega$ is the linear operator which absorbed the time derivative term $\partial_t = i\omega$ and now contains only spatial derivatives. It is then sufficient to have $\mathcal{L}_\omega(\hat{\mathbf{q}}(\mathbf{x}, \omega)) = \mathbf{0}$ for any $\omega \in \mathbb{C}$ in order to find a perturbation solution of the LHNS equations. From this point of view, the perturbation solution $\tilde{\mathbf{q}}$ may be seen as a linear combination of solutions $\hat{\mathbf{q}}$ in frequency space ω, functions of space $\mathbf{x}$. The linearity of the problem justifies why a discrete, monochromatic wave solution in terms of ω could then be assumed such that

$$\tilde{\mathbf{q}}(\mathbf{x}, t) = \tilde{\mathbf{q}}(x, y, z, t) = \hat{\mathbf{q}}(x, y, z) e^{-i\omega t} + \text{c.c.} \tag{3.31}$$

Such a wave ansatz specifies that the amplitude function depends on the three spatial coordinates and adopts a harmonic behaviour in time. When the decomposition in Eq. (3.31) is performed, the LHNS operator $\mathcal{L}$ reads, assuming Cartesian coordinates,

$$\mathcal{L} = \begin{pmatrix} 0 & \partial_x & \partial_y & \partial_z \\ \partial_x & \mathcal{D} + \partial_x \bar{u} & \partial_y \bar{u} & \partial_z \bar{u} \\ \partial_y & \partial_x \bar{v} & \mathcal{D} + \partial_y \bar{v} & \partial_z \bar{v} \\ \partial_z & \partial_x \bar{w} & \partial_y \bar{w} & \mathcal{D} + \partial_z \bar{w} \end{pmatrix} \tag{3.32}$$

where the operator $\mathcal{D}$ is defined as $\mathcal{D} = \bar{u}\partial_x + \bar{v}\partial_y + \bar{w}\partial_z - i\omega - (\partial_{xx} + \partial_{yy} + \partial_{zz})/\,\text{Re}$. Body-fitted coordinates are also considered in this thesis. For details of that coordinate system and related expressions of the stability theory equations, the reader is referred to Appendix A.

If the base flow of interest depends only upon the streamwise and wall-normal coordinates as $\bar{\mathbf{q}}(x, y)$, a further separation of variables may be undertaken as

$$\tilde{\mathbf{q}}(x, y, z, t) = \frac{1}{(2\pi)^2} \int_{\mathcal{C}_\omega} \left(\int_{\mathcal{C}_\beta} \hat{\mathbf{q}}(x, y, \beta, \omega) e^{i\beta z - i\omega t} \, d\beta \right) d\omega + \text{c.c.} \tag{3.33}$$

Thanks to the symmetry in the spanwise direction, the spanwise dependence in the amplitude function is removed and instead absorbed in the exponential phase. The parameter β is physically interpreted as the spanwise wavenumber related to a periodicity wavelength $L_z = 2\pi/\beta$. In an analogous manner as $\mathcal{C}_\omega$, $\mathcal{C}_\beta$ is the path of integration of the spanwise wavenumber in the complex plane. Therefore, the corresponding discrete ansatz reads

$$\tilde{\mathbf{q}}(x, y, z, t) = \hat{\mathbf{q}}(x, y) e^{i\beta z - i\omega t} + \text{c.c.} \tag{3.34}$$

and models a travelling wave whose phase velocity is $c = \omega/\beta$. The phase of the wave ansatz has opposite signs for the space and time coordinates. This is a requirement of the principle of causality applied to plane waves; as time increases, outgoing waves must have wavefronts that travel forwards. The operator $\mathcal{L}$ is accordingly transformed, and the LHNS equations read

$$\mathcal{L}\hat{\mathbf{q}} = \begin{pmatrix} 0 & \partial_x & \partial_y & i\beta \\ \partial_x & \mathcal{D} + \partial_x \bar{u} & \partial_y \bar{u} & 0 \\ \partial_y & \partial_x \bar{v} & \mathcal{D} + \partial_y \bar{v} & 0 \\ i\beta & \partial_x \bar{w} & \partial_y \bar{w} & \mathcal{D} \end{pmatrix} \begin{pmatrix} \hat{p} \\ \hat{u} \\ \hat{v} \\ \hat{w} \end{pmatrix} = \mathbf{0} \tag{3.35}$$

where the operator $\mathcal{D}$ becomes

$$\mathcal{D} = \bar{u}\partial_x + \bar{v}\partial_y + i(\beta\bar{w} - \omega) + \beta^2/\,\mathrm{Re} - (\partial_{xx} + \partial_{yy})/\,\mathrm{Re}\,. \tag{3.36}$$

The LPPE reads

$$\begin{aligned} \frac{\partial^2 \hat{p}}{\partial x^2} + \frac{\partial^2 \hat{p}}{\partial y^2} - \beta^2 \hat{p} + 2\Bigg(& \frac{\partial \bar{u}}{\partial x}\frac{\partial \hat{u}}{\partial x} + \frac{\partial \bar{v}}{\partial x}\frac{\partial \hat{u}}{\partial y} + i\beta\frac{\partial \bar{w}}{\partial x}\hat{u} + \\ & \frac{\partial \bar{u}}{\partial y}\frac{\partial \hat{v}}{\partial x} + \frac{\partial \bar{v}}{\partial y}\frac{\partial \hat{v}}{\partial y} + i\beta\frac{\partial \bar{w}}{\partial y}\hat{v} \Bigg) = 0. \end{aligned} \tag{3.37}$$

The LHNS equations are then dependent upon the streamwise and wall-normal coordinates in physical space whereas the frequency space is parametrised in the spanwise direction and in time. In the stability analyses of boundary layers included in this thesis, this '2.5D' ansatz is mostly used. It is appropriate to describe

flow instabilities in base flows that are homogeneous in the spanwise direction, in the presence of surface irregularities varying in the streamwise direction.

A noteworthy feature is the fact that the expansions in Eq. (3.29) and Eq. (3.33) are restrictive; an arbitrary initial perturbation is in general not expandable in such normal modes (Drazin & Reid, 2004). In other words, the set of solutions with the $\exp(-i\omega t)$ or $\exp(i\beta z - i\omega t)$ wave ansatzes does not form a vector space basis of the solutions. Fortunately, the normal modes still have an important role in the LHNS framework and their analysis is sufficient to establish general stability criteria (Drazin & Reid, 2004).

Further simplifications are not among the methodologies used in this thesis due to their inability to model the evolution of instabilities with surface features. However, the verification and validation data presented further in Chapters 5 and 6 rely on some of them. For this reason and for their historical role played in the instability analysis of boundary layers, they are succinctly presented hereinafter.

Should the base flow of interest experience mild variation in the streamwise direction, the perturbation may be sought under the following wave ansatz,

$$\tilde{\mathbf{q}}(x,y,z,t) = \hat{\mathbf{q}}(\epsilon x, y) \exp\left(i \int_x \alpha(\epsilon s)\, ds\right) e^{i\beta z - i\omega t} + \text{c.c.} \tag{3.38}$$

The amplitude function $\hat{\mathbf{q}}(\epsilon x, y)$ is slowly varying whereas the exponential part is rapidly oscillating. This is an application of the Wentzel-Kramers-Brillouin (WKB) theory, itself a special case of the method of multiple scales; for further information, the reader is referred to Nayfeh (2004). The streamwise wavenumber α appears in the phase of the perturbation to incorporate the streamwise history of the disturbance. The infinitesimal parameter[6] $\epsilon = O(1/\mathrm{Re}) \ll 1$ specifies the different scales for the base flow and for the disturbance, which are characterised by $\partial_x = O(\epsilon)$ and $\bar{v} = O(\epsilon)$ as the other quantities remain of order one. With the introduction of the ansatz (3.38) and by neglecting selected streamwise derivatives, the LHNS equations simplify to the PSE. In virtue of their quasi-parabolic nature[7] these can be solved with a marching procedure in the streamwise direction. With the same underlying assumptions except an inhomogeneous base flow in the

[6] This ϵ is different from the infinitesimal parameter ε used for the linearisation of the perturbation equations and introduced in Eq. (3.24).

[7] There is residual ellipticity in the PSE due to the $\partial_x p$ term, which renders the formulation ill-posed. It can be alleviated by using a large enough streamwise space discretisation as evidenced by Li and Malik (1995).

Table 3.1: Classification of linear stability analysis approaches with respect to amplitude $\hat{\mathbf{q}}$ and phase Θ of the wave ansatz $\hat{\mathbf{q}}(\mathbf{x})\exp(i\Theta)$

Terminology	Analysis	Base flow	Amplitude	Phase Θ
Global/HNS	TriGlobal	$\bar{\mathbf{q}}(x,y,z)$	$\hat{\mathbf{q}}(x,y,z)$	$-\omega t$
	PSE-3D	$\bar{\mathbf{q}}(\epsilon x,y,z)$	$\hat{\mathbf{q}}(\epsilon x,y,z)$	$\int_x \alpha(\epsilon s)ds - \omega t$
	BiGlobal (streamw.)	$\bar{\mathbf{q}}(x,y)$	$\hat{\mathbf{q}}(x,y)$	$\beta z - \omega t$
	BiGlobal (spanwise)	$\bar{\mathbf{q}}(y,z)$	$\hat{\mathbf{q}}(y,z)$	$\alpha x - \omega t$
Non-Local	PSE	$\bar{\mathbf{q}}(\epsilon x,y)$	$\hat{\mathbf{q}}(\epsilon x,y)$	$\int_x \alpha(\epsilon s)ds + \beta z - \omega t$
Local	LST	$\bar{\mathbf{q}}(y)$	$\hat{\mathbf{q}}(y)$	$\alpha x + \beta z - \omega t$

spanwise direction, the perturbation ansatz might be changed to

$$\tilde{\mathbf{q}}(x,y,z,t) = \hat{\mathbf{q}}(\epsilon x,y,z)\exp\left(i\int_x \alpha(\epsilon s)\,ds\right)e^{-i\omega t} + \text{c.c.} \tag{3.39}$$

This is usually referred to as PSE-3D.

Ultimately, if the base flow is homogeneous in both the streamwise and spanwise directions, $\bar{\mathbf{q}} = \bar{\mathbf{q}}(y)$, the perturbation amplitude may be accordingly sought as a function of the wall-normal coordinate only such that

$$\tilde{\mathbf{q}}(x,y,z,t) = \hat{\mathbf{q}}(y)e^{i\alpha x + i\beta z - i\omega t} + \text{c.c.} \tag{3.40}$$

As explained in Section 2.2.2, even though all the wave ansatzes described in this subsection fall into the class of linear stability analysis, the methodology based on the ansatz (3.40) is usually entitled LST in the literature. The LST ansatz is consistent with the parallel flow assumption, where the wall-normal base flow component $\bar{v}$ is neglected[8] resulting in the base flow field $\bar{\mathbf{u}} = (\bar{u}(y), 0, \bar{w}(y))^T$ and the flow perturbation amplitudes to become functions of y only as $\hat{\mathbf{q}} = (\hat{p}(y), \hat{u}(y), \hat{v}(y), \hat{w}(y))^T$.

In this harmonic framework based on the LHNS equations (3.35), two different kinds of analyses can be carried out. On the one hand, one may investigate the most linearly amplified eigenmodes naturally occurring in a base flow. The LHNS equations are then essentially an eigenvalue problem in the complex frequency ω whose eigenfunction is $\hat{\mathbf{q}}$. On the other hand, a single-frequency disturbance developing in the base flow may be generated by a localised, small-amplitude forcing at the wall. In that case, the LHNS equations become a linear system whose solution represents the response of the flow to that forcing and its further evolution.

[8] The continuity equation gives $\nabla \cdot \bar{\mathbf{u}} = \partial_x \bar{u} + \partial_y \bar{v} + \partial_z \bar{w} = \partial_y \bar{v} = 0$ which results in $\bar{v}(y) = 0$ since $\bar{v} = 0$ at a solid wall without fluid penetration.

Table 3.1 recapitulates the various approaches for the linear stability analysis with commonly adopted terminology, discussed in Section 2.2.2. The concept of *local* analysis, historically used to describe the LST approach, refers to the homogeneity and periodicity in the streamwise direction. After the extension to a *non-local* PSE approach with the streamwise marching process, the *global* or *HNS* terminology was introduced to describe the instability analysis of flows with at least two inhomogeneous spatial directions. A *TriGlobal* analysis assumes a fully 3D amplitude function whereas a *BiGlobal* analysis assumes a 2D amplitude function. Wall-forced roughness analyses are referred to as LHNS analyses.

Eigenvalue-based LHNS, or BiGlobal

The present work considers the framework of streamwise, temporal BiGlobal analysis where ω is an unknown complex eigenvalue and β a real, prescribed spanwise wavenumber. In that context, the LHNS equations (3.26) or (3.27) may be formed as a Generalised Eigenvalue Problem (GEVP),

$$\mathcal{L}(\bar{\mathbf{q}}, \beta, \mathrm{Re})\hat{\mathbf{q}} = \omega \mathcal{M} \hat{\mathbf{q}}. \tag{3.41}$$

There is no body force applied in Ω or surface force applied on $\partial\Omega$. The eigenvalue ω represents the asymptotic, long-time limit behaviour of the investigated flow perturbations in that the existence of one eigenvalue with a positive imaginary part is a sufficient condition for a globally unstable flow. Therefore, the latter will preferentially amplify in time the state which possesses the largest positive growth rate ω_i. The real part of the eigenvalue ω_r represents the frequency of the perturbation and the corresponding eigenfunction $\hat{\mathbf{q}}$ describes its spatial shape.

Wall-forced LHNS

Conversely, ω and β may be both real quantities. The disturbance response of the flow to a small-scale roughness element modelled by a surface actuation at the wall can be examined. Although such a surface actuation is able to model the effects of boundary-layer suction or blowing as well, this work mostly considers the modelling of wall roughness. The LHNS equations then reduce to

$$\mathcal{L}(\bar{\mathbf{q}}, \beta, \omega, \mathrm{Re})\hat{\mathbf{q}} = \hat{\mathbf{r}} \tag{3.42}$$

where $\hat{\mathbf{r}}$ incorporates the wall region portion of $\partial\Omega$. The assumption of infinitesimal perturbations in Eq. (3.24) indeed allows the problem to be governed by the linearised equations and to express the wall actuation with a Taylor expansion of

the no-slip condition such that for a steady roughness element,

$$\hat{u}_w(x) = -\hat{h}(x)\frac{\partial \bar{u}}{\partial y}(x,0) \tag{3.43a}$$

$$\hat{v}_w(x) = -\hat{h}(x)\frac{\partial \bar{v}}{\partial y}(x,0) \tag{3.43b}$$

$$\hat{w}_w(x) = -\hat{h}(x)\frac{\partial \bar{w}}{\partial y}(x,0) \tag{3.43c}$$

and for an unsteady roughness-induced actuation,

$$\hat{u}_w(x) = -\hat{h}(x)\frac{\partial \bar{u}}{\partial y}(x,0) \tag{3.44a}$$

$$\hat{v}_w(x) = -\hat{h}(x)\left(i\omega + \frac{\partial \bar{v}}{\partial y}(x,0)\right) \tag{3.44b}$$

$$\hat{w}_w(x) = -\hat{h}(x)\frac{\partial \bar{w}}{\partial y}(x,0). \tag{3.44c}$$

The roughness shape $h(x,z,t) = O(\varepsilon)$ enters the wall forcing model via its Fourier representation $\hat{h}(x)\exp(i\beta z - i\omega t)$. Ng and Crouch (1999) estimated that when the roughness height exceeds a threshold of 10% of the local displacement thickness, the boundary layer responds in a non-linear fashion. This provides a domain of validity for applying the LHNS framework with the Taylor expansion model.

Measures of growth

The amplitude function $\hat{q}$ is complex-valued, with the amplitude defined as $A^q(x) = |\hat{q}(x,y_0)|$ where y_0 is either a fixed wall-normal location of interest or typically the wall-normal coordinate where $|\hat{q}|$ reaches a maximum. One ideally measures quantities of interest in the streamwise direction to quantify the evolution of the perturbations. If the LST framework was employed, α would offer a natural wavenumber and growth rate with its real and imaginary parts, respectively. With a 2.5D wave ansatz, there is no Fourier decomposition in the streamwise direction and another definition must be provided. From an arbitrary amplitude quantity of interest $\hat{\phi}(x,y)$ it is possible to define a streamwise growth rate

$$\gamma(x) = \left(\frac{1}{\hat{\phi}(x,y_0)}\frac{\partial \hat{\phi}(x,y_0)}{\partial x}\right)_r \tag{3.45}$$

as well as a real streamwise wavenumber

$$\alpha(x) = \left(\frac{1}{\hat{\phi}(x, y_0)} \frac{\partial \hat{\phi}(x, y_0)}{\partial x} \right)_i \tag{3.46}$$

where $\hat{\phi}$ may be any relevant flow quantity among $\hat{u}$, $\hat{v}$ or $\hat{w}$. The total disturbance kinetic energy is defined as

$$E = \int_0^{+\infty} \left(\|\hat{u}\|^2 + \|\hat{v}\|^2 + \|\hat{w}\|^2 \right) \, dy. \tag{3.47}$$

It can equally be used as a measure of perturbation to define a growth rate, which reads

$$\gamma(x) = \frac{\partial}{\partial x} \ln \left(\sqrt{E} \right). \tag{3.48}$$

Finally, the N-factor is obtained from the growth rate as

$$N = \ln \left(\frac{A}{A_0} \right) = \int_{x_0}^{x} \gamma(x) \, dx. \tag{3.49}$$

A_0 is the initial amplitude at the streamwise location x_0 marking the first branch of neutral stability for the disturbance. The N-factor is bound to a unique frequency ω and a unique spanwise wavenumber β.

3.2.3 Non-linear harmonic Navier-Stokes approach

An extension of the linearised approach is to consider the non-linear perturbations equations (3.25) where the right-hand-side $(\tilde{\mathbf{u}} \cdot \nabla)\tilde{\mathbf{u}}$ is retained and assumed of the same order $O(\varepsilon)$ as the other terms,

$$\nabla \cdot \tilde{\mathbf{u}} = 0 \tag{3.50a}$$

$$\frac{\partial \tilde{\mathbf{u}}}{\partial t} + (\bar{\mathbf{u}} \cdot \nabla)\tilde{\mathbf{u}} + (\tilde{\mathbf{u}} \cdot \nabla)\bar{\mathbf{u}} + \nabla \tilde{p} - \frac{1}{Re} \Delta \tilde{\mathbf{u}} = -(\tilde{\mathbf{u}} \cdot \nabla)\tilde{\mathbf{u}}. \tag{3.50b}$$

Assume a time-periodic perturbation $\tilde{\mathbf{q}}$. Should $\tilde{\mathbf{q}}$ be Lebesgue integrable on its periodic interval, it can be decomposed into a Fourier series such that the total flow field is an infinite sum of normal modes,

$$\mathbf{q}(\mathbf{x}, t) = \bar{\mathbf{q}}(\mathbf{x}) + \tilde{\mathbf{q}}(\mathbf{x}, t) = \bar{\mathbf{q}}(x, y, z) + \sum_{n=-\infty}^{+\infty} \hat{\mathbf{q}}_n(x, y, z) e^{-in\omega t}. \tag{3.51}$$

The individual Fourier coefficient $\hat{\mathbf{q}}_n$ is the amplitude function of the component $n\omega$. With such an expansion, the perturbation field is assumed to oscillate in time.

Since the perturbation $\tilde{\mathbf{q}}$ is a real quantity, the Fourier coefficients necessarily obey $\hat{\mathbf{q}}_n = \hat{\mathbf{q}}^{\dagger}_{-n}$ where the dagger denotes the complex conjugate.

Once amplitude disturbance levels reach a certain threshold, the underlying assumptions of the LHNS equations are physically unjustified as the individual Fourier components do not evolve independently of each other. The ansatz of Eq. (3.51) thus allows modelling the latter stages of disturbance growth before breakdown to turbulence, by taking into account non-linear effects for finite amplitude waves. In that case, resonant wave-triad interactions are a non-negligible mechanism and the non-linear term $(\tilde{\mathbf{u}} \cdot \nabla)\tilde{\mathbf{u}}$ bears sole responsibility for transferring energy between waves of different wavenumbers (Schmid & Henningson, 2001). The assumption in Eq. (3.51) is then adapted to model subharmonic resonance in a boundary layer as well as the generation of stationary modes and higher harmonics. n and m represent multiples of the temporal and spanwise fundamental wavenumbers, respectively.

If the base flow $\bar{\mathbf{q}}(x, y)$ in inhomogeneous in the streamwise and wall-normal directions only, periodicity can be assumed in the spanwise direction which simplifies Eq. (3.51) to

$$\mathbf{q}(\mathbf{x}, t) = \bar{\mathbf{q}}(x, y) + \sum_{m=-\infty}^{+\infty} \sum_{n=-\infty}^{+\infty} \hat{\mathbf{q}}_{mn}(x, y) e^{im\beta z - in\omega t} \tag{3.52}$$

where the fundamental spanwise wavenumber β is introduced. The complex amplitude function $\hat{\mathbf{q}}_{mn}$ is now associated with the mode whose wavenumbers are $(n\omega, m\beta)$.

Introducing the Fourier series of Eq. (3.51) into Eq. (3.50) yields a system of PDEs for the amplitude function $\hat{\mathbf{q}}_n$ which can be written in a compact form as

$$\mathcal{L}_n \hat{\mathbf{q}}_n = \hat{\mathbf{f}}^{res}_n \tag{3.53}$$

where $\mathcal{L}_n$ is the LHNS operator associated with $n\omega$ and $\hat{\mathbf{f}}^{res}_n$ is the unknown Fourier component of the non-linear resonant term with respect to the known total resonant forcing $\mathcal{F}^{res}$,

$$\mathcal{F}^{res}(x, y, z, t) = \sum_{n=-\infty}^{+\infty} \hat{\mathbf{f}}^{res}_n(x, y, z) e^{-in\omega t}. \tag{3.54}$$

For Cartesian coordinates, the entries of the coefficient matrix $\mathcal{L}_n$ are the same as Eq. (3.32) except that ω is replaced by $n\omega$. The total resonant forcing is

$$\mathcal{F}^{\text{res}} = \begin{pmatrix} 0 \\ -\tilde{u}\partial_x\tilde{u} - \tilde{v}\partial_y\tilde{u} - \tilde{w}\partial_z\tilde{u} \\ -\tilde{u}\partial_x\tilde{v} - \tilde{v}\partial_y\tilde{v} - \tilde{w}\partial_z\tilde{v} \\ -\tilde{u}\partial_x\tilde{w} - \tilde{v}\partial_y\tilde{w} - \tilde{w}\partial_z\tilde{w} \end{pmatrix}. \tag{3.55}$$

In an analogous manner as in Eq. (3.53), the 2.5D assumption of Eq. (3.52) allows to write

$$\mathcal{L}_{mn}\hat{\mathbf{q}}_{mn} = \hat{\mathbf{f}}^{\text{res}}_{mn}. \tag{3.56}$$

The left-hand side of Eq. (3.56) represents the action of the LHNS operator on the mode (n, m) while the right-hand side represents the resonant interactions of other modes resulting in the excitation of (n, m). The operator $\mathcal{L}_{mn}$ is the same as Eq. (3.35) except that (ω, β) is replaced by $(n\omega, m\beta)$.

Wave interactions occur in the non-linear right-hand side $\hat{\mathbf{f}}^{\text{res}}_{mn}$ through quadratic[9] products, suggesting that a harmonic mode (ω_1, β_1) can interact with itself to create modes from the sum or difference of its wavenumber as $(2\omega_1, 2\beta_1)$ or $(0, 0)$. Moreover, two distinct harmonic modes (ω_1, β_1) and (ω_2, β_2) also interact to create modes $(\omega_1 \pm \omega_2, \beta_1 \pm \beta_2)$. Therefore, an infinity of mode interactions is generated through a resonance cascade generating lower and higher harmonics. Figure 3.2 is an illustration of such a cascade starting from initialised modes $(2, 0)$ and $(1, 1)$ and truncated for $m = n = 6$.

The modes $(n \neq 0, m = 0)$ can be referred to as stationary modes, or longitudinal vortex modes while $(n = 0, m \neq 0)$ is referred to as a travelling mode. However, the $(0, 0)$ mode clearly distinguishes itself from other modes. By definition, it has a zero frequency as does the base flow. It is a pure product of non-linearity. All other modes contribute to its generation and sustain its energy as a result of self-interactions. It is called *Mean Flow Distortion* (MFD) since it represents the difference between the undisturbed laminar boundary layer and the time-averaged plus spanwise-averaged transitional boundary layer (Hein, 2005). As the non-linear correction to the base flow, the MFD is the only mode impacting physical quantities such as the lift, drag and pressure coefficients, the displacement thickness or the momentum thickness. In the case of NLPSE, which neglects some streamwise derivatives and in particular $\partial_x\hat{p}$, the MFD is governed by the Prandtl boundary-layer equations.

[9] This is intrinsic to the incompressible Navier-Stokes equations, as interactions are cubic for compressible flow.

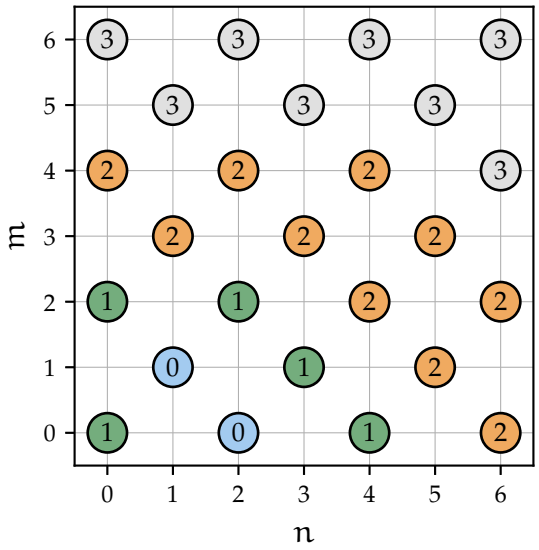

Figure 3.2: Resonance cascade for modes (n, m) where $(2, 0)$ and $(1, 1)$ have been initialised. Digits indicate the order of mode generation. Negative wavenumbers are not included.

The approach named NLHNS in this work consists in generating selected harmonic modes (m, n) by means of a wall forcing in the same fashion as with the linear approach in Eqs. (3.43) and (3.44). The purpose is to analyse mode growth and interaction phenomena induced by small-scale surface irregularities. The NLHNS analysis may then be seen as an extension and improvement of the NLPSE method in that there is no assumption of a slow streamwise evolution and the governing equations remain elliptic in the (x, y) plane. Moreover, in the NLPSE method, modes are usually initialised with tailored amplitudes at the inflow, without wall actuation. In the NLHNS approach, the shape and intensity of the wall-forcing fully determine the non-linear problem. The precise amplitude of the emergent disturbance naturally stems from the level of the forcing. If the spatial resolution is fine enough, the NLHNS may be seen as a DNS where the (z, t) coordinates are treated in Fourier space. Although in theory it comes with a burdensome cost to solve numerically, the NLHNS approach is simpler to deploy than the NLPSE method and requires less computational resource than a DNS. Unlike in the PSE model, there is indeed no need for a normalisation condition for the streamwise derivatives of amplitude functions and no phase constraint on some streamwise wavenumber. There is no requirement to supply initial amplitudes at the inflow state for the fundamental and other non-linearly generated harmonic fields. In addition, the MFD is not handled with a specific treatment in contrast to the NLPSE.

The action of a steady 3D wall roughness on the boundary layer is represented by another right-hand side term, $\hat{f}^{wr}_{mn}$ added to Eq. (3.56). The no-slip condition giving rise to the boundary condition at the wall for the velocity field materialises under

a more difficult form than in Eq. (3.43) and deserves specific attention. Assume a steady, infinitesimal wall-normal surface deformation decomposed in Fourier space for the spanwise direction of the form

$$h(x,z) = \sum_{m=-M}^{m=+M} \hat{h}_m(x) e^{im\beta z} = O(\varepsilon). \tag{3.57}$$

Using the ansatz of Eq. (3.52) for the velocity field, the no-slip condition reads

$$\begin{aligned} \mathbf{0} = \mathbf{u}(x,y,z,t) &= \bar{\mathbf{u}}(x,y) + \sum_{m=-\infty}^{+\infty} \sum_{n=-\infty}^{+\infty} \hat{\mathbf{u}}_{mn}(x,y) e^{im\beta z - in\omega t} \\ &= \bar{\mathbf{u}}(x,0) + \sum_m \sum_n \hat{\mathbf{u}}_{mn}(x,0) e^{im\beta z - in\omega t} + h(x,z) \frac{\partial \bar{\mathbf{u}}}{\partial y}(x,0) \\ &\quad + h(x,z) \sum_m \sum_n \frac{\partial \hat{\mathbf{u}}_{mn}}{\partial y}(x,0) e^{im\beta z - in\omega t} + \frac{1}{2} h^2(x,z) \frac{\partial^2 \bar{\mathbf{u}}}{\partial y^2} + o(\varepsilon^2) \end{aligned} \tag{3.58}$$

after a truncated Taylor expansion in the wall-normal coordinate. Since $\bar{\mathbf{u}}(x,0) = \mathbf{0}$,

$$\begin{aligned} \mathbf{0} &= \sum_m \sum_n \hat{\mathbf{u}}_{mn}(x,0) e^{im\beta z - in\omega t} + \left(\sum_m \hat{h}_m(x) e^{im\beta z} \right) \frac{\partial \bar{\mathbf{u}}}{\partial y}(x,0) \\ &\quad + \left(\sum_p \hat{h}_p(x) e^{ip\beta z} \right) \left(\sum_m \sum_n \frac{\partial \hat{\mathbf{u}}_{mn}}{\partial y}(x,0) e^{im\beta z - in\omega t} \right) \\ &\quad + \frac{1}{2} \left(\sum_p \hat{h}_p(x) e^{ip\beta z} \right) \left(\sum_q \hat{h}_q(x) e^{iq\beta z} \right) \frac{\partial^2 \bar{\mathbf{u}}}{\partial y^2}(x,0) + o(\varepsilon^2). \end{aligned} \tag{3.59}$$

Collecting terms with an equal wavenumber in the last two terms yields

$$\begin{aligned} \mathbf{0} &= \sum_m \sum_n \hat{\mathbf{u}}_{mn}(x,0) e^{im\beta z - in\omega t} + \sum_m \hat{h}_m(x) \frac{\partial \bar{\mathbf{u}}}{\partial y}(x,0) e^{im\beta z - i0\omega t} \\ &\quad + \sum_m \sum_n \left(\sum_{\substack{p,q \\ p+q=m}} \hat{h}_p(x) \frac{\partial \hat{\mathbf{u}}_{qn}}{\partial y}(x,0) \right) e^{im\beta z - in\omega t} \\ &\quad + \sum_m \left(\sum_{\substack{p,q \\ p+q=m}} \frac{1}{2} \hat{h}_p(x) \hat{h}_q(x) \frac{\partial^2 \bar{\mathbf{u}}}{\partial y^2}(x,0) \right) e^{im\beta z - i0\omega t} + o(\varepsilon^2). \end{aligned} \tag{3.60}$$

The penultimate term is a linear combination of wall-normal gradients of modes contributing to $\hat{\mathbf{u}}$ that are *a priori* unknown, as opposed to the base flow $\bar{\mathbf{u}}$. That term may potentially be of order $O(\varepsilon^2)$ since $h = O(\varepsilon)$ and $\hat{\mathbf{u}} = O(\varepsilon)$ although the order of magnitude of $\partial_y \hat{\mathbf{u}}$ is unclear. In the numerical implementation of the NLHNS methodology, the sums are truncated to M and N positive harmonics.

Therefore, to leading order, and according to Eq. (3.60) it is sufficient to impose the following conditions for the perturbation velocity field with $n \neq 0$,

$$\hat{\mathbf{u}}_{mn}(x,0) = -\sum_{\substack{p,q \\ p+q=m}} \hat{h}_p(x) \frac{\partial \hat{\mathbf{u}}_{qn}}{\partial y}(x,0) \tag{3.61}$$

and with $n = 0$,

$$\hat{\mathbf{u}}_{m0}(x,0) = -\hat{h}_m(x) \frac{\partial \bar{\mathbf{u}}}{\partial y}(x,0) - \sum_{\substack{p,q \\ p+q=m}} \hat{h}_p(x) \frac{\partial \hat{\mathbf{u}}_{q0}}{\partial y}(x,0). \tag{3.62}$$

In the linear approach of Section 3.2.2, amplitudes are determined up to a multiplicative constant, whereas a non-linear problem is determined uniquely by the amplitude of initialised modes and the magnitude of the imposed wall-forcing. Mode amplitudes are often presented in terms of their Root Mean Square (RMS) value, defined as

$$\begin{gathered} A^q_{rms}(n,m) = c_n r_m r_n \max_y |\hat{q}_{mn}| \\ c_i = \begin{cases} 1 & \text{if } i = 0 \\ \sqrt{2} & \text{if } i \neq 0 \end{cases} \qquad r_j = \begin{cases} 1 & \text{if } j = 0 \\ 2 & \text{if } j \neq 0. \end{cases} \end{gathered} \tag{3.63}$$

The amplitude may be based on the maximum modulus across the wall-normal direction or, for example at a fixed wall-normal location y_0.

3.3 Boundary treatment for closure

3.3.1 Nature of the harmonic Navier-Stokes system

In order to numerically solve the HNS equations and select an appropriate discretisation method, it is necessary to ascertain the nature of the underlying system of PDEs. This also guides the choice of imposition of boundary conditions to close the system. The method of characteristics is well adapted for this task. Characteristics are directly linked to the notion of Cauchy problems for first order quasi-linear PDEs. In a 2D space, a canonical form may read

$$\mathbf{A}(x,y,\boldsymbol{\phi}) \frac{\partial \boldsymbol{\phi}}{\partial x} + \mathbf{B}(x,y,\boldsymbol{\phi}) \frac{\partial \boldsymbol{\phi}}{\partial y} = \mathbf{F}(x,y,\boldsymbol{\phi}) \tag{3.64}$$

which is linear in the derivatives of $\boldsymbol{\phi}(x, y)$. The concept of Cauchy data relates to the prescription of $\boldsymbol{\phi}$ on a curve Γ in the plane (x, y), for example

$$x = x_0(s) \qquad y = y_0(s) \qquad \boldsymbol{\phi} = \boldsymbol{\phi}_0(s) \tag{3.65}$$

which determines the solution of the PDE (3.64) locally for some curvilinear coordinate s which is parametrising Γ. The Cauchy data in Eq. (3.65) together with Eq. (3.64) constitute the so-called Cauchy problem. If the value of $\boldsymbol{\phi}$ is known on the curve Γ defined by $\gamma(x, y) = 0$ but the values of $\partial\boldsymbol{\phi}/\partial x$ and $\partial\boldsymbol{\phi}/\partial y$ cannot be determined uniquely by the Cauchy data in the neighbourhood of Γ, the Cauchy problem is deemed ill-posed and Γ is called a characteristic curve. In particular, the partial derivatives cannot be determined along a curve tangent to Γ. The tangent to the curve is defined by the relation

$$d\gamma = \frac{\partial\gamma}{\partial x}dx + \frac{\partial\gamma}{\partial y}dy = 0 \tag{3.66}$$

and the differential of $\boldsymbol{\phi}$ along that tangent reads

$$d\boldsymbol{\phi} = \frac{\partial\boldsymbol{\phi}}{\partial x}dx + \frac{\partial\boldsymbol{\phi}}{\partial y}dy. \tag{3.67}$$

A characteristic curve implies that the determinant of the system formed by Eq. (3.64) and Eq. (3.67) vanishes,

$$\begin{vmatrix} \boldsymbol{A} & \boldsymbol{B} \\ \mathbf{I}dx & \mathbf{I}dy \end{vmatrix} = \begin{vmatrix} \boldsymbol{A} & \boldsymbol{B} \\ -\mathbf{I}\zeta_y dy & \mathbf{I}\zeta_x dy \end{vmatrix} = 0 \tag{3.68}$$

where Eq. (3.66) was used with the normal directions to Γ defined as $(\zeta_x, \zeta_y)^T = \nabla\gamma$, yielding the relation $\zeta_x dx + \zeta_y dy = 0$. Eventually, Eq. (3.68) becomes

$$\det(\boldsymbol{A}\zeta_x + \boldsymbol{B}\zeta_y) = 0. \tag{3.69}$$

As characteristics can be interpreted as paths along which information propagates, the nature of the system in Eq. (3.64) is directly determined by the roots of Eq. (3.69). In the event that no roots are real, the Cauchy problem is unconditionally well posed and the system of PDEs is elliptic. Figure 3.3 offers a geometrical interpretation of the nature of a system of PDEs. The solution at a point P depends on the domain of dependence while the region of influence is the portion of Ω impacted by the solution at P. For an elliptic system, information at every domain point propagates isotropically everywhere, and boundary conditions are required for

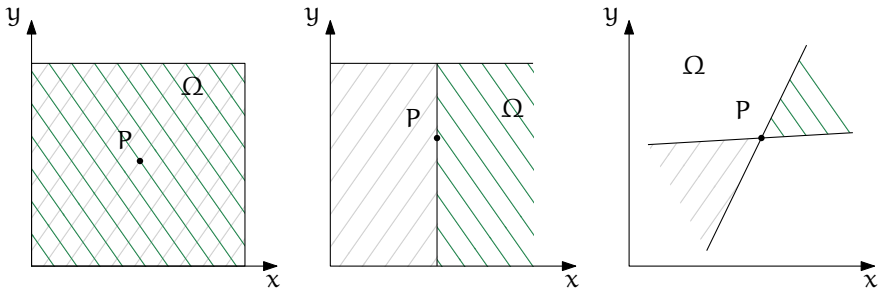

Figure 3.3: Domain of dependence (—) and region of influence (—) for an elliptic (*left*), parabolic (*centre*) and hyperbolic (*right*) system of PDEs

all domain boundaries. Otherwise, the Cauchy problem remains ill-posed. If all the roots are real, including at least two distinct roots, the system is hyperbolic. In that case, information at every point propagates in two directions delimited by the characteristic curves passing by this point. Finally, if the roots are all real with some multiplicity, the system is parabolic and information propagates in one specific direction. Should the set of roots behave differently, the system is said to be of mixed nature.

The method of characteristics is applied to the 2.5D HNS equations obtained by the ansatz (3.34). Since they are a second-order system, a transformation is required to write the system in the first-order form of Eq. (3.64). This is achieved with an extension of the flow variable vector such that

$$\boldsymbol{\Phi} = \left(\hat{p}, \hat{u}, \frac{\partial \hat{u}}{\partial x}, \frac{\partial \hat{u}}{\partial y}, \hat{v}, \frac{\partial \hat{v}}{\partial x}, \frac{\partial \hat{v}}{\partial y}, \hat{w}, \frac{\partial \hat{w}}{\partial x}, \frac{\partial \hat{w}}{\partial y}\right)^{T}. \tag{3.70}$$

Therefore, the four HNS equations must be supplemented with six additional equations. Such a choice is not unique, however it must ensure that the system in Eq. (3.69) is not singular. If the following equations are used,

$$\begin{gathered} \frac{\partial \hat{u}_x}{\partial y} - \frac{\partial \hat{u}_y}{\partial x} = 0, \qquad \frac{\partial \hat{v}_x}{\partial y} - \frac{\partial \hat{v}_y}{\partial x} = 0, \qquad \frac{\partial \hat{w}_x}{\partial y} - \frac{\partial \hat{w}_y}{\partial x} = 0, \\ \frac{\partial \hat{u}_x}{\partial y} + \frac{\partial \hat{v}_y}{\partial y} + i\beta \frac{\partial \hat{w}}{\partial y} = 0, \qquad \frac{\partial \hat{v}}{\partial x} - \partial_x \hat{v} = 0, \qquad \frac{\partial \hat{w}}{\partial y} - \partial_y \hat{w}_y = 0 \end{gathered} \tag{3.71}$$

calculating the 10×10 determinant of Eq. (3.69) reduces to

$$\frac{\zeta_x \zeta_y^9}{Re^2}(1 + \lambda^2)^3 = 0 \tag{3.72}$$

where $\lambda = \zeta_x/\zeta_y$. The non-trivial roots of this polynomial are complex conjugates, $\lambda = \pm i$. This result is not dependent upon the considered dimension, 2D, 2.5D or

3D. Therefore, the HNS equations are elliptic and boundary conditions must be imposed at every domain boundary.

3.3.2 Appropriate boundary conditions

In order to close the LHNS equations, boundary conditions on $\partial\Omega$ must be supplemented. For the eigenvalue-based approach, these must be homogeneous in order to be cast into the GEVP form of Eq. (3.41). Figure 3.4 is an illustration of the different boundaries where these must be imposed. The boundary layer in the base flow $\bar{q}$ grows from the inflow to the outflow boundary.

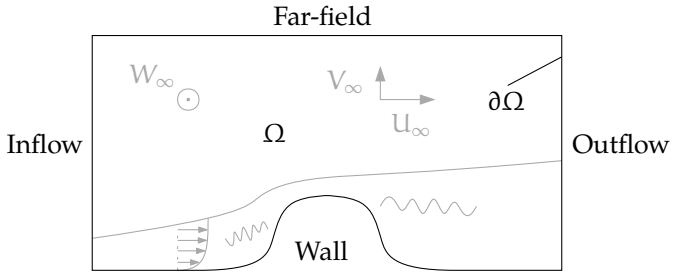

Figure 3.4: Sketch of the physical domain Ω with the different regions of its boundary $\partial\Omega$

At the far-field boundary, it can be assumed that the perturbations have exponentially decayed. An example is the TS modes which are known to decay exponentially as $\exp(-(\alpha^2+\beta^2)y)$ as $y \to +\infty$. Therefore, the homogeneous Dirichlet condition $\hat{p} = \hat{u} = \hat{w} = 0$ is imposed. It should be highlighted that explicitly prescribing a zero-pressure field at a boundary completely determines $\hat{p}$ elsewhere. In other cases, $\hat{p}$ would be determined up to a constant.

Although it is reasonable to assume the wall-normal perturbation also vanishes at the far-field region, a homogeneous Neumann boundary condition $\partial_y \hat{v} = 0$ is imposed[10] to ensure satisfaction of a divergence-free velocity field $\nabla \cdot \hat{\boldsymbol{v}} = 0$. This is a strict requirement for the MFD mode in the NLHNS approach since a variation of displacement thickness accumulated by non-linear interactions must be allowed and accounted for inside the boundary layer. In other words, such a Neumann boundary condition enables the base flow to self-correct in order to satisfy mass conservation across the domain.

The choice of appropriate boundary conditions for the inflow and outflow regions in the HNS context remains an open-ended question and has been notably discussed by Groot, Pinna and van Oudheusden (2015) for a streamwise BiGlobal approach. Numerous choices are possible. A zero-Dirichlet condition at the inflow may be

[10]This expression is only valid in Cartesian coordinates.

justified to prevent any incoming perturbation from the upstream region. It should be used for a forced HNS problem in order to not contaminate the wall actuation region. For both inflow and outflow boundaries, a radiation (or Robin) condition may be imposed such that

$$\frac{\partial \hat{\mathbf{q}}}{\partial x} = i\alpha_0 \hat{\mathbf{q}}, \qquad \mathbf{x} \in \partial\Omega \tag{3.73}$$

which is equivalent to imposing a LST-type mode $\hat{\mathbf{q}}(y)\exp(i\alpha x - i\omega t)$. The wavenumber α_0 may be obtained by a PSE computation or the application of the Gaster transformation (Gaster, 1962). The perturbation is then locally set in the vicinity of the boundary, which is a reasonable condition to impose, should the streamwise gradients of the base flow remain relatively small. Alternatively, the normal stresses can be forced to vanish following

$$\boldsymbol{\sigma} \cdot \mathbf{n} = \mathbf{0}, \qquad \mathbf{x} \in \partial\Omega \tag{3.74}$$

which is usually known as the 'do-nothing' boundary condition since it is naturally satisfied by a variational formulation of the incompressible Navier-Stokes equations. The Cauchy stress tensor $\boldsymbol{\sigma}$ was introduced in Eq. (3.12). Another possibility is to use linear extrapolation of the interior values, which is equivalent to impose

$$\frac{\partial^2 \hat{\mathbf{q}}}{\partial x^2} = 0, \qquad \mathbf{x} \in \partial\Omega. \tag{3.75}$$

At the inflow and outflow boundaries, the perturbation field should be allowed to enter or exit the domain seamlessly, without numerical reflection. Such numerical artefacts, if non-negligible, lead to a restriction of the modelled physics and potentially to a contamination of the solution near the boundaries. To curb the numerical reflections, a coarsened grid next to the boundaries could be employed in order to introduce numerical viscosity, thus preventing reflections through dissipation. However, generating a grid with multiple refinement locations when modelling a surface irregularity is impractical. An absorbing treatment at the boundaries is more amenable and contributes to preventing spurious reflections to the interior of the domain. One possible treatment is a sponge layer added as a penalty term in the HNS equations, introduced by Israeli and Orszag (1981) and further analysed by Bodony (2006) for CFD. The transformed equations read

$$\mathcal{L}(\hat{\mathbf{q}}) = -\sigma\hat{\mathbf{q}} \tag{3.76}$$

where σ is a function of spatial coordinates defining the profile of damping intensity within the sponge layer.

At a solid wall, the perturbation field always satisfies the no-slip condition $\hat{\mathbf{u}}_w = \mathbf{0}$ except, obviously, at the location where a wall forcing term is imposed. However, as mentioned in Section 3.1.3, boundary conditions for the flow variables need to ensure $\nabla \cdot \hat{\mathbf{u}} = 0$ in the eventuality the PPE formulation is used. Following Shirokoff and Rosales (2011), a zero-Dirichlet condition for the tangential velocity components are imposed and a zero-Neumann condition for the normal component are imposed. In Cartesian coordinates, this is equivalent to

$$\hat{u}_w = \hat{v}_w = 0, \qquad \left.\frac{\partial \hat{v}}{\partial y}\right|_w = 0 \tag{3.77}$$

which fulfils the divergence-free condition at the wall. The pressure boundary condition is the momentum conservation equation projected on the wall-normal coordinate, which in the case of a no-slip wall and Cartesian coordinates reduces to

$$\left.\frac{\partial \hat{p}}{\partial y}\right|_w - \frac{1}{Re}\left.\frac{\partial^2 \hat{v}}{\partial y^2}\right|_w = 0. \tag{3.78}$$

If the primitive formulation is considered, the boundary condition for the pressure at the wall is also the momentum conservation equation projected on the wall-normal coordinate in which the divergence-free condition has been substituted. This is referred to as a Pressure Compatibility (PC) condition and reads

$$\left.\frac{\partial \hat{p}}{\partial y}\right|_w + \frac{1}{Re}\left(\left.\frac{\partial^2 \hat{u}}{\partial x \partial y}\right|_w + i\beta \left.\frac{\partial \hat{w}}{\partial y}\right|_w\right) = 0. \tag{3.79}$$

Alternatively, the LPPE can be used as a boundary condition for the pressure as performed by Theofilis (2017).

3.3.3 The perfectly matched layer

In an effort to alleviate the issues mentioned in Section 3.3.2, a generic boundary treatment that models an unbounded domain and prevents reflections of spurious waves into its interior without resorting to empirical or unphysical parameters has been adopted. The approach is the Perfectly Matched Layer (PML) method, introduced in a seminal paper by Berenger (1994) in an electromagnetism framework. The underlying idea is to surround the physical domain with a layer in which the same system as in Eq. (3.26) or Eq. (3.50) is solved, yet with an added dissipation factor. In this way, wave energy is exponentially absorbed and the amplitude

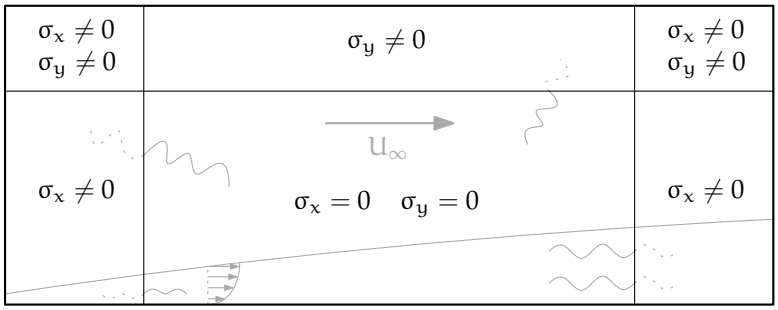

Figure 3.5: Sketch of perfectly matched layers. In the central physical domain the damping profile σ is zero, leaving the HNS equations unchanged. At the corners, the contributions from each spatial direction are summed.

of reflections arising from the domain boundaries is extensively curbed. The layer acts as a reflectionless absorbing medium, independently of the boundary condition at its outer extremity.

Consider a streamwise propagating wave in the positive streamwise direction, $\exp(i\alpha x - i\omega t)$ with $\alpha \in \mathbb{R}$ and $\alpha > 0$. The PML method relies on the concept of analytical continuation, as presented for example by Flanigan (1983). Since the function describing the wave is analytic, it can be evaluated on complex values. Denoting by $\check{x}$ the complex contour, the following coordinate transformation,

$$\check{x} = x + \frac{i}{\omega}\int_x \sigma(r)\,dr \tag{3.80}$$

allows to transform the constant amplitude wave to an exponentially-decaying wave since for some positive function σ governing the intensity of wave damping,

$$e^{i\alpha\check{x}-i\omega t} = \exp\left(-\frac{\alpha}{\omega}\int_x \sigma(r)\,dr\right) e^{i\alpha x - i\omega t}. \tag{3.81}$$

Therefore, the principle of adding a layer where $\sigma > 0$ near the outflow boundary where attenuation is sought becomes evident. The factor $\alpha/\omega = 1/c$ is the inverse of the phase velocity in the streamwise direction. It should be noted that the same absorption benefit is obtained with a layer added at the inflow since the upstream propagating waves $\alpha < 0$ would also decay in the $-x$ direction. To unify the notation with the sponge layer introduced in Eq. (3.76), σ is also referred to as the damping profile. The HNS equations are rewritten with the stretched coordinate $\check{x}$, and the partial derivatives are then transformed following

$$\frac{\partial}{\partial\check{x}} = \frac{1}{s_x}\frac{\partial}{\partial x}, \qquad \frac{\partial^2}{\partial\check{x}^2} = \frac{1}{s_{\check{x}}^2}\frac{\partial^2}{\partial x^2} - \frac{s_x'}{s_x^3}\frac{\partial}{\partial x} \tag{3.82}$$

where s_x is defined as

$$\check{x} = \int_0^x s_x(r)\, dr = \int_0^x \left(1 + \frac{i\sigma(r)}{\omega}\right) dr. \tag{3.83}$$

Extension to higher dimensions is straightforward, although in the current HNS framework absorption needs are mostly at the inflow and outflow boundaries. For example, Fig. 3.5 provides a schematic overview of the method applied in a 2D context, with absorbing layers present at the inflow, at the outflow as well as in the free-stream region of the domain.

Hu (1996) applied the technique to the linearised Euler equations. A decade later, the method was extended to non-linear Euler equations (Hu, 2006). It seems the contribution of Hagstrom et al. (2005) was the first to apply the PML method to the LHNS equations as well as to the non-linear Navier-Stokes equations. The important contribution of Hu, Li and Lin (2008) ascertained its applicability to fluid flow problems.

As the name implies, the interface between the physical domain and the PML is 'perfect', that is reflectionless for the continuous PDEs due to the analytical continuation. The method yields a zero reflection coefficient for all angles of incidence and frequencies at the interface between the physical domain and the lossy layer (Berenger, 1994). After discretisation of the PDEs, reflections unavoidably arise. However, if the resolution is fine enough, the amplitude of reflected waves remains negligible.

The discrete PML also suffers from specific deficiencies. From Eq. (3.80), it can be seen that a region of singularity is reached for significantly low frequencies which can induce spurious reflections. Zero-frequency information is not handled, therefore an alternative boundary treatment should be found for treating the MFD and other stationary modes in the NLHNS approach. Moreover, the PML performs unsuccessfully for damping evanescent waves (Roden & Gedney, 2000). Although they are by nature already decaying, Eq. (3.81) shows that for a purely imaginary wavenumber α, the PML contribution is an oscillation factor rather than an absorbing factor. The discrete reflection coefficient also becomes large for waves at grazing incidence (Collino & Monk, 1998) which travel across the parallel direction of the layer.

In the context of this work, the considered formulation is the one devised by Kuzuoglu and Mittra (1996) as well as Roden and Gedney (2000), called the Complex-Frequency-Shifted (CFS) PML which is arguably the state of the art in absorbing layers. It is an extension of the PML which improves the absorbing

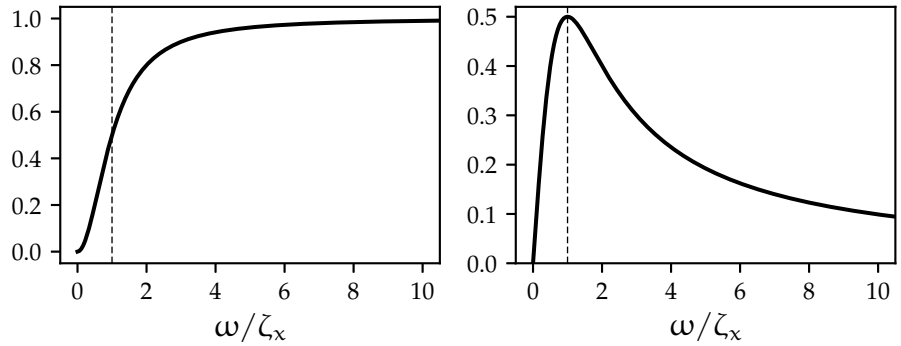

Figure 3.6: Real part $\omega^2/(\zeta_x^2+\omega^2)$ (*left*) and imaginary part $\zeta_x\omega/(\zeta_x^2+\omega^2)$ (*right*) in the CFS-PML attenuation factor. The former governs the absorption of propagating waves whereas the latter is a phase shift reaching a maximum for $\omega=\zeta_x$. This induces absorption for evanescent waves.

performance for waves at grazing incidence as well as for evanescent waves on a discrete level. A shift in the singularity allows to overcome the previously mentioned drawbacks. Remarkably, it is able to treat inhomogeneous, anisotropic and dispersive media. Bérenger (2007) highlights that the CFS-PML is 'very well suited to the optimum absorption of frequency spectra composed of both evanescent and travelling waves present in many realistic physical problems'. This formulation consists of a more general coordinate stretching than in Eq. (3.83) with the introduction of new real variables κ_x and ζ_x such that

$$s_x = \kappa_x + \frac{\sigma_x}{\zeta_x - i\omega}. \tag{3.84}$$

When Eq. (3.84) is introduced in the phase of a streamwise propagating wave, its spatial evolution becomes

$$e^{i\alpha\check{x}-i\omega t} = \exp\left(i\alpha\int_x \kappa_x - i\omega t\right)\exp\left[-\frac{\alpha}{\omega}\left(\frac{\omega^2}{\zeta_x^2+\omega^2} - i\frac{\omega\zeta_x}{\zeta_x^2+\omega^2}\right)\int_x \sigma_x\right] \tag{3.85}$$

where ζ_x is the complex-frequency shift, here assumed constant for convenience; it shifts the singularity $\omega=0$ of the basic PML transformation in Eq. (3.80) onto the complex plane. The frequency dependence of the attenuation factor in Eq. (3.85) is displayed on Fig. 3.6. For low frequencies $\omega/\zeta_x \approx 1$, the imaginary part shows that evanescent waves are attenuated, with maximum effect at a certain cut-off frequency $\omega=\zeta_x$. As depicted by the evolution of the real part, propagating waves are attenuated for large frequencies which renders the CFS-PML acting as a low-pass filter. The stretching function $\kappa_x \geqslant 1$ contributes to further dampen evanescent waves.

Deploying the PML within the HNS framework is highly convenient. Since the equations operate in frequency space, the sole application of the coordinate

stretching of Eq. (3.82) is necessary. There is no need to revert to temporal space which would significantly complicate the formulation. However, appropriate care should be considered with NLHNS-type analyses where the fundamental frequency ω is prescribed to the extent that the MFD mode is stationary by nature. Equations (3.83) and (3.84) indeed show that the PML approach is simply unable to absorb temporal zero-frequency signals. Therefore, the PML treatment is used for modes $(n \neq 0, m)$ whereas the 'classic' sponge layer of Israeli and Orszag (1981) presented in Eq. (3.76) can be deployed to absorb energy for modes $(n = 0, m)$. The numerical implementation of absorbing boundary treatments is further discussed in Chapter 4.

Another pathological case is when ω is an unknown quantity such as in the framework of BiGlobal analysis. To apply the PML and force the BiGlobal computation to obtain perturbation modes whose amplitude decays at the extremities of the domain, a constant frequency ω_0 can be set with a value matching a frequency domain of interest. Naturally, this contrivance may yield efficient absorption only for a limited frequency bandwidth and thus the functions defining the coordinate stretching should be adjusted.

Chapter 4

Numerical Framework

Eins, zwei, drei, vier, fünf, sechs, sieben, acht

—Kraftwerk, *Nummern*, *1981*

In this computational chapter, we thoroughly present the numerical methods allowing to solve HNS-based problems. The first section covers how governing equations are discretised in space as well as the practical implementation of absorbing boundary treatments. Afterwards, we present the architecture of the developed parallel computational code as well as the libraries on which it relies. We then describe the procedures and algorithms to obtain the numerical solutions of BiGlobal, LHNS or NLHNS problems. The parallel performance of the code is assessed as well as its limitations for dealing with large-scale, 3D problems.

4.1 Spatial discretisation

4.1.1 Finite difference method on non-uniform grids

Among the variety of existing numerical methods used in computational science, the Finite Difference Method (FDM) has been chosen for the discretisation of the HNS equations described in Chapter 3. It is one of the most dominant approaches, based on the approximation of derivative operators by Taylor expansions. These form linear combinations of function values evaluated on a finite number of discrete grid points $\{x_i\}$ belonging to a structured grid. The initial continuous system of PDEs is then sought to be solved on such a grid.

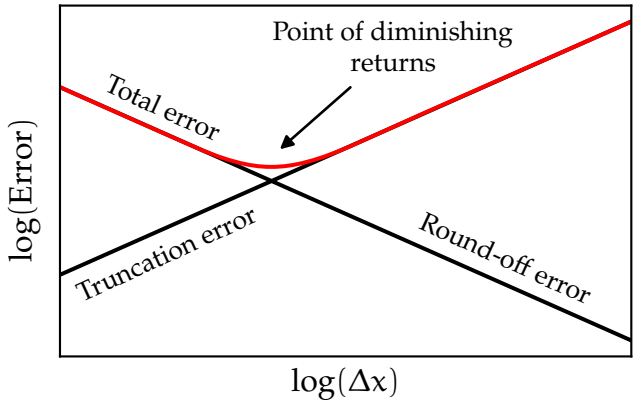

Figure 4.1: Sources of numerical error as a function of step size Δx

A finite-difference approximation has several advantages. Besides its theoretical simplicity and its inexpensive computational requirements, a high level of accuracy can be targeted with arbitrarily high approximation orders as long as the solution remains regular. Moreover, the process of discretisation by means of finite differences on a regular mesh is embarrassingly parallel and can be easily implemented. Conversely, such a discretisation method is not suited for geometrically complex domains where devising a structured mesh is tedious. In this work, domains with smooth geometrical evolutions are considered, henceforth alleviating this drawback. The assumption of a regular target solution implies that high-order finite difference methods typically suffer from a significant loss of accuracy when discontinuities are encountered or yield numerical oscillations near a shock region. Since incompressible flows are considered, no shock waves are present. However, for accuracy purposes, special care is required for functions featuring high gradients or with highly stretched grid regions.

Although fine numerical resolution could deal with such cases appropriately, controlling the total error of the FDM consists of a trade-off between managing the truncation error and managing the round-off error, as shown in Fig. 4.1. The truncation error is defined as the difference between the exact analytical solution and the numerical derivative obtained with a finite difference approximation, essentially a truncated Taylor series. As the step size Δx tends to zero, the truncation error tends to zero. The order of accuracy q of an FDM characterises the asymptotic behaviour of the truncation error as the step size decreases, or how 'fast' it tends to zero following $O(\Delta x^q)$. Instead of monotonically decreasing with the step size, the total error is reduced up to a point of diminishing returns where the round-off error, arising from the inexact representation of floating-point numbers by computers, becomes predominant and where the total error increases. The round-off error contributes to the ill-conditioned character of

matrices discretised with an FDM, which is discussed thoroughly in Section 4.3.2. A general disadvantage of numerical methods employing polynomial interpolation, the category to which FDMs belong is the occurrence of the Runge phenomenon. It manifests itself through large boundary oscillations when equispaced grids are used.

Finally, the paramount properties of finite difference schemes are consistency, stability and convergence. A numerical scheme is consistent if the discrete finite-difference derivative operators tend towards the original continuous operators of the PDE when the step size Δx tends to zero. The stability property of a finite difference scheme guarantees that round-off errors, numerical fluctuations or noise do not excessively amplify during the computation. Convergence then ensures that the numerical solution tends to a correct solution of the mathematical model. In this framework, the Lax-Richtmyer equivalence theorem (Richtmyer & Morton, 1967), also known as the fundamental theorem of numerical analysis, states that for a consistent and linear finite difference model for which the IBVP is well-posed, stability is a necessary and sufficient condition for convergence. The stability property is then essential to ascertain the degree to which the mathematical model describes the real physical phenomena. Among other seminal papers, the notion has been notably discussed by Gustafsson, Kreiss and Sundström (1972) for IBVPs. A well-known source of instability for high-order FDMs is the presence of the boundaries and the enforcement of boundary conditions, discretised from the continuous problem.

In light of all these drawbacks and characteristics, the discretisation method chosen in this research work is a stable FDM based on Lagrange interpolation with a non-uniform grid (Hermanns & Hernández, 2007). From this point onwards, it is referred to as *FD-q* where q denotes the order of discretisation. The authors followed the principle of working with an appropriate non-uniform grid in order to cluster the grid nodes and hence alleviate the aforementioned instabilities. Such a grid is computed iteratively, starting from an equispaced grid and by imposing conditions on the extrema of polynomial factors in each subdomain that influence the interpolation error. The method can be seen as an intermediary between a classic FDM and the Chebyshev spectral collocation method (for which details can be found, for example, in Canuto et al., 1988); if $n_x + 1$ denotes the total number of grid nodes, classic finite-difference stencils are retrieved when the grid is kept equispaced whereas when $q = n_x$, the resulting interpolation coefficients and grid respectively coincide with Chebyshev collocation coefficients and Chebyshev roots. The grid is unique for each value of q and n_x.

The principle of the method is exposed as follows. Let $\phi(x)$ be a sufficiently smooth function for which evaluation of its derivatives $\phi'(x)$ and $\phi''(x)$ at discrete points are sought. Consider $\{x_i\}$ as a discretisation of the spatial domain $[-1,1]$ where $i \in \{0,\dots,n_x\}$. A piecewise polynomial interpolant $I_i(x)$ of degree $q \leqslant n_x$ which satisfies $I_i(x_i) = \phi(x_i) = \phi_i$ is constructed by means of Lagrange interpolation. Each interpolant I_i is solely valid in a specific subdomain Ω_i which includes the grid node x_i, such that

$$\Omega_i = [x_{i-1/2}, x_{i+1/2}], \quad i \in \{0,\dots,n_x\} \tag{4.1}$$

and

$$\bigcup_{i=0}^{n_x} \Omega_i = [-1,1]. \tag{4.2}$$

The subdomain boundaries defined by half-integers $x_{i\pm1/2}$ are arbitrary as long as they do not overlap with other subdomains. The interpolant may then be written as a linear combination of function values ϕ_i,

$$I_i(x) = \sum_{j=s_i}^{s_i+q} l_{ij}(x)\phi_j \tag{4.3}$$

where the Lagrange coefficients l_{ij} are

$$l_{ij}(x) = \prod_{\substack{m=0 \\ s_i+m\neq j}}^{q} \frac{x - x_{s_i+m}}{x_j - x_{s_j+m}}. \tag{4.4}$$

Each seed in $\{s_i\}$, $i \in \{0,\dots,n_x\}$ is the index of the leftmost grid node which contributes to the construction of the interpolant, and specifies which grid nodes x_j define the finite difference stencil. If the polynomial degree q is chosen as even, the seed distribution reads

$$\{s_i\} = \{\underbrace{0,\dots,0}_{q/2 \text{ times}}, \underbrace{0,1,\dots,n_x-q}_{\text{centred finite difference}}, \underbrace{n_x-q,\dots,n_x-q}_{q/2 \text{ times}}\} \tag{4.5}$$

which results in centred finite difference stencils for nodes x_i located sufficiently away from the boundaries of $[-1,1]$. Figure 4.2 depicts the piecewise polynomial interpolation in the FD-q framework when $n_x = 10$ and $q = 6$ with a representation of the stencils over the domain. Stencils are gradually shifted with the proximity of the boundary, up to a one-sided stencil at the boundary. The finite difference formulae are obtained by evaluating each interpolant I_i at the grid node x_i.

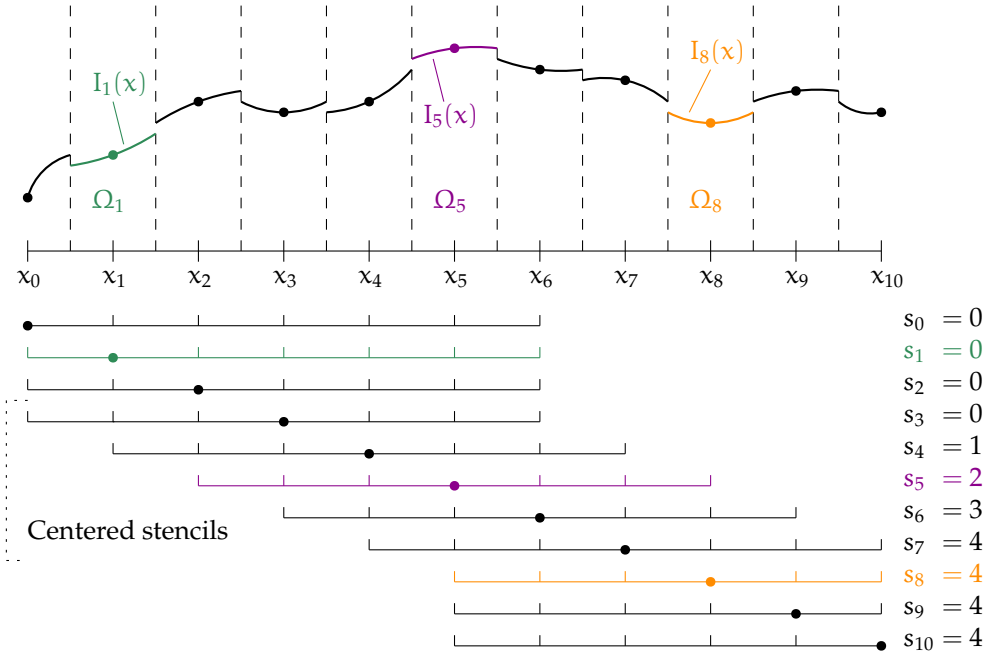

Figure 4.2: Finite difference stencils for a polynomial interpolation of order $q = 6$ using $n_x + 1 = 11$ nodes. Some stencils are centred and unaffected by the vicinity of the boundaries. Reproduced from Hermanns and Hernández (2007).

The method can be applied for arbitrary high orders of discretisation q as long as $q \leqslant n_x$. In practice the polynomial degree is kept as $q \ll n_x$ in order to benefit from small stencils of extent $q + 1$, however high orders are typically targeted with values comprised between 4 and 12. Employing a high order FDM implies a smaller error than first-order or second-order methods for the same number of grid nodes, or achieves a prescribed error level with less computational resources. In contrast to compact finite difference schemes (Lele, 1992) which employ fewer nodes, the FD-q still requires $q + 1$ nodes to reach an accuracy of order q. Nonetheless, it still leads to significant computational cost savings compared to the Chebyshev spectral collocation method where the interpolant uses all the grid nodes. For a one-dimensional discretisation as presented in Fig. 4.2, the number of non-zero elements in the differentiation matrix is indeed $(q + 1)n_x$ compared to n_x^2 for Chebyshev spectral collocation. Therefore, if $q \ll n_x$ the savings are evident.

Hermanns and Hernández (2007) established that for all degrees q the non-uniform grids preserve the stability character of the differential operator and the error decays as $1/n^q$ for one-dimensional and 2D wave equations. Moreover, for all degrees q the FD-q method correctly reproduces the transient behaviour of the differential operator for the convection-diffusion equation. The soundness of the choice of this discretisation method may be further reinforced by results obtained in the context of global stability analysis (Paredes et al., 2013); the FD-q discretisation was compared against other high-order FDMs, namely compact finite difference

schemes (Lele, 1992), Dispersion-Relation-Preserving schemes (Tam & Webb, 1993) and summation-by-parts methods (Strand, 1994). The Chebyshev spectral collocation method was also in the benchmark. From an accuracy viewpoint, discretising the linear stability operator using the FD-q method was found to outperform all the listed FDMs at any order, and to equal the Chebyshev collocation method in some cases.

4.1.2 Grid transformations

The problems considered in this work involve solving the HNS equations on relatively complex geometries incorporating surface irregularities. For accuracy purposes, regular grids spanning physical domains Ω should then mould the surface deformation accordingly and sufficiently resolve regions where large base flow gradients or perturbation gradients are expected, including the wall-normal section containing the boundary layer. In addition, the FD-q grid is formulated on the logical, computational domain Ξ spanned by coordinates $\boldsymbol{\eta} = (\xi, \eta) \in [-1, 1]^2$. The discretisation of the HNS equations occurs in this precise grid system. Therefore, a grid transformation function between Ω and Ξ must be devised to map the physical grid to the logical grid and express the spatial derivatives of the HNS equations accordingly. A variable ϕ is then transformed as

$$\phi(x, y) = \phi(x(\xi, \eta), y(\xi, \eta)) = \phi(\xi, \eta) \tag{4.6}$$

where $\mathbf{x} = (x, y)$ represents the spatial coordinates of the physical domain Ω.

Figure 4.3 provides an illustration of such a grid transformation. Besides ensuring accuracy where needed, its objective is twofold since the grid may also be rendered coarse where the solution is expected to vary little; in doing so, numerous degrees of freedom are discarded from the computation which contributes to reduce computational requirements. However, the transformation process generates many additional terms in the discretised PDEs. With the help of the chain rule, the first derivatives in the logical coordinate system may be expressed as

$$\frac{\partial \phi}{\partial x}(\xi, \eta) = \frac{\partial \xi}{\partial x}\frac{\partial \phi}{\partial \xi} + \frac{\partial \eta}{\partial x}\frac{\partial \phi}{\partial \eta}, \qquad \frac{\partial \phi}{\partial y}(\xi, \eta) = \frac{\partial \xi}{\partial y}\frac{\partial \phi}{\partial \xi} + \frac{\partial \eta}{\partial y}\frac{\partial \phi}{\partial \eta} \tag{4.7}$$

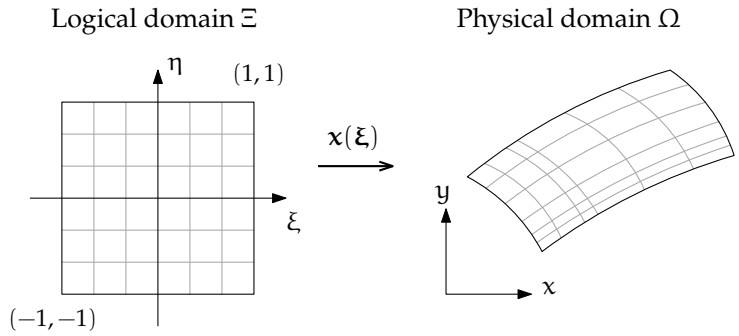

Figure 4.3: Grid mapping between the logical domain Ξ and the physical domain Ω. The transformation typically includes grid clustering, domain stretching as well as surface deformation.

and a repeated chain rule application provides the relations involving the second-order partial derivatives as well as the cross partial derivative:

$$\frac{\partial^2\phi}{\partial x^2} = \left(\frac{\partial\xi}{\partial x}\right)^2 \frac{\partial^2\phi}{\partial\xi^2} + \frac{\partial^2\xi}{\partial x^2}\frac{\partial\phi}{\partial\xi} + 2\frac{\partial\xi}{\partial x}\frac{\partial\eta}{\partial x}\frac{\partial^2\phi}{\partial\xi\partial\eta} + \frac{\partial^2\eta}{\partial x^2}\frac{\partial\phi}{\partial\eta} + \left(\frac{\partial\eta}{\partial x}\right)^2 \frac{\partial^2\phi}{\partial\eta^2} \tag{4.8a}$$

$$\frac{\partial^2\phi}{\partial y^2} = \left(\frac{\partial\eta}{\partial y}\right)^2 \frac{\partial^2\phi}{\partial\eta^2} + \frac{\partial^2\eta}{\partial y^2}\frac{\partial\phi}{\partial\eta} + 2\frac{\partial\xi}{\partial y}\frac{\partial\eta}{\partial y}\frac{\partial^2\phi}{\partial\xi\partial\eta} + \frac{\partial^2\xi}{\partial y^2}\frac{\partial\phi}{\partial\xi} + \left(\frac{\partial\xi}{\partial y}\right)^2 \frac{\partial^2\phi}{\partial\xi^2} \tag{4.8b}$$

$$\begin{aligned}\frac{\partial^2\phi}{\partial x\partial y} = {} & \frac{\partial\xi}{\partial x}\frac{\partial\xi}{\partial y}\frac{\partial^2\phi}{\partial\xi^2} + \frac{\partial^2\xi}{\partial x\partial y}\frac{\partial\phi}{\partial\xi} + \left(\frac{\partial\xi}{\partial x}\frac{\partial\eta}{\partial y} + \frac{\partial\xi}{\partial y}\frac{\partial\eta}{\partial x}\right)\frac{\partial^2\phi}{\partial\xi\partial\eta} + \frac{\partial^2\eta}{\partial x\partial y}\frac{\partial\phi}{\partial\eta} \\ & + \frac{\partial\eta}{\partial x}\frac{\partial\eta}{\partial y}\frac{\partial^2\phi}{\partial\eta^2}.\end{aligned} \tag{4.8c}$$

Equations (4.7) and (4.8) represent the effect of the grid transformation $\mathbf{x}(\boldsymbol{\xi})$ on the spatial derivative operators of the discretised HNS equations via the metric terms $\partial^k\boldsymbol{\xi}/\partial\mathbf{x}^k$. This mapping between the grid of the physical domain Ω and the grid of the computational domain Ξ results from the composition of several transformations according to the complexity of the geometry and the features of the perturbation field to be captured.

The elemental stretching transformation mapping the FD-q interval $\xi \in [-1, 1]$ to $x \in [x_a, x_b]$ in the streamwise direction is

$$x(\xi) = \frac{1}{2}\left((x_b - x_a)\xi + x_a + x_b\right). \tag{4.9}$$

As mentioned in Section 4.1.1, the grid generated by the FD-q method is non-uniform. Its clustering near the boundaries should be adjusted in order to accommodate to localised features in the streamwise direction (such as the wall-forcing region or a surface irregularity) while maintaining a rectangular grid in the logical domain. This may be accomplished with interior contraction mappings

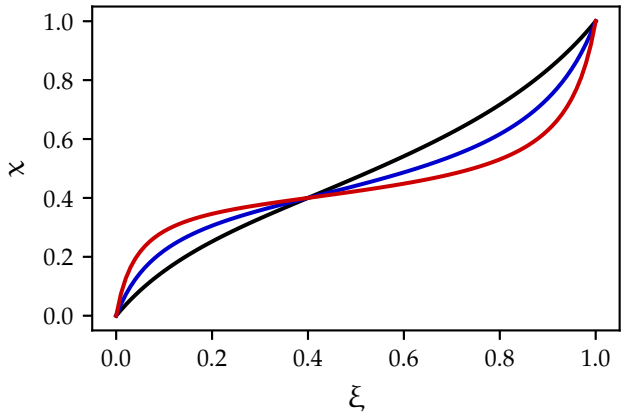

Figure 4.4: Grid transformation (4.10) with interior clustering at $\xi = 0.4$ performed with the tangential function (4.11) and $\gamma = 0.3$ (—), 0.4 (—) and 0.45 (—).

as elaborated by Liseikin (2010). For example, the definition of a function reading

$$x(\xi) = \begin{cases} x_0 \left(1 - \varphi\left(1 - \dfrac{\xi}{x_0}\right)\right) & \text{if } 0 \leqslant \xi \leqslant x_0 \\ x_0 + (1 - x_0)\varphi\left(\dfrac{\xi - x_0}{1 - x_0}\right) & \text{if } x_0 \leqslant \xi \leqslant 1 \end{cases} \tag{4.10}$$

allows to map the interval $[0, 1]$ onto $[0, 1]$ with local clustering around the location $x_0 \in [0, 1]$ if φ is a monotonically increasing function providing grid clustering near $\xi = 0$. An effective 'building block' function φ typically possesses a small value of its derivative near 0 such as a tangent function,

$$\varphi(\xi) = \frac{\tan(\pi\gamma\xi)}{\tan(\pi\gamma)} \tag{4.11}$$

or an exponentially-based clustering such that

$$\varphi(\xi) = \frac{e^{\gamma\xi} - 1}{e^{\gamma} - 1} \tag{4.12}$$

where the clustering intensity is controlled by the parameter γ. Figure 4.4 shows the interior clustering transformation in action with different values of γ.

The main objective of grid transformations in the wall-normal direction is to allow the finite-difference scheme to accurately capture the boundary layer region as well as any localised structure arising in the perturbation field. Malik (1990) notoriously introduced a bilinear mapping which divides the wall-normal grid into two separate regions with an equal number of grid points. The FD-q grid

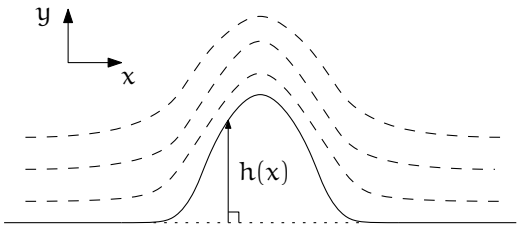

Figure 4.5: Sketch of the transformation modelling a geometry deformation in the streamwise direction defined by its height $h(x)$

defined by $\eta \in [-1, 1]$ is mapped onto $[0, y_\infty]$ by means of the transformation

$$y(\eta) = \frac{y_0 y_\infty (1+\eta)}{y_\infty - (y_\infty - 2y_0)\eta}. \tag{4.13}$$

The wall-normal position delimiting the two regions is y_0, which may be simply set to a value close to δ in general. Alternatively, a finer grid distribution might be sought thanks to the biquadratic mapping derived by Groot et al. (2017). It extends the bilinear mapping to the extent that the wall-normal domain is split into three regions that each contain one third of the grid nodes. The biquadratic transformation reads

$$y(\eta) = y_\infty \frac{a\eta^2 + b\eta + c}{d\eta^2 + e} \tag{4.14}$$

where the parameters are defined as

$$\begin{gathered} a = y_1 - 3y_0, \qquad b = \frac{3}{2}(y_1 - y_0), \qquad c = \frac{1}{2}(y_1 + 3y_0), \\ d = 2(2y_1 - 2y_0 - y_\infty), \qquad e = 2y_\infty - y_1 + y_0. \end{gathered} \tag{4.15}$$

The region delimiters are subject to the conditions $0 < y_0 < y_1 < y_\infty$, $y_1 < 9y_0$ and $9y_1 < y_0 + y_\infty$ in order to ensure a smooth and well-posed transformation.

The effect of large-scale surface deformation is modelled by means of the grid transformation of Eq. (4.6). Defining a geometrical deformation by a profile $h(x)$, the wall-normal coordinate is transformed via $\eta = y - h(x)$ to map the physical domain to a rectangular domain as shown in Fig. 4.5. In this work, some analyses are applied to wing geometries with non-negligible curvature which necessitate a body-fitted curvilinear transformation. Their treatment could be achieved in the same vein as the previous transformations, that is by incorporating the wing curvature effects via a grid transformation and the metric terms of the discretised PDEs. Instead of following that approach, the HNS equations are directly formulated in body-fitted coordinates. For further details on their derivation, the reader is referred to Appendix A.

From an accuracy point of view, it is essential to ensure the grid transformations are defined through regular functions to discard the possibility of discontinuities affecting the solution. Moreover, the grid mesh size should undergo a smooth variation; if such condition is not met, this would result in an unavoidable loss of accuracy in the finite-difference scheme (Hirsch, 2007). Consequently, evaluating the metric terms $\partial^k \xi / \partial x^k$ analytically would be tempting since the explicit transformation expressions are often available. However, it turns out that computing the metric terms numerically with the same FD-q scheme yields a smaller truncation error because of the cancellation of one term in its Taylor expansion. Handling the metric terms numerically thus improves the accuracy in situations where substantial grid clustering is employed.

4.1.3 Absorbing boundary treatment

The numerical implementation of the absorbing boundary treatments introduced in Chapter 3 is presented, namely the sponge region of Eq. (3.76) as well as the PML detailed in Section 3.3.3. Both approaches require defining a layer of sufficient width and sufficient resolution where absorption is active. Although, for equal damping intensity and for equal resolution, a larger layer allows a greater decrease in perturbation amplitude than with a small layer, it requires a larger computational domain and thus increased computational requirements. Therefore, the parameters of the absorbing treatments should be optimised to

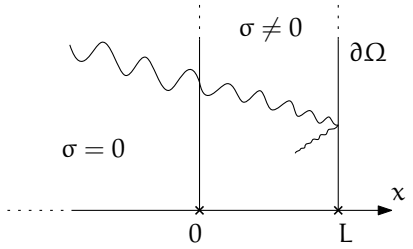

Figure 4.6: Definition of the absorbing layer which starts at $x = 0$ and extends to $x = L$

reach a prescribed 'vanished' amplitude whilst minimising the computational overhead. As depicted in Fig. 4.6 in the x direction, the followed convention is that the layer starts at $x = 0$ and is of width L. The functions that govern the absorption shall be defined. For the sponge region, the damping profile may be an exponential-type blending such that

$$\sigma(x) = \sigma_{max} \frac{e^{(x/L)^2} - 1}{e - 1}. \tag{4.16}$$

In the case of the PML, the functions forming the complex coordinate stretching (3.84) are usually taken as polynomial functions such that the damping, stretching and CFS profiles respectively read

$$\sigma_x(x) = \sigma_{max}\left(\frac{x}{L}\right)^2 \tag{4.17a}$$

$$\kappa_x(x) = 1 + (\kappa_{max} - 1)\left(\frac{x}{L}\right)^2 \tag{4.17b}$$

$$\zeta_x(x) = \zeta_{max}\left(1 - \frac{x}{L}\right) \tag{4.17c}$$

and the maximum values κ_{max}, ζ_{max} are of purely numerical nature. These profiles should vary smoothly, from 0 at the interface with the regular domain up to L at the computational boundary, and have a relatively small derivative near the start of the layer to avoid stiffness in the energy absorption. The maximum value of the damping profile σ_{max} may be derived from the reflection coefficient R_c of a plane wave at the $x = L$ boundary, given by Collino and Monk (1998) who generalised the original estimate of Berenger (1994). Assuming that a zero-Dirichlet boundary condition is enforced at the outflow region of $\partial\Omega$ and the base PML coordinate stretching of Eq. (3.83) is considered, the reflection coefficient of the PML is given by

$$R_c = -\exp\left(2i\omega\int_0^L\left(1 + \frac{i\sigma(r)}{\omega}\right)\,dr\right). \tag{4.18}$$

Equation (4.18) then suggests devising a damping such that $\int\sigma = +\infty$ to reach a zero theoretical reflection coefficient, which is impossible numerically. Instead, it should be set to a large enough value. Plugging Eq. (4.17a) into Eq. (4.18) yields the expression for σ_{max} as

$$\sigma_{max} = \frac{-3\ln(R_c)}{2L}. \tag{4.19}$$

In this numerical context, R_c may then be seen as a target reflection coefficient. The sponge layer approach as well as the PML are now tested on two distinct flow instability configurations. First, their performance is assessed on a travelling, oblique TS wave generated in a developing Blasius boundary layer and growing in a region downstream of $Re_{crit} = 519.4$. The reduced frequency, defined as

$$F = 10^6\frac{2\pi f\nu_\infty}{U_\infty^2} = 10^6\frac{\omega}{Re} \tag{4.20}$$

is $F = 25$ and the non-dimensional spanwise wavenumber is $\beta = 0.05$. Absorbing regions are set up at the inflow and at the outflow of the domain in the streamwise direction, although the emphasis is on the layer located downstream due to the significant levels of energy reached. In comparison, the amplitude levels are

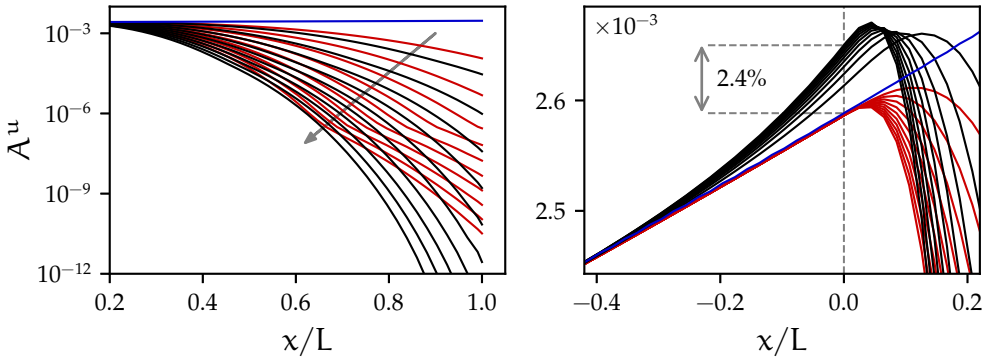

Figure 4.7: Amplitude based on $\hat{u}$ for an oblique TS wave generated in a developing Blasius boundary layer. Comparison between the PML (—) and sponge layer (—) approaches as well as without absorption (—). For the PML, the parameter R_c is varied from 10^{-1} to 10^{-10}. For the sponge layer, the parameter σ_{max} is varied from 0.1 to 1.0. *Left*, general view of the absorbing region starting at x_σ; *right*, magnified region near the start of the absorbing region.

negligible upstream of the wall-forcing site near the inflow. Damping performance is displayed in Fig. 4.7 for the streamwise perturbation velocity only, as the other flow variables undergo the same behaviour qualitatively and quantitatively. The sponge approach and the PML allow to gradually decrease the TS amplitude by several orders of magnitude up to the rightmost computational boundary, where a linear extrapolation boundary condition is imposed. The absorbing layer width is equal for both approaches, decreasing the TS amplitude smoothly at a rate determined by σ_{max}. In Fig. 4.7, the base PML stretching is employed and recovered by setting $\kappa_{max} = 1$ and $\zeta_{max} = 0$ in Eq. (3.84). From a numerical point of view, established rules of thumb for the PML include maintaining a sufficient resolution of grid points per wavelength within the layer (at least 10 to 20) and defining its width to at least half of the greatest wavelength present in the flow perturbation system.

On the one hand, the PML approach seems to absorb energy seamlessly, without impacting the solution at the interior of the domain. This is demonstrated by the right part of Fig. 4.7, for $x < 0$. On the other hand, depending on the intensity of the damping profile σ_{max} the sponge layer appears to be stiffer than the PML; the amplitude level yielded by the former slightly upstream of the layer interface is increased compared to the solution without damping as well as with the PML. A relative change in amplitude of 2.4% can be observed at the interface between the interior of the domain and the lossy layer. This feature is not critical since it merely adds a narrow non-physical region that could be discarded from the results. However, care should be taken in the case of the NLHNS approach. The elliptic character of the governing equations combined with the non-linear interactions resulting from such an amplitude change due to the absorption of oblique modes

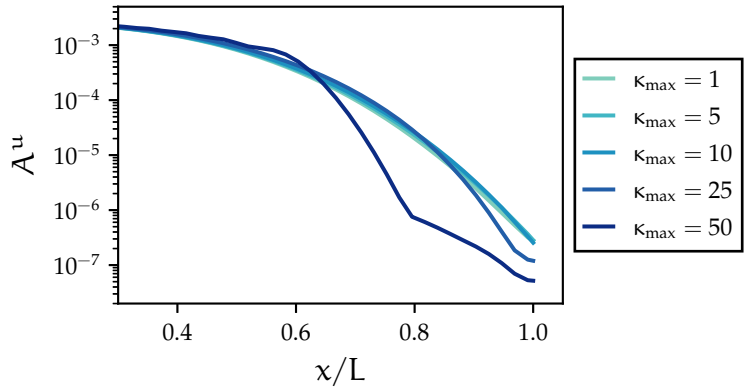

Figure 4.8: Amplitude of the TS wave within the PML as the maximal grid compression κ_{max} is adjusted. Developing Blasius boundary layer.

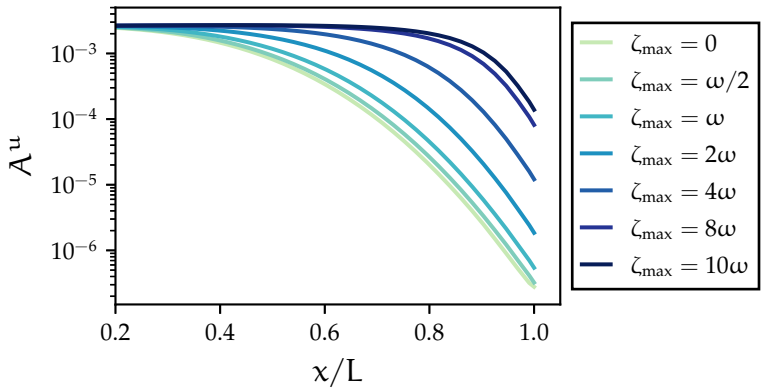

Figure 4.9: Amplitude of the TS wave within the PML as the maximal complex frequency shift ζ_{max} is adjusted. Developing Blasius boundary layer.

$(n \neq 0, m = 0)$ could detrimentally affect the harmonic evolution near the outflow boundary. In light of this, the PML appears as an efficient and seamless solution to absorb non-zero temporal frequency modes.

After witnessing its performance for the original formulation of Eq. (3.83), the impact of the parameters defining the CFS-PML approach is verified. The maximum value of the grid compression function κ, which controls the damping of evanescent waves, is varied on the same flow configuration whilst the CFS is set to 0 and $R_c = 10^{-3}$. Figure 4.8 highlights that a minor variation is obtained as κ_{max} is increased from 1 to 10, nonetheless greater values induce a deviation from a smooth absorption; lower amplitude values at the end of the domain are reached while absorption seems to suffer from stiffness as grid compression increases. An analogous observation was reported by Duru and Kreiss (2012) with respect to the time step restrictions of wave propagation governed by linear elastodynamics theory. Conversely, increasing the CFS parameter seems to restrain the absorption level of propagating waves while maintaining a smooth behaviour as Fig. 4.9 indicates, with $\kappa_{max} = 1$ and $R_c = 10^{-3}$. These observations entail that, should

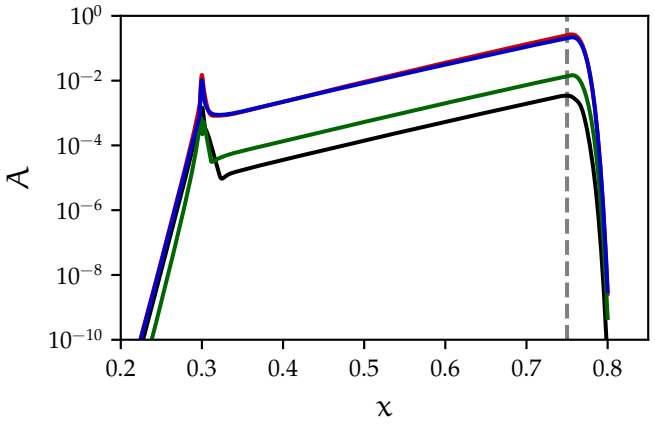

Figure 4.10: Evolution of the amplitude based on $\hat{p}$ (—), $\hat{u}$ (—), $\hat{v}$ (—) and $\hat{w}$ (—) of a crossflow instability developing in an FSC boundary layer. The sponge layer (- -) is such that $\sigma_{max} = 1$.

evanescent or grazing incidence waves are sought to be damped in situations where they have a non-negligible impact, the CFS-PML parameters shall be adjusted in order not to hinder the smooth absorption of propagating waves.

Eventually, the absorbing capability for zero temporal frequency signals and hence oblique modes in the current HNS framework is evaluated. As discussed in Section 3.3.3, the PML cannot be used for that purpose. The sponge layer is then tested on the CF instability of an FSC boundary layer which is a reasonable approximation of a 3D swept-wing boundary layer. Falkner and Skan (1931) initially introduced a class of similarity solutions to the boundary-layer equations in the presence of a non-zero pressure gradient that Cooke (1950) extended to incorporate the effect of sweep. Such a class of laminar boundary layers is governed by a set of ODEs whose solution may be obtained conveniently. In the current case, the pressure gradient (or Hartree) parameter is $\beta_H = 0.51$ which corresponds to a favourable pressure gradient and the sweep angle is $\Lambda = 55.26°$, promoting CF-type instability. A stationary disturbance is generated slightly downstream of the inflow plane characterised by $Re^*_\delta = 337.9$. The spanwise wavenumber is $\beta = 0.1$. At the end of the computational domain, a linear extrapolation boundary condition is imposed. Figure 4.10 shows efficient absorption of the amplitude functions near the outflow of the domain, without qualitative differences between flow variables. Therefore, the efficiency of the PML and sponge layer approaches in the HNS framework have been established. The following developments provide an overview of the computational tool and of the machinery set up to solve HNS problems based on the numerical discretisation presented.

4.2 Programme architecture and solution procedure

In order to deploy the 2.5D flow stability methodologies presented in Chapter 3, a parallel computation code has been developed from scratch with the objective of providing highly accurate solutions with rapid turnover times. The code is written in modern Fortran using its 2008 standard. Its design principles include modularity in order to unify all analysis methodologies under a single framework. Portability is also sought for usage either on a single workstation or on high-end parallel clusters. These principles should not be enforced to the detriment of its parallel computing capability and its efficiency. Therefore, the code relies on carefully selected state-of-the-art numerical libraries. Such a choice bears the advantage of benefitting from the best approaches encapsulated by experts in their field. Opting for a library, however, intrinsically assumes its implementation is 'optimal' while significant efforts are required to ensure it fully exploits the application code and underlying hardware.

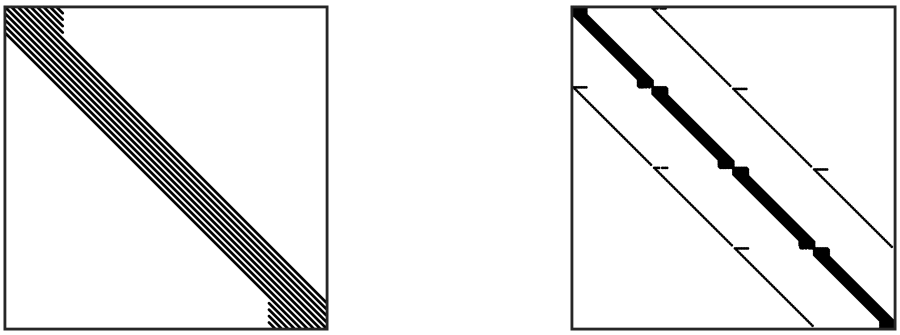

(a) With 1 MPI process/subdomain **(b)** With 4 MPI processes/subdomains

Figure 4.11: Sparsity patterns of discretised LHNS operator $\mathbf{L}$ for serial and parallel computations. The grid is formed of $n_x = 400$ and $n_y = 50$ nodes which yields a leading dimension of 80,000. Only 0.014% of the matrix entries are non-zero.

The discretisation of the HNS equations by the FD-q approach results in sparse matrices, with a significant fraction of zero entries. Additional details on the matrix assembly from the discretised equations are provided in Appendix B for the curious reader. The matrix structure is illustrated in Fig. 4.11 where sparsity patterns of the LHNS matrix operator are presented for different row ownerships. The matrices even have a banded structure, with a bandwidth[1] that increases as the number of subdomains in Ω increases due to the coupling between degrees of freedom on separate subdomains. Furthermore, since the problems in this work involve convection-dominated flows with high Reynolds numbers, the matrices are non-symmetric.

[1] The lower (respectively upper) bandwidth of a matrix $\boldsymbol{A} = (a_{ij})_{1 \leqslant i,j \leqslant n} \in \mathbb{C}^{n \times n}$ is the greatest integer k such that $a_{ij} = 0$ if $j < i - k$ (respectively $j > i + k$).

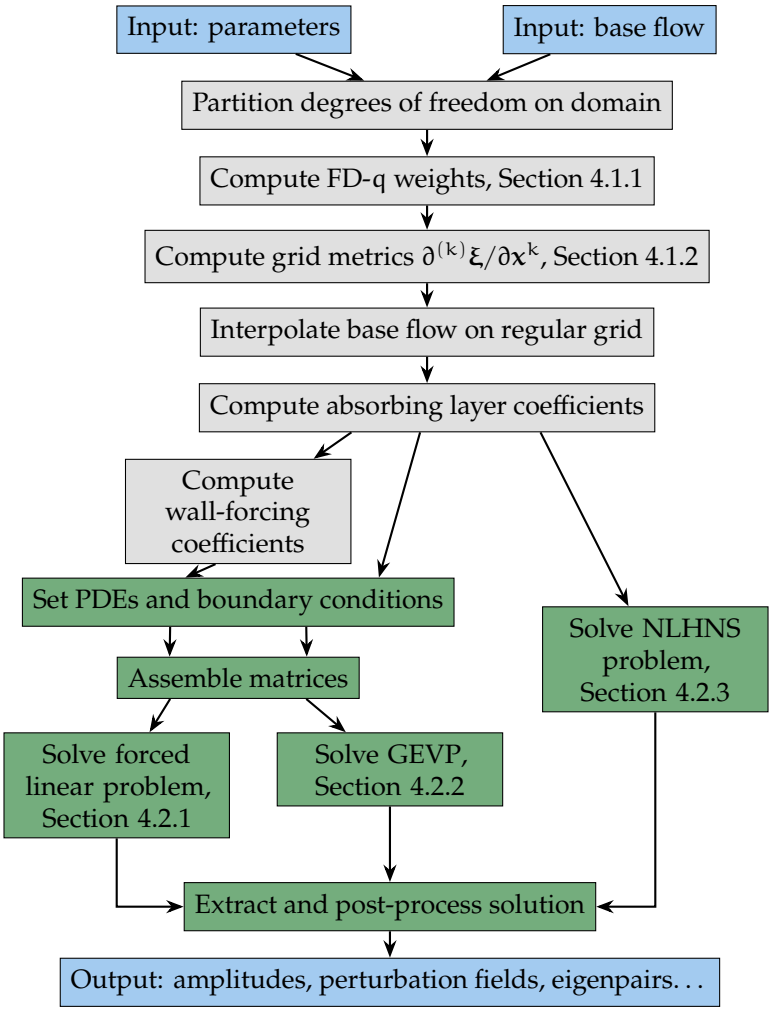

Figure 4.12: Structure of the developed code. Some stages are performed in parallel (■) or at least partially.

The choice of libraries should be structured around these properties. The Portable, Extensible Toolkit for Scientific computation (PETSc) library (Balay et al., 2020) has been chosen as the skeleton of the programme. It encompasses a suite of data structures and routines for the parallel solution of scientific applications modelled by PDEs. PETSc provides, on the one hand, parallel matrix and parallel vector assembly routines with extensive support for sparse storage formats. On the other hand, it features a variety of scalable parallel preconditioners and Krylov subspace methods that form iterative solvers for linear systems. The drawing power of PETSc is its object-oriented paradigm that enables the user to handle matrices, vectors and solvers defined by their interface rather than their data structure. Furthermore, the library is based on distributed-memory parallelism by means of the Message Passing Interface (MPI) standard library.

Figure 4.12 provides an overview of the successive stages processed by the code. The parallelism is based on a division of the logically rectangular computational

domain Ξ into distinct rectangular slices, whose degrees of freedom are owned locally by each MPI process. This is performed via the use of a PETSc 'DMDA' object which provides the topology of the local regular grid, containing information about the parallel data layout and communication with other slices. In other words, each process owns a predetermined number of rows on the matrix operators discretising the HNS equations, and fills the entries that belong to these rows during the assembly stage. After generating the computational grid, computing the FD-q weights as well as the grid metrics of the mapping with Ω, the base flow is interpolated on the computational grid using high-order B-splines. If necessary, the coefficients of the wall-forcing amplitude functions and of the functions defining the absorbing layers are computed. From that point, all the terms appearing in the discretised HNS equations have been calculated and can be collected in parallel. Before assembling matrices, the memory required to store their entries in a sparse format is preallocated for efficiency.

Depending on the nature of the problem, library procedures then solve either the linear system or the GEVP in parallel for which further details can be found respectively in Section 4.2.1 and Section 4.2.2. Treating the NLHNS approach requires a succession of more sophisticated stages which are expanded in Section 4.2.3. The verification and validation of the code is covered in Sections 5.1 and 6.1.

4.2.1 Solving linear systems

The different flow instability methodologies involved in this work require the numerical solution $\hat{\mathbf{q}}$ of a linear system of the form

$$\boldsymbol{A}\hat{\mathbf{q}} = \hat{\mathbf{f}} \tag{4.21}$$

where $\boldsymbol{A}$ is square, sparse and non-symmetric. For example, when discretising the LHNS operator with $n_x = 4{,}000$, $n_y = 120$, $q_x = 4$ and $q_y = 10$, the leading dimension of $\boldsymbol{A}$ is 1,920,000 and only 0.0014% of its entries are non-zero. It includes the degrees of freedom corresponding to boundary conditions. The numerical solution of Eq. (4.21) represents the major computational overhead to solve the discretised HNS problem. It is thus imperative to rely on the fastest and most efficient approaches for that purpose. In this work, a parallel, direct solver based on Lower-Upper (LU) decomposition called MUltifrontal Massively Parallel Solver (MUMPS) (Amestoy et al., 2001) is employed. It is interfaced with PETSc and operates in three distinct steps.

First and foremost, MUMPS pre-processes $\mathbf{A}$ in an attempt to preserve sparsity and performs a symbolic factorisation where the structure of the LU factors is mapped. The required number of floating-point operations as well as the required memory for the subsequent phases are also predicted. This analysis may be performed either serially or in parallel. Afterwards, the matrix $\mathbf{A}$ is redistributed among the processes following the mapping computed in the first phase. The factorisation is then processed on distinct subsets of elements, or frontal matrices, which can be treated simultaneously. The robustness of the factorisation can be improved by applying numerical pivoting, nonetheless increasing the fill-in of the LU factors and the number of operations. Finally, the solution is obtained via a forward elimination step followed by a backward elimination step. Its accuracy may be improved by iterative refinement.

4.2.2 Solving generalised eigenvalue problems

The Arnoldi and Krylov-Schur methods

After discretisation, the LHNS equations in which the streamwise BiGlobal ansatz has been introduced turn into a GEVP in the unknown ω,

$$\mathbf{A}\hat{\mathbf{q}} = \omega \mathbf{B}\hat{\mathbf{q}} \tag{4.22}$$

where the discrete operators $\mathbf{A}$ and $\mathbf{B}$ incorporate the degrees of freedom for which boundary conditions are imposed. In order to numerically solve Eq. (4.22) the Scalable Library for Eigenvalue Problem computations (SLEPc) was selected since it specifically targets large-scale and sparse eigenproblems. SLEPc is based on the PETSc library and provides parallel eigenvalue solvers for their numerical solution. It is also layered with the MPI standard.

A countless number of global stability analysis applications employed the method of Arnoldi (1951) whose practicality for solving large eigenproblems was established by Saad (1980). It belongs to the class of Krylov subspace methods, which essentially project the original problem onto a certain Krylov subspace of a significantly smaller dimension and whose eigenpairs approximate accurately that of the original problem. Given a matrix $\mathbf{L} \in \mathbb{C}^{n\times n}$, the m-order Krylov subspace is defined by the action of the $m \ll n$ powers of $\mathbf{L}$ on a vector $\mathbf{x}$ as

$$\mathcal{K}_m(\mathbf{L}, \mathbf{x}) = \text{span}\{\mathbf{x}, \mathbf{L}\mathbf{x}, \mathbf{L}^2\mathbf{x}, \ldots, \mathbf{L}^{m-1}\mathbf{x}\}. \tag{4.23}$$

The Arnoldi procedure then builds an orthogonal basis of $\mathcal{K}_m$ that are the columns of $\mathbf{V}_m \in \mathbb{C}^{n\times m}$ such that by construction,

$$\mathbf{L}\mathbf{V}_m = \mathbf{V}_m\mathbf{H}_m + \mathbf{r} \tag{4.24a}$$

$$\mathbf{V}_m^H\mathbf{L}\mathbf{V}_m = \mathbf{H}_m \tag{4.24b}$$

where $\mathbf{r}$ is a residual which quantifies how well the column vectors of $\mathbf{V}_m$ approximate an invariant subspace. $\mathbf{H}_m \in \mathbb{C}^{m\times m}$ is an upper Hessenberg matrix whose eigenvalues, called Ritz eigenvalues, may easily be computed. These will converge to an approximation of the largest magnitude eigenvalues of $\mathbf{L}$; the quality of the approximation naturally increases with m. Nonetheless, the convergence is only guaranteed if the initial vector $\mathbf{x}_1$ lays in an invariant subspace. Since guessing an initial vector fulfilling such a condition is tedious, the Arnoldi method is often restarted after a few iterations to recompute a new initial vector. This is known as explicit restarting, as opposed to implicit restarting where the Arnoldi method is coupled with the QR algorithm to avoid updating $\mathbf{x}_1$. The Krylov-Schur method introduced by Stewart (2002) is based on a numerically robust restarting scheme and, for this reason, may be seen as an enhancement of the implicitly restarted Arnoldi method with respect to convergence (Hernández et al., 2009). SLEPc includes a parallel version of the method, which has been logically chosen for solving BiGlobal problems in this current work.

Spectral transformation

Due to the absence of a time derivative in either the continuity equation (3.26a) or the LPPE (3.27a) and the enforcement of some boundary conditions, the mass matrix $\mathbf{B}$ is singular. Moreover, the convergence of the Krylov-Schur algorithm is optimal for eigenvalues lying at the spectrum extremities, and it is harder to extract eigenvalues located further into the interior of the spectrum. The regions of interest for linear stability problems of the kind considered in this work are typically located next to the origin. Hence, a spectral transformation such as the shift-and-invert approach must be employed to solve the GEVP. Using a shift-and-invert transformation bears the advantage of enhancing convergence of the eigenpairs in the vicinity of an interior target, or shift τ. Convergence is also inherently improved. The downside of the approach is the constraint of manually prescribing shift values in the complex plane.

Shifting the GEVP in Eq. (4.22) by the quantity $-\tau\mathbf{B}$ on both sides yields after inversion

$$(\mathbf{A} - \tau\mathbf{B})^{-1}\mathbf{B}\hat{\mathbf{q}} = \theta\hat{\mathbf{q}} \tag{4.25}$$

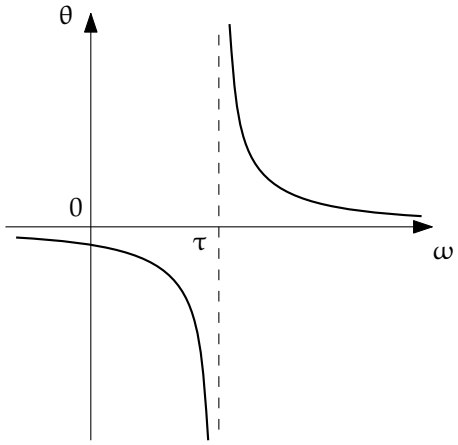

Figure 4.13: Evolution of the eigenvalue $\theta = 1/(\omega - \tau)$ after the shift-and-invert spectral transformation. This illustration assumes real quantities.

where $(\mathbf{A} - \tau\mathbf{B})$ must be invertible. The transformation leaves the eigenvector $\hat{\mathbf{q}}$ unmodified, while the relation between the original eigenvalue ω and the transformed eigenvalue θ is

$$\theta = \frac{1}{\omega - \tau}. \tag{4.26}$$

With this transformation, the eigenvalues θ of the largest magnitude sought by the Krylov-Schur method correspond to the eigenvalues closest to the shift τ as illustrated in Eq. (4.26). The improved convergence for interior eigenvalues comes with an inevitable cost of solving a linear system. However, such a task is performed only once during the Krylov-Schur iterations, and in parallel thanks to MUMPS.

Accuracy of eigenpairs

Setting up the Krylov-Schur algorithm requires the prescription of the number of sought eigenvalues. The dimension of the Krylov subspace $\mathcal{K}_m$, the maximum number of iterations and the tolerance for the convergence criterion must also be provided. The latter is based on the absolute residual norm of computed eigenpairs $(\omega, \hat{\mathbf{q}})$,

$$\|\mathbf{r}\| = \|(\mathbf{A} - \omega\mathbf{B})\hat{\mathbf{q}}\| \tag{4.27}$$

rather than a relative residual in order to avoid a loss of accuracy due to round-off errors with eigenvalues located close to the origin.

Besides, a balancing technique is applied on the shift-and-invert operator of Eq. (4.25) in an attempt to curb round-off errors when the matrices have a large norm. In that case, an appropriate implicit diagonal scaling $\mathbf{D}$ is applied on

the shift-and-invert operator $\mathbf{D}(\mathbf{A}-\tau\mathbf{B})^{-1}\mathbf{B}\mathbf{D}^{-1}$, which potentially improves the accuracy of the computation with respect to the requested tolerance.

4.2.3 Solving non-linear harmonic Navier-Stokes

General strategy

The mathematical foundations of the NLHNS approach were presented in Section 3.2.3. For its numerical application, the flow decomposition $\mathbf{q} = \bar{\mathbf{q}} + \tilde{\mathbf{q}}$ of Eq. (3.52) is truncated to N positive temporal harmonics and M positive spanwise harmonics such that

$$\tilde{\mathbf{q}}(x,y,z,t) = \sum_{m=-M}^{+M}\sum_{n=-N}^{+N} \hat{\mathbf{q}}_{mn}(x,y)e^{im\beta z - in\omega t}. \tag{4.28}$$

The discretisation of the perturbation $\tilde{\mathbf{q}}$ for the (x,y) plane is performed with the FD-q as developed in Section 4.1.1. The Fourier expansion of Eq. (4.28) assumes that in the (z,t) plane the signal $\tilde{\mathbf{q}}$ is assumed periodic with respective periods $L_z = 2\pi/\beta$ and $T = 2\pi/\omega$. Within these periods, the signal is sampled with respectively $(2M+1)$ and $(2N+1)$ equally-spaced discrete points such that the following relations hold,

$$L_z = (2M+1)\Delta z, \qquad T = (2N+1)\Delta t \tag{4.29}$$

where Δz and Δt are the constant step sizes. Equation (4.28) then becomes

$$\tilde{\mathbf{q}}(x,y,z,t) = \sum_{m=-M}^{+M}\sum_{n=-N}^{+N} \hat{\mathbf{q}}_{mn}(x,y)\exp\left(\frac{2\pi i m z}{(2M+1)\Delta z} - \frac{2\pi i n t}{(2N+1)\Delta t}\right). \tag{4.30}$$

There are as many discrete samples as interval segments due to the periodicity of the signal. Since $\forall(z,t)$, $\tilde{\mathbf{q}}(x,y,z+L_z,t+T) = \tilde{\mathbf{q}}(x,y,z,t)$, the $(2M+2)$th and $(2N+2)$th points are redundant and therefore not included in the summation. Finally, when evaluated at discrete points the spanwise coordinate and time coordinate sequences may be expressed as

$$z_k = k\Delta z, \qquad t_l = l\Delta t \tag{4.31}$$

with k and l verifying $-M \leqslant k \leqslant M$ and $-N \leqslant l \leqslant N$. Hence, the semi-discrete form in Eq. (4.30) is transformed into

$$\tilde{\mathbf{q}}(x, y, z_k, t_l) = \sum_{m=-M}^{+M} \sum_{n=-N}^{+N} \hat{\mathbf{q}}_{mn}(x, y) \exp\left(\frac{2\pi i k m}{2M+1} - \frac{2\pi i l n}{2N+1}\right). \tag{4.32}$$

Equation (4.32) is precisely the expression of the 2D inverse Discrete Fourier Transform (DFT) of the sequence $\{\hat{\mathbf{q}}_{mn}(x, y)\}$. The values of M and N should be picked large enough to encompass key interaction mechanisms for a selected problem. It however comes at the expense of computational efficiency, since the number of linear systems to solve during the NLHNS procedure increases with M and N.

The non-linear problem is triggered by a small-scale wall roughness seen by one or several (n, m) modes and modelled by boundary conditions. After spatial discretisation, the NLHNS procedure involves $(N+1) \times (2M+1)$ coupled linear systems expressed as

$$\mathbf{L}_{mn} \hat{\mathbf{q}}_{mn} = \hat{\mathbf{f}}^{\text{res}}_{mn} + \hat{\mathbf{f}}^{\text{wr}}_{mn}, \quad m \in \{-M, M\}, \quad n \in \{0, N\} \tag{4.33}$$

where $\mathbf{L}_{mn}$ is the discretised LHNS operator associated with wavenumbers $(n\omega, m\beta)$ including degrees of freedom at the domain boundaries. Due to the conjugate symmetry property of the DFT described in the following subsection, it is indeed not necessary to consider $n \in \{-N, N\}$. The right-hand side is the sum of the (n, m) Fourier coefficient of the total resonant forcing $\hat{\mathbf{f}}^{\text{res}}_{mn}$ defined in Eq. (3.55) and the (n, m) wall-forcing contribution from the roughness $\hat{\mathbf{f}}^{\text{wr}}_{mn}$ detailed in Eqs. (3.61) and (3.62). Since the resonant forcing generates non-linearity and is consequently a function of several modes, the linear systems in Eq. (4.33) are all coupled. However, in practice, an iterative procedure is applied to decouple the linear systems and solve them independently. Resonant forcing terms are updated at each iteration with information from the previous iteration until the amplitude functions of all (n, m) modes have converged with respect to a predetermined criterion.

The current NLHNS approach is a fully elliptic extension of the NLPSE approach. While the latter is notoriously known for its competitive computational cost, several numerical precautions should be undertaken to ensure the practicality of the former via computational efficiency and memory management. Figure 4.14 summarises the broad lines of the followed numerical procedure relying on PETSc and MUMPS. Each iteration implies solving linear systems described by Eq. (4.33) for which the LHNS matrices $\mathbf{L}_{mn}$ are constant along the computation. Thus,

```
SET FUNDAMENTAL FREQUENCY f AND WAVENUMBER β
SET SMALL-SCALE WALL ROUGHNESS CHARACTERISTICS
INITIALISE NON-LINEAR FORCING TERMS TO SMALL VALUE ε
GET SYMBOLIC FACTORISATION OF L_MN
WHILE RESIDUAL > TOL DO
    FOR m ← −M TO M DO
        FOR n ← 0 TO N DO
            ASSEMBLE LHNS OPERATOR L_mn
            ASSEMBLE RIGHT-HAND SIDE f̂_mn = f̂_mn^res + f̂_mn^wr
            GET NUMERIC FACTORISATION OF L_mn
            SOLVE L_mn q̂_mn = f̂_mn
        END
    END
    COMPUTE RESIDUAL
    APPLY BACKWARD DFT FROM FREQUENCY SPACE
    COMPUTE NON-LINEAR RIGHT-HAND SIDE (3.55) IN PHYSICAL SPACE
    APPLY FORWARD DFT FROM PHYSICAL SPACE
END
```

Figure 4.14: Pseudo-code algorithm for the solution of a NLHNS problem

it would be tempting to compute the different (n, m) LU decompositions at the first iteration, and to store these in memory during the whole procedure with the avowed goal of only using rapid backward and forward elimination to retrieve the solutions $\hat{\mathbf{q}}_{mn}$. Such an option is regrettably not viable due to the enormous required amount of Random-Access Memory (RAM). With $N = 4$, $M = 9$ and otherwise typical discretisation parameters, 650 GB or so would be required to be divided across processes. Storing the LU decompositions on disk instead would divide that amount by an approximate factor of 6, leading to a more amenable load for distributed-memory clusters. However, the total computation time would be detrimentally impacted due to the severe overhead associated with parallel input/output.

It turns out all matrices $\mathbf{L}_{mn}$ have the same sparsity pattern which leads to the same symbolic factorisation. Therefore, a trade-off between computation time and memory requirements can be found by computing a symbolic factorisation once and for all, before assembling $\mathbf{L}_{mn}$ and computing its numerical factorisation for every (n, m) and at every iteration. Although performing these numerical factorisations on the fly increases the total computation time, obtaining the final solution can be accelerated thanks to parallel processing. This method significantly eases memory usage, since only the structure of the LU factors is stored in RAM and the numerical LU factorisation is performed on the fly. PETSc is also able to

optimise subsequent matrix assemblies by exploiting the constant sparsity pattern via reusing information from the first assembly.

Discrete Fourier transforms

In this DFT context, the perturbation flow field has a discrete periodicity of $2N+1$ in time and of $2M+1$ in the spanwise direction. However, in the case of an infinite swept wing configuration, only the modes $(n, m) \in [0, N] \times [-M, M]$[2] need to be solved for without loss of generality. This is due to the conjugate symmetry property that ensures the perturbation $\tilde{q}$ remains a real quantity. Figure 4.15 is a schematic drawing of the property which illustrates how the total perturbation field may be reconstructed after DFT. If the base flow becomes 2D, solving the quadrant $(n, m) \in [0, N] \times [0, M]$ is sufficient. The modes are solved in frequency space. In order to calculate the total resonant forcing of Eq. (3.55) in physical space

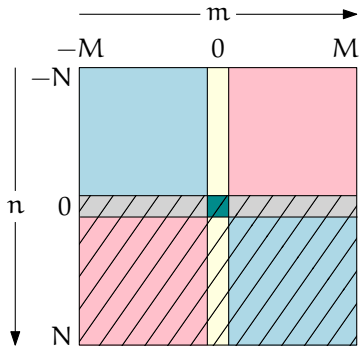

Figure 4.15: Illustration of the 2D-DFT conjugate symmetry, where colours indicate mutual complex conjugate modes. The shaded region corresponds to the modes solved for during the computation. The MFD mode (■) is real by nature.

and determine its Fourier coefficients for the following iteration, the code must rely on an implementation of the DFT. The Fastest Fourier Transform in the West (FFTW) library (Frigo & Johnson, 2005) is used for that purpose. It is remarkably able to adapt its algorithms to the hardware, offering fast and highly accurate backward and forward DFT computations.

Due to the finite, periodic nature of the DFT, high-frequency content in the continuous perturbation field may be folded back to low frequencies in the process, which is a source of error called aliasing. It may destabilise the iterative procedure when the extremities of the wavenumber spectrum become energetic. For example, with $M = N = 2$ the $(4, 4)$ mode arising from the interaction of $(2, 2)$ with itself would be indistinct from the $(-1, 1)$ mode. Since the NLHNS products presented in Eq. (3.55) are quadratic, doubling the number of modes in each coordinate and

[2] $(n, m) \in [-N, N] \times [0, M]$ is also an appropriate choice.

zeroing the Fourier coefficients for $n > 2$ and $m > 2$ allows to curb aliasing errors. This process is known as 'zero-padding'. However, it is sufficient to extend the DFT dimensions to $3N/2$ and $3M/2$ to annihilate aliasing with quadratic products (Canuto et al., 1988), which is famously known as the $3/2$ zero-padding rule. That anti-aliasing precaution is integrated in the NLHNS procedure during transforms between physical space and Fourier space.

Monitoring the convergence

The convergence of the procedure is monitored at a specific streamwise station x_0 typically located close to the outflow region. The criterion is based on the relative residual in ℓ_2-norm of the harmonic amplitudes which must vary less than a predetermined tolerance between two successive iterations k, such that

$$\frac{\|A_{x_0}^{q_i}(n, m, k) - A_{x_0}^{q_i}(n, m, k-1)\|_2}{\|A_{x_0}^{q_i}(n, m, k-1)\|_2} < \text{tol} \tag{4.34}$$

with the harmonic velocity field $\{q_i\} = (u, v, w)$ taken into consideration. For the first iteration, the Fourier coefficients of the resonant forcing $\hat{\mathbf{f}}^{\text{res}}$ corresponding to the interior of the domain Ω are initialised to a small value, typically 10^{-50}. This arrangement avoids the tedious computation of a null-space basis or the computation of an obvious zero solution.

The NLHNS approach, like the NLPSE approach, is able to compute the evolution of mode interactions for non-linear regimes. An outstanding question is how far in the non-linear regime can the NLHNS computation remain stable and to what extent its elliptic character may hinder that purpose, as opposed to the stable quasi-parabolic NLPSE approach. The MFD mode should provide some evidence, since it carries a significant level of energy which could destabilise the computation.

A significant MFD indeed leads to the iteratively-computed right-hand side potentially carrying more weight than the LHNS operator on the left-hand side. To improve the stability of the procedure, an under-relaxation approach can be used to update the resonant forcing, following

$$\hat{\mathbf{f}}_{mn}^{\text{res}} = (1 - \tau)\hat{\mathbf{f}}_{mn}^{\text{res,old}} + \tau\hat{\mathbf{f}}_{mn}^{\text{res,new}} \tag{4.35}$$

where $\tau \in [0, 1]$ is the relaxation parameter and values computed at the current and previous iterations are used. This improves the robustness in cases where non-linear interactions dominate, such as in the harmonic saturation regime. Another stabilising approach procedure is to work with gradual amplitude increments,

allowing the NLHNS algorithm to converge first for intermediate levels of the final, target amplitude of wall-forcing or wave amplitude. The computation corresponding to the next increment is then kick-started by using the previously converged solution.

4.3 Performance and limitations

4.3.1 Parallel efficiency

In the context of High-Performance Computing (HPC), relevant metrics include the raw computation time and the scalability of the code as the number of CPUs increases. Since the developed code relies on a distributed-memory parallelism, it is important to ascertain the memory scalability, that is how evenly a large-scale computation can be divided among the different processes. This allows to formulate problems with many degrees of freedom on clusters when the memory requirements are too high on a single workstation. This section elaborates on the run-time scalability of the code. The backbone of the three different methodologies presented in Section 4.2 is the numerical solution of a linear system computed with MUMPS. Therefore, assessing its performance is critical for solving large 2.5D-type problems as it is the most time-consuming task during execution; the first few non-parallel stages listed in Fig. 4.12 necessitate in practice a negligible amount of time in comparison.

At this point a distinction should be made between strong scaling and weak scaling. For $n_p > 1$ MPI processes, the former quantifies how much faster the solution can be computed as the total problem size remains constant, the ideal case being n_p times faster. The latter rather assesses whether the solution of a n_p times larger problem can be computed in the same time as with one process; this corresponds to a total problem size increasing at the same rate as the number of processes, and a constant problem size per process.

In order to provide a fair estimation of the parallel *speed-up*, a few precautions should be applied. First and foremost, it is essential to ensure each process owns a sufficient number of degrees of freedom (such as 20,000) to not suffer from overhead due to intra-process communications. Appropriate options should be passed to the Fortran compilers to enable code optimisation and to tailor the instruction sets to the underlying CPU architecture. Furthermore, computations should be repeated several times to guarantee reproducibility. Load balancing shall be performed as far as possible to ensure each process deals with a near equal number of degrees of freedom. Finally, the affinity of MPI processes with respect

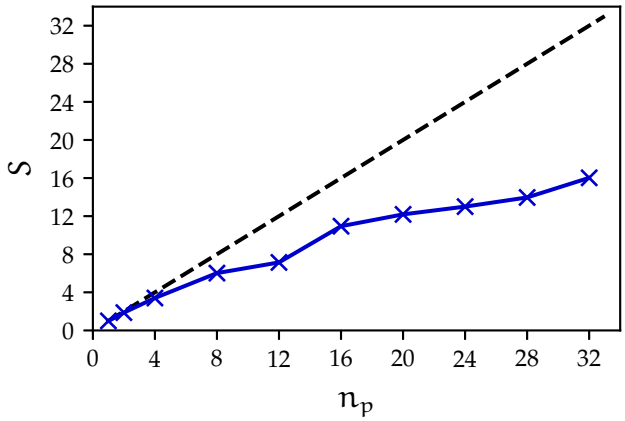

Figure 4.16: Strong speed-up S (—) as a function of the number of MPI processes n_p when solving a linear system with MUMPS. Comparison with ideal scalability (--). The leading dimension of the matrix is 2,160,000 which means each process owns 67,500 degrees of freedom in the $n_p = 32$ case.

to hardware also has a non-negligible impact, since it is well-known that sparse matrix operations are memory-bound rather than compute-bound. Therefore, the physical binding of MPI processes should maximise the available memory bandwidth.

Insight on the strong scaling behaviour of the code is provided in Fig. 4.16, where the relative[3] strong scaling speed-up defined as

$$S_s = \frac{t(1)}{t(n_p)} \tag{4.36}$$

is displayed. The leading dimension of the matrix is 2,160,000 as the grid is formed on 4,500 points in the streamwise direction and 120 in the wall-normal direction with 4th- and 8th-order discretisation, respectively. The three different steps of the LU-based procedure detailed in Section 4.2.1 are processed with parallel computing. However, Fig. 4.16 clearly demonstrates a sub-linear behaviour for strong scaling; this is a well-known feature of sparse direct solvers, which generally do not scale well with many processes. Past $n_p = 4$ processes, there is a gradual departure from the ideal scalability behaviour. The parallelism is only near-half-effective when using 32 MPI processes since it yields only a speed-up of approximately 16.

Several factors may contribute to such a sub-linear speed-up. A first one may be the inevitable occurrence of serial tasks during the execution. In addition, the parallel computation most likely sees significant message passing between MPI processes. This is probably accentuated by the high-order FDM typically used

[3] as opposed to absolute speed-up, where $t(1)$ would be computed by means of an optimised, completely serial code.

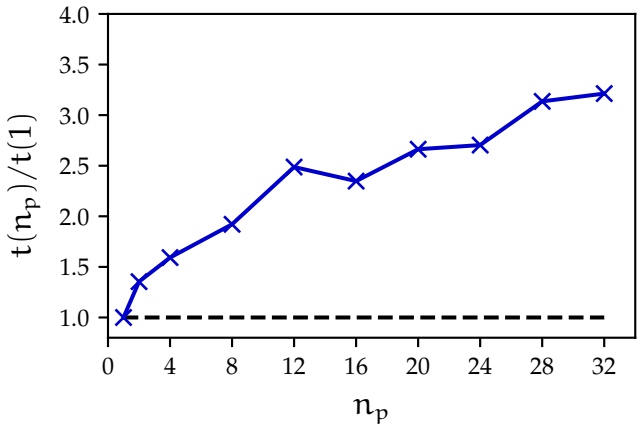

Figure 4.17: Weak scaling: evolution of $t(n_p)/t(1)$ (—) with the number of MPI processes n_p to solve a linear system in parallel where each process owns 120,000 degrees of freedom. Comparison with an ideal, embarrassingly parallel case (--).

in the wall-normal direction for the HNS framework. The larger extent of the stencil when using an 8th- to 12th-order FD-q is indeed likely to couple degrees of freedom located in different slices of the domain more strongly, thereby requiring increased levels of data communication between relevant processes. Overhead arising from CPU cache effects is also plausible. A further contributing factor is the architecture of the clusters on which the code has been run. The analysis of Fig. 4.16 involves a compute node with four sockets. These are physical entities associated with a local memory bank where a group of CPUs is placed. In this case, each socket features eight physical CPUs. Memory bandwidth for memory-bound applications is usually the highest when a single MPI process is used on each socket. In the current benchmark, several MPI processes per socket are used when $n_p > 4$ and compete for the available bandwidth. Although by means of process binding, an even MPI process distribution among sockets was enforced when $n_p > 4$, intra-socket memory access is faster than extra-socket memory access, detrimentally affecting the parallel speed-up.

These observations are correlated by the weak scaling behaviour of the code presented in Fig. 4.17. As the workload per process remains constant, the relative run-time $t(n_p)/t(1)$ quantifies how much longer the solution of a linear system whose leading dimension is n_p-times larger can be computed in the same amount of time. The ownership range of each process comprises 120,000 degrees of freedom, while computations have been run with matrices resulting from 4th-order discretisation in both spatial directions to maintain symmetry in the workload as the number of processes is increased. The monotonically increasing trend indicates that the amount of communication between processes grows in a non-negligible way as the total number of degrees of freedom increases. Concurrently, there

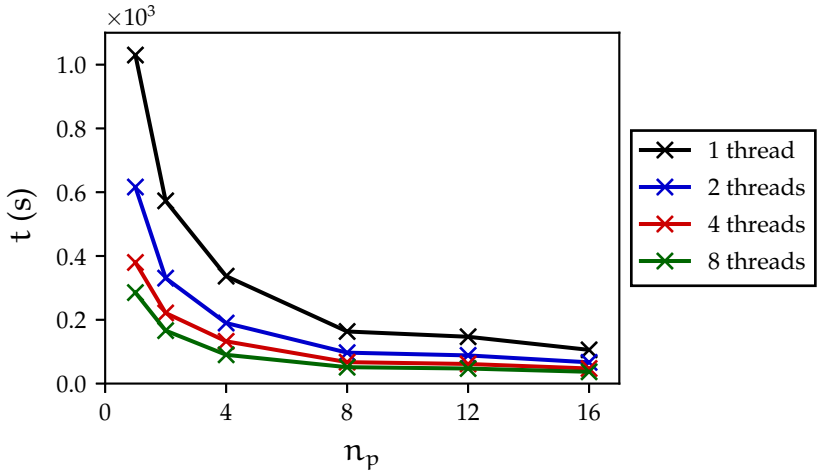

Figure 4.18: Strong scaling performance with hybrid MPI/OpenMP parallelism. Computation time required to solve a linear system with 120,000 degrees of freedom per MPI process.

may also be a fraction of serial work that is gradually increasing. The significant deviation with the ideal case demonstrates that solving the linear system in parallel via LU factorisation with MUMPS is far from being an embarrassingly parallel problem and involves significant data communication between processes.

Regardless of the weak scaling and strong scaling performance, the deployed parallel machinery enables the user to retrieve solutions in more than reasonable computation time for highly-resolved 2.5D problems. With a more typical discretisation leading to 37,500 degrees of freedom per process, solving a linear system with $n_p = 16$ lasts only one minute on a cluster node of two sockets and eight cores per socket, with Intel® Xeon® E5-2680 (Sandy Bridge) CPU architecture.

For a given number of MPI processes, MUMPS is further able to exploit shared-memory multiprocessing via OpenMP. Figure 4.18 summarises the benefit of exploiting hybrid MPI/OpenMP parallelism where the evolution of the computation time to solve a linear system is presented for several threads per MPI process. As MPI processes are bound to hardware sockets, the different threads are attached to the different cores placed on the socket. The multithreading-induced gains are evident for a few MPI processes since the multithreading speed-up is comparable to the MPI speed-up. For higher values of n_p that are effectively used in this work, the run-time decrease remains more marginal yet several dozens of seconds can be saved when solving the linear system. This may be exploited for NLHNS-type problems which require many numerical factorisations during the computation.

4.3.2 Aspects of 3D discretisation

The choice of an FD-q discretisation and the deployment of parallel numerical libraries held a significant promise for the analysis of large-scale flow stability problems, including solving equations discretised in 3D space. In that case, the spanwise direction would have been discretised in physical space with the FD-q rather than in frequency space. The destabilising effect of a genuine 3D roughness element could have been investigated more seamlessly, by means of TriGlobal or 3D-LHNS analyses.

Direct solvers remain prohibitively expensive

Although the code machinery and the distributed-memory parallelism allow to easily construct a discretised 3D matrix, applying a direct solver such as MUMPS to solve the associated 3D linear system is simply too expensive due to the high memory requirements that ensue from the fill-in of the LU factors during the factorisation phase. Fill-in occurs during Gaussian elimination as new non-zero elements are dynamically introduced at locations where the entries of the original matrix are zero. In other words, although a matrix $\mathbf{A} = \mathbf{L}\mathbf{U}$ is sparse, the factors $\mathbf{L}$ and $\mathbf{U}$ typically contain a much greater number of non-zero elements nnz.

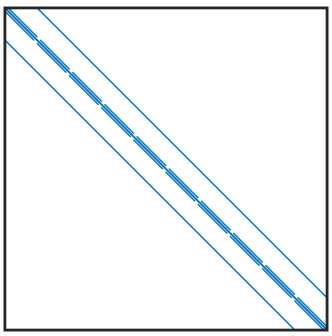

(a) Original matrix $\mathbf{A}$, nnz $= 6{,}400$

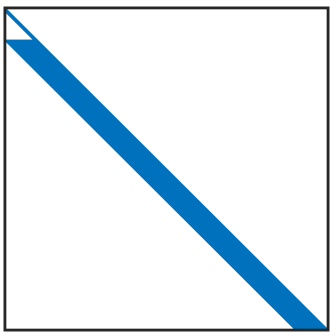

(b) Lower factor $\mathbf{L}$, nnz $= 91{,}909$

Figure 4.19: Sparsity patterns of a matrix $\mathbf{A}$ and of its lower factor $\mathbf{L}$ from the LU factorisation, computed without reordering. In this case, $\mathbf{A}$ is the discretised 3D Laplacian using the classic 7-point stencil with a leading dimension of $n^3 = 10^3$.

An example is provided in Fig. 4.19 with a 3D Laplace operator discretised with an FDM and a 7-point stencil using $n = 10$ grid nodes in each spatial direction. The original matrix has approximately nnz $= 7n^3$ non-zero elements and a lower bandwidth of n^2. Using Gaussian elimination, the lower factor has the same bandwidth but new non-zero elements populate it such that $\mathbf{L}$ has roughly nnz $= n^5$ entries in total. Unfortunately, fill-in occurs regardless of the original level of sparsity and even intensifies with increasing discretisation order. As mentioned in Section 4.3.1, wider stencils create coupling between degrees of

Table 4.1: Computational complexity of sparse LU factorisation where N is the leading dimension of the matrix

Approach	General		Multifrontal	
Reordering	No		Yes	
Dimension	2D	3D	2D	3D
Flops	$O(N^2)$	$O(N^{7/3})$	$O(N^{3/2})$	$O(N^2)$
Memory	$O(N^{3/2})$	$O(N^{5/3})$	$O(N \log N)$	$O(N^{4/3})$

freedom located in more distant rows of the matrix, which inevitably generates more fill-in during the factorisation. However, the level of fill-in may be bounded by finding an optimal ordering of the degrees of freedom during their elimination. This is what MUMPS determines during the symbolic factorisation phase as the rows and columns of the original matrix are permuted to minimise fill-in. Among the existing reordering techniques, the nested dissection method introduced by George (1973) has been extensively employed.

The requirements of sparse LU factorisation in terms of flops and storage space are summarised in Table 4.1 for a general approach without reordering and for a multifrontal approach with reordering based on nested dissection. For a 2.5D problem and thus a 2D discretised HNS operator with a leading dimension of $N = n^2$, the flop complexity of the multifrontal factorisation is $O(N^{3/2})$, while the memory requirements for the LU factors behave as $O(N \log N)$. A rather dramatic increase occurs in 3D with $N = n^3$ unknowns to the extent that the multifrontal method respectively requires $O(N^2)$ operations and $O(N^{4/3})$ storage for the LU factors. This implies that even with optimal reordering, the multifrontal factorisation of MUMPS remains not applicable in practice for sparse matrices issued from 3D discretisation, since HNS problems typically require a grid formed of $n_x = O(10^3)$, $n_y = O(10^2)$ and $n_z = O(10^2)$ nodes.

Lack of robustness of iterative solvers

A natural workaround to the substantial cost of applying a direct LU solver for the current HNS formulation is to apply an iterative solver. As the name suggests, such a solver requires an initial guess to build gradually improved solutions to the linear system. In contrast, iterative solvers require little computational resources and are generally highly scalable. Their main downside is their robustness with respect to the convergence towards the numerical solution.

The convergence behaviour of iterative methods is impacted by the condition number κ of the matrix $\mathbf{A}$,

$$\kappa(\mathbf{A}) = \|\mathbf{A}\|\|\mathbf{A}^{-1}\| \underset{\|\cdot\|_2}{=} \frac{\sigma_{\max}(\mathbf{A})}{\sigma_{\min}(\mathbf{A})} \geqslant 1 \tag{4.37}$$

where σ denotes a singular value of the matrix. In the context of linear systems, κ is a measure of the sensitivity of the solution to perturbations or round-off errors in the right-hand side. It essentially quantifies how close $\mathbf{A}$ is from being singular. A large condition number is a telltale sign of a slow convergence with an iterative solver as well as a serious loss of precision in the significant digits of the solution during the computation. In this work, accurate condition numbers of the LHNS operator discretised with the FD-q have been computed for reasonably small leading dimensions of the matrix, typically 10^4 to 10^5. It has been observed that κ ranges from 10^5 to 10^7, rendering the discretised LHNS operator ill-conditioned.

It should be highlighted that the Navier-Stokes equations, as many 'real-world' equations, yield naturally ill-conditioned matrices after discretisation with a numerical method. This is especially important for convection-dominated flows with high Reynolds numbers which are of interest in this thesis. In a finite element context, the corresponding matrices are known to be non-symmetric, negative-definite and ill-conditioned. For diffusion-dominated or low-Reynolds flows, the matrices are symmetric, positive-definite and well-conditioned. The fine spatial resolution typically required in the streamwise direction with the FDM of the current work is an aggravating factor; the ℓ_2-norm condition number associated to the sole discrete Laplacian in 2D using the classic 5-point stencil scales as $O(1/\Delta x^2)$ as discussed by LeVeque (2007). Significant efforts have been devoted to minimising κ in the current HNS context, including assessing the impact of boundary conditions or the non-dimensionalisation of the equations and their relative scaling. Comparing the primitive and LPPE formulations has also been tried. These different investigations led to little success in decreasing the condition number by at least an order of magnitude.

With such large condition numbers, applying an iterative solver may be simply hopeless. An efficient preconditioner should be applied beforehand to form an equivalent linear system with the same solution yet with a much lower condition number. This is the drawing power of PETSc which offers out-of-the-box parallel preconditioners that may be used in a flexible way with numerous iterative solvers based on Krylov subspace methods. The structure of the spectrum of the LHNS operator provides further insight into the potential convergence behaviour of that class of methods. Computed for a reasonable number of degrees of freedom, an

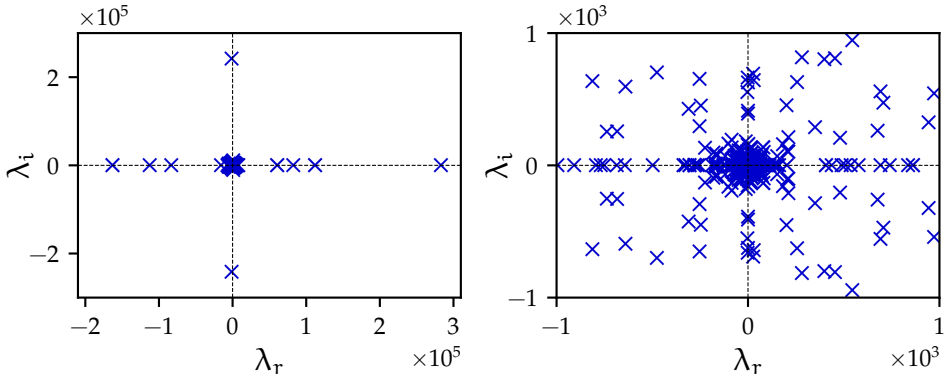

Figure 4.20: *Left*, complete spectrum of the discretised LHNS operator with a leading dimension of 10,000; *right*, magnified region centred around the origin.

example of LHNS spectrum is presented in Fig. 4.20. It is clear that in relative terms, a few isolated eigenvalues of large magnitude exist on the real axis as well as on the imaginary axis. Furthermore, there are many eigenvalues located near the origin of the complex plane. While the former feature contributes to indefiniteness in choosing an appropriate pair of preconditioner and Krylov subspace method, the latter is a manifestation of ill-conditioning to the extent that the LHNS operator is close in norm to some singular matrix, which could be reached by a numerical perturbation. This diminishes the chances of reaching convergence with that class of iterative solvers. In contrast, a well-conditioned matrix with a clustered spectrum around a point is likely to offer robust convergence of Krylov methods.

Many pairs of parallel preconditioners have been extensively tested in an effort to alter the structure of the spectrum of Fig. 4.20 and alleviate the need for a direct solver. Simple preconditioners included Jacobi, block Jacobi or additive Schwarz applied on the whole matrix. The employed iterative Krylov methods were the Generalised Minimal Residual (GMRES) method introduced by Saad and Schultz (1986) as well as its flexible variant. Unfortunately, none of these options yielded satisfactory convergence in spite of tweaking relevant numerical parameters. The Algebraic Multigrid (AMG) preconditioner would have been an excellent candidate for the purpose of solving large-scale HNS problems. It is recognised as one of the fastest numerical methods to solve elliptic PDEs, able to reach an $O(N)$ complexity regardless of the dimension (Trottenberg et al., 2001). Once more, no convergence was reached for the current HNS formulation. Regrettably, the multigrid approach is known to lack robustness when dealing with incompressible, high-Reynolds Navier-Stokes equations. The use of highly stretched grids may also be another source of poor performance from the AMG (Balay et al., 2020).

Discretising the incompressible LHNS equations expressed in primitive form yields a saddle point problem, whose resolution by preconditioned Krylov subspace

methods has been extensively studied as recapitulated in the contribution of Benzi and Wathen (2008). With the current formulation, attempts at solving such a problem have incorporated a sophisticated feature of PETSc allowing to simultaneously apply separate preconditioners to individual fields, namely the pressure and velocity components following the philosophy that the physical model should be decoupled to the solver settings. No improvement of the convergence behaviour has been noted by exploiting that feature.

Although the poor performance of preconditioners with iterative solvers on the current formulation may be exacerbated by discretising the governing equations with an FDM, it may be argued that preconditioning techniques applied to the incompressible Navier-Stokes equations have remained an active area of research, whereas the theory associated to the simpler Stokes equations where $\mathrm{Re} \to 0$ is well understood. The paper of Elman et al. (2008) provides a classification of a few approaches available for incompressible Navier-Stokes equations at moderate Reynolds numbers. However, it is only recently that preconditioners robust to higher Reynolds numbers have started to emerge. Farrell, Mitchell and Wechsung (2019) and Farrell et al. (2020) extended the augmented Lagrangian preconditioner devised by Benzi and Olshanskii (2006) to devise highly scalable solvers for the 3D stationary incompressible Navier-Stokes equations with robustness to a Reynolds number increase, yet subject to a carefully chosen discretisation. The underlying principle is the so-called *grad-div* stabilisation, denoting the term added in the equations. Such preconditioners should then appropriately capture the kernel of the term to ensure their efficiency. Tested on a slightly lower range of Reynolds numbers, Moulin, Jolivet and Marquet (2019) applied the modified augmented Lagrangian preconditioner (Benzi, Olshanskii & Wang, 2011) to compute 3D unstable modes in a linear instability problem with high scalability.

Chapter 5

Linear Stability of Boundary Layers with Surface Features

> It is very hard to predict, especially the future.
>
> —Niels Bohr

We appraise in this chapter the physical modelling aspects of the developed code on the linear instability of two significantly different boundary-layer flows. The first configuration of interest is a flat-plate boundary layer subjected to smooth indentations with varying depths, whereas the second configuration is a boundary layer developing on a swept wing on which slightly rounded backward- and forward-facing steps are placed. We investigate the existence of temporally unstable and self-sustained global modes via streamwise BiGlobal analysis. Furthermore, we discuss the impact of the smooth indentations on TS waves. Prior to the instability analysis, we assess the correctness of the discretisation and the accuracy of the eigenvalue solver using reference data on the Blasius boundary layer and on the swept Hiemenz flow.

5.1 Verification

5.1.1 Blasius boundary layer

Naturally, the simplicity of the Blasius boundary layer leaves it as an ideal verification case. Its temporal and spatial stability have been extensively studied and well-documented for various linear stability approaches such as LST,

PSE and BiGlobal analysis in the last decades. In a first instance, the temporal eigenvalue spectrum of a Blasius profile at Re = 580 and $\alpha = 0.179$ is computed to ascertain the correctness and accuracy of the BiGlobal solver. It is compared against the results of Mack (1976) who was the first to state, by means of a numerical analysis and integrating the Orr-Sommerfeld equation, that only a finite number of discrete modes exist. The number of discrete modes was found to increase as either the Reynolds number or the streamwise wavenumber increases. The location of discrete modes is also compared with the set reported by Malik (1990) who used LST. Further LST results from Pinna (2012), and from Niessen (2017) who computed the spectrum through a spanwise BiGlobal analysis are also added for a comprehensive comparison. In the latter work, the base flow remained dependent solely upon the wall-normal direction and was simply duplicated in the spanwise direction.

With the introduction of an appropriate similarity variable $\eta = y\sqrt{U_\infty/2\nu x}$ and a stream function $\psi = \sqrt{2\nu x U_\infty} f(\eta)$, the boundary-layer equations and their boundary conditions remain invariant. Therefore, the solution of the Blasius ODE,

$$f'''(\eta) + f(\eta)f''(\eta) = 0 \tag{5.1}$$

is self-similar. It is completed by boundary conditions which are $f(0) = 0$, $f'(0) = 0$ and $f''(\infty) = 1$. In this current work, an 8th-order Runge-Kutta method is used to integrate Eq. (5.1). The only missing information to initiate the process is the value of $f''(0)$, which is recovered by means of a shooting method. In this context, its principle is based on providing an initial guess of the missing value $f''(0)$ and 'shooting' the Runge-Kutta method to recover the values at the final integration point. A Newton iteration method is used to minimise $\|f''(\infty) - 1\|$ by adjusting $f''(0)$. The Jacobian matrix is computed by a first-order FDM, which is not affecting the accuracy due to the iterative nature of the Newton process.

The Blasius ODE is integrated from the wall position $\eta = 0$ to a coordinate $\eta_f = 11$ where f and its derivatives have reached their asymptotic behaviour. They are then extended to a truncated free-stream value $\eta_\infty = 150$ by analytical continuation. After a few 'shots', the method is converged; the value $f''(0)/\sqrt{2} = 0.33205733621519630$[1] matches the eight significant digits provided by Criminale, Jackson and Joslin (2003) and most importantly equals the correct value reported by Boyd (1999) with 17 digits of accuracy.

[1] In some references the similarity variable is defined as $\eta = y\sqrt{U_\infty/\nu x}$ and the Blasius equation reads $2f''' + ff'' = 0$ which explains the factor $\sqrt{2}$ difference.

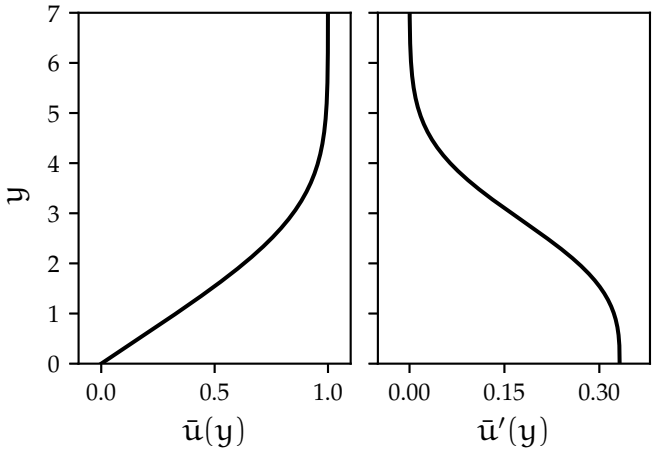

Figure 5.1: Non-dimensional streamwise velocity component $\bar{u}$ of the base flow (*left*) and its first derivative for the Blasius boundary layer case, $Re = 580$

Using the similarity transformation, the base flow components $\bar{u}$ and $d\bar{u}/dy$ are computed. Under the parallel flow assumption, they are the only non-zero base flow terms in the LHNS equations (3.35). To mimic the LST computations for the current BiGlobal setting, a 2D discretisation domain is considered with a streamwise length $L_x = 2\pi/\alpha$ equal to one wavelength of the perturbation. Figure 5.1 shows the base streamwise velocity as well as its wall-normal derivative which are replicated along the streamwise direction. Naturally, the BiGlobal problem is solved with the imposition of periodic boundary conditions in the streamwise direction. An infinite spanwise wavelength of the perturbations is prescribed as $\beta = 0$. The length scale of the problem is the Blasius boundary layer thickness,

$$\ell = \sqrt{\frac{\nu x}{U_\infty}}$$

on which the Reynolds number is based, such that

$$Re = \frac{U_\infty \ell}{\nu} = \sqrt{\frac{U_\infty x}{\nu}} = \sqrt{Re_x} = 580$$

and the Reynolds number based on the displacement thickness is equivalently $Re_{\delta^*} = 998.06$. The wall-normal domain is truncated at $y_\infty = 300$, a value sufficiently large to enable the modes to decay and reach negligible amplitude at the far-field boundary. In the same spatial direction, the bilinear mapping of Eq. (4.13) is applied with $y_h = 3.5$. An FD-10 method is used to target high accuracy in the wall-normal direction. Given the homogeneity of the artificially extruded base flow in the streamwise direction, it is more than sufficient to discretise the latter with an FD-4 method. In the following developments, the eigenpairs resulting from the BiGlobal computation are computed with an absolute

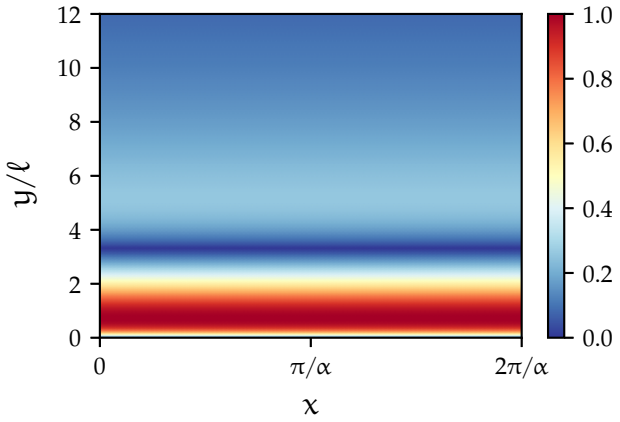

Figure 5.2: Normalised streamwise component $|\hat{u}|$ of the unstable TS mode for the Blasius boundary layer case with $Re = 580$, $\alpha = 0.179$ and $\beta = 0$. The base flow is homogeneous in the x direction.

Table 5.1: Wall-normal convergence of the growth rate ω_i of the unstable TS mode for the Blasius boundary layer case with $Re = 580$, $\alpha = 0.179$ and $\beta = 0$. The streamwise grid is formed of $n_x = 40$ nodes.

n_y	Primitive	LPPE
60	0.**0079**668653588242	0.**00795597**437012544
70	0.**0079**596542800415	0.**00795597**350570389
80	0.**0079**662103690574	0.**00795597**333924045
90	0.**0079**435117732367	0.**00795597**329959726
100	0.**0079**605175004127	0.**00795597**328822816
110	0.**0079**605175004127	0.**00795597**328512932
120	0.**0079**624832962253	0.**00795597**328293444

convergence tolerance of 10^{-14} and sought near the complex plane location of the unstable TS mode.

As a matter of fact, the incompressible streamwise parallel Blasius boundary layer features a unique, discrete unstable TS mode. Its structure is presented in Fig. 5.2 where its homogeneity in the x direction is evident. It reaches maximum amplitude relatively close to the wall. The present verification case relies on the accurate computation of its dynamics as well as those of three other stable discrete modes. At this point it is opportune to assess the numerical behaviour of the primitive and LPPE formulations of the LHNS equations. These are compared in Table 5.1 with respect to the wall-normal convergence of the growth rate of the TS mode. While the primitive formulation yields four converged significant digits as n_y is increased from 60, already seven digits are converged with its LPPE counterpart. Furthermore, the final value of the growth rate obtained via the LPPE formulation may be considered as converged with ten digits, whereas the convergence of the primitive formulation seems more erratic and tends to fluctuate.

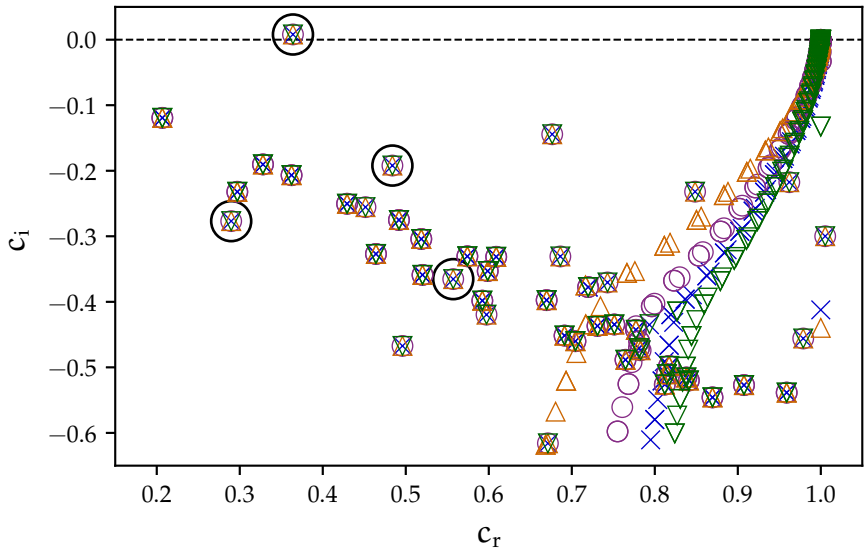

Figure 5.3: Convergence of the streamwise BiGlobal, phase velocity spectrum with $n_y = 60$ (△), 80 (○), 100 (×) and 120 (▽). The four modes usually compared in the literature are indicated (○). Blasius boundary layer case with $Re = 580$, $\alpha = 0.179$ and $\beta = 0$.

Another illustration of the numerical convergence is the temporal spectrum in Fig. 5.3; modes are presented in terms of the phase velocity defined as $c = \omega/\alpha$.

The spectrum of the parallel Blasius boundary layer is formed of two distinct branches, namely a set of discrete modes including the sole unstable TS mode as well as the discretised version of a continuous branch which is typical of unbounded flows such as boundary layer flows. For the Blasius boundary layer, the 'exact' continuous branch is a vertical line extending in the stable region and located at $c_r = 1$ (Schmid & Henningson, 2001) whereas the wall-normal resolution affects how much its numerical counterpart deviates from such a line. For incompressible flows, the modes that belong to the continuous branch are of viscous nature. Jordinson (1971) seems to be the first to have numerically uncovered the existence of the continuous branch of the Blasius boundary layer solving the Orr-Sommerfeld equation, besides the discrete modes revealed by Mack (1976). Later, Grosch and Salwen (1978) formally demonstrated the existence of the continuous spectrum for the Orr-Sommerfeld equation with any unbounded shear flow and for both temporal and spatial stability problems. The continuous modes are actually required to form a complete set together with the discrete modes in order to describe arbitrary perturbations (Salwen & Grosch, 1981), an aspect that has been briefly discussed in Section 3.2.2. Other discrete modes present in Fig. 5.3 are spurious and arise from the BiGlobal discretisation treating the x direction in physical space.

Table 5.2: Numerical values of the phase velocity $c = \omega/\beta$ for the four eigenmodes of the Blasius boundary layer case with $Re = 580$, $\alpha = 0.179$ and $\beta = 0$. Current BiGlobal results are obtained with a resolution of $(n_x, n_y) = (40, 60)$.

Reference	Eqns.	Method	c_r	c_i	c_r	c_i
Mack (1976)	Incp.	OS	0.3641—	0.0080—	0.2897—	−0.2769—
Malik (1990)	Comp.	LST	0.3641—	0.0079—	0.2897—	−0.2768—
Pinna (2012)	Incp.	LST	0.364113	0.007952−	0.289712	−0.276858
Pinna (2012)	Comp.	LST	0.364123	0.007960−	0.289714	−0.276866
Current	Incp.	LST	0.364123	0.007960−	0.289714	−0.276699
Niessen (2017)	Comp.	BiG	0.364129	0.0079597	—	—
Current	Incp.	BiG	0.364115	0.0079597	0.289710	−0.276862
Mack (1976)	Incp.	OS	0.4839—	−0.1921—	0.5572—	−0.3653—
Malik (1990)	Comp.	LST	0.4839—	−0.1921—	0.5571—	−0.3655—
Pinna (2012)	Incp.	LST	0.483876	−0.192098	0.557921	−0.368070
Pinna (2012)	Comp.	LST	0.483929	−0.192068	0.557197	−0.365342
Current	Incp.	LST	0.483929	−0.192068	0.557197	−0.365342
Current	Incp.	BiG	0.483922	−0.192066	0.557191	−0.365336

The discrete modes found in Fig. 5.3 seem converged even for the smallest value of $n_y = 60$. Although the base flow is homogeneous in the streamwise direction, the perturbations $\hat{\mathbf{q}}$ have a non-zero wavenumber and information is carried in this direction via $\bar{u}$, necessitating more than a few grid nodes to reach convergence. It has been found that $n_x = 40$ streamwise points is an adequate choice to ensure an appropriate mesh convergence. The phase velocity values for the TS mode and three other stable modes of interest highlighted in Fig. 5.3 are gathered in Table 5.2. These are compared against the references described at the beginning of this section. Current results have been obtained with incompressible LHNS equations; to deal with the current incompressible case, the authors using tools based on compressible flow equations prescribed in general a value of $Ma = 10^{-6}$, a Prandtl number $Pr = 0.7$ as well as a free-stream temperature $T_\infty = 300\,K$ to reach the incompressible limit. The four modes obtained with the LST approach implemented in the current tool are also included, and match the streamwise BiGlobal values. Remarkably, when using an FD-10 discretisation, only 60 wall-normal nodes are sufficient to obtain excellent agreement with external contributions with at least four or five significant digits of accuracy. In particular the real part and imaginary part of the complex phase velocity of the TS mode computed with spanwise BiGlobal by Niessen (2017) correlate well. This excellent agreement is further confirmed by the wall-normal evolution of the TS mode extracted at the middle of the BiGlobal computational domain, $x = \pi/\alpha$. Figure 5.4 represents the eigenfunction amplitude for the different flow variables normalised with the maximum value reached by $\hat{u}$. Since $\beta = 0$ and there is no spanwise

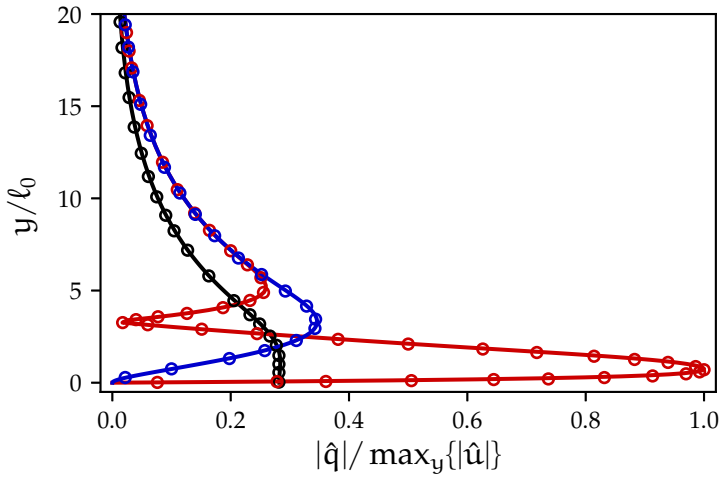

Figure 5.4: Normalised wall-normal profiles of the TS mode eigenfunction extracted at $x = \pi/\alpha$: $|\hat{p}|$ (—), $|\hat{u}|$ (—) and $|\hat{v}|$ (—). Comparison with Niessen (2017) (○). Blasius boundary layer case, $Re = 580$, $\alpha = 0.179$ and $\beta = 0$.

base flow component, the z-momentum equation is decoupled from the other governing equations resulting in eigenmodes with $\hat{w}$ being identically zero. A perfect agreement is reached with the TS eigenfunction computed by Niessen (2017) with a spanwise BiGlobal analysis.

In light of these quantitative results, the current code can be considered verified. However, the parallel Blasius boundary layer features $\bar{v} = \bar{w} = 0$, which prevents one from fully ascertaining the accuracy of the BiGlobal solver since numerous terms of the LHNS equations vanish. For this reason, a boundary layer configuration with three non-zero mean velocity components is also investigated.

5.1.2 Swept attachment-line boundary layer

The second verification case considered is that of the temporal instability of a plane stagnation-point flow. It occurs when a uniform flow impinges with normal incidence on a flat plate. Also known as *Hiemenz* flow, it is an appropriate model to characterise incompressible flow in the vicinity of the leading edge of aerofoils when the boundary layer thickness is negligible compared to the radius of curvature of the surface (Rosenhead, 1963). A swept attachment-line flow results when a homogeneous free-stream spanwise velocity component W_∞ is introduced. The sweep angle then satisfies $\tan(\Lambda) = W_\infty/U_\infty$.

As depicted in Fig. 5.5, the flow is dependent on the chordwise coordinate x and the wall-normal coordinate y defined in a Cartesian system. The attachment line extends homogeneously in the spanwise direction z following an infinite swept assumption. A remarkable feature of the Hiemenz flow is the fact that it is an exact

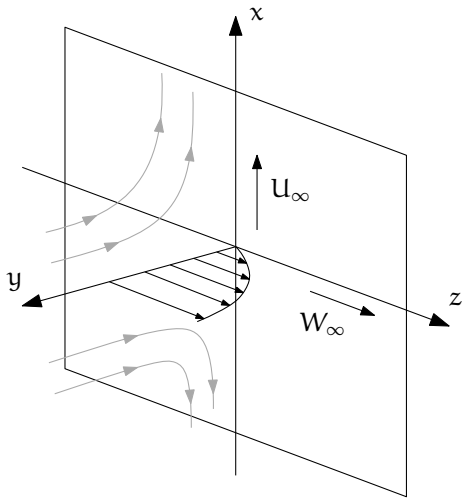

Figure 5.5: Attachment-line region of the swept Hiemenz flow. Streamlines in the chordwise direction as well as the spanwise velocity are depicted.

solution not only to the boundary-layer approximation equations, but also to the full Navier-Stokes equations. Furthermore, analogously to the Blasius boundary layer, the Hiemenz flow is a similarity solution[2] and can be solved conveniently as a system of ODEs to compute the solution with very high accuracy.

The free-stream velocity components U_∞ and W_∞ are independent, while the other parameters of the flow are

$$\Delta = \sqrt{\frac{\nu L}{U_\infty}}, \quad \mathrm{Re} = \frac{W_\infty \Delta}{\nu} \tag{5.2}$$

where Δ is a boundary-layer length scale and L an additional streamwise length scale. The velocity components are all functions of the wall-normal coordinate, while only the streamwise velocity is assumed to also increase linearly in the streamwise direction such that

$$\bar{u}(x,y) = \frac{\bar{u}}{W_\infty} = \frac{-x f'(y)}{\mathrm{Re}}, \quad \bar{v}(y) = \frac{\bar{v}}{W_\infty} = \frac{f(y)}{\mathrm{Re}}, \quad \bar{w}(y) = \frac{\bar{w}}{W_\infty} = g(y) \tag{5.3}$$

where f and g are solutions to the following system of ODEs,

$$f''' + (f')^2 - f f'' - 1 = 0 \tag{5.4a}$$

$$g'' - f g' = 0. \tag{5.4b}$$

These are supplemented by the boundary conditions $f'(0) = 0$, $f(0) = 0$, $f'(\infty) = -1$, $g(0) = 0$ and $g(\infty) = 1$.

[2] The Hiemenz ODE is a particular case of the FSC boundary layer introduced in Section 4.1.3 with $\beta_H = 1$, whereas the Blasius ODE is retrieved when $\beta_H = 0$.

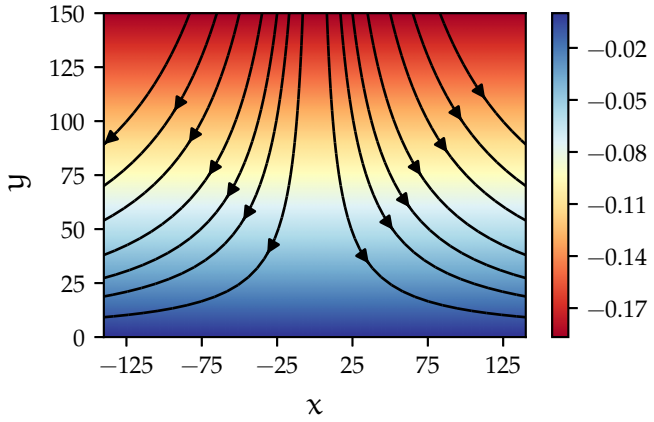

Figure 5.6: Contours of the wall-normal velocity component $\bar{v}$ with several streamlines for the swept, orthogonal Hiemenz flow at Re $= 800$.

Obtaining the base flow requires solution of the system of equations in Eq. (5.4). To this end, and as in Section 5.1.1, an 8th-order Runge-Kutta method is used together with a shooting method which adjusts the initial guess in order to yield the correct boundary conditions at the free-stream location.

Solutions of f and g are first computed with the Runge-Kutta scheme from the wall location $y = 0$ up to $y = 9.2$ where they have reached their asymptotic behaviour. They are then extended analytically up to the truncated free-stream location $y_\infty = 200$. Considering eight significant digits, the values at the wall $f''(0) = -1.23258765$ and $g'(0) = 0.57046525$ exactly match the values reported by Lin and Malik (1996), thus providing a highly accurate basic flow for the stability analysis and verification of the code. The streamlines in Figure 5.6 highlight the stagnation point and how the impinging flow is divided into two symmetric parts.

BiGlobal results for the incompressible Hiemenz flow were first reported by Lin and Malik (1996) for the parameters Re $= 800$ and $\beta = 0.255$. This current verification case is based on these parameters while results from Theofilis et al. (2003), Robitaillié-Montané (2005) and Paredes et al. (2013) are also included. It consists in the retrieving of a family of four unstable modes, two having a symmetric structure (GH, S2) as well as two having an antisymmetric structure (A1 and A2) first highlighted by Lin and Malik (1996). The most unstable symmetric mode was first uncovered by Hall et al. (1984) using the so-called Görtler-Hämmerlin methodology. In that approach, the perturbation ansatz follows that of the basic flow in Eq. (5.3), namely a wall-normal dependence of the disturbance with only the streamwise perturbation depending linearly on the streamwise coordinate. For this reason and in accordance with the literature, the most unstable symmetric

Table 5.3: Mesh convergence of the GH mode for the swept, orthogonal Hiemenz flow with $Re = 800$ and $\beta = 0.255$

$n_x \times n_y$	c_r		c_i	
	Primitive	LPPE	Primitive	LPPE
50^2	0.**35840979**	0.**35840965**	0.**5853**3385	0.**585**28028
70^2	0.**35840**855	0.**35840976**	0.**585**16542	0.**58532**533
90^2	0.**358**34009	0.**35840978**	0.**5**9367580	0.**58532**884
110^2	0.**35840977**	0.**35840979**	0.**5853**3377	0.**58532**932

mode S1 is denoted as GH, although Lin and Malik (1996) termed the mode as 'HMP' as a reference to Hall et al. (1984).

For the current BiGlobal computations, an FD-8 method is used in both spatial directions. The domain extent is such that $x \in [-200, 200]$ and $y \in [0, 150]$. In the wall-normal direction, the bilinear mapping of Eq. (4.13) is used with $y_h = 2.5$. Except for that parameter, the domain and discretisation settings match those of Paredes et al. (2013), whereas results from Theofilis et al. (2003) and Robitaillié-Montané (2005) were computed on shorter domains. Linear extrapolation from the interior of the domain is employed at the inflow and outflow boundaries to close the BiGlobal problem along the streamwise direction. The GEVP is solved by requesting 50 converged eigenvalues in the vicinity of the GH mode and a Krylov subspace of dimension 200 is used. Finally, the relative tolerance for the convergence of the Krylov-Schur method is set to 10^{-13}.

The impact of grid resolution on the numerical GH eigenvalue is summarised in Table 5.3 under the form of the complex phase velocity $c = \omega/\beta$. Primitive and LPPE formulations are also compared. Similarly to the verification case of Section 5.1.1, the convergence behaviour of the LPPE formulation seems more consistent than its primitive counterpart. Although both formulations yield the same eigenvalue with four significant digits for the finest resolution, a significant departure from the ultimately converged value is observed for $n_x \times n_y = 90^2$ with the BiGlobal equations formulated in primitive form, a larger fluctuation relative to what has been observed for the parallel Blasius boundary layer case. With 50^2 grid nodes, c_r and c_i are converged with respectively six and almost four significant digits when using the LPPE formulation.

Figure 5.7 shows the structure of the spectrum obtained via BiGlobal analysis with $n_x \times n_y = 110^2$ and features the physically relevant discrete modes as well as continuous branches of modes. The predominant family of unstable eigenvalues is a series of modes that alternate between symmetric and antisymmetric eigenfunctions

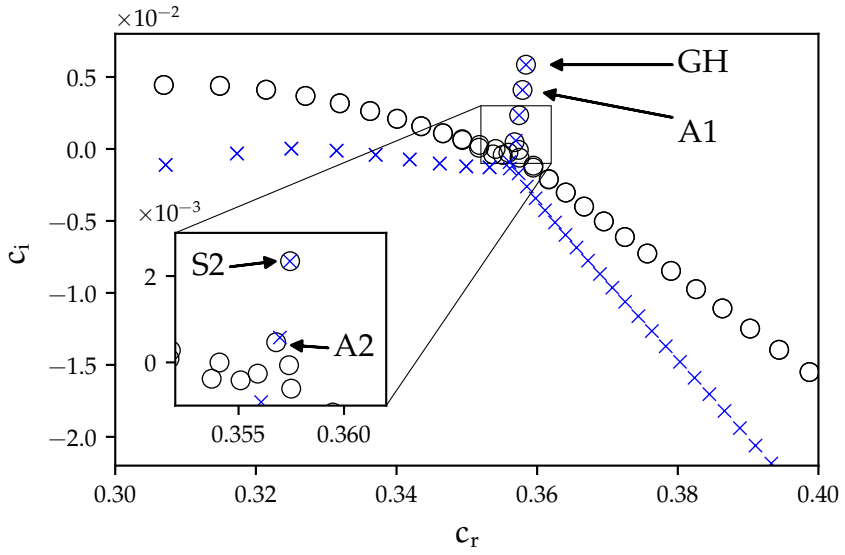

Figure 5.7: Eigenvalue spectrum of the swept, orthogonal Hiemenz flow after BiGlobal analysis with Re $= 800$ and $\beta = 0.255$ in terms of the phase velocity $c = \omega/\beta$. The four relevant modes GH, S2, A1 and A2 are indicated. Comparison between the primitive (○) and LPPE (×) formulations.

as the growth rate decreases, such that $c_i(\mathrm{GH}) > c_i(\mathrm{A1}) > c_i(\mathrm{S2}) > c_i(\mathrm{A2}) > 0$. The relative closeness of these eigenvalues is an excellent test for the eigenvalue solver as its convergence and separation of clustered eigenvalues may be constrained. How the BiGlobal equations are formulated clearly alters the continuous spectrum distribution, however no visible differences are observed for the four discrete modes except for A2. Since the latter mode is close in magnitude to continuous modes, its computation might be affected.

Considering other references that all based their BiGlobal computations on incompressible equations, there is generally an excellent agreement with the current results as compacted in Table 5.4. For the GH, A1 and S1 modes the values of c_r and c_i coincide with at least five significant digits. Values are more scattered across references with respect to the S2 mode, indicating a greater sensitivity to numerical parameters. Regardless, the current value is in good agreement. It shall be highlighted once again that the code performs interpolation of the base flow to the BiGlobal grid which is a source of numerical bias; adjusting the order of B-spline interpolants was found to change c_i beyond seven significant digits. The verification of the code is further established by lingering on the evolution of c_i with β. Figure 5.8 indicates that the GH, A1, S2 and A2 modes coexist for a limited range of spanwise wavenumbers and in that case always satisfy $c_i(\mathrm{GH}) > c_i(\mathrm{A1}) > c_i(\mathrm{S2}) > c_i(\mathrm{A2}) > 0$. Current BiGlobal results lay between the values of Lin and Malik (1996) and those of Theofilis et al. (2003). This further demonstrates the correctness of the developed tool.

Table 5.4: Numerical values of the phase velocity $c = \omega/\beta$ for the four eigenmodes of the swept, orthogonal Hiemenz flow with $Re = 800$ and $\beta = 0.255$

	c_r(GH)	c_i(GH) $\times 10^2$	c_r(A1)	c_i(A1) $\times 10^2$
Lin et al.	0.35840982	0.58532472	0.35791970	0.40988667
Theofilis et al.	0.35840980	0.585327—	0.35791953	0.409872—
Robitaillié-Montané	0.35840961	0.58512010	0.35791964	0.40968751
Paredes et al.	0.35840991	0.58532658	0.35791980	0.40988576
Current	0.35840979	0.58532932	0.35791967	0.40989096
	c_r(S2)	c_i(S2) $\times 10^2$	c_r(A2)	c_i(A2) $\times 10^2$
Lin et al.	0.35743540	0.23430008	0.35695687	0.05857129
Theofilis et al.	0.35743981	0.234523—	0.35694358	0.058446—
Robitaillié-Montané	0.35743483	0.23410857	0.35696896	0.06604485
Current	0.35743546	0.23430556	0.35696028	0.05757787

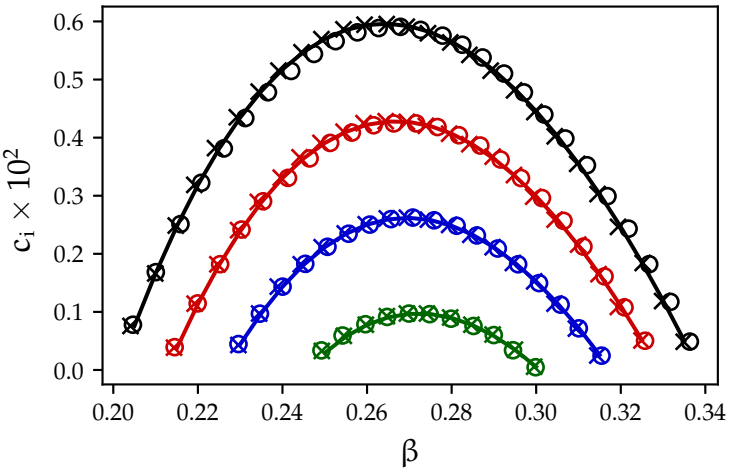

Figure 5.8: Variation of c_i with β for the four modes of the swept, orthogonal Hiemenz flow with $Re = 800$ and $\beta = 0.255$: GH (—), A1 (—), S2 (—) and A2 (—). Comparison with Lin and Malik (1996) (×) and Theofilis et al. (2003) (○).

After demonstrating that the numerical BiGlobal machinery is correct, the approach may now be applied on more complex boundary layer configurations to investigate temporal instability. The first analysis pertains to a 2D boundary layer subject to smooth indentations defined by a cosine profile with increasing height.

5.2 Flat plate with smooth indentations

In the work of Xu et al. (2017b) where they computed incompressible boundary layer flows convecting over localised 3D surface indentations, LSBs arose in the confined area of the indentation. The presence of LSBs was found to lead to rapid TS destabilisation and thus to trip the laminar flow to turbulence downstream, even at low Reynolds numbers. The authors studied how a pre-existing 2D TS disturbance is transformed into a 3D form as it convects through the 3D separation bubble. The LSBs were found to have a significant impact on the advected disturbances, in that the TS destabilisation was linked to the inflectional instability of the separated shear layer. As an extension of the work of Xu et al. (2017b), the current objective is to investigate the existence of unstable, global temporal eigenmodes related to the 2D LSBs with BiGlobal analysis. Different indentation depths, and thus the impact of different separation bubble intensities, are examined to assess the potential existence of global modes. The other issue examined with forced receptivity analysis is the effect of naturally distributed 2D surface forcing on pre-existing TS disturbances as they convect through the LSBs.

5.2.1 Base flow computation

The 3D base flows were computed by Xu et al. (2017b) by means of DNS using a spectral/hp element discretisation within the Nektar++ package (Cantwell et al., 2015), which supports h-refinement and p-refinement respectively pertaining to grid size and polynomial order. The full non-linear Navier-Stokes equations were solved with a stiffly stable splitting scheme which decouples the velocity and pressure fields. Time integration was achieved by a second-order accurate implicit-explicit scheme. The authors applied the spectral element method with a hybrid mesh formed of quadrilaterals and triangles, with 5,425 elements in the streamwise/wall-normal plane and a 5th-degree polynomial expansion imposed within each element. A Fourier expansion with 180 modes was performed in the spanwise direction. The localised surface deformation was defined in the

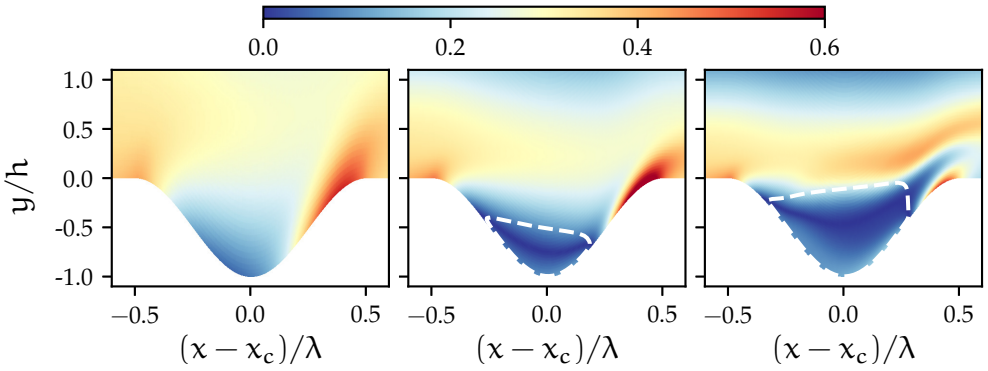

Figure 5.9: Contours of non-dimensional vorticity $|\nabla \times \bar{\mathbf{u}}|$ of the base flows with smooth indentations. *Left*, $h = 0.81\,\text{mm}$; *centre*, $h = 1.62\,\text{mm}$; *right*, $h = 2.17\,\text{mm}$. The white dashed line indicates the reversed streamwise velocity region.

streamwise direction, as

$$y(r) = \begin{cases} -\dfrac{h}{2}\left(\cos\left(\dfrac{2\pi r}{\lambda}\right) + 1\right) & \text{if } r \leqslant \lambda/2 \\ 0 & \text{if } r > \lambda/2 \end{cases} \tag{5.5}$$

in which the radial coordinate $r = \sqrt{(x - x_c)^2}$ measures the distance to the indentation centre position x_c. Xu et al. (2017b) undertook a convergence study by p-type refinement to ensure mesh independence. They also reached convergence in terms of spanwise Fourier modes, and obtained steady solutions by time-marching the equations until an appropriate steady-state convergence criterion was met. Across the whole computational domain, the ℓ_2-norm relative error of the computed velocity fields was less than 10^{-6}.

Figure 5.9 depicts the 2D base flows for three different indentation depths, extracted along the streamwise symmetric plane of the 3D indentations. The flows can be considered as incompressible since the Mach number satisfies $Ma = 0.05 \ll 0.3$. Moreover, the free-stream unit Reynolds number is $Re_\infty = 1.2 \times 10^6$ with a reference free-stream velocity $U_\infty = 18\,\text{m}\,\text{s}^{-1}$. The indentation width is $\lambda = 81\,\text{mm}$. Base flows for different indentation depths were computed, namely $h = 0.81\,\text{mm}$, $1.62\,\text{mm}$ and $2.17\,\text{mm}$. The intensity of the LSB appears to grow with increasing depth and increasing peak reversed-flow velocity, the latter expressed as percentages. The cases respectively correspond to $\lambda/h = 100$ (0%), $\lambda/h = 50$ (3%) and $\lambda/h = 37.3$ (9%). For further details, the reader is referred to Xu et al. (2017b).

5.2.2 Destabilisation of Tollmien-Schlichting waves

For the stability computations, a total of $n_x = 1{,}500$ grid points are used in the streamwise direction and $n_y = 100$ in the wall-normal direction. The chosen length scale is the corresponding zero pressure gradient Blasius boundary layer thickness at x_c, $L = \delta_h = 0.735\,\text{mm}$. The computational domain extends from $Re_\delta = 600$ to 1,149 in the streamwise direction, that is over a distance of roughly 10λ. Furthermore, the far-field boundary is set sufficiently far away from the wall as $y_\infty = 150\delta_h$ in an attempt to reduce any influence of the domain truncation on the solution in the interior of the domain. An FD-6 discretisation is employed in the streamwise direction while high accuracy is targeted in the wall-normal direction with an FD-12 method. The streamwise grid is clustered around the centre point of the indentation using the interior contraction mapping of Eqs. (4.10) and (4.11) with $\gamma = 0.4$.

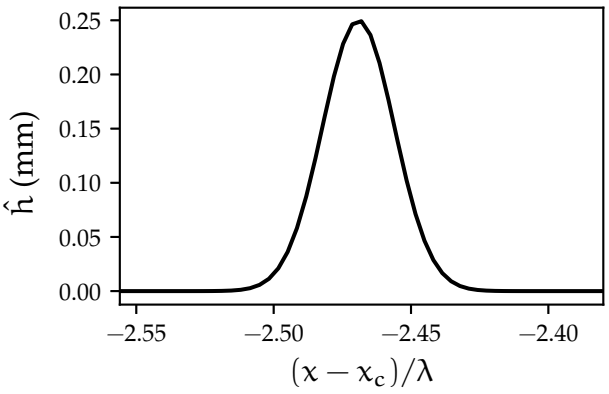

Figure 5.10: Wall-forcing shape $\hat{h}$ enforced to generate a TS wave upstream of the indentation area

In the first instance, the destabilisation of TS waves generated by a small-scale, time-periodic surface element placed ahead of the surface indentation is investigated. The surface actuation generates a purely 2D perturbation field, that is for $\beta = 0$. A Gaussian profile defines the streamwise surface deformation shape of the forcing as shown in Fig. 5.10. Its maximum is located 450 mm after the nominal leading edge, or roughly 1.97λ before the streamwise station marking the beginning of the indentation. Its maximum deformation off the base surface is 0.25 mm which is negligible relative to the indentation depth h. The full width at half-maximum is 4.5 mm which corresponds to $\lambda/18$. Naturally, within the scope of the linearised framework, the deformation maximum height prescribed in the analysis is in fact irrelevant since any amplitude result can be simply scaled to fit.

The prescribed frequency of the TS wave is $f = 172\,\text{Hz}$ and corresponds to a reduced frequency of $F = 50$ defined in Eq. (4.20). Fig. 5.11 depicts the evolution

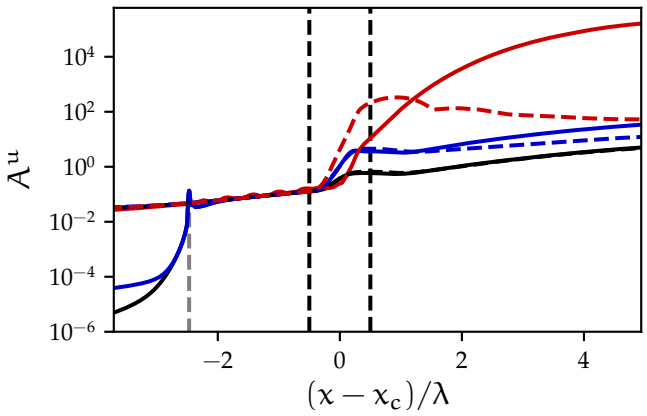

Figure 5.11: Amplitude evolution of the TS wave for the three indentation cases. LHNS results: $h = 0.81$ mm (—), $h = 1.62$ mm (—) and $h = 2.17$ mm (—). Corresponding dashed lines are from PSE-3D theory. The wall-roughness forcing location (- -) is upstream of the indentation region (- -).

of the amplitude of $\hat{u}$ across the streamwise direction for the three different indentation depths. Results from the present LHNS-based approach are compared with PSE-3D results. It is obvious that the indentation region acts as a destabiliser of the TS wave. Unlike the forced LHNS approach where initial amplitude information is computed as part of the solution process, the PSE theory only yields the streamwise evolution of the perturbation without quantitative information about the imposed initial disturbance level. In linear PSE simulations, a local, normalised eigenfunction of the same frequency f is imposed at the inflow and the state of amplification is monitored relative to this initial disturbance magnitude. An excellent match is noted between the two approaches when $h = 0.81$ mm. The discrepancies growing with increasing depth may be due to a number of reasons. The underlying hypothesis of the PSE-3D is that of a slowly varying streamwise base flow, whereas the LHNS formulation makes no such assumption. Some higher-order derivatives are neglected in the PSE-3D equations whereas they might be significant in the indentation region, given the base flow gradient magnitude. However, it should also be noted that the PSE-3D performs streamwise marching of spanwise planes, taking into account the three-dimensionality of the base flow whereas the current LHNS-based simulations are purely 2D and thus computed with a different base flow.

For the $h = 2.17$ mm setting, the LHNS approach predicts very large amplitudes in the wake of the indentation which, in all practical sense, should then undergo a strongly non-linear mechanism given the significant magnitude of the disturbance. Nonetheless, of particular interest is the behaviour predicted upstream of the indentation region. In Fig. 5.11, the surface-based Gaussian actuation is located at $(x - x_c)/\lambda \approx -2.47$ for all three indentations. The $h = 0.81$ mm and 1.62 mm

results are as expected in that the TS amplitudes decay significantly upstream of the actuation location, grow linearly downstream and then undergo further destabilisation as the waves convect over the indentation, and then in the wake region. However, the behaviour predicted for the $h = 2.17\,\text{mm}$ indentation is radically different. Although the location, shape and magnitude of actuation remain unchanged compared to the shallower indentations, it is presumed that the low-magnitude forcing appears to be completely 'swamped' by a very strong upstream effect arising from the indentation field. It is likely that the TS wave experiences a scattering effect with the generation of acoustic or pressure waves travelling upstream, as described by Wu and Hogg (2006). This feature would be entirely modelled by the LHNS model, whereas the asymptotic approach based on the triple-deck theory is by nature approximate.

Next, a parametric sweep for a range of actuation frequencies f to determine the most destabilising TS disturbances is undertaken. The frequency f is swept between 77 Hz and 229 Hz with a constant step of $\Delta f = 19\,\text{Hz}$. This corresponds to a non-dimensional angular frequency ω ranging between 0.02 and 0.06. The maximum amplitude of the TS wave across the wall-normal direction is monitored. Figures 5.12 and 5.13 present the evolution of the maximum amplitude for the frequency range aforementioned, respectively for $h = 0.81\,\text{mm}$ and 1.62 mm. For all frequencies, a sudden amplitude increase can be observed at about one-third of the way across the indentation region. Further downstream, amplification continues except for frequencies above 200 Hz, approximately. For these higher frequencies the maximum amplitude decays in the wake of the indentation. The effectiveness of the PMLs causing a significant reduction of the TS wave amplitudes in the outflow region is clearly evident. These cases are relatively benign compared to the $h = 2.17\,\text{mm}$ case displayed in Figure 5.14. In a more accentuated manner than the two smaller depths, the streamwise location of the sharp rise in TS wave amplitude in the indentation moves downstream as the wave frequency increases. Moreover, in all the frequency values examined, the wave amplitudes continue growing substantially downstream of the indentation, until where the artificially imposed PML domain becomes active. As alluded to earlier, strong upstream propagating waves may arise in all cases. Only the presence of the PML at the inflow boundary acts to diminish wave amplitudes. Although the domain extends approximately 5λ beyond the indentation, potential decay may occur further downstream. Of significant note is that TS disturbance amplitudes increase by a factor of 10^6 relative to amplitude levels at the indentation centre.

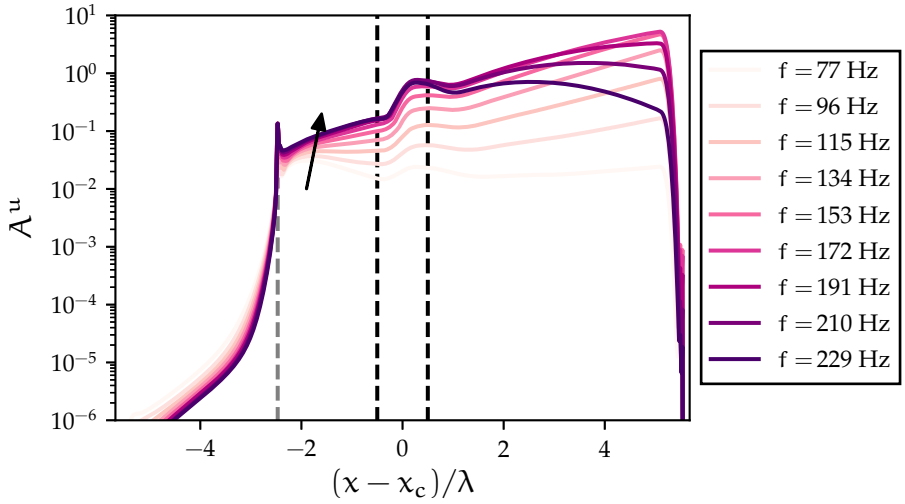

Figure 5.12: Evolution of the amplitude across the streamwise domain for the $h = 0.81\,mm$ indentation case. The arrow shows the direction in which frequency is increased.

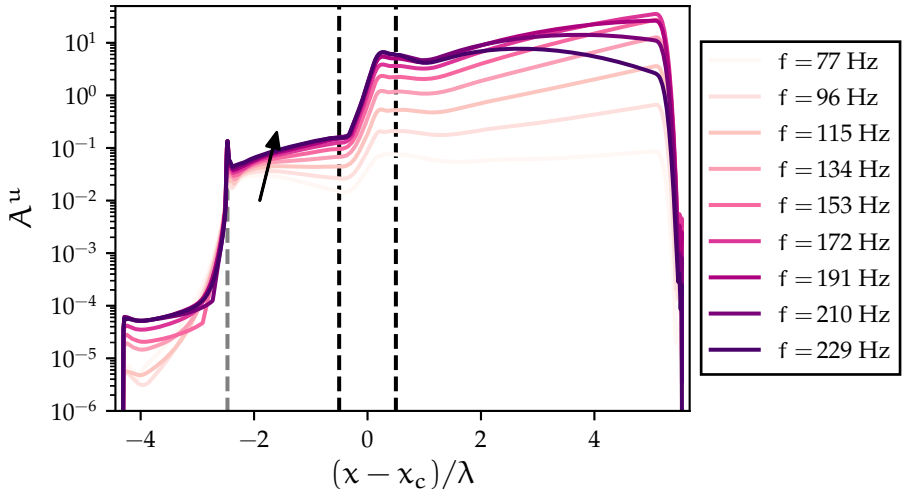

Figure 5.13: Evolution of the amplitude across the streamwise domain for the $h = 1.62\,mm$ indentation case. The arrow shows the direction in which frequency is increased.

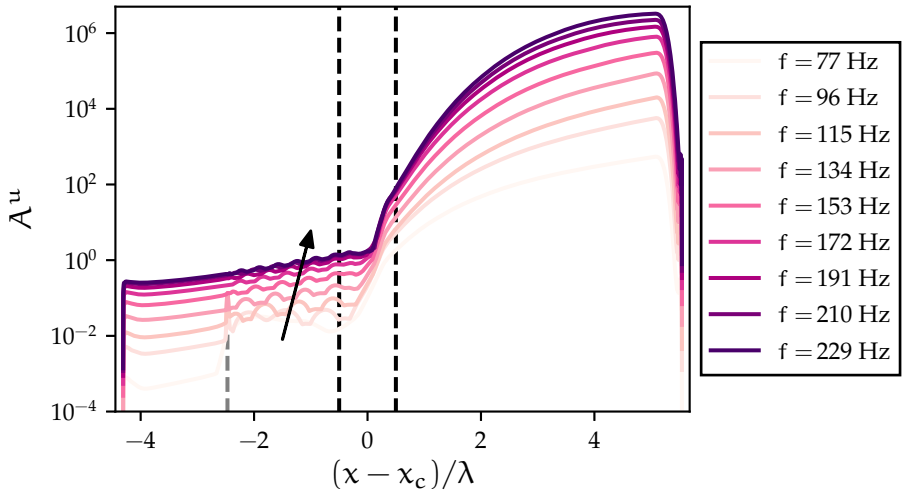

Figure 5.14: Evolution of the amplitude across the streamwise domain for the $h = 2.17\,mm$ indentation case. The arrow shows the direction in which frequency is increased.

5.2.3 Streamwise temporal BiGlobal analysis

In this BiGlobal analysis, there is no pre-existing TS wave ahead of the indentation. Instead, the existence of self-sustained global modes is investigated. A total of 600 eigenvalues are sought in the vicinity of the origin with a Krylov subspace of dimension 1,200. The relative tolerance for eigenvalue convergence is set to 10^{-10}. Different boundary treatments at the inflow and outflow are compared, including the PML introduced in Section 3.3.3 and the radiation boundary condition of Eq. (3.73). Figure 5.15 presents the physically relevant portion of the temporal eigenvalue spectra for the indentations of depth $h = 1.62\,\text{mm}$ and $2.17\,\text{mm}$ with $\beta = 0$. The non-dimensional angular frequency is $\omega_r = \delta_h \omega_r^* / U_\infty$ and the amplification rate ω_i is scaled in the same way. The eigenmodes forming the dense, inverse U-shaped, continuous spectrum branches located near $\omega_i = -0.01$ can be distinguished from branches including wall modes branches, TS modes as well as 'boundary condition' modes; these may be considered as physically spurious since they have a spatial distribution localised exclusively at the outflow of the computational domain. Unfortunately, the computation of the laminar boundary layer base flow was limited to approximately 5λ positions downstream of the indentation streamwise extent, thus restricting the computation of the full spatial streamwise mode structure.

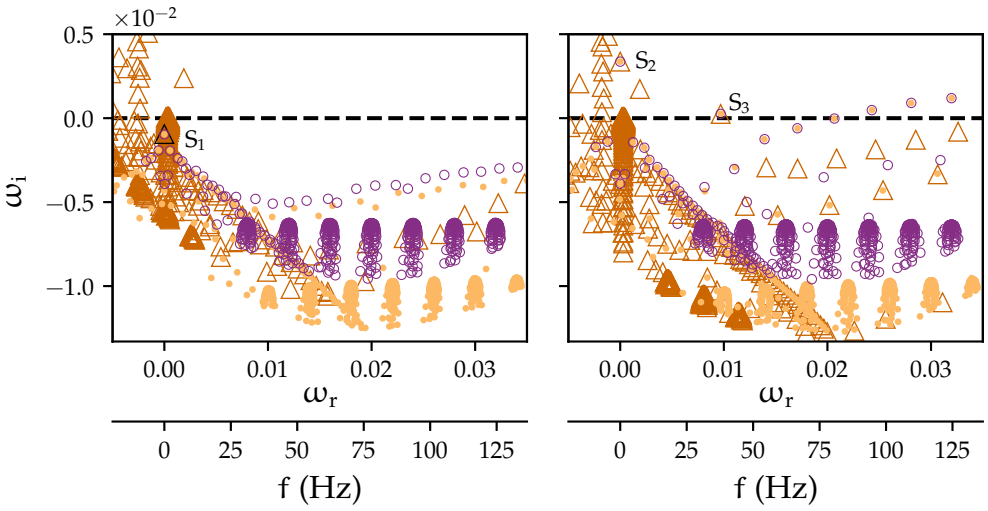

Figure 5.15: Temporal spectra obtained with $\beta = 0$ for the $h = 1.62\,\text{mm}$ (*left*) and the $h = 2.17\,\text{mm}$ (*right*) cases. Comparison between different sets of inflow/outflow boundary treatment: PML/PML (△), zero Dirichlet/Robin (●) and Robin/Robin (○). One of the symbols for the mode S_1 is changed to (△) for clarity.

The focus is on the few most unstable and least stable global modes retrieved by the analysis. All the different boundary treatments, including the PML, are able to recover the least stable global mode denoted S_1 as well as the unstable global modes indicated by S_2 and S_3 in Fig. 5.15. No physically relevant temporal

Table 5.5: Numerical values of the least stable and most unstable global modes for the $h = 1.62$ mm and 2.17 mm indentation cases, $\beta = 0$

Mode	h (mm)	Stability	ω_r	ω_i
S_1	1.62	Stable	2.06×10^{-7}	-9.66×10^{-4}
S_2	2.17	Unstable	-1.78×10^{-9}	3.37×10^{-3}
S_3	2.17	Unstable	9.70×10^{-3}	2.55×10^{-4}

global modes arose in the shallow $h = 0.81$ mm indentation which does not give rise to an LSB and does not feature reversed flow. That is the reason why the corresponding spectrum is not included. The choice of boundary conditions affects the distribution of the spectra but not the location of the global modes. Table 5.5 summarises their numerical values. Looking at the eigenvalue distribution, the boundary layer corresponding to $h = 2.17$ mm is more temporally unstable than in the $h = 1.62$ mm case. As expected, the application of the PML method yields additional branches of non-physical eigenvalues. The almost matching branches on the right-hand-side of Fig. 5.15 may be arising from the imposition of zero Dirichlet inflow (△/ ●) and Robin-type outflow (● / ○) boundary conditions.

The two unstable modes found in the case where the peak reversed-flow velocity is 9% remain inactive in the intermediate 3% case. This is consistent with the observations of Rodríguez and Theofilis (2010) and Rodríguez et al. (2013), who suggested the centrifugal instability mode becomes unstable above the threshold of 7%. However, such a peak reversed-flow criterion might not be valid for all kinds of LSBs encountered in boundary layers. Further criteria require investigation, such as the relative position of the inflection point with respect to the recirculation region (Avanci, Rodríguez & Alves, 2019).

Then, the manner in which the spatial distribution of these modes is affected by allowing the existence of spanwise periodic modes is examined. The non-dimensional spanwise wavenumber $\beta = \delta_h \beta^*$ has been varied from 0.01 to 1. In what follows, results are shown with a zero Dirichlet inflow and a Robin boundary condition at the outflow. Figure 5.16 shows the contour plots of $|\hat{u}|$ for the least stable mode S_1, which is stationary and remains stable when β is increased to 1. For a purely 2D perturbation field, the mode structure extends from a region of small velocity in the indentation and grows in magnitude further downstream. Near the outflow boundary, the streamwise perturbation velocity is at a maximum. Given the aforementioned difficulty of dealing with a short base flow streamwise domain, the spatial extent of the structure cannot be fully described. As β increases, the mode remains stable. However, the region of maximum streamwise perturbation velocity is gradually transferred to a region localised in the indentation area,

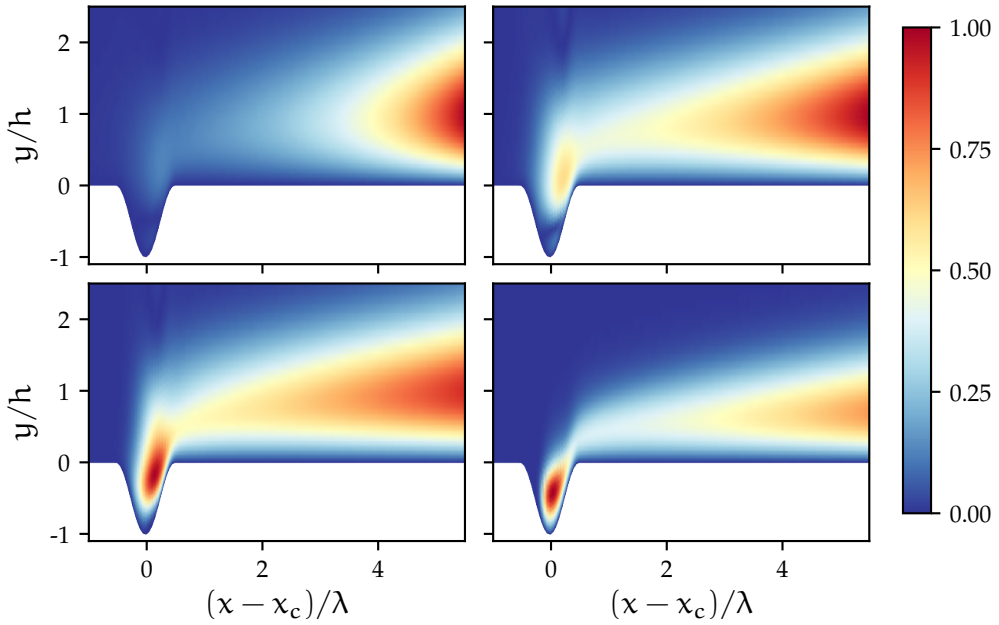

Figure 5.16: Spatial distribution of streamwise perturbation velocity amplitude $|\hat{u}|$ with increasing values of β for the least stable temporal mode S_1 in the $h = 1.62$ mm indentation case. *Top left*, $\beta = 0$; *Top right*, $\beta = 0.04$; *Bottom left*, $\beta = 0.1$; *Bottom right*, $\beta = 1$.

suggesting that two superimposed modes might coexist and merge at greater spanwise wavenumbers. The values of β for which the stationary mode is the least stable are 0.1 to 0.2 corresponding to L_z in the range 14.25 to 28.50h.

For the deepest indentation case and $\beta = 0$, the global temporal instability corresponds to a localised feature above the indentation region and slightly shifted downstream, as seen in the top-left part of Figure 5.17. The mode is stationary, $\omega_r = 0$ to numerical accuracy and unstable up to $\beta = 0.5$ corresponding to $L_z \approx 4.25h$. It becomes stable as β further increases and L_z decreases. Hence, the global instability of the boundary layer is weakened by smaller periodicity wavelengths. The localised structure is stretched in the streamwise direction as the wavenumber β increases.

The second relevant unstable mode S_3 resembles a wave-like mode and could be attributed to a Kelvin-Helmholtz mechanism of frequency $f = 37.8$ Hz. Figure 5.18 represents the corresponding streamwise and spanwise perturbation velocity developing spatially in the wake of the indentation region for $\beta = 0.01$. The mode becomes rapidly stable, beyond $\beta = 0.02$ and the wave-like structure is found to degenerate with further increments in β.

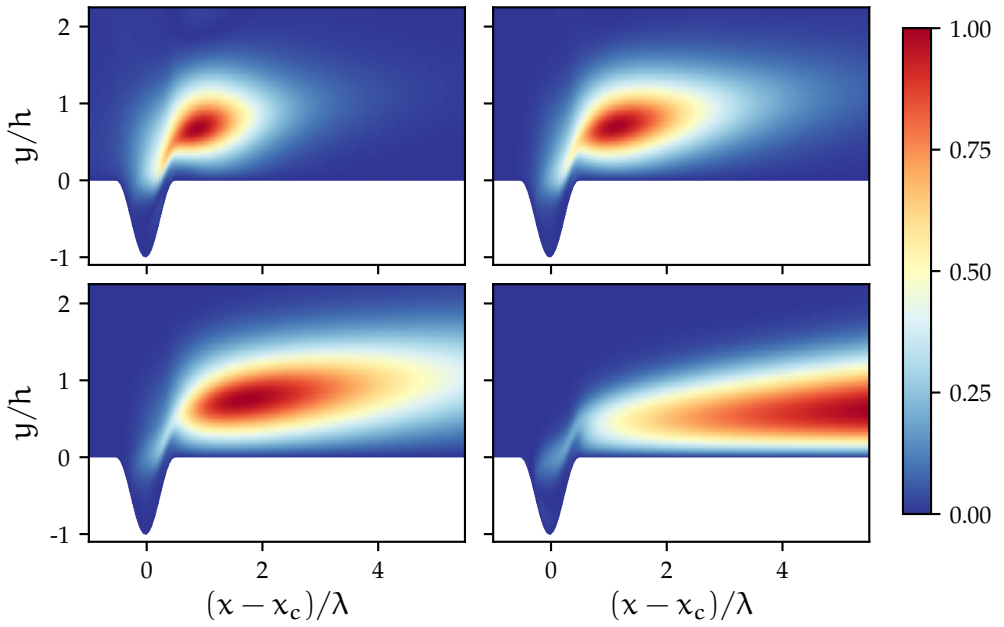

Figure 5.17: Spatial distribution of streamwise perturbation velocity amplitude $|\hat{u}|$ with increasing values of β for the most unstable temporal mode S_2 in the $h = 2.17\,\text{mm}$ indentation case. *Top left*, $\beta = 0$, unstable; *Top right*, $\beta = 0.05$, unstable; *Bottom left*, $\beta = 0.1$, unstable; *Bottom right* $\beta = 1$, stable.

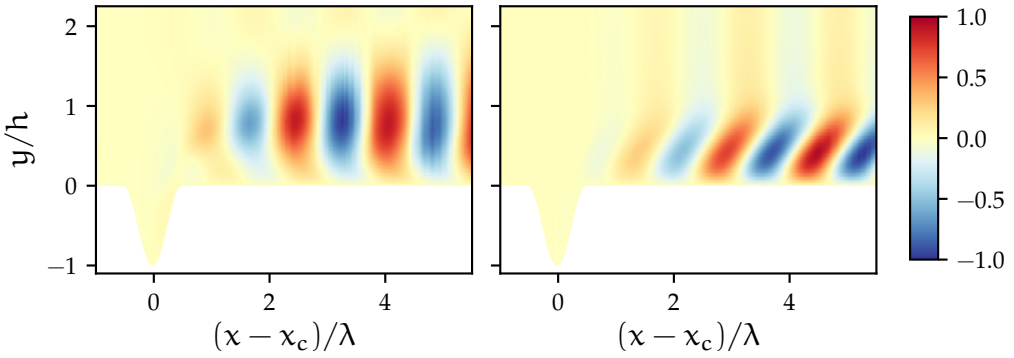

Figure 5.18: Spatial distribution of streamwise perturbation $\hat{u}_i$ (*left*) and spanwise perturbation $\hat{w}_i$ (*right*) for the unstable mode S_3 in the $h = 2.17\,\text{mm}$ indentation case with $\beta = 0.01$

5.2.4 Conclusions

In this investigation of how localised surface indentations impact the stability of a developing boundary layer featuring 2D LSBs, the indentation with the greatest depth, and hence strongest laminar separation bubble intensity distinguishes itself from the shallower indentations. Two distinct analyses were undertaken with a 2D steady base flow assumption together with a periodicity assumption of instabilities in the spanwise direction.

In the temporal BiGlobal analysis, consistent with literature, it was found that the flow is firstly temporally unstable due to a stationary mode localised near the indentation region, and secondly due to a travelling Kelvin-Helmholtz mode. However, the former was found to become stable below spanwise periodicity lengths of $4.25h$ while the latter is stabilised when L_z remains below $100h$, approximately. The receptivity analysis that has been performed showed that a pre-existing, incoming TS wave is amplified in the wake of the $h = 0.81\,\text{mm}$ and $1.62\,\text{mm}$ indentations over a limited range of frequencies. The deepest indentation features significant levels of amplification and a potential manifestation of a pressure wave or acoustic wave, since the LHNS framework suggests a strong upstream and downstream propagating structure; the physical mechanism of which requires to be clarified. This could potentially be tied in with the occurrence and prediction of the unstable stationary mode found with the BiGlobal analysis.

5.3 Swept wing with backward- and forward-facing steps

Steps, commonly encountered in the aeronautical field (for instance at the leading-edge/wing box junction), are known to be capable of triggering an early transition to turbulence as discussed in Sections 2.4.1 and 2.4.2. Previous numerical contributions in the literature have mostly focused on 2D base flows. For 2.5D swept-wing flows, the existing studies have been rare and for the most part experimental, except the numerical contributions of Tufts et al. (2017) and Cooke et al. (2019). The current analysis, using BiGlobal methodology, seeks to shed light on temporal instability mechanisms potentially arising due to a BFS or an FFS located on a 2.5D wing profile. To the author's best knowledge, there is no existing application of the method on such a geometry. Its application to a curved, 2.5D swept body on which surface steps and LSBs are present is a novelty.

Table 5.6: Ratio of step height h to boundary layer thickness δ and to displacement thickness δ^* at the step location on the clean geometry. AERAST swept wing case.

Parameter	δ				δ^*			
Step height (μm)	413	619	825	893	413	619	825	893
10% chord (%)	25	37	49	53	98	147	129	212
20% chord (%)	18	27	36	38	68	102	136	148

5.3.1 Base flow computation

Following an experimental campaign on swept-wing CF transition due to roughness effects (Sunderland & Sawyers, 2009), a numerical investigation was undertaken by Cooke et al. (2019) to study 2.5D step-destabilisation of travelling and stationary CF disturbances. The geometry is the AERAST wing, featuring a section with a chord along the line of flight $c = 0.8\,m$ and a span $b = 1.2\,m$. In the later experiments of Saeed et al. (2016), CF instability was promoted with a large sweep angle, $\Lambda = 40°$, together with the placement of periodically-aligned roughness elements shaped as circular disks. These were placed at the neutral stability point and forwards of the location of the steps. The numerical study of Cooke et al. (2019) aimed at replicating those experimental flow conditions. To this end, the authors set a Reynolds number based on chord $Re_c = 10^6$. The Mach number, $Ma = 0.3$, corresponds to the upper limit of the incompressibility assumption regime. The effect of BFSs and FFSs located at either 10% or 20% chord was not measured in the experimental test campaign of Saeed et al. (2016). As such, the purely numerical BFSs and FFSs investigations undertaken by Cooke et al. (2019) aimed at providing guidelines for possible future experiments involving surface steps.

The authors computed base flows with BFSs, FFSs and their combination to form surface humps on the aerofoil profile. While most literature work focused on sharp-edged steps, the step geometry considered in the work of Cooke et al. (2019) is slightly rounded. This introduces an additional curvature parameter and modifies the physics of the flow in the vicinity of the step edges. The presence of a recirculation bubble on the top of the FFS is generally reported in studies featuring sharp FFSs, however in the current base flows no such reversed flow region is found. The absence of the bubble on top of the FFS might well be due to the slight rounding of the step corners and to the fact that the steps are located in an overall favourable-pressure-gradient section of the aerofoil. On the other hand, a tiny recirculation bubble exists near the concave corner in front of the step.

Four roughness heights were chosen: $h_1 = 413\,\mu m$, $h_2 = 619\,\mu m$, $h_3 = 825\,\mu m$ and $h_4 = 893\,\mu m$, which correspond to a certain fraction of boundary layer parameters

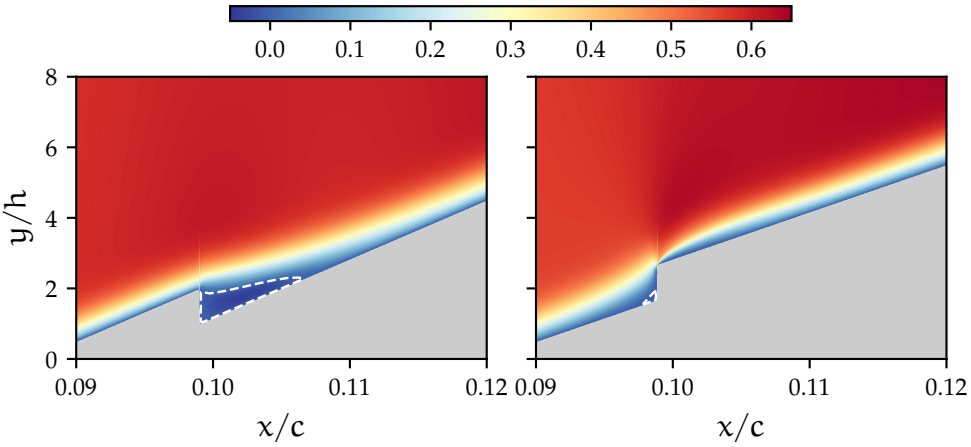

Figure 5.19: Contours of non-dimensional base streamwise velocity $\bar{u}$ for the BFS (*left*) and the FFS (*right*) in the greatest height case $h_4 = 893\,\mu m$. The white dashed line delimits the region of reversed flow. For viewing purposes, the wall-normal coordinate is distorted and not aligned with the normal to surface direction. The vertical artefact extending above the step location is a feature of the spline interpolation used for visualisation, due to the sharp gradients.

on the clean geometry as detailed in Table 5.6. The aforementioned absence of a recirculation bubble just downstream of the FFS can be observed in Fig. 5.19, which is also the case for smaller heights. The small step heights relative to the local boundary layer thickness may be a further potential reason for the absence of the bubble on top of the FFS. A large reversed flow region of length $\approx 2h_4$ is located after the BFS location, whereas a much smaller one exists at the base of the FFS. The base flow generation followed a hybrid approach, in that the overall, steady flow regime for the complete aerofoil was first computed with a RANS approach by means of the flow solver TAU (Kroll, Langer & Schwöppe, 2014). A transition switch was set beyond 60% of the chord length, ensuring steady laminar flow in the region of interest. Then, using far-field boundary conditions provided by the RANS solution, Cooke et al. (2019) undertook an embedded steady DNS using a spectral/hp element discretisation within the Nektar++ software. In this way, they accurately captured any modifications arising in the laminar boundary layer region on introduction of the step features. A stiffly stable splitting scheme which decouples the velocity and pressure fields was employed, and time integration was achieved by a second-order accurate implicit-explicit scheme. A combination of triangular and quadrilateral elements formed the mesh with low-order and higher-order polynomial expansions, besides a Fourier expansion in the spanwise direction to define a 2.5D solution. Mesh independence was assessed, and steady laminar solutions were assumed to be reached once the relative error in the ℓ_2-norm of velocity fields was less than 10^{-5} on the entire domain.

5.3.2 Streamwise temporal BiGlobal analysis

In the streamwise direction, the grid formed of $n_x = 4{,}000$ points is clustered near the step location ($x/c = 0.1$ or $x/c = 0.2$) by means of the interior contraction mapping coupled with the tangential function described in Eqs. (4.10) and (4.11), where the parameter γ is set to 0.48. A 6th-order FD-q method is used and the domain extends over a length of approximately $145h_4$, that is $x/c \in [0.05, 0.18]$ for the 10% case and $x/c \in [0.15, 0.28]$ for the 20% case. In the wall-normal direction, the bilinear mapping of Eq. (4.13) is employed; $y = 1.8h_4$ is the coordinate delimiting the two regions, whereas the wall-normal domain is truncated at $y_\infty = 100h_4$, yielding a sufficiently large extent to minimise the influence of the far-field boundary condition. A total of 150 grid points form the discretised wall-normal domain together with an 8th-order FD-q.

In the analysis, the non-dimensional spanwise wavenumber β spans a range of geometrically-spaced values from 0 to 10. For each value of the shift, a total of 20 eigenvalues are requested in the upper half of the (ω_r, ω_i) plane, that is the temporally unstable region of the spectrum. The corresponding dimension of the Krylov subspace is $\dim(\mathcal{K}_m) = 100$ and the convergence of the eigenvalues is monitored with a prescribed tolerance of 10^{-11} below which the absolute error estimate on the associated eigenvalues should fall. In this numerical study, the velocity scale is the free-stream streamwise velocity U_∞ and the greatest step height $h_4 = 893\,\mu\text{m}$ is the length scale of the problem.

A well-known feature of BiGlobal analyses conducted in the streamwise/wall-normal plane is the sensitivity of eigenvalues to the streamwise length of the computational domain as well as to the choice of inflow and outflow boundary conditions. Therefore, some numerical precautions have been deployed. For the different height and chord location cases, it has been verified that physically relevant eigenvalues do not undergo significant value changes when the streamwise length of the computational domain is varied, namely that the modulus of unstable eigenvalues of interest have been modified by no more than 6%. Other numerical parameters have been kept constant. This is evidenced, for example, in Fig. 5.20 with the two physically relevant modes of the BFS of height $h_4 = 893\,\mu\text{m}$ and located at 10% of the chord. Furthermore, only a very slight eigenvalue magnitude change has been observed when inflow and outflow boundary conditions have been varied, as shown by Fig. 5.21 for the same BFS case. This is a noteworthy feature, given the well-known issues of spectrum convergence with respect to inflow/outflow boundary conditions discussed in several literature contributions. In addition, mesh independence has also been confirmed.

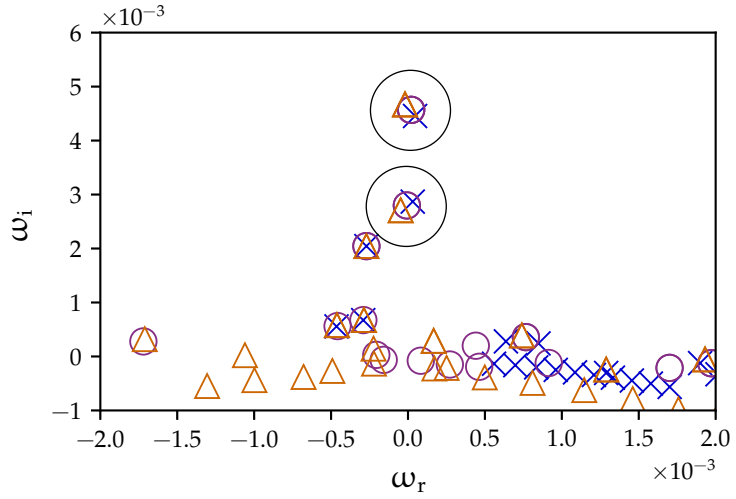

Figure 5.20: Eigenvalue spectra associated to the $h_4 = 893\,\mu m$ BFS located at 10% chord, with variation of streamwise domain length: $x/c \in [0.03, 0.28]$ (×), $x/c \in [0.04, 0.23]$ (○) and $x/c \in [0.05, 0.18]$ (△). The two physically relevant eigenvalues are indicated (○).

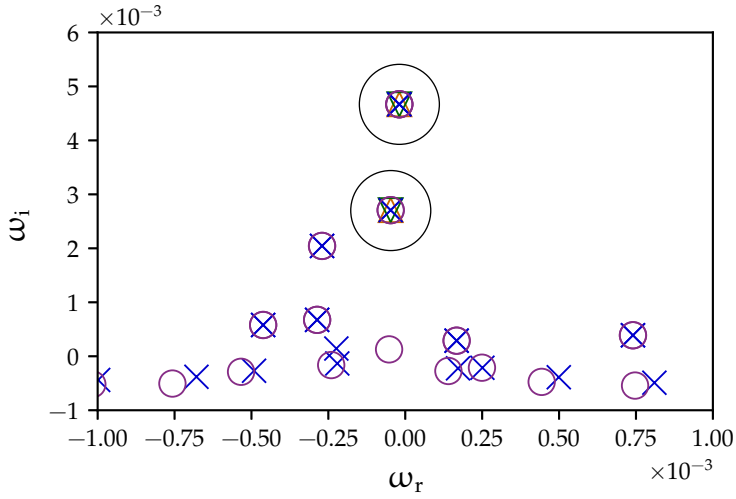

Figure 5.21: Eigenvalue spectra associated to the $h_4 = 893\,\mu m$ BFS located at 10% chord, with variation of inflow/outflow boundary conditions: zero-Dirichlet/'do-nothing' (×), zero-Dirichlet/radiation (○), radiation/'do-nothing' (△) and radiation/linear extrapolation (▽). The two physically relevant eigenvalues are indicated (○).

The existence of temporally unstable modes for the four height cases and the two chordwise step locations is presented in Table 5.7. Their physical validity has been assessed by their relative independence to numerical parameters and the observation of associated eigenfunctions. No temporal instability is found for the smallest step heights for both the FFS and BFS cases at the two chordwise positions, while the highest step features unstable modes for solely the BFS. The slightly rounded character of the step seems detrimental for the FFS; the absence of a recirculation region just downstream of the FFS in the steady solutions may be heavily impacting the stability characteristics. In comparison, Tufts et al. (2017) found evidence of a reasonably large recirculating laminar bubble on the top of

Table 5.7: Presence of temporal instabilities for the step feature, height and chord location cases on the AERAST swept wing

h (µm)	BFS 10%	BFS 20%	FFS 10%	FFS 20%
413	No	No	No	No
619	Yes	No	Yes	Yes
825	Yes	Yes	Yes	No
893	Yes	Yes	No	No

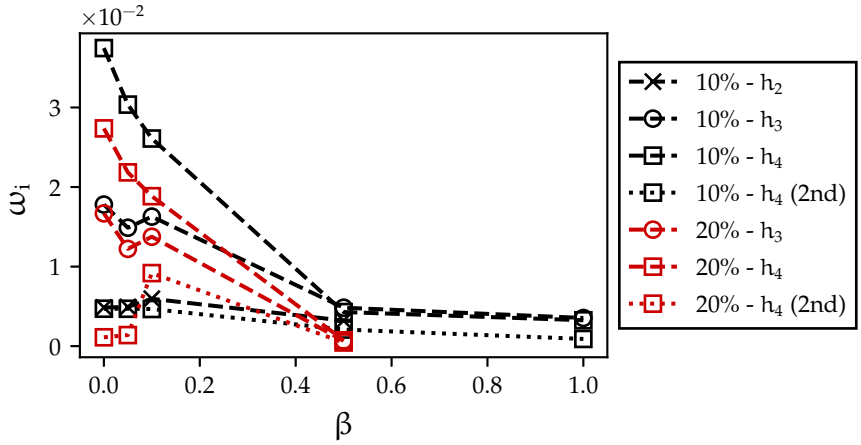

Figure 5.22: Growth rates ω_i of the unstable eigenvalues as a function of the spanwise wavenumber β. Cases correspond to the BFS. When applicable, the second most unstable modes (2nd) are included.

the FFS, however their step was sharp. In the experiment of Rius Vidales et al. (2018), the infrared thermography technique used to identify the transition front did not enable its presence to be determined. Temporal instabilities are predicted to arise with current computations in the two intermediate height cases for both step configurations, although little correlation with the chordwise location of the step can be established. The results in Table 5.7 have been related to Re_{hh} to devise a potential relationship. However, this has so far remained inconclusive.

Figure 5.22 compares growth rates of unstable eigenvalues found for the BFSs on varying the spanwise wavenumber β. Most eigenvalues are found to become stable or even leave the area of interest of the complex plane beyond $\beta = 1$. For the greatest height, two unstable eigenvalues are found. The variation of β turns out to not be necessarily discriminating between the different cases, as most unstable modes are monotonically stabilised up to $\beta = 1$ except in the 0 to 0.1 region. A general trend is how higher BFSs appear to be associated with larger growth rates. At a glance, the 10% chord BFS yields more unstable eigenvalues than its 20% chord counterpart. Moreover, the second-most unstable eigenvalues in the greatest height cases have a much lower growth rate than the primary instability modes. Remarkably, the growth rate of the three unstable eigenmodes retrieved

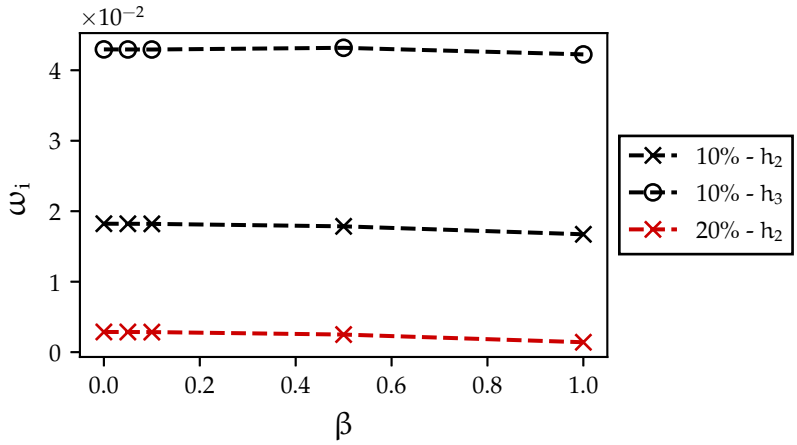

Figure 5.23: Growth rates ω_i of the unstable eigenvalues as a function of the spanwise wavenumber β. Cases correspond to the FFS.

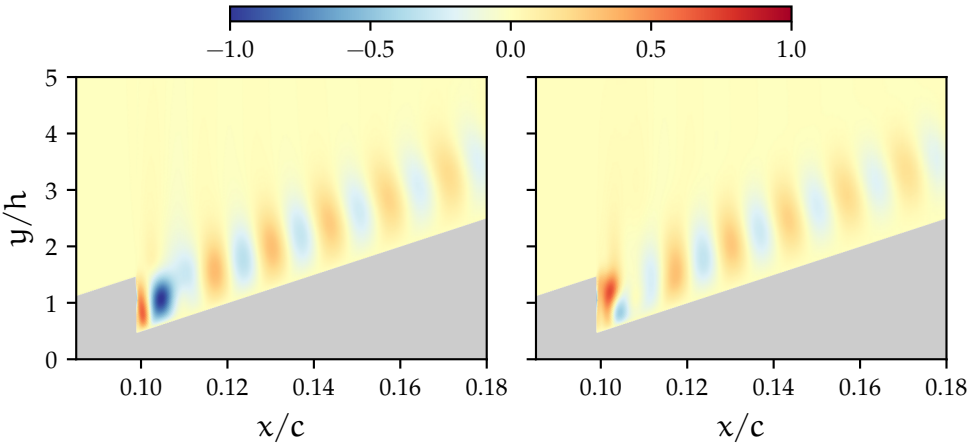

Figure 5.24: Contours of non-dimensional streamwise perturbation velocity $\hat{u}_i$ (*left*) and spanwise perturbation velocity $\hat{w}_i$ (*right*) for the most unstable mode in the greatest height case $h_4 = 893\,\mu m$ of the BFS, with $\beta = 0.5$

for the FFSs seems independent of the spanwise wavenumber β as can be seen in Fig. 5.23. This remains to be explained. Regardless, the higher step possesses a larger growth rate just as the BFS case. For equal step heights, the 20% chord location does not seem as temporally destabilising as the 10% chord location. A plausible explanation may be the thicker boundary layer at 20% chord, where h/δ is smaller than at 10% chord according to Table 5.6.

For both step types, the existing unstable eigenmodes are stationary ($\omega_r \approx 0$) except in a narrow band of spanwise wavenumbers comprised between 0.01 and 0.1. Two kinds of mode structure have been classified in the case of BFSs, namely localised regions of relatively large streamwise and spanwise velocity magnitude as well as wave-like structures extending from the step height down to the lower BFS corner and convected further downstream as in Fig. 5.24. For the FFSs, the

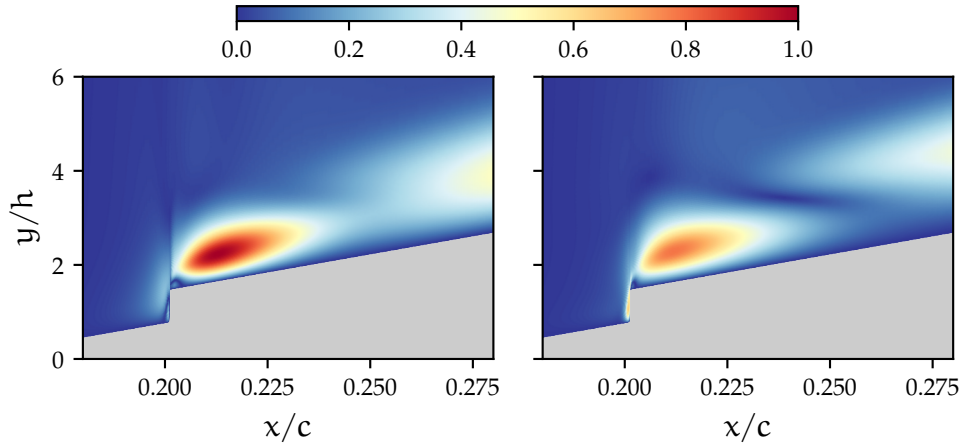

Figure 5.25: Contours of non-dimensional streamwise perturbation velocity $|\hat{u}|$ (*left*) and spanwise perturbation velocity $|\hat{w}|$ (*right*) for the most unstable mode in the second-greatest height case $h_3 = 613\,\mu m$ of the FFS, with $\beta = 0.1$

eigenfunctions feature regions of relatively high streamwise and spanwise velocity magnitudes located above the step, just downstream as can be seen in Fig. 5.25.

5.3.3 Conclusions

The temporal stability of a boundary layer developing on a swept wing and undergoing destabilisation due to steps has been investigated. Preliminary results have been provided on moderately smooth backward- and forward-facing steps by means of streamwise BiGlobal analysis. Unstable modes have been found for step heights exceeding the clean geometry local boundary layer displacement thickness. Nevertheless, the highest forward-facing step has not been found to display instability, with only the intermediate step heights yielding unstable modes; the concept of critical step height discussed in previous works might not be applicable in this context due to the roundness of the steps considered. Owing to limited dataset availability, the analysis at the two step locations was insufficient in scope to allow any conclusions to be drawn on the instability behaviour. A more exhaustive investigation on larger datasets is required for the elucidation of self-sustained instability mechanisms arising in swept-wing boundary layers.

Chapter 6

Non-Linear Growth of Boundary Layer Instabilities

All models are wrong, but some are useful.

—George E. P. Box

This penultimate chapter focuses on the developed NLHNS method. We use available NLPSE and experimental results for three different boundary layer configurations to verify and validate the model. These are undertaken either in a stationary or travelling instability setting. Afterwards, we test the potential of the method on two application cases. First, we model the interaction of a TS wave with a stationary cylinder located on a zero-pressure-gradient surface, reproducing the base flow and replicating the features of the experiment of de Paula et al. (2017). The NLHNS model is then applied on an industrially relevant configuration. We compute the swept-wing boundary layer on the AERAST geometry directly from experimental data, and analyse the aspects of the stationary CF induced by a cylinder placed on the leading edge.

6.1 Verification and validation

In the first instance, the correctness of the developed NLHNS approach and its validity as a physical model shall be assessed. To this end, this section presents the test bed formed of three different verification cases. These have been considered in the literature with a NLPSE methodology. The results that ensued are used to assess the correctness and accuracy of the NLHNS framework developed in

this thesis. The same base flows as in Section 5.1 are the basis of the current verification and validation procedure, namely the self-similar Blasius boundary layer and the self-similar swept attachment-line boundary layer. Therefore, details on their numerical computation are overlooked. The NLHNS approach solves in physical space the 'boundary-layer' plane, that is the streamwise and wall-normal directions whereas the temporal and spanwise directions are numerically solved in Fourier space. The procedure developed in Section 4.2.3 is then tested on the case of a purely 2D temporal interaction, followed by a 3D unsteady interaction case and finally a stationary 3D interaction case.

6.1.1 Travelling 2D interaction

The first verification and validation case is that of the non-linear evolution of a TS wave introduced in a developing Blasius boundary layer. It was first documented by Bertolotti (1991) and has been a customary benchmark for NLPSE solvers in the literature. In this problem, the Reynolds number is defined in terms of the Blasius boundary layer thickness ℓ,

$$\mathrm{Re} = \frac{U_e \ell}{\nu_e} = \sqrt{\frac{U_e x}{\nu_e}} = \sqrt{\mathrm{Re}_x}. \tag{6.1}$$

Results are presented for an initial RMS amplitude of $A^u_{\mathrm{rms}} = 0.25\%$ at the streamwise location corresponding to $\mathrm{Re} = 400$. The non-linear evolution is monitored for $N = 5$ positive temporal harmonics with a reduced frequency $F = 86$. This corresponds to an angular frequency $\omega = 0.0344$. Pure 2D disturbances are considered, therefore $M = 0$ and the spanwise wavenumber $\beta = 0$. The Blasius length ℓ_0 at the streamwise position corresponding to $\mathrm{Re} = 400$ is the length scale for this NLHNS computation.

The computational domain extends from $\mathrm{Re} = 200$ to 1,100. As mentioned in Section 3.2.3, in the NLPSE approach the different initial harmonic amplitudes must be directly prescribed at $\mathrm{Re} = 400$ to kick-start the streamwise marching procedure. To meet the target amplitude for the current NLHNS approach, a constant wall forcing is imposed upstream (near $\mathrm{Re} = 287$) with its amplitude tweaked to reach the correct 0.25% amplitude level at $\mathrm{Re} = 400$ for the $(1, 0)$ mode. Throughout the algorithm iterations, the amplitude A^u_{rms} at $\mathrm{Re} = 400$ is monitored. Once it is stabilised, the amplitude of the wall forcing is adjusted. However, to ensure a PSE-type initialisation at that streamwise location the non-linear terms are zeroed upstream.

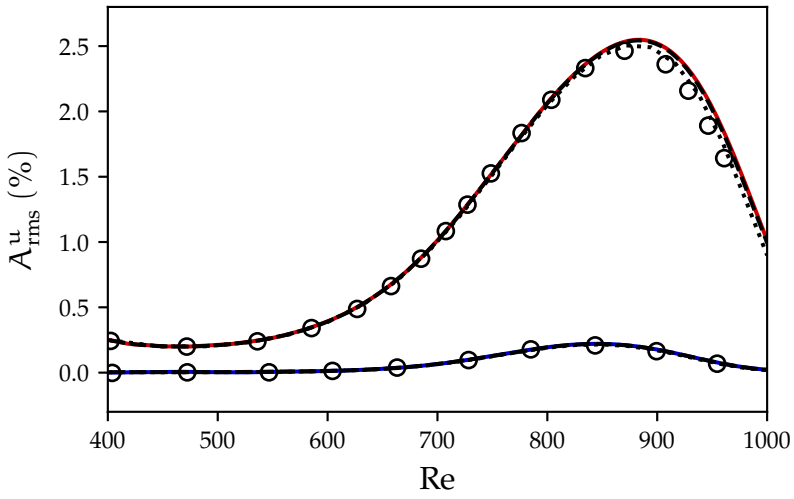

Figure 6.1: Amplitude based on $\hat{u}$ of modes $(1,0)$ (—) and $(2,0)$ (—) for the travelling 2D, $F = 86$ Blasius boundary layer case. Comparison with results from Zanus, Miró Miró and Pinna (2018) (--), Hein (2005) (···) and Bertolotti (1991) (○).

Mesh convergence has been ensured with the choice of $n_x = 3{,}500$, $n_y = 100$, $q_x = 4$ and $q_y = 8$. Absorbing inflow and outflow layers are activated; the outflow layer starts at $Re = 1{,}080$ while a radiation boundary condition is imposed at the end of the computational domain. In the wall-normal direction, the domain extends up to $y_\infty = 200$ with $y_h = 4.5$ in use for the bilinear mapping. The streamwise grid is clustered near the wall forcing location, which is defined as a pulsating step function seen by the $(1,0)$ mode.

The convergence tolerance described by Eq. (4.34) is 10^{-6}. Figure 6.1 shows the evolution of the initially forced fundamental mode $(1,0)$ as well as its higher harmonic counterpart $(2,0)$ generated by non-linearity. They both undergo destabilisation before decaying further downstream. To meet the specified tolerance, a total of 46 global iterations were required to obtain convergence with the 0.25% amplitude level. Such a long convergence process is explained by the strong instability regime when the target amplitude is slightly increased. In his analysis, Bertolotti (1991) described that for an initial amplitude of 0.30%, the $(1,0)$ disturbance monotonically grows and reaches a level of 4% near $Re = 925$. Present results are compared with NLPSE computations of Bertolotti (1991), with results from Zanus, Miró Miró and Pinna (2018) using the VESTA code developed at VKI and with the NOLOT code (Hein, 2005) developed at DLR. There is overall an excellent agreement with the different NLPSE references in Fig. 6.1. A minor discrepancy is the location and value of peak amplitude. Bertolotti reports a maximum amplitude of 2.44% at $Re = 877$, while the $(1,0)$ disturbance seems to reach 2.55% at $Re = 883$ for the current NLHNS approach and NOLOT. It was found that the peak characteristics are sensitive to streamwise grid convergence.

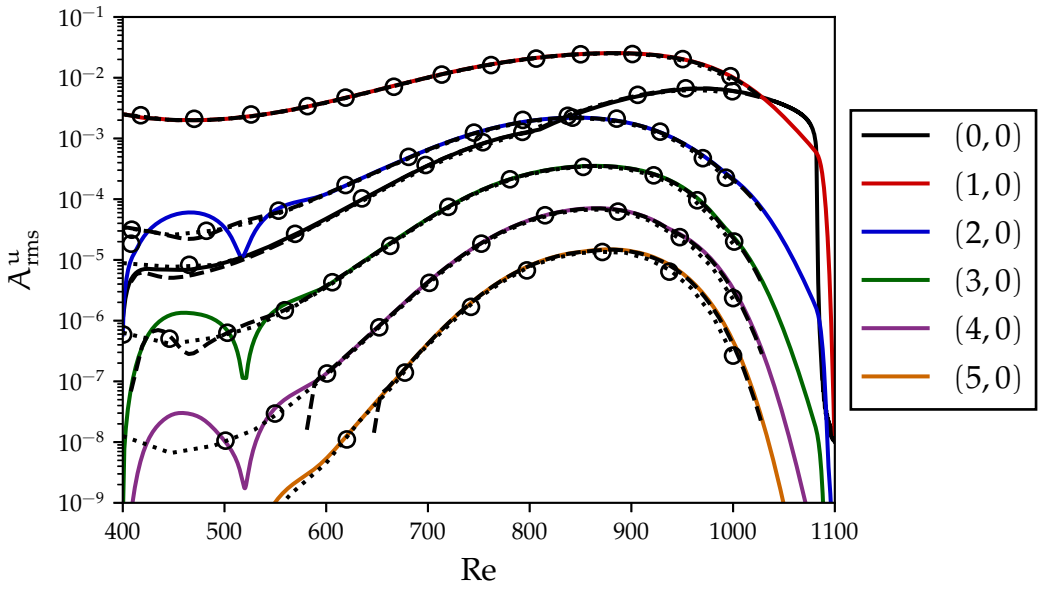

Figure 6.2: Amplitude based on $\hat{u}$ of all temporal modes. Travelling 2D, $F = 86$ Blasius boundary layer case. Comparison with results from Zanus, Miró Miró and Pinna (2018) (**--**), Hein (2005) (⋯) and Bertolotti (1991) (○).

On a broader level, a near-perfect agreement is found for all the harmonics as suggested by Fig. 6.2 on a portion of the domain comprised between $Re = 600$ and 1,000. The mode decay in the absorbing layer region near the outflow of the domain is efficient for all modes, including the MFD. The wobbly behaviour of NLHNS modes before $Re = 600$, except $(1, 0)$ which is forced upstream, is explained by the PSE-type initialisation mentioned earlier. Naturally, a certain streamwise domain extent acts as a transient region for the higher harmonics to set in.

The performance of the NLHNS code is also assessed by comparing streamwise velocity profiles at the location $Re = 796$. Figure 6.3 shows the wall-normal evolution of the amplitude for the MFD mode and the three higher harmonic modes. Profiles are superimposed with VESTA results and NLPSE results of Airiau (1994). Once again, the two different approaches are in excellent agreement as can be seen from the profiles of the non-stationary modes. For the MFD mode, there is a fine match with the result from Airiau (1994) and a discrepancy on the second peak with the VESTA result. This could be expected as there are various approximations intrinsic to the PSE-based MFD model. The disparity lies in the retention of PDE terms in the NLHNS model governing the MFD. The streamwise pressure gradient term is kept and the momentum equation projected in the wall-normal direction is also retained in its entirety. In contrast, the PSE model assumes $\partial_x \hat{p} = \partial_y \hat{p} = 0$.

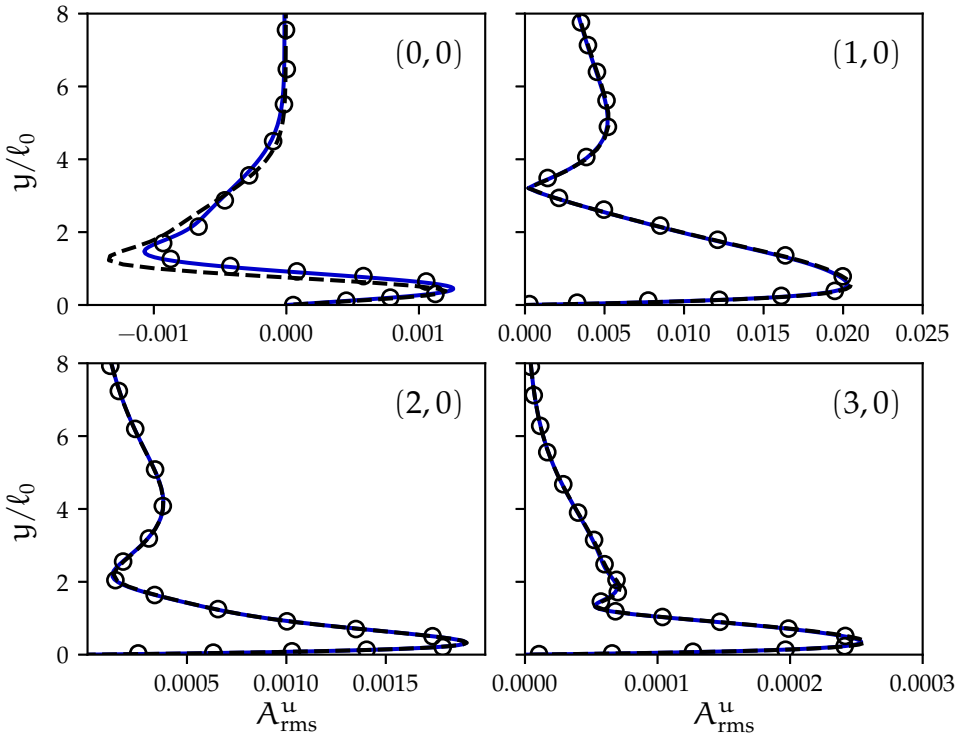

Figure 6.3: Wall-normal profiles (—) of $\hat{u}$ located at $Re = 796$ for the MFD mode, the fundamental mode as well as two higher harmonics. Travelling 2D, $F = 86$ Blasius boundary layer case. Comparison with results from Zanus, Miró Miró and Pinna (2018) (--) and Airiau (1994) (○). The MFD mode is displayed in terms of peak-to-peak amplitude.

6.1.2 Travelling 3D interaction

The previous Blasius boundary layer case solely involves temporal resonance and does not allow to verify the correctness of the whole NLHNS machinery implemented, especially with respect to the 2D DFTs. Therefore, the verification of the NLHNS solver is now undertaken on a case with both temporal and oblique, or travelling 3D resonance. Kachanov and Levchenko (1984) experimentally investigated the resonant interaction of a plane TS wave with a pair of oblique waves. The objective is to reproduce numerically and with high fidelity their experimental data as well as to compare NLHNS results with NLPSE results obtained by other authors. This would demonstrate a capability for the NLHNS solver to accurately model any kind of wave triad interactions occurring within an incompressible boundary layer.

The base flow is also a developing Blasius boundary layer. A $(2, 0)$ disturbance characterised by $2F = 124$ as well as a pair of oblique waves $(1, \pm 1)$ with $\beta = 0.14$ are introduced at $Re = 420$. The corresponding reduced spanwise wavenumber is $b = \beta/Re = 3.333 \times 10^{-4}$. Besides, the free-stream velocity is $U_\infty = 9.18\,\mathrm{m\,s^{-1}}$, matching the value of Kachanov and Levchenko (1984). The discretisation settings are those of the previous test case, except $y_h = 3.5$ and the pulsating step roughness

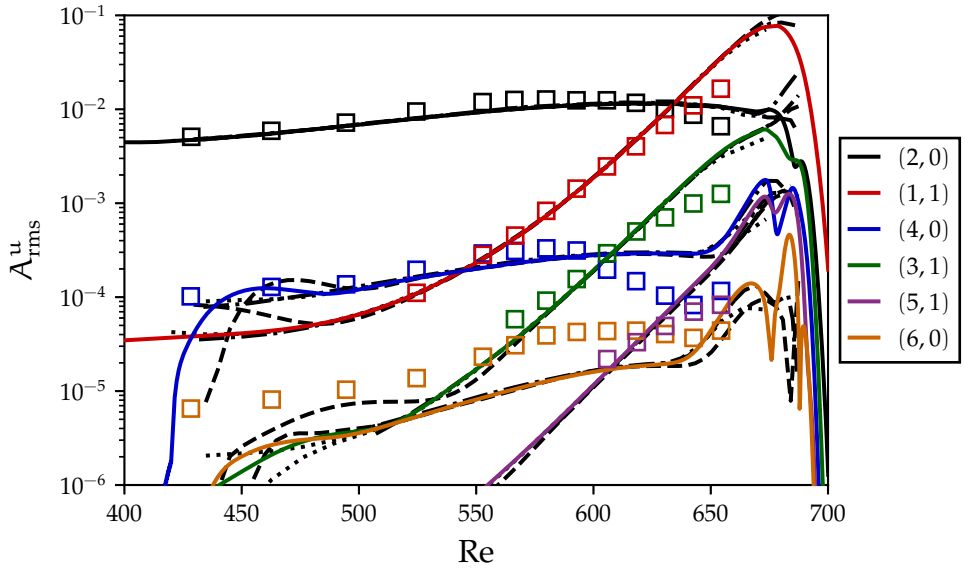

Figure 6.4: Amplitudes based on $\hat{u}$ (—) and measured at $y/\ell = 1.3$ for the travelling 3D, $F = 62$ and $\beta = 0.14$ Blasius boundary layer case. Comparison with experimental data of Kachanov and Levchenko (1984) (□) as well as NLPSE results from Bertolotti (1991) (-·), Hein (2005) (- -) and Zanus and Pinna (2018) (···).

seen by the $(2, 0)$ and $(1, \pm 1)$ modes that is imposed near $Re = 314$. The Fourier series describing the perturbation is now truncated at $M = 6$ and $N = 3$, matching the parameters of authors referencing the present case, except for Hein (2005) who truncated the Fourier series at $M = 7$ and $N = 5$. Finally, the computational domain extends from 200 to 700 and features absorbing layers at the outflow, starting at $Re = 670$. In an analogous fashion to the 2D temporal resonance, the $(2, 0)$ and $(1, \pm 1)$ modes are forced well upstream to reach respective RMS amplitudes of 4.6×10^{-3} and 3.7×10^{-5} at the location $Re = 420$, before which non-linear interactions are deactivated.

Figure 6.4 represents the amplitude evolution for six modes across the domain. For this test case, amplitudes are not defined in terms of the wall-normal maximum but rather measured at a fixed wall-normal location $y/\ell = 1.3$. The NLHNS and NLPSE approaches yield identical results for the initialised modes $(2, 0)$ and $(1, \pm 1)$ across the whole domain, and also for the other modes further downstream after the transient region. The NLPSE results from Zanus and Pinna (2018), Hein (2005) and Bertolotti (1991) gradually differ past $Re \approx 640$ where a strongly non-linear regime is established and the NLPSE approach starts to diverge. For the NLHNS approach, the absorbing layers have been positioned as far downstream as possible before the computation becomes unstable. Once again, the effectiveness of the PML is clearly evident as it seamlessly decreases mode amplitude by several orders of magnitude at $Re = 700$. Figure 6.4 represents the case with the farthest absorbing layer interface location, $Re = 670$, that yielded numerical convergence. Downstream of

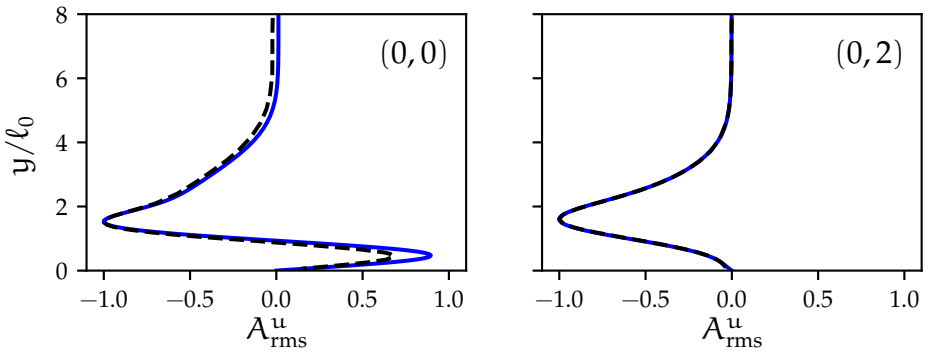

Figure 6.5: Normalised wall-normal profiles of $\hat{u}$ (**—**), peak-to-peak amplitude extracted at $Re = 608$ for the MFD mode and the $(0, 2)$ mode. Travelling 3D, $F = 62$ and $\beta = 0.14$ Blasius boundary layer case. Comparison with NLPSE results from Bertolotti (1991) (**- -**).

that location, the computation tends to diverge as opposed to results obtained with absorbing layers shifted more upstream. The near-unstable behaviour within the PML is evident as the amplitude of the $(2, 0)$, $(4, 0)$, $(5, 1)$ and $(6, 0)$ harmonics is wobbly compared to the monotonously decreasing $(1, 1)$ and $(3, 1)$ modes. The PSE also diverges in the same region, where the disturbance field is most likely highly non-linear and the boundary layer close to breakdown. These observations tend to slightly curb the hopes for computing mode interaction far in the non-linear regime once the general disturbance level exceeds a certain threshold. It shall be stressed once more that the NLHNS equations and all harmonic modes are treated in a fully elliptic way and solved in a 'global' manner. At the point of potential breakdown, there could be a sudden thickening of the boundary layer or stronger pressure gradients that could be captured by the NLHNS model.

Regardless of those aspects, the NLHNS approach accurately reproduces the evolution of the $(2, 0)$ and $(1, 1)$ modes in the experiment of Kachanov and Levchenko (1984). Only the $(6, 0)$ mode is underestimated by the NLHNS and NLPSE approaches across the domain. Better agreement is obtained for the $(4, 0)$, $(3, 1)$ and $(5, 1)$ modes. The disagreement between the numerical computations and the experiment for the $(6, 0)$ mode may be due to a number of issues. The mode amplitude is relatively low, adding uncertainty in the accurate quantification of the inflow state and in the ability to experimentally measure it with sufficient accuracy.

Further insight into the NLHNS accuracy may be gained by monitoring the wall-normal profiles of the mode amplitude where non-linear interactions gain a significant level. Figures 6.5 and 6.6 show the wall-normal evolution of A^u_{rms} at $Re = 608$ for relevant modes. Similar to the purely 2D temporal interaction case investigated earlier, a discrepancy on one of the peak values of the MFD is observed. This could be attributed to the streamwise resolution of the NLPSE

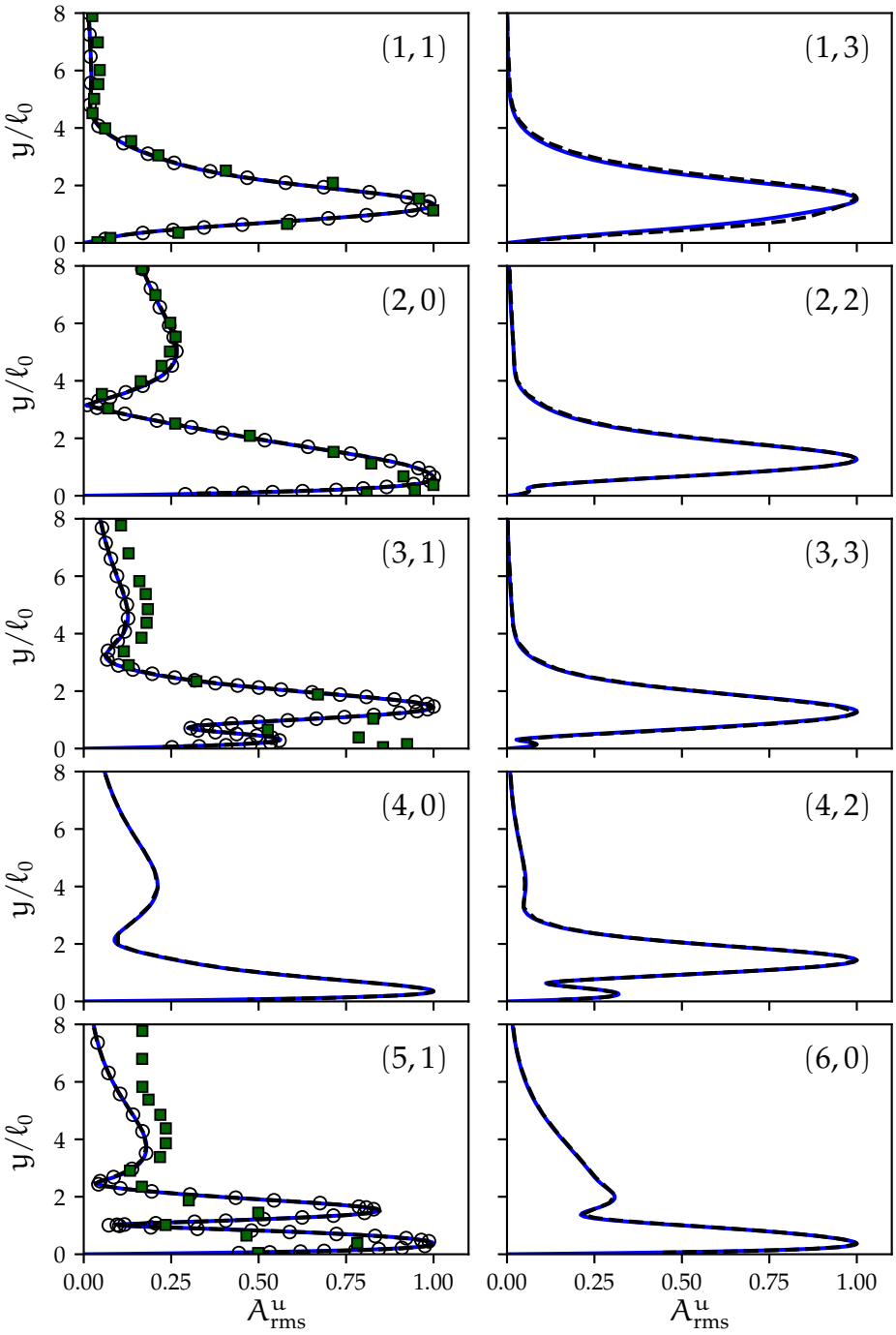

Figure 6.6: Normalised wall-normal profiles (—) of $\hat{u}$, zero-to-peak amplitude extracted at $Re = 608$. Travelling 3D, $F = 62$ and $\beta = 0.14$ Blasius boundary layer case. Comparison with NLPSE results from Bertolotti (1991) (**--**), Airiau (1994) (○) and experimental data of Kachanov and Levchenko (1984) (■).

computation and to the different MFD model in the PSE formulation for the stationary mode. While all the viscous diffusion terms, the streamwise *and* wall-normal pressure gradient terms are retained for the MFD description in the current NLHNS, numerical convergence is achieved in the PSE when $\partial_x \hat{p}$ is zeroed. On the other hand, an excellent agreement is found with the NLPSE profiles for all the other modes. The $(1,1)$ and $(2,0)$ modes correlate well with the experimental data whereas a larger discrepancy exists for the $(3,1)$ and $(5,1)$ modes further away from the wall. The profiles in Fig. 6.6 are normalised. However, the magnitude of the latter modes is in practice smaller than that of $(1,1)$ and $(2,0)$ and the difficulty to experimentally measure the higher harmonics could be invoked to explain the disparity.

6.1.3 Stationary 3D interaction

After assessing the computational tool in the presence of temporal resonance, the final verification case aims at assessing the NLHNS approach in a pure spanwise resonance setting, or 'stationary CF' setting. Naturally, the swept Hiemenz flow discussed in Section 5.1.2 is an appropriate model problem for mimicking the attachment-line region of a swept wing.

Comparisons are undertaken on the oblique breakdown case in the swept Hiemenz flow investigated by Malik, Li and Chang (1994) and later revisited by Janke and Balakumar (1999), both with NLPSE. The swept Hiemenz flow is characterised by the free-stream streamwise velocity increasing linearly with the streamwise coordinate,

$$U_\infty(x) = kx \tag{6.2}$$

allowing to define the global length scale of the problem,

$$L = \sqrt{\frac{\nu}{k}} \tag{6.3}$$

representing the typical thickness of the attachment-line boundary layer. Then, the boundary-layer dynamics are represented via a variable streamwise Reynolds number and a constant spanwise Reynolds number, respectively defined as

$$Re = \frac{U_\infty(x)L}{\nu} \qquad \overline{Re} = \frac{W_\infty L}{\nu} \tag{6.4}$$

where W_∞ is the velocity scale for the current problem.

The current stationary case ($F = 0$) considers $\overline{Re} = 500$, for which most linearly amplified disturbances are close to $\beta = 0.4$, the value retained in the NLPSE

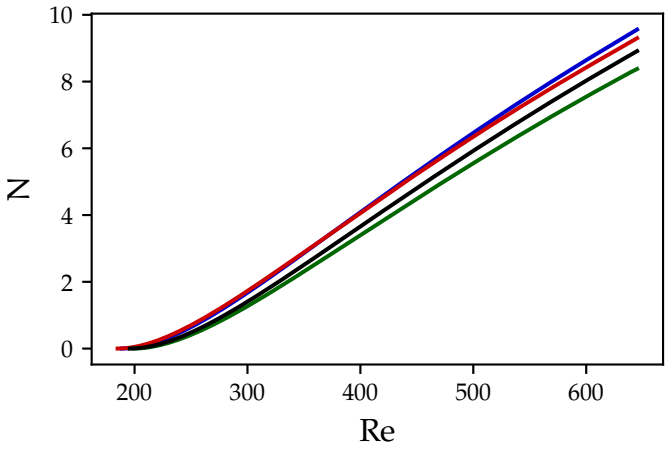

Figure 6.7: Linear N-factors computed with LHNS for the swept Hiemenz boundary layer with $\overline{Re} = 500$, $F = 0$ and $\beta = 0.4$ based on $\hat{u}$ (—), $\hat{v}$ (—), $\hat{w}$ (—) and E (—)

computations of Malik et al. (1994) and Janke and Balakumar (1999). This set of parameters yields very large N-factors past $Re = 500$, ranging between 6 to 10 as shown in Fig. 6.7. The near-parabolic character of NLPSE yields very stable computations even in such large N-factor regions exhibiting significant growth rates, whereas the fully elliptic NLHNS approach is rather likely to suffer from numerical stiffness to reach a converged state.

Parameters for current NLHNS computations are set as follows. The Fourier resolution in the spanwise direction includes $M = 8$ modes. In the wall-normal direction truncated at $y_\infty = 100$, a total of $n_y = 100$ discretisation points are used with $q_y = 8$ and a bilinear mapping set at $y_h = 2$. Malik et al. (1994) introduced the primary mode $(0, \pm 1)$ at $Re = 186$ with an initial amplitude $A^{u,w}_{rms} = 0.1\%$ where $A^{u,w}$ is defined as

$$A^{u,w} = \frac{1}{W_\infty} \max_y \left\{ \sqrt{\hat{u}^2 + \hat{w}^2} \right\}. \tag{6.5}$$

As in the previous verification cases, a Gaussian-shaped suction wall-forcing is enforced shortly after the inflow plane located at $Re = 50$. Its amplitude is set to match the required level of amplitude at $Re = 186$, while prior to this point non-linear interactions are deactivated. Sponge layers of sufficient streamwise extent have been set both at the inflow and at the outflow with $\sigma_{max} = 20$ given the large linear amplification reached in the weakly non-linear region. While NLPSE results are reported up to $Re = 650$, the NLHNS convergence has been reached only when the sponge layers started at $Re = 500$ in spite of numerous attempts to devise amplitude increments before reaching the target amplitude. The outflow plane is then located at $Re = 520$, where a radiation boundary condition is imposed for all modes. The streamwise domain is discretised with $n_x = 4{,}000$ and $q_x = 4$.

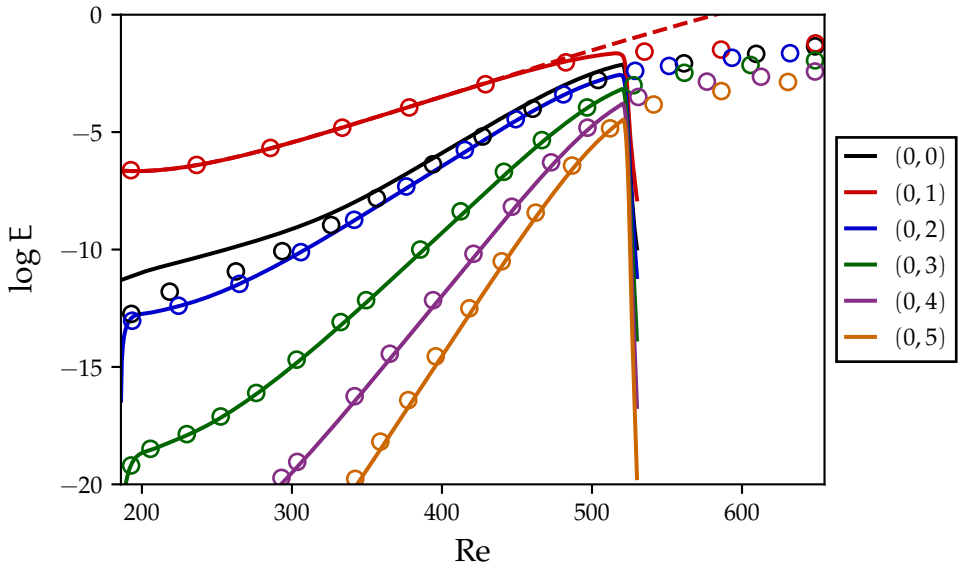

Figure 6.8: Levels of total disturbance energy E yielded by NLHNS for the MFD and the first harmonic modes for the swept Hiemenz case, $\overline{Re} = 500$, $F = 0$ and $\beta = 0.4$. Comparison with the NLPSE results of Malik, Li and Chang (1994) (○). The linear response of the primary mode is included (**--**).

The tolerance for harmonic convergence has been set to 10^{-6} while 48 global iterations were necessary. Two amplitude increments were used, starting at 50% of the target primary mode amplitude at $Re = 186$. The total disturbance energy E of the MFD, the primary mode and the first four subharmonic modes are presented in Fig. 6.8. As expected from the large linear amplification rates reached in Fig. 6.7, the harmonic modes undergo significant amplification across the streamwise domain. The NLHNS procedure had to be halted shortly before the saturation region where harmonics tend to plateau. In view of the linear response of the primary mode, only a tiny streamwise extent of the saturation has been computed before the sponge layers are activated. The difficulty of obtaining convergence is most likely due to the large N-factors reached in that region leading to a much larger $\|\hat{\mathbf{f}}^{res}\|$ than the norm of the left-hand side formed of the LHNS operator. Nonetheless, an excellent agreement with the NLPSE results of Malik et al. (1994) is obtained for all displayed subharmonic modes. The difference in MFD between NLHNS and NLPSE in the Re region from 186 to 350 lies in its alternative numerical treatment in the quasi-parabolic method.

The remarkable agreement on the primary mode is transcribed in the individual velocity amplitude functions presented in Fig. 6.9 in which solutions from the two NLPSE external investigations are indicated. Good agreement is also found in terms of the growth rate based on E for the primary mode, shown in Fig. 6.10 across the streamwise domain where convergence was reached with the current NLHNS approach. There is a slight gap near the initialisation region between the HNS

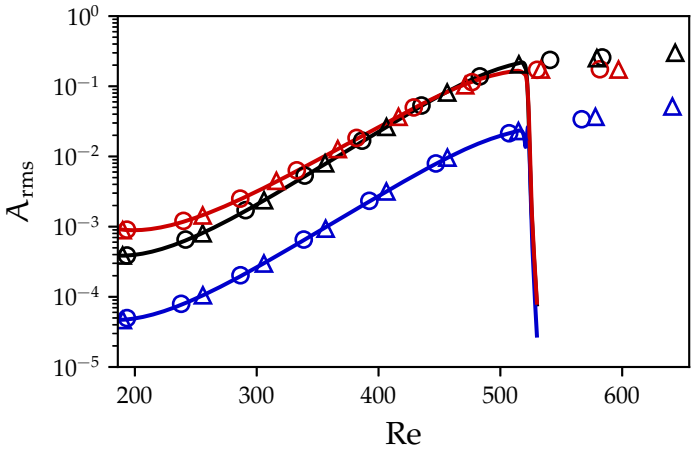

Figure 6.9: Amplitude functions of the primary mode for the NLHNS swept Hiemenz case with $\overline{Re} = 500$, $F = 0$ and $\beta = 0.4$: $\hat{u}$ (—), $\hat{v}$ (—) and $\hat{w}$ (—) compared with NLPSE results of Malik, Li and Chang (1994) (○) and Janke and Balakumar (1999) (△)

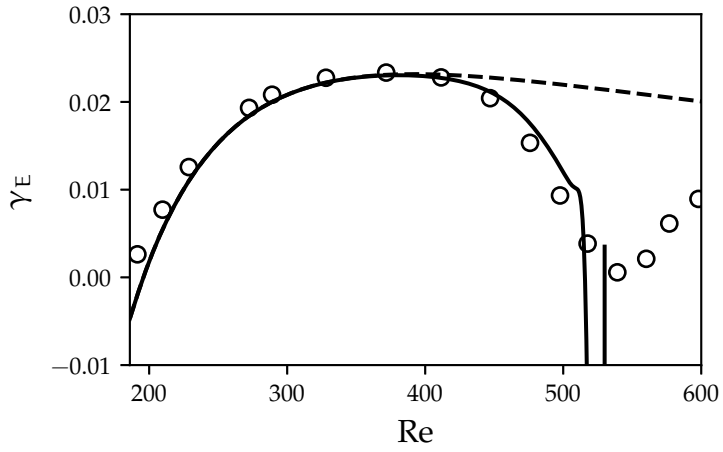

Figure 6.10: Growth rate of the primary mode based on disturbance energy resulting from NLHNS (—), from the NLPSE computations of Janke and Balakumar (1999) (○) and from LHNS (- -) for the swept Hiemenz case, $\overline{Re} = 500$, $F = 0$ and $\beta = 0.4$

methods and the NLPSE. Besides the upstream influence of the outflow sponge layer affecting γ_E, the linear growth behaviour is, overall, correctly computed by the NLHNS in a pure stationary CF configuration.

In light of these comparisons, the NLHNS methodology is deemed verified and validated. It may now be employed to investigate the weakly non-linear growth of boundary layer instabilities for more complex flows in presence of stationary roughness. Nevertheless, in view of the difficulty of stabilising the NLHNS procedure in the saturation or highly non-linear regimes, appropriate care should be taken in order to extend the computations as far downstream as possible.

6.2 Cylinder on a zero-pressure-gradient surface

The modelling capability of the NLHNS is first assessed with a 3D cylindrical roughness located on a zero-pressure-gradient surface on which a 2D boundary layer develops. The stationary distortion of the boundary layer field induced by the roughness is analysed before investigating its interaction with a travelling TS wave. The present case is motivated by the wind-tunnel experiments of de Paula et al. (2017), carried out on a zero-pressure-gradient section of the so-called XIS40MOD aerofoil model on which the 3D cylinder roughness was mounted. Hot-wire measurements enabled the authors to quantify the scattering of the incoming 2D TS waves into 3D TS waves and to confirm the cylindrical element is able to trigger a secondary instability of the fundamental type, or 'K-type' (Klebanoff, Tidstrom & Sargent, 1962).

6.2.1 Problem definition and base flow

The chord of the aerofoil model is $c = 0.6\,m$. It features a relatively large extent of zero pressure gradient and negligible surface curvature where measurements were performed. Its geometry in the chordwise direction is visible on Fig. 6.11, while the aerofoil is symmetrical and spanwise invariant. In the experimental study of de Paula et al. (2017), a cylinder with a diameter of 10 mm and of varying height was positioned at $x/c = 40\%$ where Re_{δ^*} matched the value of 950. The

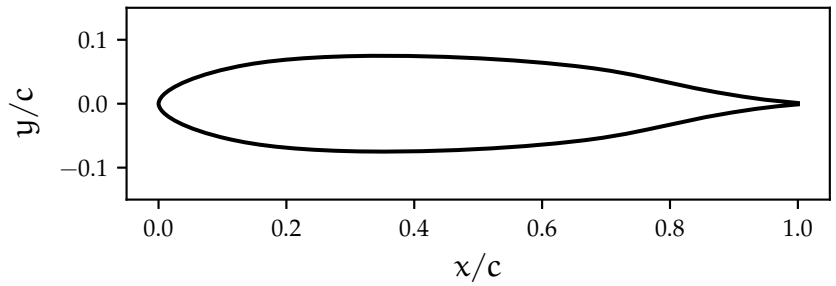

Figure 6.11: Geometry of the XIS40MOD aerofoil model

last streamwise station for data acquisition was located at $Re_{\delta^*} = 1{,}180$. Since the region of interest is characterised by a negligible surface curvature, the question arises whether a base flow based on a developing Blasius boundary layer or corresponding to the aerofoil geometry should be computed as an input to the NLHNS.

As there is no plausible way to determine which base flow reproduces *a priori* the features of the experiment accurately, such a choice may be orientated by the quantitative evolution of the TS growth rates past the location of the roughness

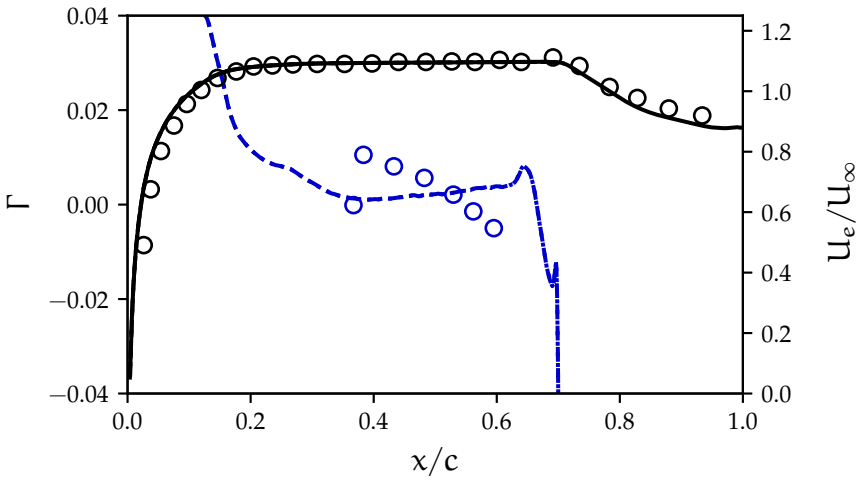

Figure 6.12: Base flow based on the XIS40MOD aerofoil with a −3.3° angle of attack: streamwise edge velocity yielded by the in-house solver (**--**), XFOIL (**—**), COCO (⋯) and experimental data of de Paula et al. (2017) (○); pressure gradient parameter from the base flow computed with the in-house solver (**--**), COCO (⋯) and experimental data (○)

when the latter is absent, measured experimentally by de Paula et al. (2017). To generate the base flow based on a Blasius boundary layer, the procedure described in Section 5.1.1 is repeated, specifying the free-stream Reynolds number $Re_\infty = 9.4 \times 10^5$, based on c and $U_\infty = 25\,m\,s^{-1}$. As for the base flow based on the aerofoil geometry, the XIS40MOD aerofoil coordinates are used to determine the pressure distribution along the geometry by means of the XFOIL software (Drela, 1989). Forced transition is tripped on upper and lower surfaces at $x/c = 70\%$ in order to prevent the appearance of LSBs near the trailing edge, which was also enforced in the experiment. The outstanding parameter is the angle of attack (AoA) of the aerofoil which should be set to match closely the TS growth rates with nominally zero roughness height in the experiment. Finally, the base flow is computed via an in-house, non-similar boundary-layer equations solver that is based on the Prandtl equations and uses the pressure coefficient distribution c_p as an input.

A first check for the validity of the aerofoil base flow can be found in Fig. 6.12, where the experimental edge velocity distribution and pressure gradient parameter,

$$\Gamma = \frac{\theta^2}{\nu_e}\frac{dU_e}{dx} \tag{6.6}$$

are compared against the corresponding numerical base flow in the case of a −3.3° angle of attack. In Eq. (6.6) θ denotes the local boundary-layer momentum thickness. First, there is a perfect agreement between the numerical edge velocity distributions along the streamwise direction. For verification purposes, the COCO programme (Schrauf, 1998) was also solicited to compute the base flow. An

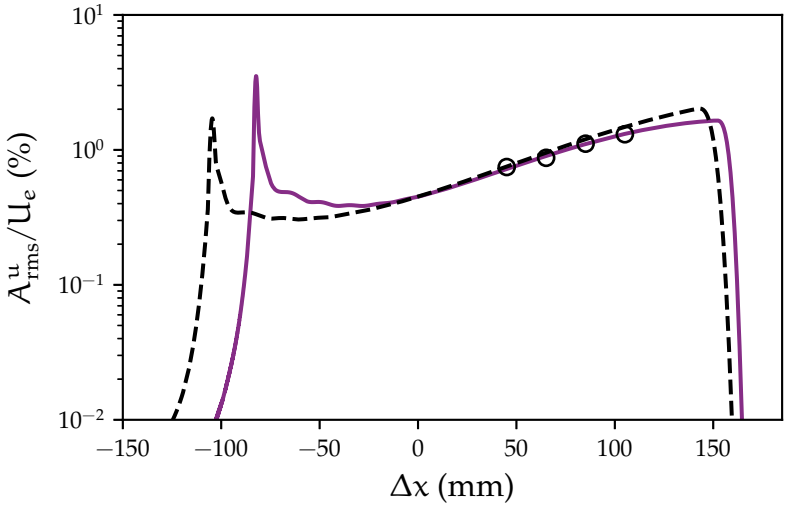

Figure 6.13: TS amplitude computed with LHNS as a function of the distance from the roughness location Δx, with $F = 90$ and $A_0 = 0.45\%$. Base flow based on the XIS40MOD geometry with AoA $= -3.3°$ (—) and based on a developing Blasius boundary layer (- -), compared with experiments of de Paula et al. (2017) (○).

excellent agreement with experiments is reached in the region of interest, that is between 40% and 60%, where the edge velocity remains almost constant. This is confirmed by the pressure gradient parameter Γ which is numerically close to zero in the same region and falls within the interval defined by the experimentally measured data. Therefore, the assumption of a zero-pressure-gradient region justifying the potential use of a Blasius boundary layer is acceptable. Once again a perfect agreement for Γ is found between the in-house boundary-layer solver and COCO on the whole domain.

In the experiment, de Paula et al. (2017) selected two TS wave frequencies, namely $F = 90$ and $F = 120$ and two levels of amplitude at the roughness location, namely $A_0 = 0.45\%$ and $A_0 = 0.75\%$. To assess whether the NLHNS method applied on the base flows is likely to replicate appropriately the characteristics of the experiments, LHNS computations are undertaken to compute the TS evolution downstream of the roughness location, in the case where no roughness is present. For that purpose, a synthetic unsteady wall-forcing is generated upstream to generate the TS instability. Due to the linearity, it is possible to apply a multiplicative constant to match the required level of amplitude at the roughness location $x/c \approx 40\%$. Fig. 6.13 illustrates the application of such method. Since the aerofoil curvature is negligible in the region of measurements, the curvature terms of the HNS equations are deactivated and computations are undertaken in the framework of Cartesian coordinates. The base flow relying on a Blasius profile seems to slightly overestimate the experimentally measured TS amplitude whereas fine

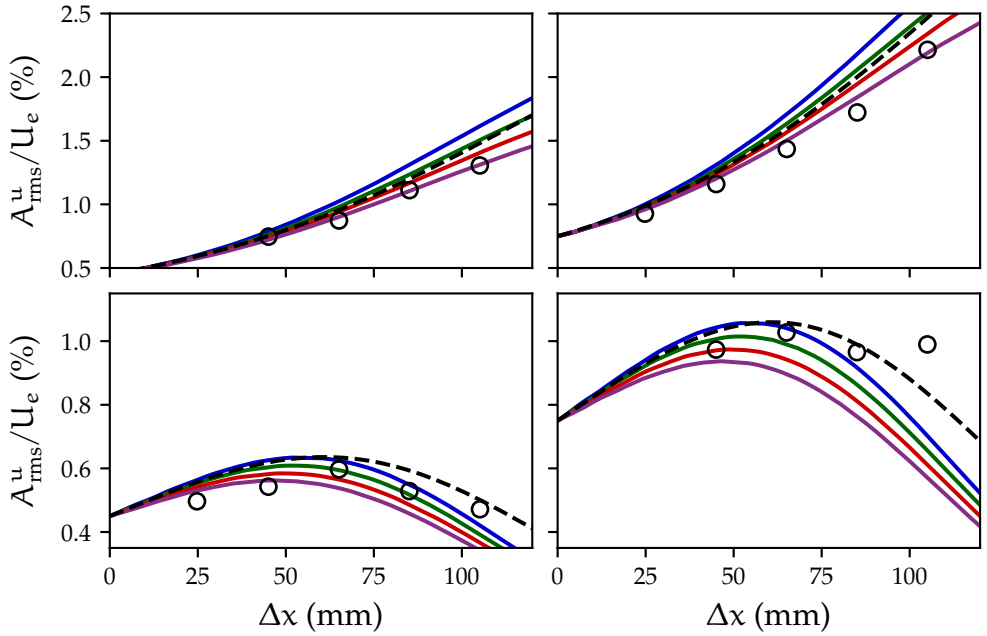

Figure 6.14: TS amplitude computed with LHNS as a function of the distance from the roughness location Δx. *Top*, $F = 90$; *bottom*, $F = 120$; *left*, $A_0 = 0.45\%$; *right*, $A_0 = 0.75\%$. Base flow based on the XIS40MOD geometry with AoA $= -3.0°$ (—), $-3.1°$ (—), $-3.2°$ (—), $-3.3°$ (—) and based on the Blasius profile (- -). Comparison with the experimental data of de Paula et al. (2017) (○).

agreement is observed with the base flow computed on the XIS40MOD geometry with AoA $= -3.3°$.

Such AoA value has been retained after varying the parameter by steps of 0.1°. Figure 6.14 shows a magnified view of the measurement region and overviews the four frequency and amplitude cases, comparing the Blasius-based and aerofoil-based flows. The LHNS results indicate that the $F = 90$ is linearly unstable whereas $F = 120$ is linearly stable. With respect to the secondary instability behaviour, de Paula et al. (2017) report that $A_0 = 0.75\%$ is unstable regardless of the frequency. In contrast, the $F = 90$ and $A_0 = 0.45\%$ case is a weakly unstable case whereas the $F = 120$ and $A_0 = 0.75\%$ scenario is stable. Particular attention is then drawn to the $F = 90$ case, more prone to secondary instability in this context. Overall, the variation of the angle of attack substantially affects the amplification rates past $\Delta x > 0$, where Δx measures the distance from the location of the roughness. The Blasius base flow yields amplitude levels similarly encountered in the XIS40MOD base flow for $F = 90$ whereas a greater difference can be noted for the higher frequency value. The base flow distinction for the $F = 120$ frequency case seems rather inconclusive, while for $F = 90$ the base flow with AoA $= -3.3°$ yields excellent agreement with the experimentally measured amplitudes for $A_0 = 0.45\%$ and the best agreement among the others when $A_0 = 0.75\%$. An even better agreement with the growth rates could be expected if the c_p distribution was

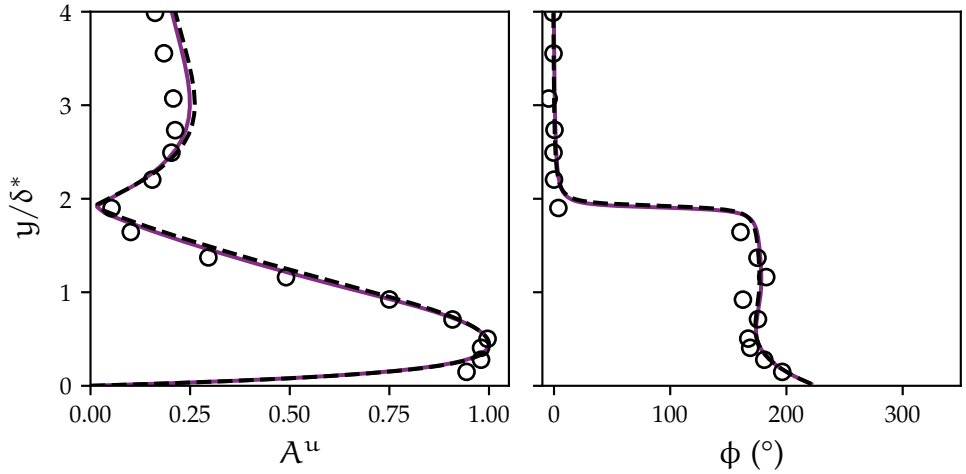

Figure 6.15: Normalised amplitude (*left*) and phase (*right*) of the TS wave at the roughness location when $F = 120$ computed via LHNS with the Blasius base flow (**--**) and the AoA $= -3.3°$ base flow (**—**). Comparison with experimental data of de Paula, Wurz and Medeiros (2008) (○).

adjusted to match the experimental edge velocity in Fig. 6.12 near the leading edge region.

A further concern raised by de Paula, Wurz and Medeiros (2008) is to establish the two-dimensionality of the generated TS wave to ensure the only source of three-dimensionality is due to the placement of the cylindrical roughness. The authors ascertained the TS wave was fundamentally 2D by measuring its characteristics across the spanwise direction and noted these remained almost constant. They also compared the steady mean flow profiles against a Blasius profile. Figure 6.15 precisely compares the experimental profile measured at the roughness location with a nominally zero roughness height, against LHNS theory for both Blasius and aerofoil base flows and $F = 120$. In essence, the TS profile generated on the aerofoil base flow both qualitatively and quantitatively matches the corresponding profile obtained using the 2D Blasius boundary layer. This is evident from the wall-normal evolution of either the amplitude or the phase. Moreover, these agree remarkably well with experimental data. It further reinforces the legitimacy of the base flow based on the XIS40MOD geometry, which consistently reproduces the TS growth behaviour presented in Fig. 6.14. With respect to the TS amplitude profile, the latter flow seems slightly closer to experimental data than its Blasius counterpart. de Paula et al. (2017) report that the experimentally measured displacement thickness at the roughness location is $\delta^*_h = 0.55\,\text{mm}$. The theoretically computed value with the XIS40MOD base flow with AoA $= -3.3°$ is $\delta^*_h = 0.5548\,\text{mm}$, matching closely the value.

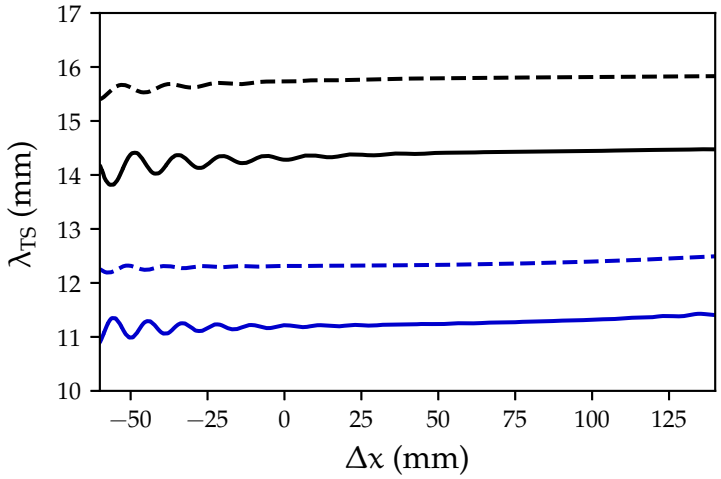

Figure 6.16: Wavelength of the TS wave near the roughness location and further downstream, computed with LHNS for F = 90 (—) and F = 120 (—) for the AoA = −3.3° base flow, and for the corresponding Blasius base flow, respectively (--) and (--)

As previously mentioned, the diameter of the cylindrical element used in the experiment was 10 mm. This is lower than the TS wavelength at the roughness location shown in Fig. 6.16. Hence, the TS wave propagation and its characteristics may not be impacted by the streamwise extent of the cylinder. Its scattering by the cylinder, however, is likely to be impacted since the roughness was designed to act as a pulse of steady spanwise modes, which makes the streamwise extent less detrimental than the spanwise extent regarding secondary instability (Medeiros, personal communication, September 2020).

6.2.2 Modelling the cylindrical roughness

In the 2.5D NLHNS approach, a Fourier expansion of the flow perturbation is employed in the spanwise direction. Therefore, a 3D, steady roughness element $h(x,z)$ should also be treated accordingly. Decomposing such function into its Fourier series reads

$$h(x,z) = \sum_{m=-\infty}^{m=+\infty} \hat{h}_m(x) e^{2\pi i m z/L_z} \approx \sum_{m=-M}^{m=+M} \hat{h}_m(x) e^{i m \beta z} \tag{6.7}$$

assuming a period of $L_z = 2\pi/\beta$ and a truncated summation over M positive spanwise harmonics. The expression of the m-th Fourier coefficient $\hat{h}_m(x)$ is determined via

$$\hat{h}_m(x) = \frac{1}{L}\int_L h(x,z) e^{-2\pi i m z/L_z}\, dz = \frac{\beta}{2\pi}\int_{-L/2}^{L/2} h(x,z) e^{-i m \beta z}\, dz \tag{6.8}$$

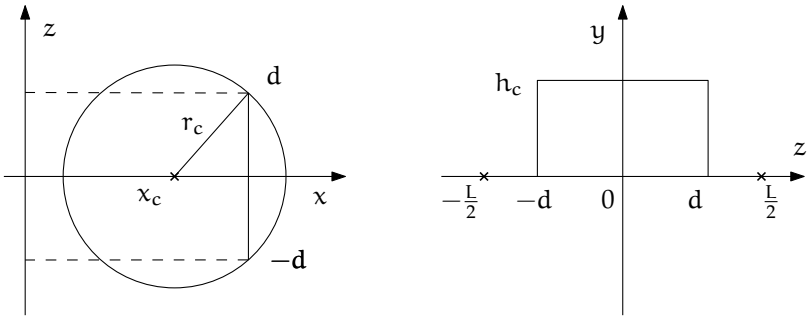

Figure 6.17: Geometrical characteristics of the cylindrical roughness element seen in the (x, z) plane (*left*) and in the (y, z) plane (*right*)

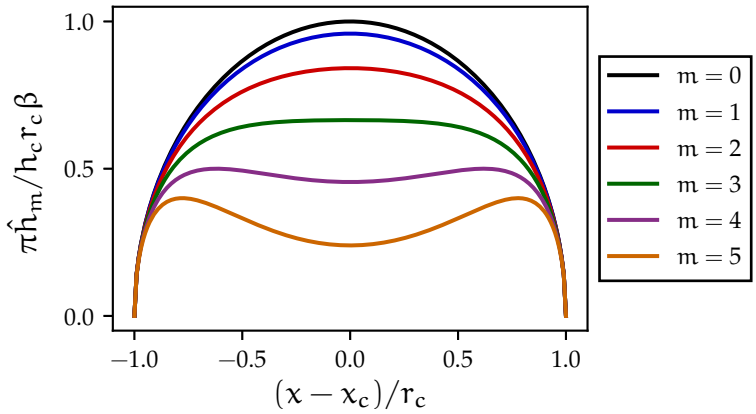

Figure 6.18: First Fourier coefficients of the cylindrical roughness

which is seen by most harmonic modes during the NLHNS procedure following the no-slip conditions in Eqs. (3.61) and (3.62). Consider the case of a cylindrical roughness element located at $x = x_c$ with radius r_c and height $h_c = O(\varepsilon)$ described in Fig. 6.17. It can be seen that in the (z, y) plane the function describing the spanwise shape of the cylinder is a rectangular function of width $d(x) = \sqrt{r^2 - (x - x_c)^2}$. In that case, the support of the integrand in Eq. (6.8) is $[-d(x), d(x)]$ and the Fourier coefficients reduce to

$$\hat{h}_m(x) = \begin{cases} \dfrac{\beta d(x)}{\pi} & \text{if } m = 0 \\ \dfrac{\sin(m\beta d(x))}{m\pi} & \text{if } m \neq 0. \end{cases} \tag{6.9}$$

Figure 6.18 depicts the first harmonic modes describing the cylindrical element in the physical streamwise direction and in the Fourier space associated to the spanwise direction.

6.2.3 Stationary distortion

As a first step, the stationary distortion of the boundary layer induced by the cylinder is computed. With a constant radius of $\lambda = 5\,\text{mm}$, the cylindrical roughness centre is placed at $s/c \approx 0.397$ where $\text{Re}_{\delta^*} = 950$. Its height h is gradually increased during the NLHNS procedure, starting with $h/\delta^*_h = 10\%$. The pre-defined tolerance of the procedure is 10^{-6}.

Since only the stationary boundary-layer distortion is of interest, the frequency is $F = 0$ and $N = 0$. The cylinder is reconstructed with $M = 10$ harmonics in the spanwise direction. The amplitude of the first ten modes is not affected for greater values of M such as 30 or 50. Furthermore, the choice of the spanwise wavenumber consists of a trade-off between capturing short scales or rather longer scales. Based on the radius of the cylinder and the disturbance spectra of the experiments described by de Paula et al. (2017), the fundamental spanwise wavenumber is set to $\beta^* = 125.66\,\text{m}^{-1}$ which allows spanning a domain of $L_z = 10\lambda$. The corresponding non-dimensional value, scaled with δ^*_h is $\beta = 0.07$.

In the streamwise direction, the computational grid is characterised by $n_x = 4{,}500$ and $q_x = 4$, discretising the domain extending from $s/c = 0.31$ to $s/c = 0.65$. The grid is clustered near the centre of the cylinder using the tangential-based mapping defined in Eq. (4.10) with $\gamma = 0.30$. For all stationary harmonics, sponge regions are devised from $s/c = 0.62$ with $\sigma_{max} = 10$. At the outflow boundary, a radiation boundary condition is imposed. The discretised grid in the wall-normal direction is formed of $n_y = 100$ with $q_y = 8$, and the free-stream truncation is set at $y_\infty = 100$. The used bilinear mapping is defined with $y_h = 1.5$.

In what follows, the streamwise evolution of disturbances is presented in terms of the dimensional distance measured from the centre of the cylinder, Δx. Despite setting an under-relaxation parameter $\tau = 0.5$, the NLHNS method diverges once the cylinder height is greater than 22% of the local displacement thickness. Results are therefore only reported for a h/δ^*_h ratio of 10%, 15% and 20%.

Figures 6.19 and 6.20 show the amplitude evolution of stationary modes past the cylinder location at $\Delta x = 0$ respectively for $h/\delta^*_h = 10\%$ and 20%. Both cylinder heights yield a weak MFD relative to the amplitude level of the fundamental and higher harmonics. The MFD amplitude is reduced along the streamwise domain. The sudden jump near the outflow of the domain may well be attributed to the presence of the sponge region. Two opposite effects are competing, namely the damping due to the sponge region and the other harmonics contributing to the growth of the MFD. Since the considered streamwise domain corresponds to a

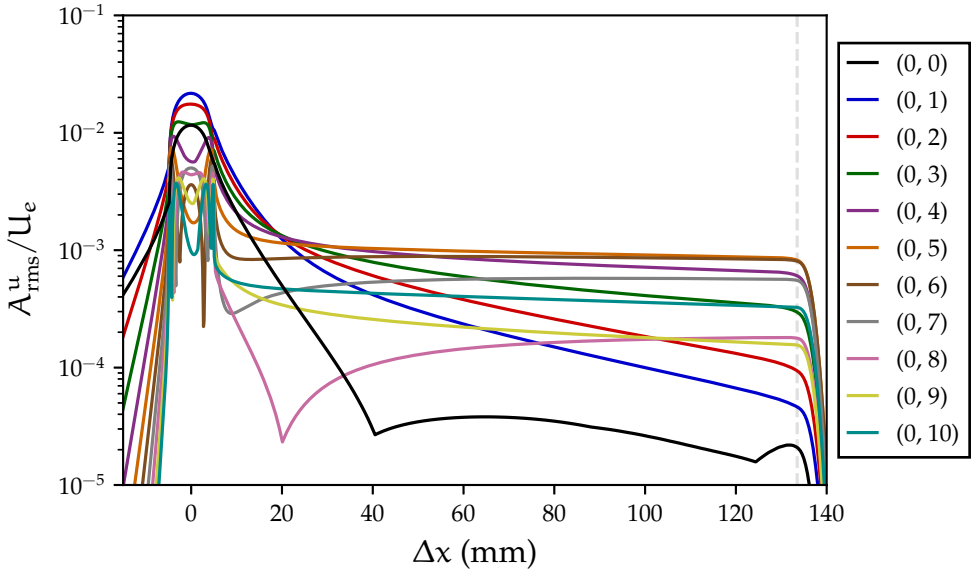

Figure 6.19: Harmonic amplitude based on $\hat{u}$. The sponge region interface is indicated (- -). XIS40MOD aerofoil flow case, stationary distortion with $\beta = 0.07$ and $h/\delta^*_h = 10\%$.

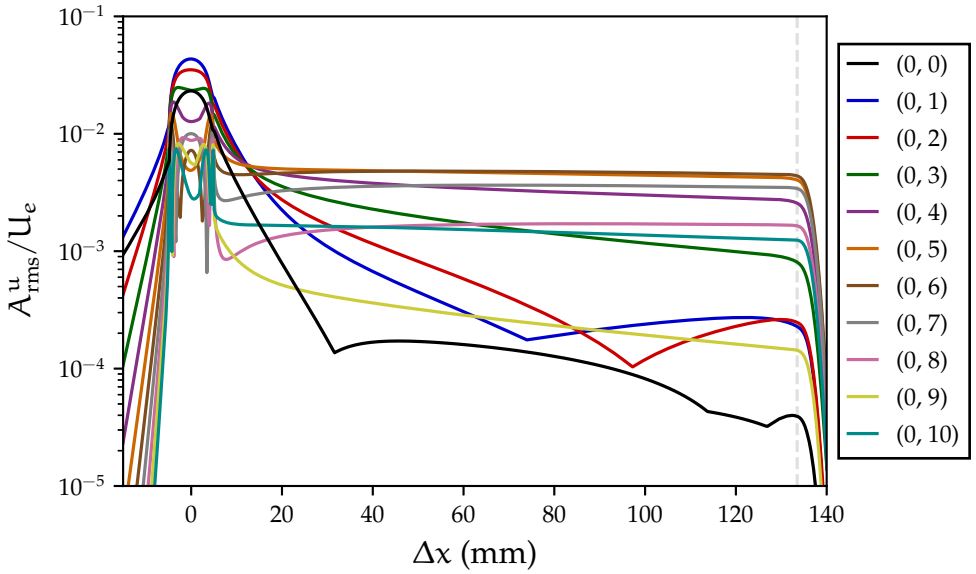

Figure 6.20: Harmonic amplitude based on $\hat{u}$. The sponge region interface is indicated (- -). XIS40MOD aerofoil flow case, stationary distortion with $\beta = 0.07$ and $h/\delta^*_h = 20\%$.

region with negligible curvature and hence near-zero pressure gradient, the flow is close to a developing Blasius boundary layer, thus stationary waves are naturally not amplified. The cylinder creates a pulse of spanwise modes whose amplitude indeed decays downstream. However, at any fixed streamwise position and for both cylinder heights, the amplitude level increases from $(0,1)$ to $(0,5)$ except for the cylinder with $h/\delta^*_h = 20\%$ past $\Delta x = 80\,\text{mm}$. The higher harmonics involving the $(0,6)$ mode to the $(0,10)$ mode see a decrease in their amplitude level.

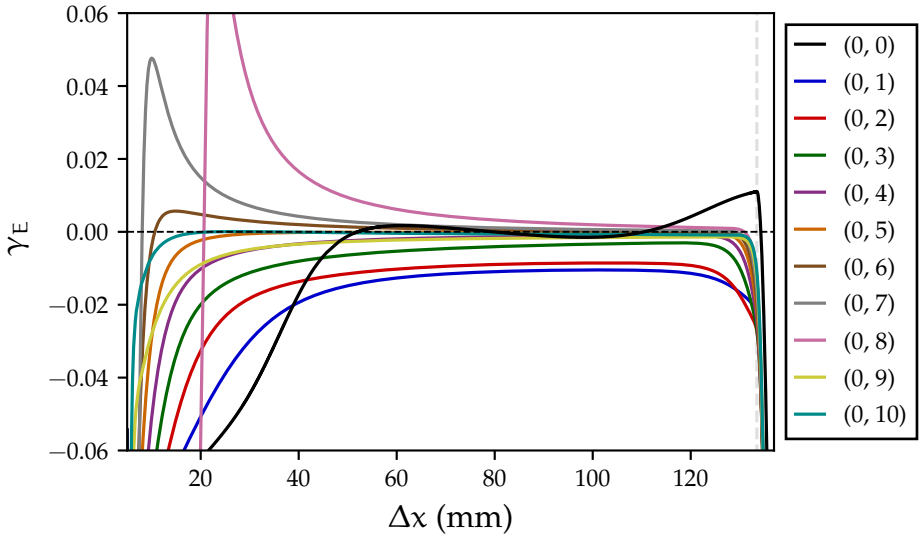

Figure 6.21: Growth rate based on total disturbance energy of the stationary modes for $h/\delta^*_h = 10\%$. The sponge region interface is indicated ( ). XIS40MOD aerofoil flow case with $\beta = 0.07$.

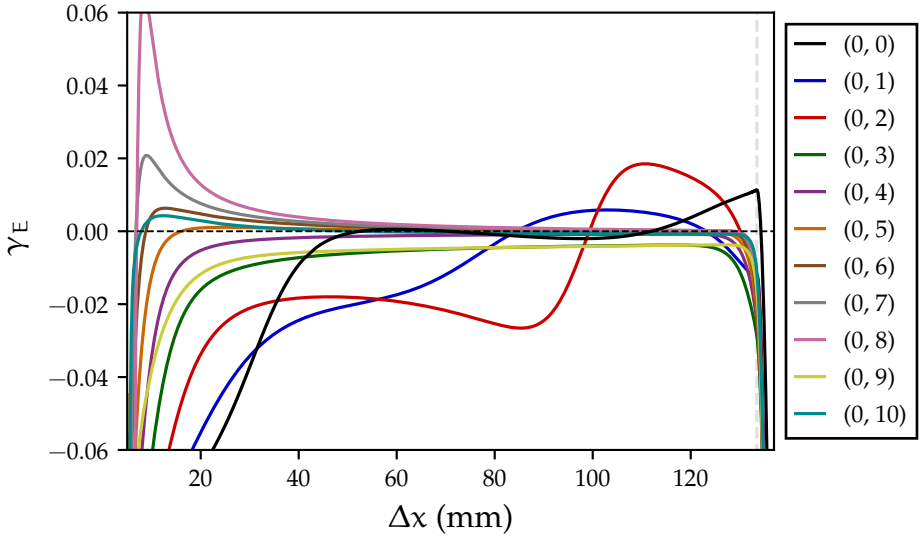

Figure 6.22: Growth rate based on total disturbance energy of the stationary modes for $h/\delta^*_h = 20\%$. The sponge region interface is indicated ( ). XIS40MOD aerofoil flow case with $\beta = 0.07$.

Overall, most harmonics tend to behave in a stable fashion for the cylinder of height $h/\delta^*_h = 10\%$. There is an exception for the $(0,6)$, $(0,7)$ and $(0,8)$ modes which are mildly amplified downstream of the cylinder. Similar features can be seen with the higher cylinder in Fig. 6.20. Nonetheless, the $(0,6)$ mode seems very close to neutral stability. There is furthermore a notable change of slope for the primary mode and the $(0,2)$ mode, which become amplified approximately after a distance of 7 to 8 cylinder diameter lengths.

Such observations are confirmed by visualising the growth rates based on E that are presented in Figs. 6.21 and 6.22. Their value stabilises downstream of $\Delta x = 20\,\text{mm}$ after the amplification due to the cylindrical roughness. Consistently with harmonic amplitudes, a majority of modes have a growth rate close to zero demonstrating near-neutral stability regardless of the cylinder height.

As the relative height increases from 10% to 20%, the primary mode becomes slightly amplified as well as the $(0, 2)$ mode with an even larger growth rate. The evolution of the MFD is similar for both heights. It shall be highlighted that the stationary distortion information with $h/\delta^*_h = 15\%$ has also been computed. However, no significant differences in qualitative harmonic behaviour have been found compared to the presented cases. Hence, the latter case is not presented when displaying mode amplitudes and growth rates.

The steady distortion induced by the cylinder can be observed in the (y, z) plane in Fig. 6.23, in which the streamwise perturbation velocity $\tilde{u}$ is plotted at the first streamwise station covered by the experiments of de Paula et al. (2017), corresponding to $\Delta x = 25\,\text{mm}$ after the cylinder. These slices correspond to one wavelength L_z in the spanwise direction.

Naturally, the streamwise velocity deficit downstream of the cylinder increases with its height and extends over two times the displacement thickness in the wall-normal direction. Fig. 6.23 also indicates levels of streamwise vorticity distortion defined as

$$\nabla \times \tilde{u}|_x = \frac{\partial \tilde{w}}{\partial y} - \frac{\partial \tilde{v}}{\partial z}. \tag{6.10}$$

Relatively to the benign $h/\delta^*_h = 10\%$ case, there are vorticity regions of similar intensity extending near one displacement thickness for $h/\delta^*_h = 15\%$. The cylinder with $h/\delta^*_h = 20\%$ features even greater streamwise vorticity levels near the wall on both sides of the roughness. It has been observed that downstream of $\Delta x = 25\,\text{mm}$, the perturbation velocity distribution remains fairly constant while the observed vorticity levels vanish rapidly past $\Delta x = 45\,\text{mm}$. Unquestionably, the velocity distortion due to the cylinder is weak in magnitude; for $h/\delta^*_h = 20\%$, it reaches only 2% of the base streamwise flow.

These first stability results involve the sole impact of the stationary cylinder on the boundary layer. They show that there is no significant instability due to the cylinder alone, even with a height of $h/\delta^*_h = 20\%$ for which non-linear effects are likely to dominate with pre-existing disturbances of sufficient amplitude. Current stationary computations provide a first insight and comparative basis with respect

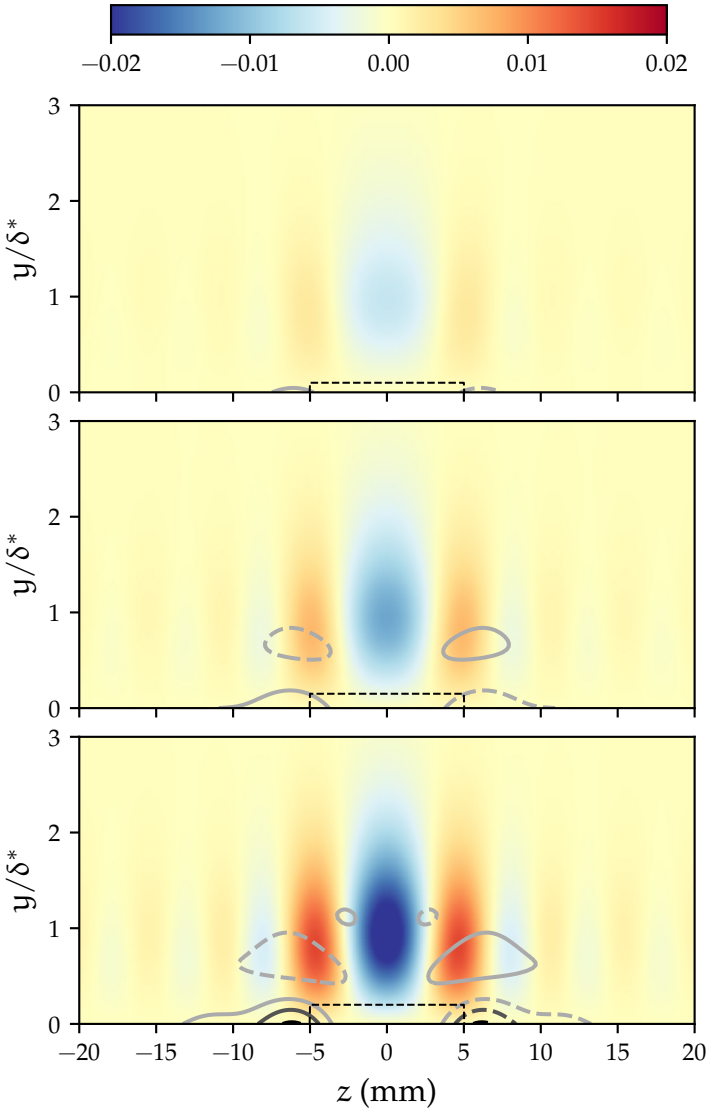

Figure 6.23: Contours of streamwise perturbation velocity $\tilde{u}$ in the (y, z) plane at $\Delta x = 25\,\text{mm}$ for $h/\delta^*_h = 10\%$ (*top*), 15% (*centre*) and 20% (*bottom*) viewed from upstream. Streamwise vorticity levels are described by contour lines: 1.5×10^{-3}, 3×10^{-3} and 4.5×10^{-3}. Dashed lines indicate negative values. The shape of the cylinder is indicated (**--**).

to the interaction of the cylinder with an incoming TS wave, which is discussed next.

6.2.4 Interaction with a Tollmien-Schlichting wave

The focus is now set on the interaction between the stationary cylindrical roughness and a TS wave generated upstream on the XIS40MOD aerofoil geometry. In the experimental investigation of de Paula et al. (2017), the 2D TS disturbances were generated by a slit at $s/c = 0.25$ or equivalently at $\text{Re}_{\delta^*} = 700$. This certainly generated a whole wave packet of travelling modes. The authors were able to

monitor the RMS amplitude of the TS wave at the roughness position A_0. For the current NLHNS computations, only the $(1,0)$ mode is initialised upstream as a first understanding stage, since sufficient information on the initial disturbance spectrum was not available to ensure an equal input with the experimental harmonic forcing scenario. In the preliminary NLPSE simulations conducted by de Paula et al. (2017), they reported initialising a 2D wave with a pair of oblique modes of the same frequency as the fundamental. It is nonetheless anticipated that some experimental features of the TS/cylinder interaction are recovered by the current approach by initialising only the fundamental travelling mode. The higher travelling harmonics are then triggered as the $(1,0)$ wave passes over the cylinder.

Compared to the stationary distortion computations in Section 6.2.3, the streamwise domain is extended to accommodate the initialisation of the TS wave. It covers the region between $s/c = 0.18$ and $s/c = 0.62$ while the PML and the sponge region are activated at $s/c = 0.59$. This means that the computational domain of interest, within which meaningful physical features can be extracted, extends until $\Delta x \approx 110\,\text{mm}$ downstream of the cylinder. The target reflection coefficient of the PML is set at $R_c = 10^{-4}$ and the grid compression factor is $\kappa_{max} = 7$.

The larger domain requires a greater number of grid points to ensure mesh convergence, and it is thus set at $n_x = 5{,}000$. For the deployment of the NLHNS, the Fourier series are truncated at $N = 4$ temporal harmonics and $M = 8$ spanwise harmonics. The same three cylinder heights as in the previous subsection are considered: 10%, 15% and 20%. In the last two cases, the under-relaxation coefficient has been set to 0.6 and 0.5 to improve the convergence behaviour. The other parameters remain the same otherwise.

The streamwise evolution of mode amplitudes based on $\hat{u}$ for $h/\delta^*_h = 10\%$ and 20% is presented in Figs. 6.24 and 6.25, respectively. The initial amplitude at the cylinder location is $A_0 = 0.75\%$. Due to the spanwise symmetry of the present configuration, only the modes with $m \geqslant 0$ are displayed. Compared to the stationary distortion where the TS wave was absent, the stationary modes with $n = 0$ directly triggered by the roughness are all unstable downstream of $\Delta x = 0$. The travelling modes have undergone significant amplification at the roughness location, and follow qualitatively the same evolution. In average, their amplitude is reduced by roughly one order of magnitude as the multiple n of the temporal wavenumber is incremented by one from 1 to 4. The presence of the TS wave and the contributions from a greater number of modes also alter the level of MFD. Its amplitude steadily increases along the streamwise direction and has grown by a factor of 10 compared to the NLHNS simulations without a pre-existing TS

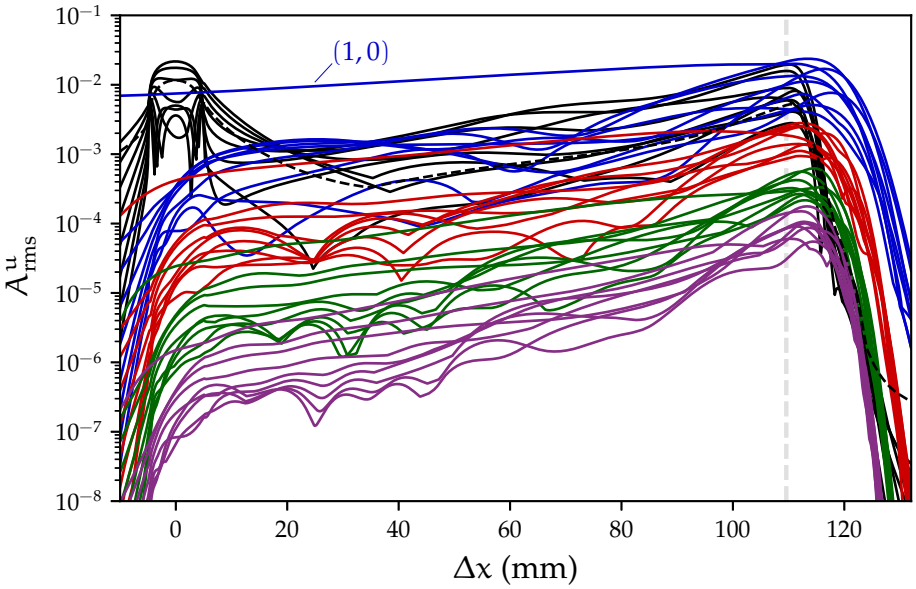

Figure 6.24: Amplitude evolution of the MFD (**--**) and all other modes (n, m) based on $\hat{u}$ for $A_0 = 0.75\%$ and $h/\delta^*_h = 10\%$. These are grouped in terms of $n = 0$ (**—**), $n = 1$ (**—**), $n = 2$ (**—**), $n = 3$ (**—**) and $n = 4$ (**—**). The absorbing region interface is indicated (**--**).

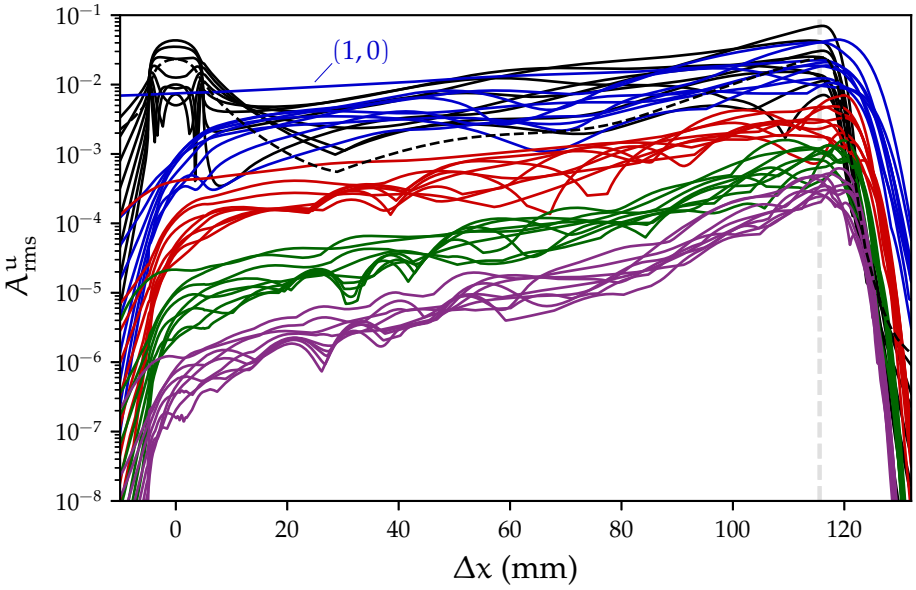

Figure 6.25: Amplitude evolution of the MFD (**--**) and all other modes (n, m) based on $\hat{u}$ for $A_0 = 0.75\%$ and $h/\delta^*_h = 20\%$. These are grouped in terms of $n = 0$ (**—**), $n = 1$ (**—**), $n = 2$ (**—**), $n = 3$ (**—**) and $n = 4$ (**—**). The absorbing region interface is indicated (**--**).

wave. The efficiency of the absorbing layers is evident for all modes, including the MFD and should be highlighted. Both the PML and sponge layer offer smooth and gradual decay from the domain interface to the outflow, where energy levels drop by several orders of magnitude.

Furthermore, there is no significant difference in harmonic evolution between the 10% and 20% height cases. For the latter case, a few stationary modes and

travelling modes of the fundamental wavenumber reach the level of the $(1,0)$ mode at a more upstream location. There is also a lesser dispersion of the amplitude level within groups of equal travelling wavenumber modes. Overall, the response of the boundary layer to the cylinder and the TS wave seems to remain linear until the last physically relevant streamwise station situated at $\Delta x \approx 110\,\text{mm}$. Current computations have been tailored to match the streamwise domain covered by the experiments; a natural objective is to push the NLHNS procedure until the end of the zero-pressure-gradient region.

Figure 6.26 breaks down the visualisation of the MFD and the three higher stationary modes across the region behind the cylinder. For a nominally zero cylinder height, only the MFD remains within the same orders of magnitude as the cases where the cylinder height increases, since it is the only source of spanwise excitation. The amplitude of modes $(0,1)$, $(0,2)$ and $(0,3)$ with zero roughness is indeed not visible and negligible in comparison to other cases. The amplification of the stationary modes may clearly be attributed to the TS wave interacting with the cylinder and generating oblique modes through non-linear mechanisms. In the $A_0 = 0.45\%$ case, the difference in MFD induced by the cylinder of height $h/\delta^*_h = 10\%$ is barely perceptible, indicating the absence of a weakly non-linear regime in the investigated region. No significant disparity should be noted between the two different initial amplitudes, except for the $(0,2)$ mode whose amplification is shifted more upstream with $A_0 = 0.75\%$. It also undergoes a steep growth rate change near $\Delta x \approx 100\,\text{mm}$.

As previously discussed in Section 3.2.3, the MFD is the sole mode impacting the integral quantities of the boundary layer and allows to compare the averaged transitional boundary layer and the laminar boundary layer represented by the base flow. Transition to turbulence is usually marked by a steep rise in the skin-friction coefficient c_f and by a sharp decrease of the shape factor H. The laminar and transitional streamwise skin-friction coefficients are respectively defined as

$$c_{f,\text{lam}} = \frac{\mu_e}{\frac{1}{2}\rho_e U_e^2} \left.\frac{\partial \bar{u}}{\partial y}\right|_w, \qquad c_{f,\text{tr}} = \frac{\mu_e}{\frac{1}{2}\rho_e U_e^2} \left.\frac{\partial (\bar{u} + \hat{u}_{00})}{\partial y}\right|_w \tag{6.11}$$

while the shape factor reads

$$H = \frac{\delta^*}{\theta} \tag{6.12}$$

where the momentum thickness θ is defined as

$$\theta = \int_0^{+\infty} \frac{u}{U_e}\left(1 - \frac{u}{U_e}\right)\,dy. \tag{6.13}$$

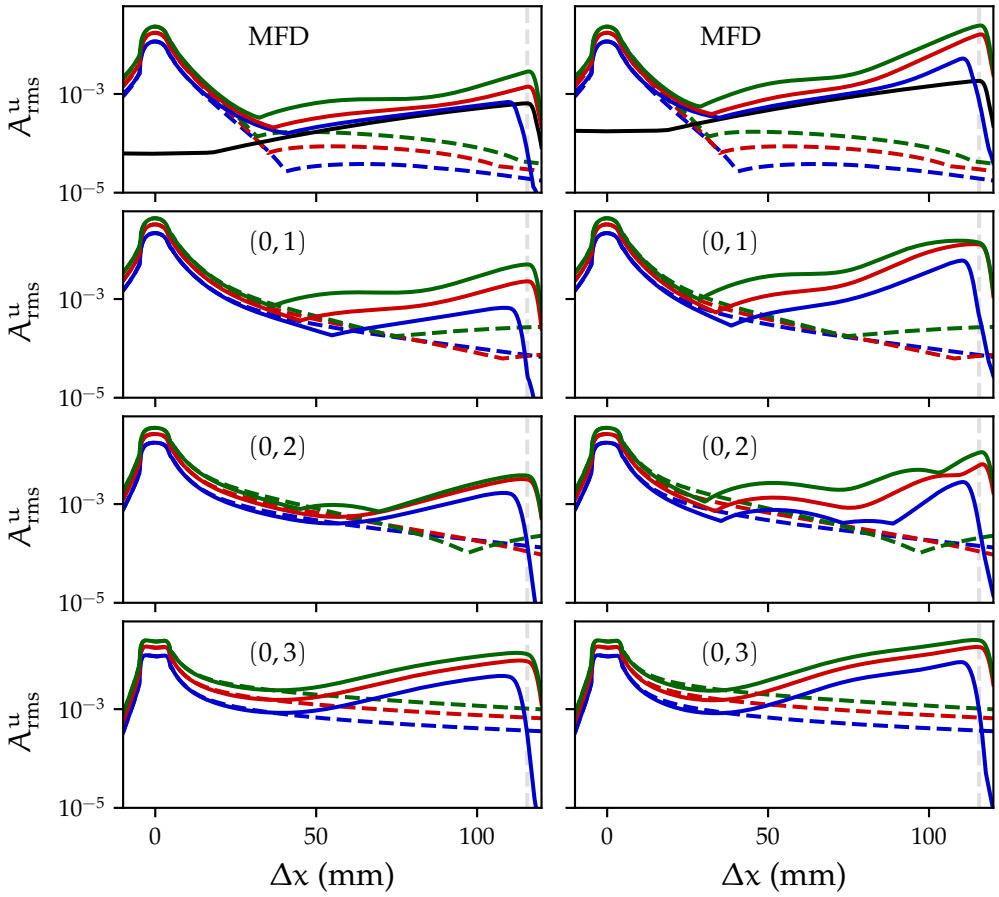

Figure 6.26: Amplitude based on $\hat{u}$ for the first four stationary modes. The initial TS amplitude at the cylinder location is 0.45% (*left*) and 0.75% (*right*). Comparison between $h/\delta^*_h = 0\%$ (—), 10% (—), 15% (—) and 20% (—). Dashed lines correspond to the stationary distortion without the incoming TS wave.

These quantities are plotted in Fig. 6.27 for the various initial amplitude and cylinder height cases. Only the streamwise extent with the most palpable differences between laminar and transitional boundary layers is displayed. Those differences are clearly larger when $A_0 = 0.75\%$ whereas regardless of the cylinder height, the values corresponding to $A_0 = 0.45\%$ lie relatively close to the laminar case. As expected, the increase of skin-friction coefficient and decrease of shape factor relate to the cylinder height. However, even at the last streamwise station before absorbing layers, the current NLHNS results indicate the boundary layer is not close to transition with respect to secondary instability. The analysed base flow in the zero-pressure-gradient region closely resembles that of a developing Blasius boundary layer, for which the value of H in a transitional region typically ranges from 1.3 to 1.4 (Schlichting & Gersten, 2017). Hein (2005) reported by means of NLPSE a noticeable skin-friction variation of $O(1)$ drag counts, or $O(10^{-4}c_f)$, when investigating a TS/CF interaction scenario. In the present case, the skin-friction

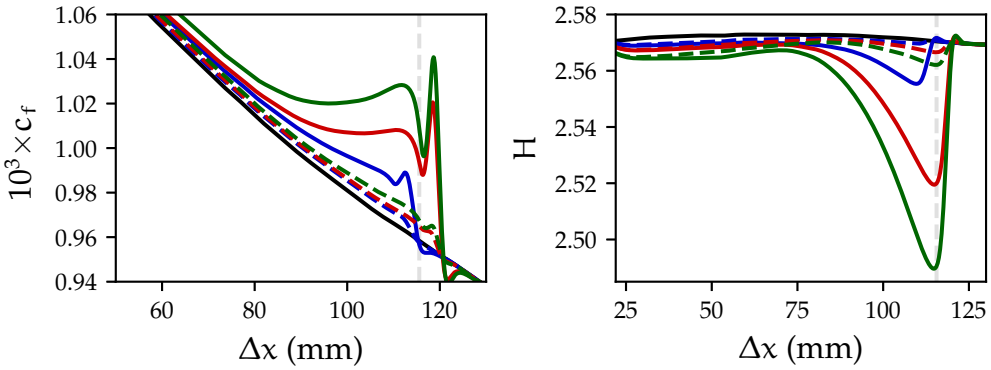

Figure 6.27: Streamwise skin-friction coefficient (*left*) and shape factor (*right*) downstream of the cylinder location. The laminar boundary layer (—) is compared to the transitional boundary layer with $h/\delta^*_h = 10\%$ (—), $h/\delta^*_h = 15\%$ (—) and $h/\delta^*_h = 20\%$ (—). Dashed and plain lines respectively correspond to $A_0 = 0.45\%$ and $A_0 = 0.75\%$.

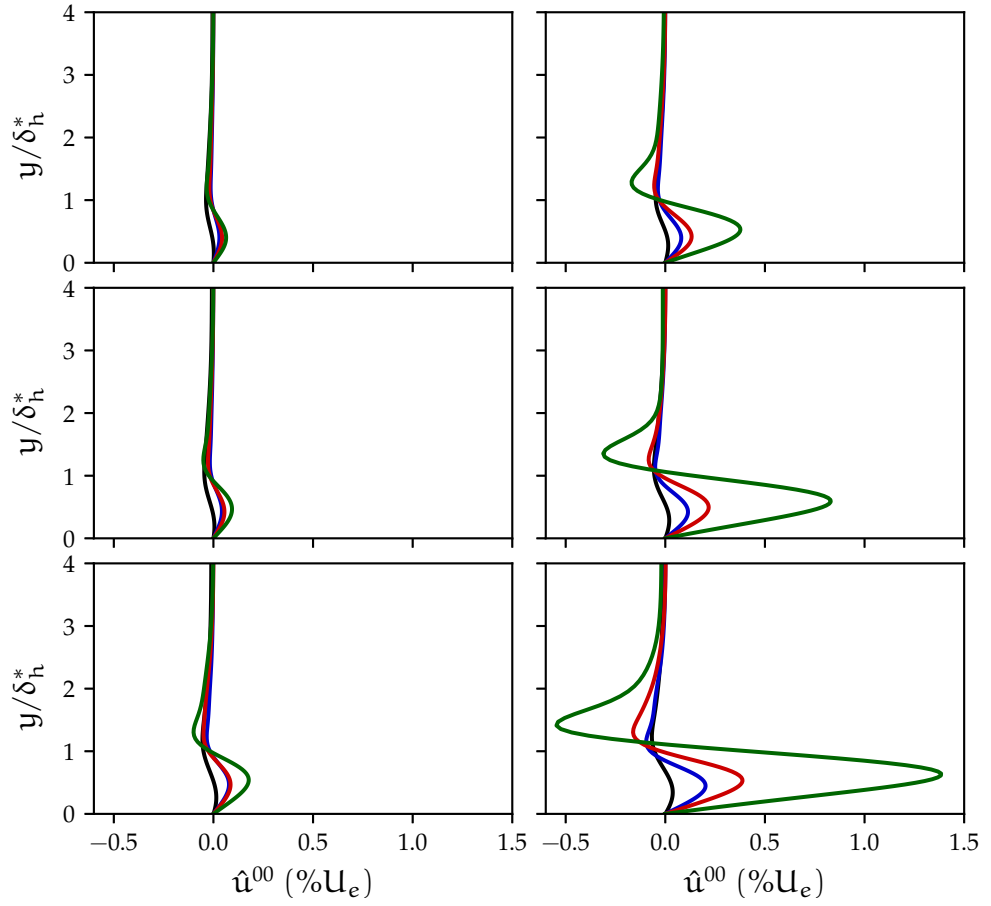

Figure 6.28: Wall-normal profiles of streamwise MFD $\hat{u}_{00}$ at $\Delta x = 25$ mm (—), 65 mm (—), 85 mm (—) and 105 mm (—). *Top*, $h/\delta^*_h = 10\%$; *centre*, $h/\delta^*_h = 15\%$; *bottom*, $h/\delta^*_h = 20\%$. The initial TS amplitude at the cylinder location is 0.45% (*left*) and 0.75% (*right*).

variation remains milder at the most downstream location. This correlates well with Fig. 6.25 where no explosive mode growth is visible.

A similar predominance of the TS frequency over the cylinder height may be observed in the wall-normal profiles of the MFD, displayed in Fig. 6.28. These

correspond to a time- and spanwise-averaged state of the streamwise velocity in the boundary layer. On the whole, the level of streamwise modulation grows from $h/\delta_h^* = 10\%$ to 20% and increases gradually with the distance to the cylinder. Figure 6.28 highlights that the distortion reaches a maximum of 1.4% of the local edge velocity for $h/\delta_h^* = 20\%$ at the most downstream station. The wall-normal location corresponding to the maximal MFD moves away from the wall in the wake of the cylinder, from nearly 50% of the displacement thickness at the roughness location to 75% at $\Delta x = 105\,\text{mm}$. De Paula et al. (2017) have not reported the corresponding experimental wall-normal maximum. Nonetheless, for the higher frequency they considered, $F = 120$, they observed that the wall-normal location remains close to $0.75\delta_h^*$. When $A_0 = 0.45\%$, the difference of streamwise distortion between $\Delta x = 65\,\text{mm}$ and 85 mm remains marginal. In addition, the streamwise velocity deficit is more pronounced with $A_0 = 0.75\%$ in contrast to the lower frequency case, potentially showing a greater non-linear amplification of the TS wave. The deficit reaches a local maximum near $y/\delta_h^* = 1.5$ at the last displayed streamwise station.

The flow field can be reconstructed in the physical z-direction after gathering the $2M + 1$ spanwise harmonics and applying a DFT. This allows to display the distortion of the TS wave relative to the nominally zero cylinder height case. In Fig. 6.29 are represented the distortions of amplitude based on the maximum streamwise velocity along the centreline for the fundamental mode characterised by $n = 1$. Alongside the features of the MFD profiles, the TS distortion is more pronounced in the higher frequency case and its maximum value grows with the streamwise distance to the cylinder. For $h/\delta_h^* = 15\%$ and 20%, the distortion reaches more than 4% of the local edge velocity at the last streamwise station when $A_0 = 0.75\%$. However, the TS distortion at $\Delta x = 65\,\text{mm}$ is smaller than at the more upstream station, with a different modulation along the wall-normal direction since two distinct lobes appear. Their location seems to equal the wall-normal coordinates where the MFD reaches maximum deficit and maximum net gain. Between those, just above one displacement thickness, the distortion is close to zero. For other streamwise stations, the wall-normal location of maximal distortion does not necessary correlate with that of the MFD, since it hovers near $y/\delta_h^* = 1.25$. The TS distortion at $\Delta x = 85\,\text{mm}$ is quantitatively similar as its $\Delta x = 25\,\text{mm}$ value just behind the cylinder in the $A_0 = 0.45\%$ case. Finally, the presence of the cylinder induces a slight streamwise amplitude reduction in the immediate neighbourhood of the wall.

A more general view of the TS amplitude evolution behind the cylinder is suggested in Fig. 6.30. These 3D visualisations correspond to the amplitude at a constant

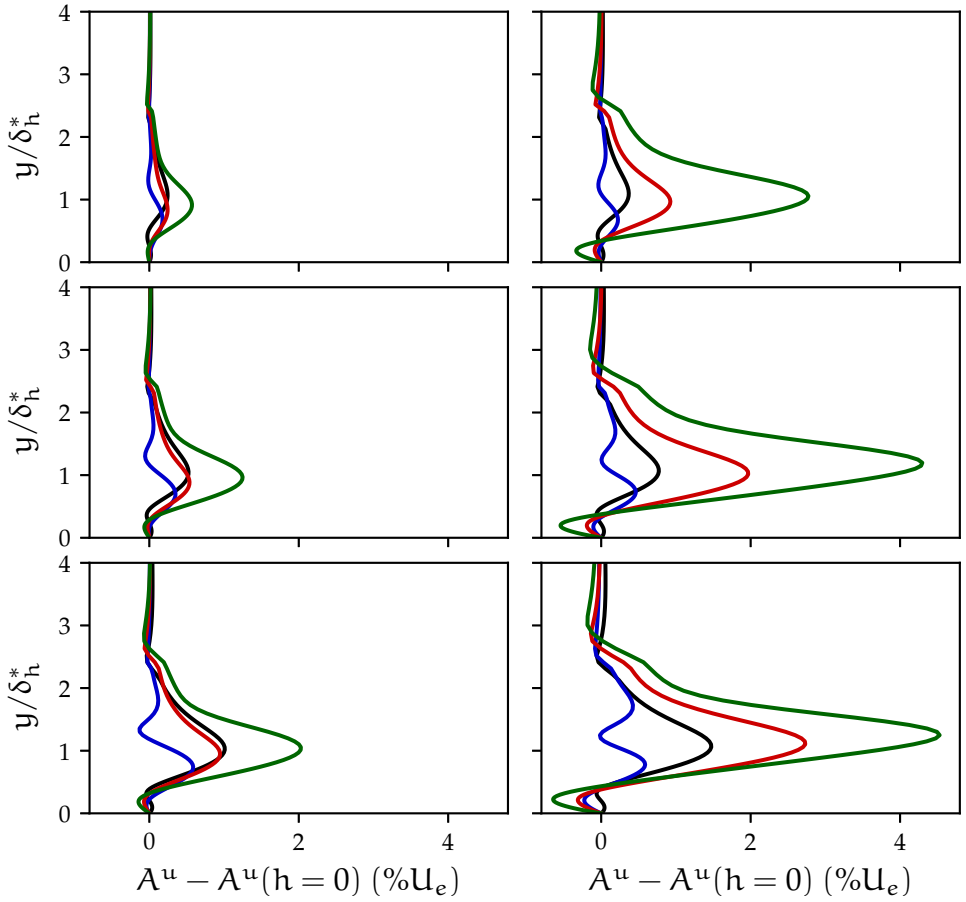

Figure 6.29: Distortion of TS wave amplitude relative to the zero cylinder height case along the centreline $z = 0$ mm and at several streamwise positions: $\Delta x = 25$ mm (—), 65 mm (—), 85 mm (—) and 105 mm (—). *Top*, $h/\delta^*_h = 10\%$; *centre*, $h/\delta^*_h = 15\%$; *bottom*, $h/\delta^*_h = 20\%$. The initial TS amplitude at the cylinder location is 0.45% (*left*) and 0.75% (*right*).

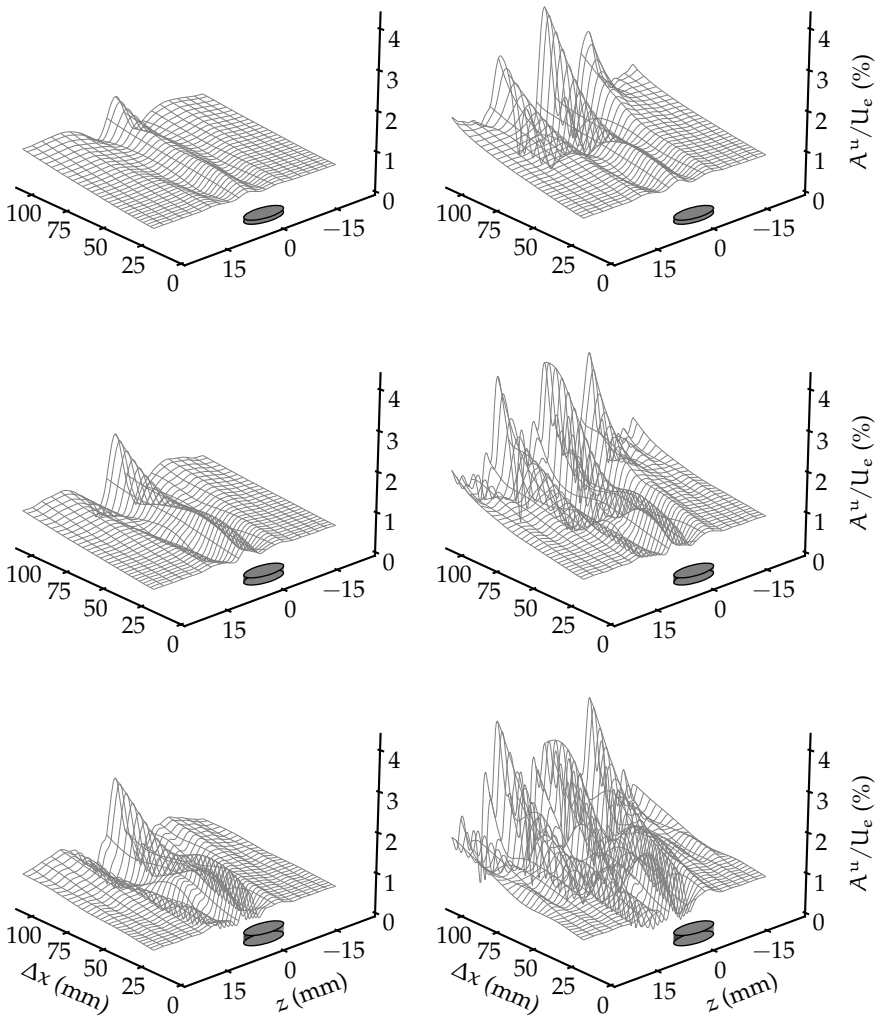

Figure 6.30: TS wave amplitude evolution at $y/\delta^*_h = 0.75$ downstream of the cylinder. For viewing purposes, the streamwise location of the cylinder has been shifted by 10 mm. *Top*, $h/\delta^*_h = 10\%$; *centre*, $h/\delta^*_h = 15\%$; *bottom*, $h/\delta^*_h = 20\%$. The initial TS amplitude at the cylinder location is 0.45% (*left*) and 0.75% (*right*).

wall-normal position $y/\delta^*_h = 0.75$. It shall be reminded that current NLHNS computations assume a spanwise-periodic domain and the figures represent one wavelength in that direction. From a pure amplitude viewpoint, Fig. 6.30 emphasises the scattering of the TS wave by the cylinder. In the lower frequency case, $A_0 = 0.45\%$, a mild scattering is visible downstream of the cylinder although most of the amplitude variation remains along its centreline. At that spanwise location, the amplitude fluctuates before soaring up near $\Delta x = 100$ mm. This is the case for all cylinder heights, which display a similar amplitude evolution pattern. For $A_0 = 0.75\%$, the roughness clearly generates a 3D amplitude field. A remarkable feature is that the amplitude at the last streamwise station and along the centreline slightly decreases with the height of the cylinder, whereas the maximum amplitude is reached at locations close to the spanwise edges of the cylinder. This was also highlighted by de Paula et al. (2017) in one of the cases with

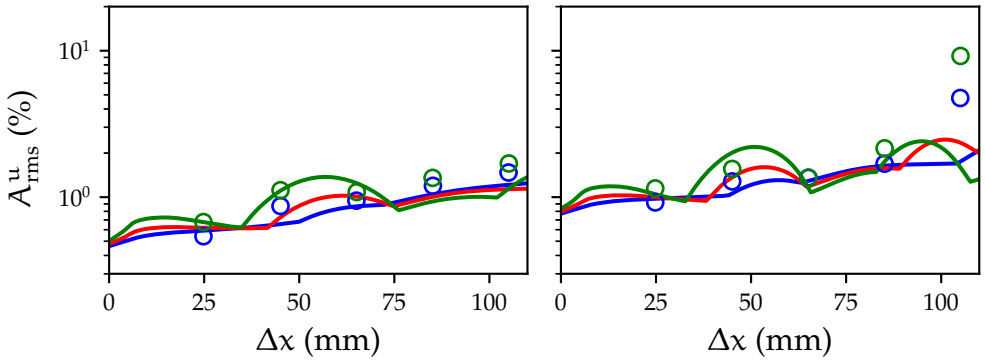

Figure 6.31: Streamwise perturbation velocity amplitude of the fundamental ($n = 1$) mode at $z = -5\,\text{mm}$ for $h/\delta^*_h = 10\%$ (—), 15% (—) and 20% (—). The corresponding experimental streamwise velocity fluctuations of de Paula et al. (2017) are indicated (○). *Left*, $A_0 = 0.45\%$; *right*, $A_0 = 0.75\%$.

a lower initial amplitude and a higher frequency case. The generated structure becomes 3D as it gets gradually closer to the cylinder with increasing height. There is a complex pattern in the $h/\delta^*_h = 20\%$ case. For the current analysis, the spanwise wavenumber has been chosen large enough to clearly distinguish the different spanwise scales, thus constraining the physical domain to a few multiples of the cylinder diameter. Although the correctness of the NLHNS approach has been established, the solution is likely to be mildly contaminated as a result of using such a restrained domain with the spanwise-periodic assumption. Such effect should be carefully assessed.

A comparison with the experiments of de Paula et al. (2017) is presented in Fig. 6.31. The amplitude based on the maximum streamwise velocity is extracted at the $z = -5\,\text{mm}$ location. NLHNS results are computed using all spanwise modes corresponding to $n = 1$. From the frequency content of the streamwise velocity fluctuations, de Paula et al. (2017) report that for $A_0 = 0.45\%$ the fundamental frequency encompasses almost all the signal energy. This justifies the soundness of the followed approach to compare the NLHNS-induced amplitude using the $(1, m)$ modes, and may also explain the reasonable agreement with experimental values. In the $A_0 = 0.75\%$ case and at $\Delta x = 105\,\text{mm}$, there is a non-negligible peak in the spectrum of velocity fluctuations matching the higher harmonic $n = 2$ (de Paula et al., 2017) which is discarded in Fig. 6.31. Among other reasons, it might explain the higher amplitude level discrepancy past $\Delta x = 75\,\text{mm}$. It is indeed possible that the truncation of temporal and spanwise modes at respectively 4 and 8 to maintain reasonable computation time is too severe to reconstruct accurately all the flow field features past the cylinder. For $A_0 = 0.45\%$, the predicted amplitude past $\Delta x = 75\,\text{mm}$ is slightly lower for $h/\delta^*_h = 20\%$ than for 10%, which is qualitatively inconsistent with the experiments.

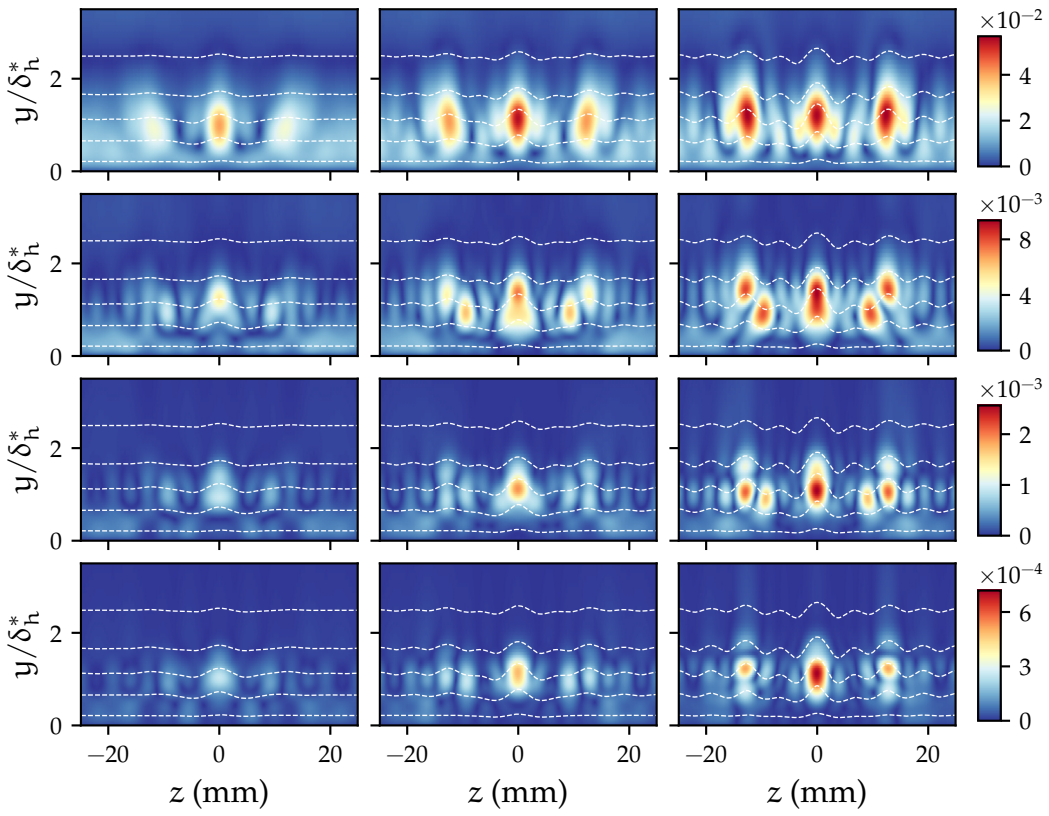

Figure 6.32: Contours of A^u_{rms} for the first travelling modes at $\Delta x = 105\,mm$. From top to bottom: fundamental $n = 1$, $n = 2$, $n = 3$ and $n = 4$. The cylinder height is $h/\delta^*_h = 10\%$ (*left*), 15% (*centre*) and 20% (*right*). The isolines of the total, time-averaged streamwise velocity $\bar{u}+\tilde{u}(z)$ are plotted with dashed lines from the bottom away from the wall, starting from 0.1 to 0.9 with a spacing of 0.2. $F = 90$, $A_0 = 0.75\%$ case.

Further insight into the travelling disturbances may be gathered from their spatial structure. Fig. 6.32 shows the contours of the streamwise amplitude for each temporal wavenumber, superimposed with the contour lines of the time-averaged base flow as isolines. The slices correspond to the most downstream streamwise location. Besides the region at the centreline, the fundamental mode features regions of large amplitude near the edges of the cylinder in accordance with Fig. 6.30. Considering the other higher harmonics, the travelling disturbances feature structures which are localised in space, extending near $y = \delta^*_h$. This suggests that the choice of $M = 8$ is sufficient to resolve them, however it may be increased to confirm the topology of travelling modes, especially for modes corresponding to larger values of n. The shape of such regions tends to not be altered as the cylinder height increases, nonetheless the level of amplitude grows. Their location in the spanwise direction correlates with the regions where the time-averaged streamwise velocity reaches local extrema. Besides, the upper limit of the structures is the isoline of total streamwise velocity corresponding to 70%

of its free-stream value. It shall be further noted that the amplitude of localised structures decreases nearly by an order of magnitude as the temporal wavenumber is incremented.

6.3 Cylinder on the leading edge of a swept-wing

In this final section, the NLHNS capability is demonstrated on a swept-wing geometry, accounting for the effects of surface curvature. The effect of a cylindrical element placed on its leading edge is analysed. As in Section 5.3, the geometry considered is the AERAST profile, that Saeed et al. (2016) used to investigate the influence of steps and gaps on CF instabilities.

6.3.1 Problem definition and base flow

A different path is followed compared to the numerical base flows computed by Cooke et al. (2019) with the clean AERAST geometry, or with the presence of steps or bumps. Here, the base flow is generated directly from the experimental data of Saeed et al. (2016) and their acquisition of pressure distribution. Figure 6.33 shows the aerofoil geometry. On the upper surface, the favourable pressure gradient section extends up to approximately 70% of the chord length, with mild fluctuations in the pressure distribution from 20% up to 50% chord, as shown in Fig. 6.34.

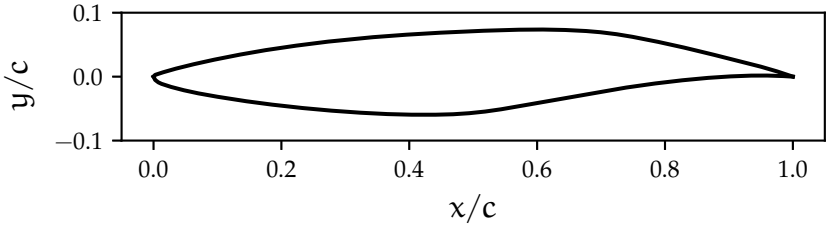

Figure 6.33: AERAST aerofoil geometry in the normal-to-leading-edge direction

The experimental c_p distribution is interpolated with splines before computing the boundary-layer profiles with the in-house solver. Unlike Cooke et al. (2019) who increased the Mach number for numerical stability reasons, the base flow corresponds to a genuine incompressible case, $Ma = 0.0572$, matching the experimental value. The free-stream Reynolds number is $Re_\infty = 10^6$, while the sweep angle matches the experimental value of $\Lambda = 40°$.

Figure 6.35 portrays the streamwise and spanwise base velocities in the boundary layer region. From a boundary-layer instability viewpoint, the most dangerous stationary CF perturbation is then sought by means of LHNS across the domain

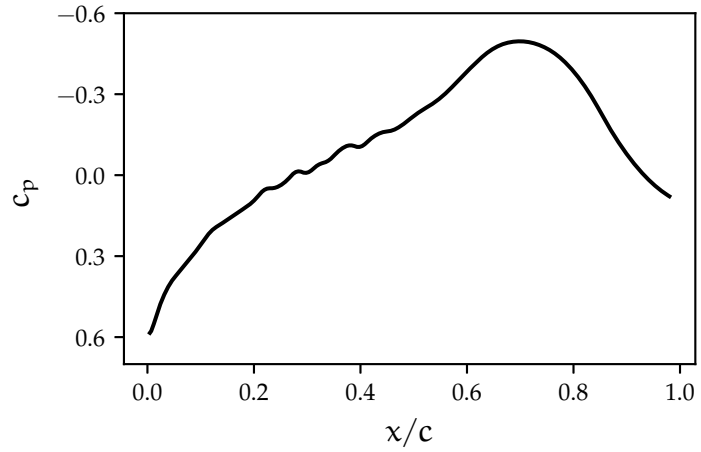

Figure 6.34: Upper-surface pressure coefficient c_p of the AERAST aerofoil in the normal-to-leading-edge direction, interpolated from the experiments of Saeed, Mughal and Morrison (2016)

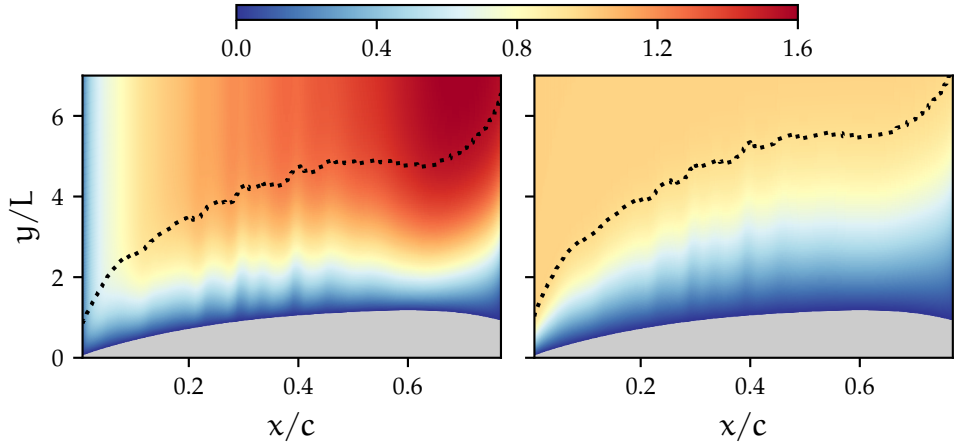

Figure 6.35: Contours of $\bar{u}$ (*left*) and $\bar{w}$ (*right*) scaled by W_∞ on the AERAST aerofoil geometry, with respective boundary layer thicknesses (···). For viewing purposes, the aerofoil geometry is distorted and the wall-normal coordinate is not aligned with the normal to surface direction.

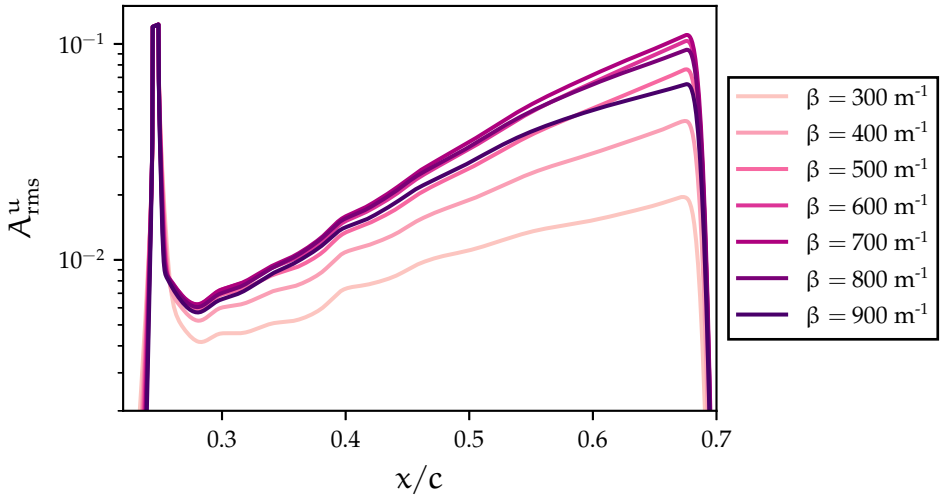

Figure 6.36: Linear amplitudes based on the streamwise velocity and scaled by $\sqrt{U_e^2 + W_e^2}$, obtained by LHNS for various selected values of β on the AERAST aerofoil geometry

by sweeping β. An artificial step roughness element is imposed near the leading edge for that purpose before monitoring the linear response, shown in Fig. 6.36 for a few values of β. It is thus clear that the most linearly amplified stationary disturbance lies near $\beta = 700\,\mathrm{m}^{-1}$. A finer sweep of the spanwise wavenumber has led to characterise the most amplified stationary disturbance at $\beta = 698\,\mathrm{m}^{-1}$, corresponding to $L_z = 9\,\mathrm{mm}$.

6.3.2 Stationary crossflow

The CF disturbance is generated by a small-scale cylindrical element whose radius is $\lambda = 2\,\mathrm{mm}$, close to the optimal value for the excitation of most dangerous CF waves (Saeed et al., 2016). Its centre is located at $s/c = 0.05$, or equivalently $x/c = 0.052$ just downstream of the neutral point reported as $x/c = 0.02$. The cylinder location is characterised by $Re^*_\delta = 129$. The cylinder height is gradually increased from 10 μm to 80 μm, stopping before the convergence of the NLHNS ceases due to severe non-linearity near the outflow of the domain.

In order to compute the stationary CF response, the cylinder is modelled with $M = 10$ Fourier modes in the spanwise direction with $\beta = 698\,\mathrm{m}^{-1}$. Hence, the periodic spanwise domain covers $L_z = 9\,\mathrm{mm} = 4.5\lambda$. Starting at $s/c = 0.0015$, the streamwise domain extends up to $s/c = 0.63$. It is discretised with $n_x = 5{,}500$ points and $q_x = 4$. In the wall-direction, the domain is truncated at $y/\delta^*_0 = 100$ where δ^*_0 is the streamwise displacement thickness of the base flow at $s/c = 0.2$. The discretisation is based on $n_y = 100$ points, $q_y = 8$ and a bilinear mapping set with $y_h = 2.5$ to ensure sufficient resolution in the boundary layer along the wing chord. The computations rely on body-fitted coordinates, while the interface of the outflow sponge regions is located at $s/c = 60\%$, where $Re^*_\delta = 600$. They are defined with $\sigma_{max} = 10$. A radiation boundary condition is employed at the outflow boundary. Finally, the tolerance for the convergence of the NLHNS procedure is set at 10^{-5}. In order to ensure a smoother convergence behaviour for large cylinder heights, the under-relaxation coefficient is set to $\tau = 0.5$.

The difference in harmonic response between the cylinder of 20 μm height and of 80 μm height is shown in Fig. 6.37 in terms of the disturbance kinetic energy. The cylinder heights correspond to $h/\delta^*_h = 8.8\%$ and 35.2%, respectively, where δ^*_h is the streamwise displacement thickness of the base flow at the cylinder location. All the stationary modes generated by the cylinder actuation are non-linearly forced just downstream of the cylinder and remain unstable across the streamwise direction. It is evident that the energy of the primary mode is attenuated by non-linear effects along the wing surface, in contrast to its linear behaviour in

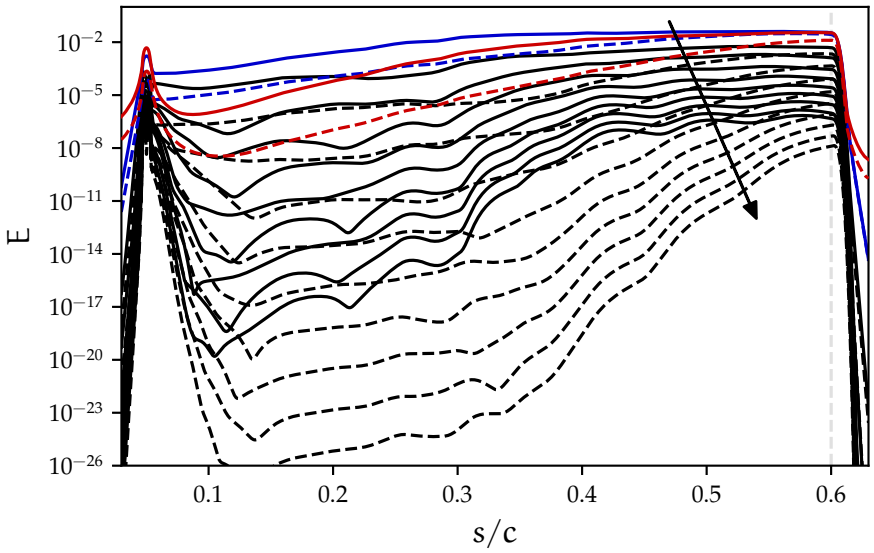

Figure 6.37: Total disturbance kinetic energy of stationary modes, namely the MFD (—), the primary mode (—) and higher harmonics (—) in the direction of the arrow with $h = 80\,\mu m$. Dashed lines correspond to the $h = 20\,\mu m$ case. AERAST stationary CF case, $\beta = 698\,m^{-1}$.

Fig. 6.36. Upstream of $s/c = 0.2$, all modes compete with respect to their role on the non-linear instability evolution, until the domination of $(0, 1)$ mode is established. From this location onwards, higher harmonics thus lock in on to the primary mode. Current NLHNS computations predict a saturated state past $s/c \approx 0.35$ due to the significant non-linear mode interaction. The saturation is much stronger for $h = 80\,\mu m$, for which the MFD and other modes stabilise from $s/c \approx 0.45$. The kinetic energy of some higher harmonics even starts to decline near the sponge layer interface. On the other hand, the stationary modes generated by the $h = 20\,\mu m$ cylinder maintain a larger growth until $s/c = 0.6$. Further evidence of the mode saturation relies on the primary modes of both heights that converge to almost equal values, whereas the discrepancy in E is clear for the MFD and higher harmonics. In spite of important non-linear interactions, the stationary modes retain their ordering across the streamwise direction.

As expected, such mode behaviour is also found when examining the growth rates presented in Fig. 6.38. Only the region past $s/c = 0.1$ is displayed due to the influence of the cylinder upstream that misrepresent the values. In accordance with Fig. 6.37, the mode growth is most important just downstream of $s/c = 0.3$ for $h = 80\,\mu m$ before the saturation. This translates into minimised growth rates hovering near neutral stability after $s/c = 0.4$. In the $h = 20\,\mu m$ case, at $s/c \approx 0.4$, the growth rates attain a smaller maximum value on the whole domain than with the higher cylinder. However, the stationary modes have a larger growth rate in the region downstream, which implies a weaker mode saturation near the domain outflow. The growth rates remain strictly positive as opposed to their counterparts

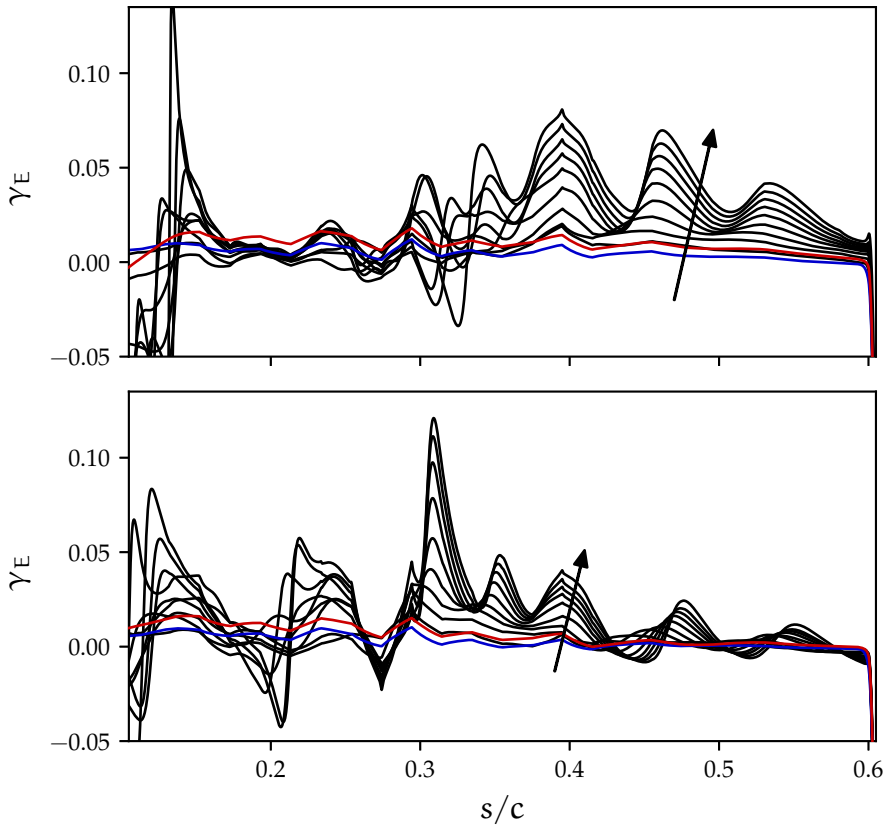

Figure 6.38: Growth rates based on E of stationary modes, namely the MFD (—), the primary mode (—) and higher harmonics (—) in the direction of the arrow. *Top*, $h = 20\,\mu m$; *bottom*, $h = 80\,\mu m$. AERAST stationary CF case, $\beta = 698\,m^{-1}$.

associated with the higher cylinder case. It is also noted that the mode ordering is conserved, as the growth rate magnitude increases with the wavenumber $m\beta$; the MFD and primary mode tend to not fluctuate.

The phase-locking mechanism of higher harmonics to the primary mode is confirmed by the evolution of streamwise wavenumbers in Fig. 6.39. In the NLHNS framework, these were computed by means of Eq. (3.46), adding the curvature term and using the quantity $\sqrt{\hat{u}^2 + \hat{w}^2}$, evaluated where $\sqrt{|\hat{u}|^2 + |\hat{w}|^2}$ reaches its wall-normal maximum. The higher harmonics are in phase with the primary mode downstream of the cylinder location, as their wavenumber lies close to an m-multiple of the wavenumber of the primary mode.

Figure 6.40 shows the difference between total and base wall vorticity distribution, defined as

$$\sqrt{\left(\frac{\partial u}{\partial y}\right)^2 + \left(\frac{\partial w}{\partial y}\right)^2} - \sqrt{\left(\frac{\partial \bar{u}}{\partial y}\right)^2 + \left(\frac{\partial \bar{w}}{\partial y}\right)^2}. \tag{6.14}$$

The cylinder induces a ridged pattern of vorticity in its wake with an increasing value along the wing surface. It seems modulated by the wavy variation of c_p

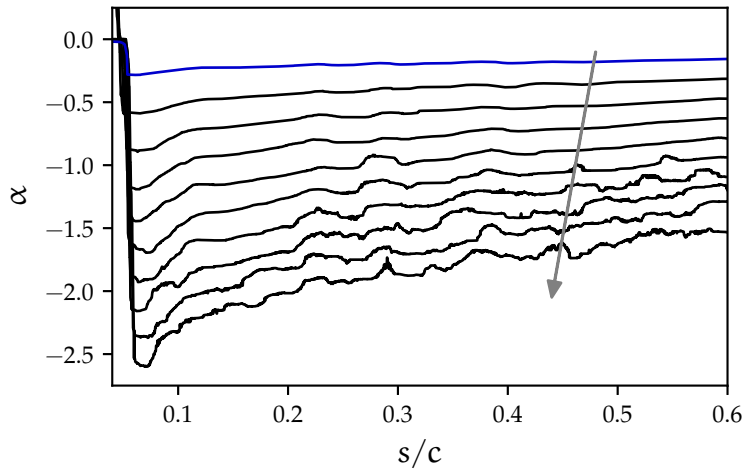

Figure 6.39: Non-linear wavenumbers for the primary mode (—) and higher harmonics (—) in the direction of the arrow. AERAST stationary CF case, $h = 80\,\mu m$ and $\beta = 698\,m^{-1}$.

seen in Fig. 6.34, where the wall shear due to the cylinder is locally increased. The location $s/c \approx 0.3$ marking the start of the region with maximum values of vorticity correlates with the beginning of the mode saturation region. The striations are slightly tilted with respect to the spanwise direction and are the typical signature of stationary vortices.

Furthermore, the total streamwise and spanwise wall shear are displayed in Fig. 6.41 near the cylinder region. It is recalled that the cylindrical roughness is not meshed but modelled via a Taylor expansion of the no-slip condition for the velocity field at the wall surface. An intermediate (50 μm) and the highest (80 μm) cylinders are shown. Due to the wing sweep, the cylinder induces wall patterns of negative streamwise and spanwise shear moulding its radius, and whose magnitude increases with height. In view of the local flow orientation, such regions with negative shear are predicted correctly. This shows the soundness of the Taylor expansion model used within the NLHNS approach.

Such shear behaviour may be expressed through the skin-friction coefficient and shape factor values altered by the presence of the cylinder. Figure 6.42 is a comparison of these integral quantities between the base flow and the transitional flow with various cylinder heights. The streamwise expressions were given in Eqs. (6.11) and (6.12) while the spanwise skin-friction coefficients are defined as

$$c_{fw,lam} = \frac{\mu_e}{\frac{1}{2}\rho_e U_e^2}\frac{\partial \bar{w}}{\partial y}\bigg|_w, \qquad c_{fw,tr} = \frac{\mu_e}{\frac{1}{2}\rho_e U_e^2}\frac{\partial (\bar{w} + \hat{w}_{00})}{\partial y}\bigg|_w. \tag{6.15}$$

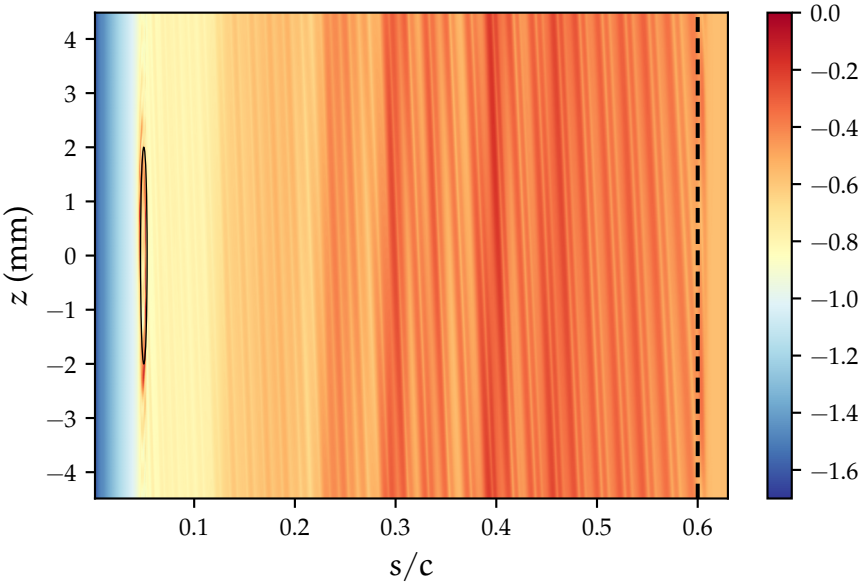

Figure 6.40: Total wall vorticity distribution from the leading edge to the sponge region (**--**). Only one spanwise wavelength is represented. AERAST stationary CF case, $\beta = 698\,\mathrm{m}^{-1}$ and $h = 80\,\mu\mathrm{m}$.

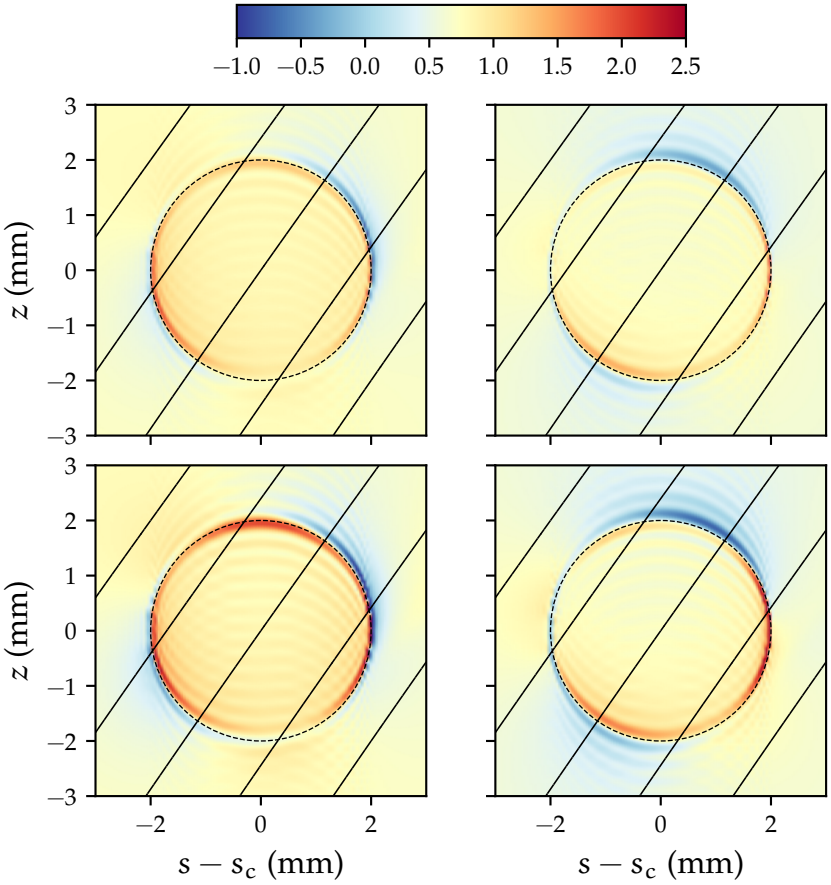

Figure 6.41: Contours of total streamwise (*left*) and spanwise (*right*) wall shear near the cylinder actuation (**--**). *Top*, $h = 50\,\mu\mathrm{m}$; *bottom*, $h = 80\,\mu\mathrm{m}$. The inviscid flow vector is represented (**—**). s_c denotes the streamwise coordinate of the roughness centre. AERAST stationary CF case, $\beta = 698\,\mathrm{m}^{-1}$.

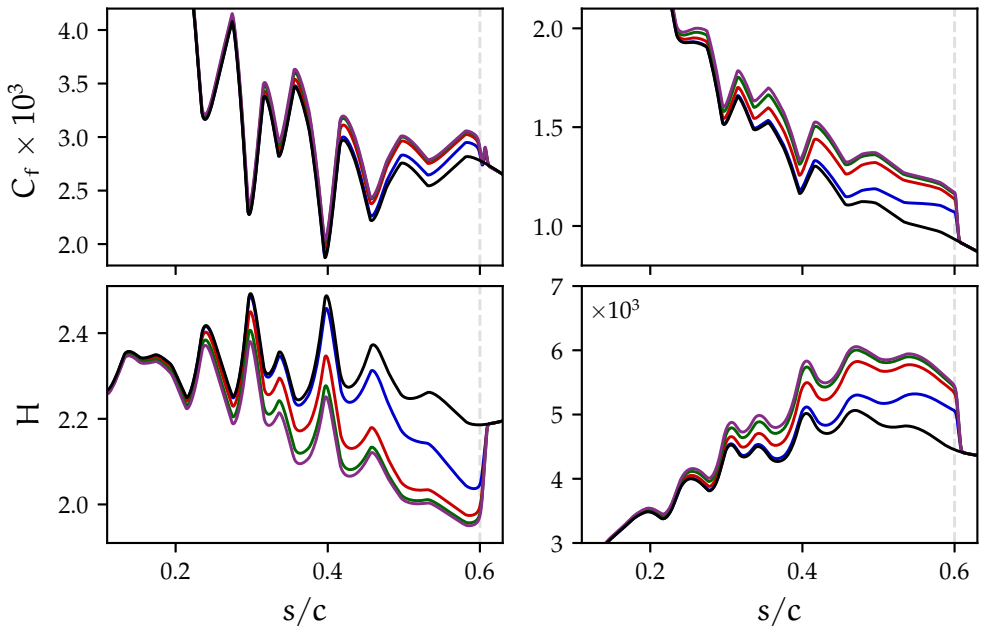

Figure 6.42: Streamwise (*left*) and spanwise (*right*) skin-friction coefficient (*top*) and shape factor (*bottom*) downstream of the cylinder location. The laminar boundary layer (—) is compared to the transitional boundary layer with $h = 20\,\mu m$ (—), $50\,\mu m$ (—), $70\,\mu m$ (—) and $80\,\mu m$ (—). AERAST stationary CF case, $\beta = 698\,m^{-1}$.

The spanwise shape factor is defined as the ratio of the spanwise displacement thickness,

$$\delta^* = -\int_0^{+\infty} \frac{w}{U_e}\,dy \tag{6.16}$$

to the spanwise momentum thickness defined as

$$\theta = -\int_0^{+\infty} \frac{uw}{U_e^2}\,dy. \tag{6.17}$$

The fluctuation observed for all cases stems from the wobbly variation of c_p along the wing surface. For the given fundamental spanwise wavenumber, the given geometrical characteristics of the cylinder and location on the leading edge, the skin-friction and shape factors are marginally affected by the variation of cylinder height. Even for $h = 80\,\mu m$, the quantities of Fig. 6.42 evolve along the same qualitative behaviour as the transitional behaviour and no sudden skin-friction rise, or decline of shape factor is noted. The deviation of quantities occurs most from a nominally zero height to $h = 50\,\mu m$ whereas it seems to stagnate for greater heights. This is another indicator of the intense mode saturation occurring in the most downstream section of the wing involved in the computations.

Figure 6.43 represents, for several streamwise stations, the ratio of the $(0, 1)$ mode amplitude between LHNS and NLHNS methods. Such amplitude is based on the maximum wall-normal value of $\sqrt{|\hat{u}|^2 + |\hat{w}|^2}$. The line at the bottom shows

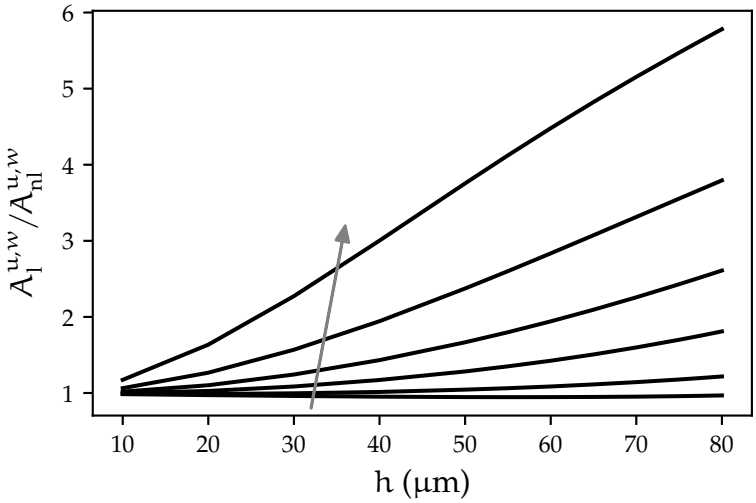

Figure 6.43: Linear to non-linear ratio of amplitude for the primary mode, based on $\sqrt{|\hat{u}|^2 + |\hat{w}|^2}$ and evaluated at several streamwise locations: $s/c = 0.30$ to 0.55 in steps of 0.05 indicated by the arrow. AERAST stationary CF case, $\beta = 698\,\mathrm{m}^{-1}$.

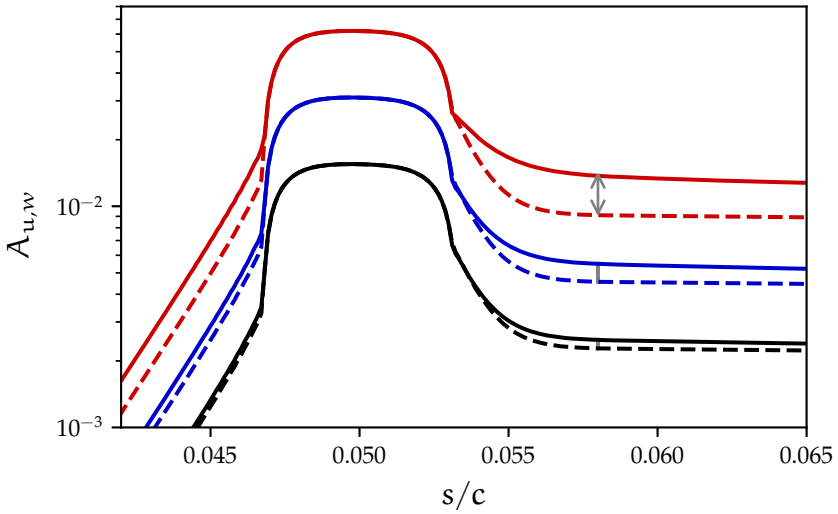

Figure 6.44: Non-linear amplitude of the primary mode near the actuation site for $h = 20\,\mu\mathrm{m}$ (—), 40 μm (—) and 80 μm (—) compared with linear amplitude (dashed lines). AERAST stationary CF case, $\beta = 698\,\mathrm{m}^{-1}$.

that the non-linear interactions mildly amplify the primary mode at $s/c = 0.30$ relative to its linear value for all cylinder height. Had the receptivity and the growth of disturbances been linear, all the curves in Fig. 6.43 would have been straight lines. The departure from the linear regime occurs above approximately $h = 20\,\mu\mathrm{m}$. As the distance from the leading edge is greater and the cylindrical height increases, the mode saturation intensity gradually reduces the non-linear amplitude response. For $h = 80\,\mu\mathrm{m}$, the non-linear $(0, 1)$ amplitude at $s/c = 0.55$ is only 20% of its linear counterpart.

The discussion on the disturbance field features along the chordwise wing extent is briefly stepped aside in order to focus on the region surrounding the cylinder.

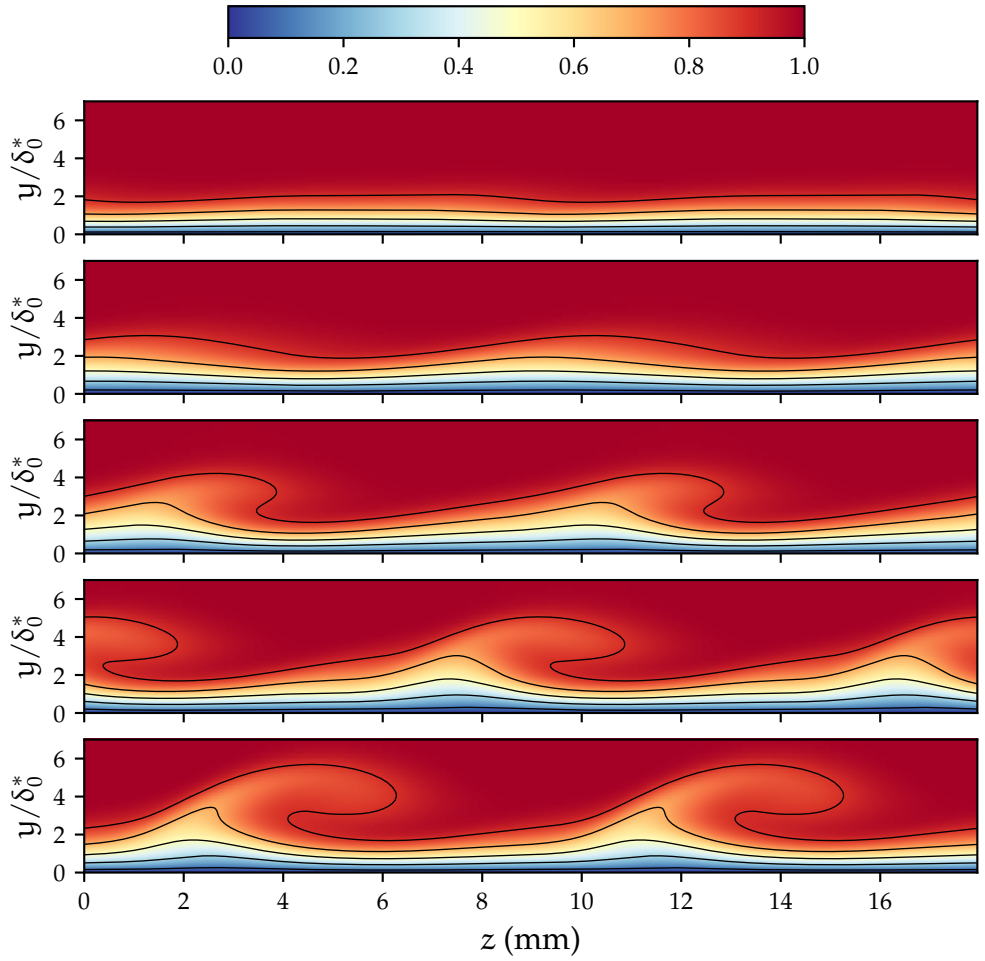

Figure 6.45: Contours of total streamwise velocity viewed from upstream at $s/c = 0.15$, 0.25, 0.35, 0.45 and 0.55 from top to bottom. Two spanwise wavelengths are represented, with isolines from 0.1 to 0.9 in steps of 0.2. AERAST stationary CF case, $\beta = 698\,\mathrm{m}^{-1}$.

As mentioned in Section 2.2.2, the HNS approach incorporates the effects of receptivity. Figure 6.44 shows the amplitude of the primary mode in the vicinity of the cylindrical roughness element. The NLHNS amplitudes are displayed alongside the equivalent linear response for various roughness heights. Although the non-linear amplitude evolves linearly just downstream of the cylinder location, there is a distinct augmentation compared to the linear response. The fact that this occurs at such a minute distance from the actuation site is evidence of a non-linear receptivity mechanism. These features demonstrate that the NLHNS method can capture both non-linear growth of instabilities and non-linear receptivity of the boundary layer to surface roughness.

The stationary disturbance streamwise velocity induced by the cylinder with $h = 80\,\mu\mathrm{m}$ and superimposed on the streamwise base flow component is presented in Fig. 6.45. It shall be recalled that these are visualised from upstream, in the

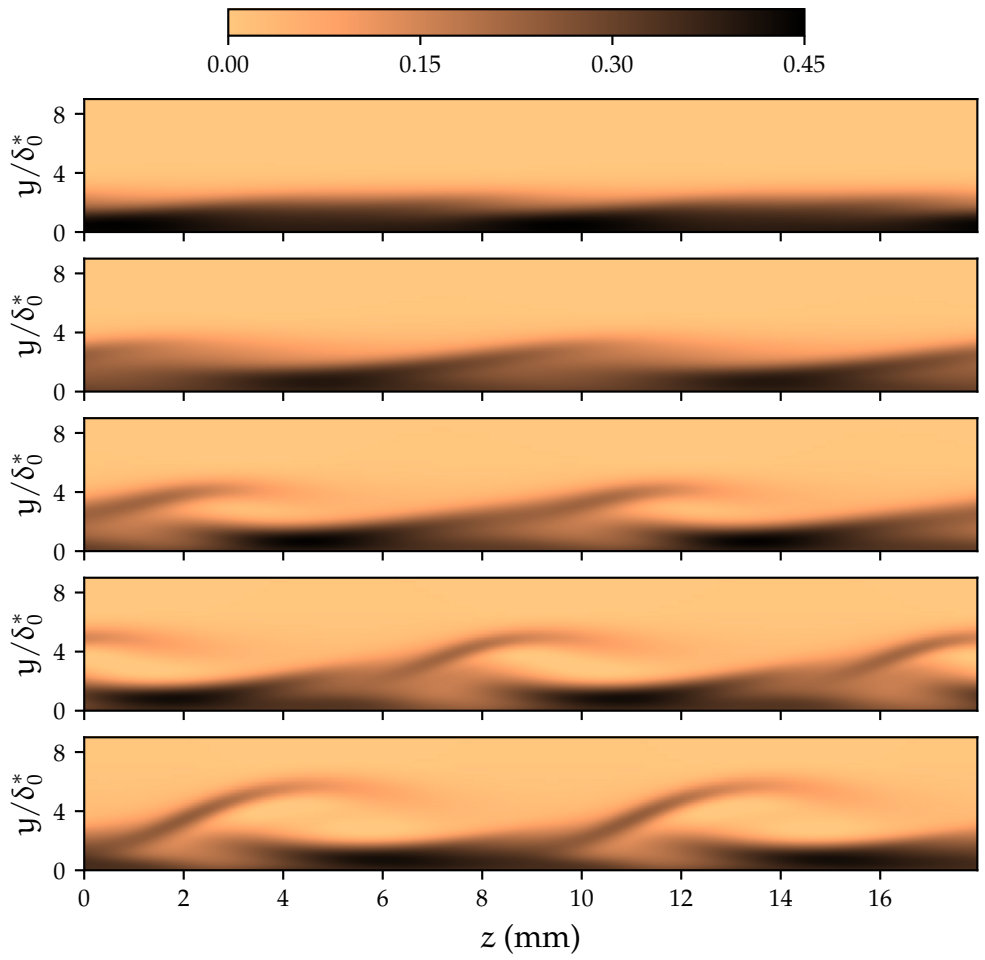

Figure 6.46: Contours of total streamwise vorticity viewed from upstream at $s/c = 0.15$, 0.25, 0.35, 0.45 and 0.55 from top to bottom. Two spanwise wavelengths are represented. AERAST stationary CF case, $\beta = 698\,\mathrm{m}^{-1}$ and $h = 80\,\mu\mathrm{m}$.

normal-to-leading edge coordinate system. Past 30% of the chord length, the formation of CF vortices with a 'half-mushroom' u-structure is noticeable. Near $s/c = 0.55$, these vortices extend up to approximately six times the streamwise displacement thickness at the cylinder centre. The corresponding total streamwise vorticity field is shown in Fig. 6.46 at the same locations along the chord. The CF vortices tow low-velocity flow regions away from the wall and drag high-velocity flow regions towards the wall. The distinctive 'cat's eye' shape commonly observed in experiments is clearly visible.

Lastly, the amplitude functions of the three velocity components for the $(0, 1)$ and $(0, 2)$ modes are displayed in Fig. 6.47. These wall-normal profiles correspond to $s/c = 0.50$ where the phase-locked and saturation regimes are established according to Fig. 6.37. The amplitude of the wall-normal component is systematically smaller than the two others, by nearly an order of magnitude. As the cylinder height increases from $h = 20\,\mu\mathrm{m}$ to $h = 80\,\mu\mathrm{m}$, the velocity mode amplitude grows

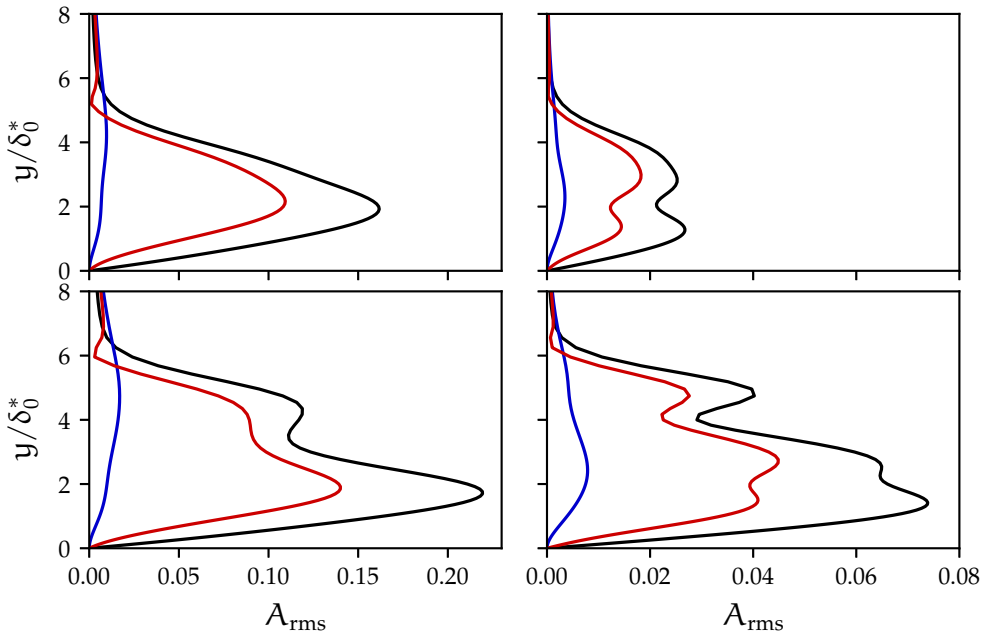

Figure 6.47: Amplitude functions of the primary mode (*left*) and of the $(0, 2)$ mode (*right*) at $s/c = 0.50$: $\hat{u}$ (—), $\hat{v}$ (—) and $\hat{w}$ (—). *Top*, $h = 20\,\mu m$; *bottom*, $h = 80\,\mu m$. AERAST stationary CF case, $\beta = 698\,m^{-1}$.

and the greater non-linear interaction results in an additional inflection point in the $\hat{u}$ and $\hat{w}$ amplitude profiles. A strong secondary instability is likely to ensue from such highly inflectional profiles. Very similar observations were given by Haynes and Reed (2000) in their NLPSE investigation of the development of stationary CF vortices on a swept wing.

6.4 Discussion

The capability of the NLHNS to model non-linear interactions of instabilities has been established. Overall, an excellent agreement with NLPSE results is obtained on the three verification and validation configurations, which ascertains the correct implementation of the method.

As underlined by the swept Hiemenz case in Section 6.1.3, the iterative procedure tends to diverge when the growth rates of modes is high or when the level of non-linear mode interactions is substantial. Resorting to gradual increments of the roughness height or the amplitude of incoming waves is an essential approach to stabilise the underlying algorithm. Numerical experimentation also suggested that the use of the under-relaxation factor described in Eq. (4.35) has helped to improve the robustness in some cases. A further possibility to serve the same purpose is to adjust the governing equations to include the MFD in the left-hand side to form a 'modified' LHNS operator. As a matter of fact, when the amplitude of the

MFD is significant it leads to cascading considerable weight in the resonant forcing terms on the right-hand side of Eq. (3.56). This is likely to be the reason why it then destabilises the iterative procedure of the non-linear numerics. Including the $(0,0)$ mode in the left-hand side was suggested by other authors in the context of NLPSE, such as Chang (2004). Implementing this feature within the NLHNS would however potentially result in a loss of computational efficiency, since the sparsity pattern of the matrix discretising the left-hand side would change after an update of the resonant forcing field; it would then require recomputation of a new symbolic factorisation at each global iteration, as explained in Section 4.2.3.

In order to demonstrate the potential of the NLHNS methodology and its improvement over the NLPSE approach, it has been deployed in the framework of boundary-layer instabilities generated by a roughness element. Its modelling relies on a Taylor expansion of the no-slip condition at the wall surface. In the two application cases of this chapter, the contribution associated with the travelling modes $(n \neq 0, m)$ in Eq. (3.61) had to been discarded. It is recalled that the said term,

$$\sum_{\substack{p,q \\ p+q=m}} \hat{h}_p(x) \frac{\partial \hat{u}_{qn}}{\partial y}(x,0) \tag{6.18}$$

is formed *a priori* of unknown amplitude functions. However, in virtue of the hypotheses intrinsic to the Taylor expansion process, these can be computed over the course of a simulation without the roughness, prior to the NLHNS simulation with the roughness. This was attempted, but it led to the destabilisation of the procedure even in weakly non-linear regimes where convergence is otherwise readily reached. As a general point, the impact of including the additional contribution of Eq. (6.18) should be carefully assessed. The first-order roughness model based on the Taylor series is nevertheless widely acceptable as evidenced, among others, by Mughal and Ashworth (2013) in numerical approaches, by Smith (1982) in theoretical analysis based on triple-deck models and by Ng and Crouch (1999) in the framework of finite Reynolds-number theory.

From a broader perspective, the NLHNS results showed some consistency with the experimental data of de Paula et al. (2017) concerning the TS behaviour downstream of the cylinder. The clear advantage of the NLHNS method compared to NLPSE is its ability to quantify disturbance amplitude accurately just downstream of the roughness, which is crucial with respect to the state of engendered secondary instability. The NLPSE is incapable of capturing the short-scale evolution of the latter processes. Further efforts are required to numerically quantify the scattering of the TS waves in the same way as the experimental investigation of de Paula et al.

(2017). The numerical strategies for stabilisation of the NLHNS iterative process mentioned above may be used to extend the simulations downstream where a more strongly non-linear stage is reached, in order to confirm numerically that the secondary instability of K-type is the dominant mechanism.

The method was finally showcased in the context of a swept-wing boundary layer destabilised by a cylindrical roughness element located on the leading edge. The NLHNS demonstrated its aptitude to directly yield the harmonic response generated by roughness elements of varying heights; insights on regions of negative shear near the cylinder location were offered together with evidence of non-linear receptivity increasing with the roughness height. The computational tool is henceforth set to replicate the surface excrescence arrangement of Saeed et al. (2016), who conducted a parametric investigation on the influence of 2D strips of varying heights and location downstream of the cylinder.

Chapter 7

Conclusions and Future Research

Still today, the complexity of modelling laminar-turbulent transition presents severe challenges due to the multitude of possible routes and phenomena responsible for heralding the transition stages. This is particularly true for boundary layers developing on curved geometries in the presence of surface irregularities, that are representative of aircraft wings. Transition modelling usually relies on two classes of approaches.

On the one hand, the all-encompassing DNS features unsurpassed levels of detail and accuracy. However, extracting the saturated state of stationary CF on a wing geometry would require many weeks or months usage of a dedicated HPC cluster utilising hundreds of CPUs—an unacceptable turnaround time for industry. Such constraints are critical since industrial design invariably involves parametric optimisation with hundreds of variables.

On the other hand, applied aerodynamics and design engineers have resorted to LST and linear PSE conjointly with the e^N method, enabling solutions in a matter of minutes if not seconds. However, correlating semi-empirically the transition location solely with the growth of the disturbance is oversimplified for real-world applications. Little should be also expected from the application of LST, which neglects surface curvature, the growth of the boundary layer and non-linear interactions. Next to LST, the PSE model is a substantial improvement. Nevertheless, it remains unable to incorporate strong streamwise gradients and upstream-propagating disturbances arising from any abrupt change in surface topography, embodied for example by rivet heads or hail dents.

This thesis has endeavoured to fill the void between these two approaches by presenting a robust and efficient computational framework based on the 'DNS' equivalent of stability theory: the HNS methodology. In a 2.5D context, the

only assumptions of the model are a time-harmonic and spanwise-harmonic decomposition of the disturbance field. The temporal BiGlobal analysis embraces the HNS assumptions and differs only in the philosophy of the sought instabilities, namely the retrieval of self-sustained mechanisms as an eigenvalue-based approach. We also focused on the spatial development of disturbances by considering the LHNS model. In this work we developed the NLHNS concept, seen as an extension and as a significant enhancement of the NLPSE model. The scope of this thesis has been restrained to boundary layers in incompressible flows as a first step.

First, we applied streamwise BiGlobal analysis to a set of flat-plate boundary-layer flows featuring LSBs induced geometrically by 2D surface indentations. The temporally amplified mechanisms are in accordance with the literature and the corresponding unstable modes arise past a certain threshold of peak reversed flow velocity. The subsequent investigation in Section 5.3 is, to our best knowledge, the first occurrence of a streamwise BiGlobal analysis performed on a swept-wing geometry with steps. We numerically exhibited the existence of temporally amplified modes as the step height exceeds the boundary-layer displacement thickness of the clean geometry at the step location, and found that the BFSs are generally more detrimental than FFSs in that respect. This particular ascertainment pertaining to BiGlobal analysis is in line with the experimental or 2D numerical studies on surface steps in boundary layers, although the available dataset was limited; the fixed sweep angle, the fixed Mach number and the few height and location cases offered a rather narrow parametric study opportunity.

We also validated the ability of the NLHNS to model non-linear interactions against three reference cases of a different nature. One of them featured experimental data from Kachanov and Levchenko (1984). The capability of the NLHNS to model resonant wave-triad interactions in the presence of surface roughness has been demonstrated by replicating numerically the experimental setup of de Paula et al. (2017). In the first place, we computed the stationary distortion induced by a cylindrical element located on a zero-pressure-gradient section of an aerofoil. Then, the interaction between an incoming 2D TS wave and the cylinder was investigated. We analysed the scattering of the impinging wave due to the presence of the 3D localised roughness. Under the current state of insight provided by the NLHNS, we noted some consistency with the experimental results about the behaviour of the TS wave downstream of the cylinder, which preferentially excites unsteady oblique modes. Remarkably, this was obtained by considering only a few Fourier modes to reconstruct the spanwise and temporal fields. Afterwards, we applied the NLHNS to an industrially-relevant swept-wing boundary layer developing on the AERAST geometry. The base flow was computed directly from the experimental surface

pressure distribution. This culminated in the quantification of stationary CF created by a cylindrical roughness of increasing height, placed on the leading edge. Besides capturing the phase-locked and harmonic saturation regimes, the NLHNS has demonstrated its ability to incorporate the effects of non-linear receptivity to surface roughness.

Those studies were facilitated by an efficient numerical machinery that we presented throughout Chapter 4. We have used a high-order FDM that yields sparse discretised operators. The code is based on parallel libraries for their formation and for the numerical solution of linear systems (for LHNS/NLHNS) or eigenvalue problems (for BiGlobal analysis). Although the scalability of LU solvers is inferior relatively to iterative solvers, the raw performance of MUMPS enabled us to solve such problems in a relatively short time compared to a DNS thanks to a hybrid MPI/OpenMP parallelisation scheme.

As a rough order of magnitude, solving a 2.5D LHNS problem in parallel with 16 MPI processes and typical discretisation parameters usually takes one minute. A (2.5D) BiGlobal problem requires between ten minutes and an hour, depending on the spectrum convergence. Without such a reasonable performance, the parametric study involving BiGlobal analysis on the swept wing in Section 5.3 with multiple height and location cases would have been unfeasible. Moreover, a global NLHNS iteration for a 3D stationary (or a 2D travelling) computation with $N = 0$ and $M = 8$ lasts approximately ten minutes. For a travelling 3D NLHNS problem with, for example, $M = 8$ and $N = 4$, a global iteration requires between 45 minutes and an hour.

However, the computational code had to be run on distributed-memory clusters whose hardware featured sub-optimal process affinity within a computational node. This implies there is additional performance hold in reserve and a potentially improved scalability of MUMPS. Most NLHNS computations used 16 to 48 MPI processes and one to six OpenMP threads per MPI process to yield highly-converged results. Following the non-linear development of disturbances with such high-fidelity modelling in similar CPU times with DNS would have been intractable, irrespective of hardware power.

Conversely, we also emphasised the limitations of the computational tool. Even though MUMPS uses data structures based on the sparsity of discretised matrices, their banded structure is not fully exploited. This is characterised by significant fill-in of the LU factors, thereby making the numerical solution of a 3D problem discretised in physical space impossible due to extreme memory requirements. A first-rate parallel scalability would be obtained with iterative solvers. When

applied to our formulation with HNS equations and the numerical method, they systematically led to divergence regardless of the choice of built-in preconditioner. This is imputable to the significant ill-conditioning of the discretised operators. Lastly, the single regular grid associated with the FDM is only able to mesh smooth surface irregularities. For example, sharp steps cannot be processed unless a multi-block approach with connected sub-domains is implemented, or unless roughness elements are small enough so that they can be modelled using the Taylor expansion model.

The BiGlobal analyses of Chapter 5 may be naturally expanded by decoding more accurately the physical mechanisms involved in global modes, and considering the relative importance of individual terms in the governing equations. In this light, the energy budget based on the Reynolds-Orr equation is the tool of choice, as shown by Malik et al. (1999) and Schmid and Henningson (2001). A further extension of the work could involve solving the associated *adjoint* problem. Its solution completes the original (*direct*) problem by locating regions with higher receptivity of the boundary layer to external perturbations (Hill, 1995). Considering the two approaches together has potential to theoretically devise strategies aimed at flow control. Such further numerical insights would enhance the analyses of Chapter 5, since the current understanding of the various transition mechanisms related to 3D LSBs within surface irregularities of increasing height is still in its infancy. Moreover, in the context of 2.5D BFSs and FFSs, the changeover from a gradual forward transition movement to bypass transition and turbulent breakdown also remains unexplained.

Due to the cumbersome application of the BiGlobal analysis and its difficulty to ascertain physical relevancy of eigenmodes, it is unlikely that the method can be presently used in routine transition analysis as part of a CFD-based optimisation loop for aerodynamic design. Future work may be undertaken to demonstrate that BiGlobal analysis is capable of efficiently explaining sensitivity to roughness for realistic configurations such as flight tests. In that case, it could be of industrial use for the purpose of setting manufacturing and performance tolerances by running through a range of boundary-layer and roughness parameters.

In comparison to LST and PSE, the HNS model can be seen as the model most fitted for tracking the evolution of disturbances in a boundary layer with complex geometries. None of the former models would have captured the probable acoustic wave propagating upstream of the indentations in Section 5.2.2 which the LHNS captures, for a hardly greater computational overhead compared to PSE.

As an exact representation of the flow disturbance problem, there is a clear predominance of the NLHNS approach introduced in this thesis compared to the level of modelling offered by the NLPSE. The verification and validation procedure followed in Section 6.1 has demonstrated the correctness of the method and a near-perfect match with NLPSE on the considered cases. We stress anew that the NLHNS can seamlessly incorporate the effect of short-scale features or the influence of geometrically-induced LSBs. Additional work is required to ascertain the performance of the method in highly non-linear regimes. The approaches mentioned in Section 6.4 have potential to further stabilise the iterative algorithm based on the self-correction of resonant forcing. This would be of utmost importance in those regimes where the MFD sustains high amplitude right before breakdown.

Furthermore, the cylindrical roughness element in the application cases of Sections 6.2 and 6.3 is not *meshed*, but *modelled* via a Taylor expansion of the no-slip velocity field on the wall surface. We note that surface suction or blowing can be modelled similarly. Tempelmann et al. (2012) compared the two approaches in their study involving a localised cylindrical element on a swept wing. They noted an excellent agreement in the receptivity amplitude between the meshed roughness and the modelled roughness when its height remains below 10% of the displacement thickness at the roughness position. Nonetheless, there was a 14% difference when the roughness height was increased to 30%, and an increasing gap for greater heights. This provides an important rule of thumb to assess the validity of the roughness model. Future work may involve assessing how the truncation order of the Taylor expansion affects the accuracy of the approach.

The application cases in Sections 6.2 and 6.3 feature 'simple' transition scenarios; the incoming TS wave has been modelled as a $(1, 0)$ monochromatic wave, while only the stationary CF has been considered on the AERAST swept wing. If more light is shed on the outstanding questions above and the NLHNS maturity is further established, the capability may be deployed for more complex transition scenarios. For instance, experiments with precise mode initialisation or spectral content may be matched and numerically replicated. This would include any known breakdown mechanism, whether it is a fundamental resonance of K-type, a subharmonic resonance of 'H-type' (Herbert, 1988) or oblique breakdown ('O-type'). For example, the travelling CF generated by an unsteady disturbance and interacting with a roughness element on a swept-wing could be investigated. Another possibility is the stabilisation of TS waves via arrays of miniature vortex generators (Shahinfar et al., 2013). The NLHNS method also opens up prospects for preliminary studies involving HLFC, such as the control of CF vortices using

distributed roughness elements (Saric et al., 1998; Hosseini et al., 2013; Mughal & Ashworth, 2013).

One might conceivably contemplate that the NLHNS is an appropriate complement to the wind tunnel, since it is convenient to extract quantities of interest that remain difficult to measure experimentally. An example is the streamwise vorticity in the wake of an isolated roughness element. In addition, the NLHNS embodies an accurate transition prediction capability. Just as the NLPSE, the method is able to capture the sudden increase of averaged wall shear resulting from the contribution of the MFD. The added value relies on the detection of absolute instability or reversed-flow regions, made possible by the ellipticity of the method. Streamwise regions with negative wall shear could characterise unsteady flow separation in the transition region, as suggested by Chang and Malik (1994).

The NLHNS ellipticity also reinforces the attractiveness of the method with compressible flows featuring long-range acoustic feedback loops that drive global modes. Typical problems include the generation of tonal noise around aerofoils, or flows over open rectangular cavities. By its very nature, the NLHNS also entails an advantage over another method allowing global stability analysis, namely resolvent analysis. The latter approach has been associated with the measure of the flow system response to harmonic forcing from an input-output viewpoint. External noise, or surface roughness are examples of such forcings. The resolvent represents the dynamics of the linearised Navier-Stokes operator, which are described via the spatial distribution of inputs, outputs and the associated amplification (gain). Although Rigas, Sipp and Colonius (2021) extended the approach to account for non-linear interactions in boundary layers using a harmonic balance method, resolvent analysis remains limited to globally stable systems. On the other hand, NLHNS is able to operate in a globally unstable framework.

It is worth mentioning that one drawback of the NLHNS is the restriction to work in harmonic space, where stability is by nature associated to asymptotically long times. This makes it unsuitable to describe transient phenomena. In that sense, it is less flexible than time-stepping DNS. Nonetheless, there is a broad range of flow problems where the modal approach is justified, particularly in transition analysis. The NLHNS would appear as a candidate for being adopted as an industrial tool only if the associated computational requirements could be reduced at least by an order of magnitude. Computation times represent only a fraction of an equivalent DNS but remain greater than the cost of NLPSE with our implementation. We specifically devised the method to be memory-efficient so that the spanwise and temporal Fourier series could be truncated to $O(10)$

modes. Unless the performance of the LU factorisation is improved, there would be significant time overhead in performing $(2M+1) \times (N+1)$ numerical factorisations with truncations involving $O(100)$ modes.

Lastly, the modularity of the developed code could alleviate the issues related to excessive computing requirements for fully 3D problems. We have indeed used an FDM and a matrix-forming approach to discretise the operators associated with the HNS equations. The main bottleneck to faster turnaround times is the LU solver, which also restrains the discretisation to 2.5D base flows since the memory requirements remain prohibitive for 3D base flows. From the assessment of Abdelfattah et al. (2020),

> 'One of the challenges with high-order methods is that a global sparse matrix is no longer a good representation of a high-order linear operator, both with respect to the [flop]s needed for its evaluation, as well as the memory transfer needed for a [matrix-vector multiplication].'

Such numerical libraries that build on these concepts provide efficient alternative high-order discretisation methods which could form a new bedrock for the considered HNS problems. These could offer a performance breakthrough when used conjointly with recent preconditioners targetting incompressible Navier-Stokes equations mentioned in Section 4.3.2.

– Bibliography –

Abdelfattah, A., Barra, V., Beams, N., Brown, J., Camier, J.-S., Dobrev, V., Dudouit, Y., Ghaffari, L., Kolev, T., Medina, D., Rathnayake, T., Thompson, J. L. & Tomov, S. (2020) *libCEED user manual*. Version 0.7. DOI: 10.5281/zenodo.4302737.

Airbus (2019) *Global market forecast 2019–2038: cities, airport & aircraft*. Airbus SAS, Blagnac, France.

Airiau, C. (1994) *Stabilité linéaire et faiblement non linéaire d'une couche limite laminaire incompressible par un système d'équations parabolisé (PSE) [Linear and weakly non-linear stability of an incompressible laminar boundary layer using Parabolised Stability Equations (PSE)]*. PhD thesis. École Nationale Supérieure de l'Aéronautique et de l'Espace, Toulouse, France.

Åkervik, E., Brandt, L., Henningson, D. S., Hœpffner, J., Marxen, O. & Schlatter, P. (2006) Steady solutions of the Navier-Stokes equations by selective frequency damping. *Physics of Fluids*. 18 (6), 068102. DOI: 10.1063/1.2211705.

Alam, M. & Sandham, N. D. (2000) Direct numerical simulation of 'short' laminar separation bubbles with turbulent reattachment. *Journal of Fluid Mechanics*. 410, 1–28. DOI: 10.1017/s0022112099008976.

Amestoy, P. R., Duff, I. S., L'Excellent, J.-Y. & Koster, J. (2001) A fully asynchronous multifrontal solver using distributed dynamic scheduling. *SIAM Journal on Matrix Analysis and Applications*. 23 (1), 15–41. DOI: 10.1137/s0895479899358194.

Andersson, P., Henningson, D. S. & Hanifi, A. (1998) On a stabilization procedure for the parabolic stability equations. *Journal of Engineering Mathematics*. 33 (3), 311–332. DOI: 10.1023/a:1004367704897.

Appel, T., Cooke, E., Mughal, S. & Ashworth, R. (2021) BiGlobal stability analysis of swept-wing boundary layers with forward and backward facing steps. In: Sherwin, S., Schmid, P. & Wu, X. (eds.), *Laminar-Turbulent Transition: 9th IUTAM Symposium, London, UK, September 2–6, 2019*. IUTAM, 38. Cham, Switzerland, Springer. DOI: 10.1007/978-3-030-67902-6_30.

Appel, T., Mughal, S. & Ashworth, R. (2019) Global stability analysis of a boundary layer with surface indentations. In: *2019 AIAA Aviation Forum, Fluid Dynamics Conference, 17–21 June 2019, Dallas, TX*. AIAA Paper 2019-3537. DOI: 10.2514/6.2019-3537.

Arnal, D. (1989) Transition prediction in transonic flow. In: Zierep, J. & Oertel, H. (eds.), *Symposium Transsonicum III. IUTAM Symposium, 24–27 May 1988, Göttingen, Germany*. IUTAM Symposia. Berlin, Heidelberg, Germany, Springer, pp. 253–262. DOI: 10.1007/978-3-642-83584-1_21.

Arnal, D. (1994) Boundary layer transition: predictions based on linear theory. In: *Special Course on Progress in Transition Modelling*. Report number: AGARD-R-793.

Arnal, D. & Casalis, G. (2000) Laminar-turbulent transition prediction in three-dimensional flows. *Progress in Aerospace Sciences*. 36 (2), 173–191. DOI: 10.1016/s0376-0421(00)00002-6.

Arnoldi, W. E. (1951) The principle of minimized iterations in the solution of the matrix eigenvalue problem. *Quarterly of Applied Mathematics*. 9 (1), 17–29. DOI: 10.1090/qam/42792.

Ashworth, R. & Mughal, S. (2015) Modeling three dimensional effects on cross flow instability from leading edge dimples. *Procedia IUTAM*. 14: *IUTAM_ABCM Symposium on Laminar Turbulent Transition*, 201–210. DOI: 10.1016/j.piutam.2015.03.041.

Avanci, M. P., Rodríguez, D. & Alves, L. S. de B. (2019) A geometrical criterion for absolute instability in separated boundary layers. *Physics of Fluids*. 31 (1), 014103. DOI: 10.1063/1.5079536.

Balay, S., Abhyankar, S., Adams, M. F., Brown, J., Brune, P., Buschelman, K., Dalcin, L., Dener, A., Eijkhout, V., Gropp, W. D., Karpeyev, D., Kaushik, D., Knepley, M. G., May, D. A., McInnes, L. C., Mills, R. T., Munson, T., Rupp, K., Sanan, P., Smith, B. F., Zampini, S., Zhang, H. & Zhang, H. (2020) *PETSc users manual*. Argonne National Laboratory, Lemont, IL. Report number: ANL-95/11 - Revision 3.13.

Benzi, M. & Olshanskii, M. A. (2006) An augmented Lagrangian-based approach to the Oseen problem. *SIAM Journal on Scientific Computing*. 28 (6), 2095–2113. DOI: 10.1137/050646421.

Benzi, M., Olshanskii, M. A. & Wang, Z. (2011) Modified augmented Lagrangian preconditioners for the incompressible Navier-Stokes equations. *International Journal for Numerical Methods in Fluids*. 66 (4), 486–508. DOI: 10.1002/fld.2267.

Benzi, M. & Wathen, A. J. (2008) Some preconditioning techniques for saddle point problems. In: Schilders, W. H. A., van der Vorst, H. A. & Rommes, J. (eds.), *Model Order Reduction: Theory, Research Aspects and Applications*. Mathematics in Industry, 13. Berlin, Heidelberg, Germany, Springer, pp. 195–211. DOI: 10.1007/978-3-540-78841-6_10.

Berenger, J.-P. (1994) A perfectly matched layer for the absorption of electromagnetic waves. *Journal of Computational Physics*. 114 (2), 185–200. DOI: 10.1006/jcph.1994.1159.

Bérenger, J.-P. (2007) *Perfectly Matched Layer (PML) for computational electromagnetics*. Synthesis Lectures on Computational Electromagnetics, 8. San Rafael, CA, Morgan & Claypool. DOI: 10.2200/S00030ED1V01Y200605CEM008.

Bertolotti, F. P. (1991) *Linear and nonlinear stability of boundary layers with streamwise varying properties*. PhD thesis. Ohio State University, Colombus, OH.

Bhatnagar, P. L., Gross, E. P. & Krook, M. (1954) A model for collision processes in gases. I. Small amplitude processes in charged and neutral one-component systems. *Physical Review*. 94 (3), 511–525. DOI: 10.1103/PhysRev.94.511.

Bodony, D. J. (2006) Analysis of sponge zones for computational fluid mechanics. *Journal of Computational Physics*. 212 (2), 681–702. DOI: 10.1016/j.jcp.2005.07.014.

Boeing Commercial Airplane Group (1999) *High Reynolds number Hybrid Laminar Flow Control (HLFC) flight experiment IV. Suction system design and manufacture*. National Aeronautics and Space Administration, Hampton, VA. Report number: NASA/CR-1999-209326.

Bouthier, M. (1972) Stabilité linéaire des écoulements presque parallèles [Linear stability of quasi-parallel flows]. *Journal de Mécanique [Journal of Mechanics]*. 11 (4), 599–621.

Bouthier, M. (1973) Stabilité linéaire des écoulements presque parallèles. Partie II. La couche limite de Blasius [Linear stability of quasi-parallel flows. Part II. The Blasius boundary layer]. *Journal de Mécanique [Journal of Mechanics]*. 12 (1), 75–95.

Boyd, J. P. (1999) The Blasius function in the complex plane. *Experimental Mathematics*. 8 (4), 381–394. DOI: 10.1080/10586458.1999.10504626.

Cantwell, C. D., Moxey, D., Comerford, A., Bolis, A., Rocco, G., Mengaldo, G., De Grazia, D., Yakovlev, S., Lombard, J.-E., Ekelschot, D., Jordi, B., Xu, H., Mohamied, Y., Eskilsson, C., Nelson, B., Vos, P., Biotto, C., Kirby, R. M. & Sherwin, S. J. (2015)

Nektar++: an open-source spectral/hp element framework. *Computer Physics Communications*. 192, 205–219. DOI: 10.1016/j.cpc.2015.02.008.

Canuto, C., Hussaini, M. Y., Quarteroni, A. & Zang, T. A. (1988) *Spectral methods in fluid dynamics*. Springer Series in Computational Physics. New York, NY, Springer. DOI: 10.1007/978-3-642-84108-8.

Casalis, G. & Arnal, D. (1996) *ELFIN II, subtask 2.3: database method. Development and validation of a simplified method for pure crossflow instability at low speed*. Office National d'Études et de Recherches Aérospatiales, France. Report number: 119/5618.16.

Cebeci, T. & Egan, D. A. (1989) Prediction of transition due to isolated roughness. *AIAA Journal*. 27 (7), 870–875. DOI: 10.2514/3.10194.

Chang, C.-L. (2004) *Langley Stability and Transition Analysis Code (LASTRAC) version 1.2 user manual*. National Aeronautics and Space Administration, Hampton, VA. Report number: NASA/CR-2004-213233.

Chang, C.-L. & Choudhari, M. (2005) Boundary-layer receptivity and integrated transition prediction. In: *43rd AIAA Aerospace Sciences Meeting and Exhibit, 10–13 January 2005, Reno, NV*. AIAA Paper 2008-0526. DOI: 10.2514/6.2005-526.

Chang, C.-L. & Malik, M. R. (1994) Oblique-mode breakdown and secondary instability in supersonic boundary layers. *Journal of Fluid Mechanics*. 273, 323–360. DOI: 10.1017/s0022112094001965.

Chapman, S. & Cowling, T. G. (1970) *The mathematical theory of non-uniform gases: an account of the kinetic theory of viscosity, thermal conduction and diffusion in gases*. 3rd ed. Cambridge, United Kingdom, Cambridge University Press.

Chorin, A. J. (1967) A numerical method for solving incompressible viscous flow problems. *Journal of Computational Physics*. 2 (1), 12–26. DOI: 10.1016/0021-9991(67)90037-X.

Chorin, A. J. (1968) Numerical solution of the Navier-Stokes equations. *Mathematics of Computation*. 22, 745–762. DOI: 10.1090/S0025-5718-1968-0242392-2.

Citro, V., Luchini, P., Giannetti, F. & Auteri, F. (2017) Efficient stabilization and acceleration of numerical simulation of fluid flows by residual recombination. *Journal of Computational Physics*. 344, 234–246. DOI: 10.1016/j.jcp.2017.04.081.

Collino, F. & Monk, P. B. (1998) Optimizing the perfectly matched layer. *Computer Methods in Applied Mechanics and Engineering*. 164 (1–2), 157–171. DOI: 10.1016/S0045-7825(98)00052-8.

Cooke, E., Mughal, S., Sherwin, S., Ashworth, R. & Rolston, S. (2019) Destabilisation of stationary and travelling crossflow disturbances due to steps over a swept wing. In: *2019 AIAA Aviation Forum, Fluid Dynamics Conference, 17–21 June 2019, Dallas, TX*. AIAA Paper 2019-3533. DOI: 10.2514/6.2019-3533.

Cooke, J. C. (1950) The boundary layer of a class of infinite yawed cylinders. *Mathematical Proceedings of the Cambridge Philosophical Society*. 46 (4), 645–648. DOI: 10.1017/S0305004100026220.

Cossu, C. & Brandt, L. (2004) On Tollmien-Schlichting-like waves in streaky boundary layers. *European Journal of Mechanics - B/Fluids*. 23 (6), 815–833. DOI: 10.1016/j.euromechflu.2004.05.001.

Criminale, W. O., Jackson, T. L. & Joslin, R. D. (2003) *Theory and computation of hydrodynamic stability*. Cambridge, United Kingdom, Cambridge University Press. DOI: 10.1017/CBO9780511550317.

Crouch, J. D. (1997) Transition prediction and control for airplane applications. In: *28th Fluid Dynamics Conference, 29 June–2 July 1997, Snowmass Village, CO*. AIAA Paper 97-1907. DOI: 10.2514/6.1997-1907.

Crouch, J. D., Crouch, I. W. M. & Ng, L. L. (2002) Transition prediction for three-dimensional boundary layers in computational fluid dynamics applications. *AIAA Journal*. 40 (8), 1536–1541. DOI: 10.2514/2.1850.

Crouch, J. D. & Kosorygin, V. S. (2020) Surface step effects on boundary-layer transition dominated by Tollmien-Schlichting instability. *AIAA Journal*. 58 (7), 2943–2950. DOI: 10.2514/1.j058518.

Crouch, J. D., Kosorygin, V. S. & Ng, L. L. (2006) Modeling the effects of steps on boundary-layer transition. In: Govindarajan, R. (ed.), *IUTAM Symposium on Laminar-Turbulent Transition*. Fluid Mechanics and Its Applications, 78. Springer, pp. 37–44. DOI: 10.1007/1-4020-4159-4_4.

Crouch, J. D. & Ng, L. L. (2000) Variable N-factor method for transition prediction in three-dimensional boundary layers. *AIAA Journal*. 38 (2), 211–216. DOI: 10.2514/2.973.

Dagenhart, J. R. (1981) *Amplified crossflow disturbances in the laminar boundary layer on swept wings with suction*. National Aeronautics and Space Administration, Hampton, VA. Report number: NASA TP-1902.

Dagenhart, J. R. & Saric, W. S. (1999) *Crossflow stability and transition experiments in swept-wing flow*. National Aeronautics and Space Administration, Hampton, VA. Report number: NASA/TP-1999-209344.

De Paula, I. B., Wurz, W. & Medeiros, M. A. F. (2008) Experimental study of a Tollmien-Schlichting wave interacting with a shallow 3D roughness element. *Journal of Turbulence*. 9, N7. DOI: 10.1080/14685240701790706.

De Paula, I. B., Würz, W., Mendonça, M. T. & Medeiros, M. A. F. (2017) Interaction of instability waves and a three-dimensional roughness element in a boundary layer. *Journal of Fluid Mechanics*. 824, 624–660. DOI: 10.1017/jfm.2017.362.

Deyhle, H. & Bippes, H. (1996) Disturbance growth in an unstable three-dimensional boundary layer and its dependence on environmental conditions. *Journal of Fluid Mechanics*. 316, 73–113. DOI: 10.1017/s0022112096000456.

Diwan, S. S. & Ramesh, O. N. (2009) On the origin of the inflectional instability of a laminar separation bubble. *Journal of Fluid Mechanics*. 629, 263–298. DOI: 10.1017/s002211200900634x.

Drake, A., Bender, A. M., Korntheuer, A. J., Westphal, R. V., Rohe, W., Dale, G., McKeon, B. J. & Geraschchenko, S. (2010) Step excrescence effects for manufacturing tolerances on laminar flow wings. In: *48th AIAA Aerospace Sciences Meeting Including the New Horizons Forum and Aerospace Exposition*, *4–7 January 2010*, *Orlando, FL*. AIAA Paper 2010-0375. DOI: 10.2514/6.2010-375.

Drake, A., Bender, A. M. & Westphal, R. V. (2008) Transition due to surface steps in the presence of favorable pressure gradients. In: *26th AIAA Applied Aerodynamics Conference*, *18–21 August 2008*, *Honolulu, HI*. AIAA Paper 2008-7334. DOI: 10.2514/6.2008-7334.

Drazin, P. G. & Reid, W. H. (2004) *Hydrodynamic stability*. 2nd ed. Cambridge Monographs on Mechanics and Applied Mathematics. Cambridge, United Kingdom, Cambridge University Press. DOI: 10.1017/CBO9780511616938.

Drela, M. (1989) XFOIL: an analysis and design system for low Reynolds number airfoils. In: Mueller, T. J. (ed.), *Low Reynolds Number Aerodynamics: Proceedings of the Conference Notre Dame, Indiana, USA, 5–7 June 1989*. Lecture Notes in Engineering, 54. Berlin, Heidelberg, Germany, Springer, pp. 1–12. DOI: 10.1007/978-3-642-84010-4_1.

Drela, M. (2003) Implicit implementation of the full e^N transition criterion. In: *21st AIAA Applied Aerodynamics Conference*, *23–26 June 2003*, *Orlando, FL*. AIAA Paper 2003-4066. DOI: 10.2514/6.2003-4066.

Duncan Jr., G. T., Crawford, B., Tufts, M. W., Saric, W. S. & Reed, H. L. (2014) Effects of step excrescences on a swept wing in a low-disturbance wind tunnel. In: *52nd Aerospace Sciences Meeting, 13–17 January 2014, National Harbor, MD*. AIAA Paper 2014-0910. DOI: 10.2514/6.2014-0910.

Durbin, P. A., Jacobs, R. G. & Wu, X. (2002) DNS of bypass transition. In: Launder, B. E. & Sandham, N. D. (eds.), *Closure Strategies for Turbulent and Transitional Flows*. Cambridge, United Kingdom, Cambridge University Press, pp. 449–463. DOI: 10.1017/cbo9780511755385.018.

Duru, K. & Kreiss, G. (2012) A well-posed and discretely stable perfectly matched layer for elastic wave equations in second order formulation. *Communications in Computational Physics*. 11 (5), 1643–1672. DOI: 10.4208/cicp.120210.240511a.

Edwards, W. S., Tuckerman, L. S., Friesner, R. A. & Sorensen, D. C. (1994) Krylov methods for the incompressible Navier-Stokes equations. *Journal of Computational Physics*. 110 (1), 82–102. DOI: 10.1006/jcph.1994.1007.

Ellingsen, T. & Palm, E. (1975) Stability of linear flow. *Physics of Fluids*. 18 (4), 487. DOI: 10.1063/1.861156.

Elman, H., Howle, V. E., Shadid, J., Shuttleworth, R. & Tuminaro, R. (2008) A taxonomy and comparison of parallel block multi-level preconditioners for the incompressible Navier-Stokes equations. *Journal of Computational Physics*. 227 (3), 1790–1808. DOI: 10.1016/j.jcp.2007.09.026.

Emmons, H. W. (1951) The laminar-turbulent transition in a boundary layer—Part I. *Journal of the Aeronautical Sciences*. 18 (7), 490–498. DOI: 10.2514/8.2010.

Eppink, J. L. (2020) Mechanisms of stationary cross-flow instability growth and breakdown induced by forward-facing steps. *Journal of Fluid Mechanics*. 897 (A15). DOI: 10.1017/jfm.2020.367.

Eppink, J. L., Wlezien, R. W., King, R. A. & Choudhari, M. (2018) Interaction of a backward-facing step and crossflow instabilities in boundary-layer transition. *AIAA Journal*. 56 (2), 497–509. DOI: 10.2514/1.j056267.

Ergin, F. G. & White, E. B. (2006) Unsteady and transitional flows behind roughness elements. *AIAA Journal*. 44 (11), 2504–2514. DOI: 10.2514/1.17459.

Eriksson, L. E. & Rizzi, A. (1985) Computer-aided analysis of the convergence to steady state of discrete approximations to the Euler equations. *Journal of Computational Physics*. 57 (1), 90–128. DOI: 10.1016/0021-9991(85)90054-3.

European Commission (2012) *Flightpath 2050 - Europe's vision for aviation: report of the High-Level Group on aviation research*. European Commission, Brussels, Belgium. DOI: 10.2777/15458.

Fage, A. (1943) *The smallest size of a spanwise surface corrugation which affects boundary-layer transition on an aerofoil*. Aeronautical Research Council, United Kingdom. Report number: 2120.

Falkner, V. M. & Skan, S. W. (1931) Solutions of the boundary-layer equations. *The London, Edinburgh, and Dublin Philosophical Magazine and Journal of Science*. 12 (80), 865–896. DOI: 10.1080/14786443109461870.

Farrell, B. F. (1988) Optimal excitation of perturbations in viscous shear flow. *Physics of Fluids*. 31 (8), 2093–2102. DOI: 10.1063/1.866609.

Farrell, P. E., Mitchell, L., Scott, L. R. & Wechsung, F. (2020) A Reynolds-robust preconditioner for the Reynolds-robust Scott-Vogelius discretization of the stationary incompressible Navier-Stokes equations. ArXiv. [Preprint] Available from: 2004.09398 [math.NA].

Farrell, P. E., Mitchell, L. & Wechsung, F. (2019) An augmented Lagrangian preconditioner for the 3D stationary incompressible Navier-Stokes equations at high Reynolds number. *SIAM Journal on Scientific Computing*. 41 (5), A3073–A3096. DOI: 10.1137/18m1219370.

Fasel, H. F., Meitz, H. L. & Bachman, C. R. (1997) DNS and LES for investigating transition and transition control. In: *28th Fluid Dynamics Conference, 29 June–2 July 1997, Snowmass Village, CO*. AIAA Paper 97-1820. DOI: 10.2514/6.1997-1820.

Flanigan, F. J. (1983) *Complex variables: harmonic and analytic functions*. New York, NY, Dover.

Franco Sumariva, J. A., Hein, S. & Valero, E. (2020) On the influence of two-dimensional hump roughness on laminar-turbulent transition. *Physics of Fluids*. 32 (3), 034102. DOI: 10.1063/1.5131577.

Fransson, J. H. M., Brandt, L., Talamelli, A. & Cossu, C. (2005) Experimental study of the stabilization of Tollmien-Schlichting waves by finite amplitude streaks. *Physics of Fluids*. 17 (5), 054110. DOI: 10.1063/1.1897377.

Frigo, M. & Johnson, S. G. (2005) The design and implementation of FFTW3. *Proceedings of the IEEE*. 93 (2), 216–231. DOI: 10.1109/jproc.2004.840301.

Fuller, R. M., Saunders, W. M. & Vandsburger, U. (1997) Neural network estimation of disturbance growth using a linear stability numerical model. In: *35th Aerospace Sciences Meeting and Exhibit, 6–9 January 1997, Reno, NV*. AIAA Paper 97-0559. DOI: 10.2514/6.1997-559.

Gaster, M. (1962) A note on the relation between temporally-increasing and spatially-increasing disturbances in hydrodynamic stability. *Journal of Fluid Mechanics*. 14 (2), 222–224. DOI: 10.1017/S0022112062001184.

Gaster, M. (1965) A simple device for preventing turbulent contamination on swept leading edges. *The Journal of the Royal Aeronautical Society*. 69 (659), 788–789. DOI: 10.1017/s0368393100081748.

Gaster, M. (1967) On the flow along swept leading edges. *Aeronautical Quarterly*. 18 (2), 165–184. DOI: 10.1017/S0001925900004170.

Gaster, M. (1974) On the effects of boundary-layer growth on flow stability. *Journal of Fluid Mechanics*. 66 (3), 465–480. DOI: 10.1017/s0022112074000310.

Gaster, M., Grosch, C. E. & Jackson, T. L. (1994) The velocity field created by a shallow bump in a boundary layer. *Physics of Fluids*. 6 (9), 3079–3085. DOI: 10.1063/1.868132.

Gaster, M. & Jiang, F. (1994) A rapid scheme for estimating transition on wings by linear stability theory. In: *Proceedings of the 19th Congress of the International Council of the Aeronautical Sciences. 18–23 September 1994, Anaheim, CA*. Vol. 2. Washington, DC, American Institute of Aeronautics & Astronautics, pp. 1104–1113.

George, A. (1973) Nested dissection of a regular finite element mesh. *SIAM Journal on Numerical Analysis*. 10 (2), 345–363. DOI: 10.1137/0710032.

Germano, M., Piomelli, U., Moin, P. & Cabot, W. H. (1991) A dynamic subgrid-scale eddy viscosity model. *Physics of Fluids A: Fluid Dynamics*. 3 (7), 1760–1765. DOI: 10.1063/1.857955.

Goldstein, M. E. (1985) Scattering of acoustic waves into Tollmien-Schlichting waves by small streamwise variations in surface geometry. *Journal of Fluid Mechanics*. 154, 509–529. DOI: 10.1017/s0022112085001641.

Görtler, H. (1941) Instabilität laminarer Grenzschichten an konkaven Wänden gegenüber gewissen dreidimensionalen Störungen [Instability of laminar boundary layers on concave walls against certain three-dimensional disturbances]. *Zeitschrift für Angewandte Mathematik und Mechanik [Journal of Applied Mathematics and Mechanics]*. 21 (4), 250–252. DOI: 10.1002/zamm.19410210408.

Granville, P. S. (1953) *The calculation of the viscous drag of bodies of revolution*. David W. Taylor Model Basin, Washington, DC. Report number: 849.

Gray, W. E. (1952) *The effect of wing sweep on laminar flow*. Royal Aircraft Establishment, Farnborough, United Kingdom. Report number: 255.

Gregory, N., Stuart, J. T. & Walker, W. S. (1955) On the stability of three-dimensional boundary layers with application to the flow due to a rotating disk. *Philosophical Transactions of the Royal Society of London. Series A, Mathematical and Physical Sciences*. 248 (943), 155–199. DOI: 10.1098/rsta.1955.0013.

Gresho, P. M. & Sani, R. L. (1987) On pressure boundary conditions for the incompressible Navier-Stokes equations. *International Journal for Numerical Methods in Fluids*. 7 (10), 1111–1145. DOI: 10.1002/fld.1650071008.

Groot, K. (2018) *BiGlobal stability of shear flows: spanwise & streamwise analyses*. PhD thesis. Delft University of Technology, Netherlands. DOI: 10.4233/uuid:60ef07b2-00db-418b-9495-5a9baf6105df.

Groot, K. J., Pinna, F. & van Oudheusden, B. W. (2015) On closing the streamwise BiGlobal stability problem: the effect of boundary conditions. *Procedia IUTAM*. 14: *IUTAM_ABCM Symposium on Laminar Turbulent Transition*, 459–468. DOI: 10.1016/j.piutam.2015.03.074.

Groot, K. J., Serpieri, J., Kotsonis, M. & Pinna, F. (2017) Secondary stability analysis of crossflow vortices using BiGlobal theory on PIV base flows. In: *55th AIAA Aerospace Sciences Meeting, 9–13 January 2017, Gravepine, TX*. AIAA Paper 2017-1880. DOI: 10.2514/6.2017-1880.

Grosch, C. E. & Salwen, H. (1978) The continuous spectrum of the Orr-Sommerfeld equation. Part 1. The spectrum and the eigenfunctions. *Journal of Fluid Mechanics*. 87 (1), 33–54. DOI: 10.1017/s0022112078002918.

Gubisch, M. (26 April 2018) ILA: Airbus encouraged by laminar-winged A340 trial. *FlightGlobal*. Available from: URL: https://www.flightglobal.com/airframers/ila-airbus-encouraged-by-laminar-winged-a340-trial/127896.article [Accessed 23 December 2020].

Gubisch, M. (13 February 2019) Clean Sky 2 to test hybrid laminar-flow demonstrators. *FlightGlobal*. Available from: URL: https://www.flightglobal.com/clean-sky-2-to-test-hybrid-laminar-flow-demonstrators/131372.article [Accessed 23 December 2020].

Gustafsson, B., Kreiss, H.-O. & Sundström, A. (1972) Stability theory of difference approximations for mixed initial boundary value problems. II. *Mathematics of Computation*. 26, 649–686. DOI: 10.1090/S0025-5718-1972-0341888-3.

Hagstrom, T., Goodrich, J., Nazarov, I. & Dodson, C. (2005) High-order methods and boundary conditions for simulating subsonic flows. In: *11th AIAA/CEAS Aeroacoustics Conference, 23–25 May 2005, Monterey, CA*. AIAA Paper 2005-2869. DOI: 10.2514/6.2005-2869.

Hall, P. (1983) The linear development of Görtler vortices in growing boundary layers. *Journal of Fluid Mechanics*. 130, 41–58. DOI: 10.1017/s0022112083000968.

Hall, P., Malik, M. R., Poll, D. I. A. & Stuart, J. T. (1984) On the stability of an infinite swept attachment line boundary layer. *Proceedings of the Royal Society of London. A. Mathematical and Physical Sciences*. 395 (1809), 229–245. DOI: 10.1098/rspa.1984.0099.

Hammond, D. A. & Redekopp, L. G. (1998) Local and global instability properties of separation bubbles. *European Journal of Mechanics - B/Fluids*. 17 (2), 145–164. DOI: 10.1016/s0997-7546(98)80056-3.

Hanifi, A. (2015) *RECEPT final report*. KTH Royal Institute of Technology, Stockholm, Sweden.

Harlow, F. H. & Welch, J. E. (1965) Numerical calculation of time-dependent viscous incompressible flow of fluid with free surface. *The Physics of Fluids*. 8 (12), 2182–2189. DOI: 10.1063/1.1761178.

Haynes, T. S. & Reed, H. L. (2000) Simulation of swept-wing vortices using nonlinear parabolized stability equations. *Journal of Fluid Mechanics*. 405, 325–349. DOI: 10.1017/S0022112099007260.

Hein, S. (2000) Linear and nonlinear nonlocal instability analyses for two-dimensional laminar separation bubbles. In: Fasel, H. F. & Saric, W. S. (eds.), *Laminar-Turbulent Transition. IUTAM Symposium, 13–17 September 1999, Sedona, AZ*. IUTAM Symposia. Berlin, Heidelberg, Germany, Springer, pp. 681–686. DOI: 10.1007/978-3-662-03997-7_106.

Hein, S. (2005) *Nonlinear nonlocal transition analysis*. PhD thesis. University of Stuttgart, Germany.

Hein, S., Bertolotti, F. P., Simen, M., Hanifi, A. & Henningson, D. (1994) *Linear nonlocal instability analysis - the linear NOLOT code*. Deutsches Zentrum für Luft- und Raumfahrt, Germany. Report number: DLR-IB 223-94 A56.

Henke, R. (1999) 'A 320 HLF fin' flight tests completed. *Air & Space Europe*. 1 (2), 76–79. DOI: 10.1016/s1290-0958(99)80019-7.

Herbert, T. (1988) Secondary instability of boundary layers. *Annual Review of Fluid Mechanics*. 20, 487–526. DOI: 10.1146/annurev.fl.20.010188.002415.

Herbert, T. (1997) Parabolized stability equations. *Annual Review of Fluid Mechanics*. 29, 245–283. DOI: 10.1146/annurev.fluid.29.1.245.

Herbert, T. & Bertolotti, F. P. (1987) Stability analysis of nonparallel boundary layers. *Bulletin of the American Physical Society*. 32, 2079.

Hermanns, M. & Hernández, J. A. (2007) Stable high-order finite-difference methods based on non-uniform grid point distributions. *International Journal for Numerical Methods in Fluids*. 56 (3), 233–255. DOI: 10.1002/fld.1510.

Hernández, V., Román, J. E., Tomás, A. & Vidal, V. (2009) *Krylov-Schur methods in SLEPc*. Universitat Politècnica de València, Spain. Report number: STR-7.

Hildebrand, N., Choudhari, M. M. & Paredes, P. (2020) Predicting boundary-layer transition over backward-facing steps via linear stability analysis. *AIAA Journal*. 58 (9), 3728–3734. DOI: 10.2514/1.j059713.

Hill, D. C. (1995) Adjoint systems and their role in the receptivity problem for boundary layers. *Journal of Fluid Mechanics*. 292, 183–204. DOI: 10.1017/s002211209 5001480.

Hirsch, C. (2007) *Numerical computation of internal and external flows*. Vol. 1: *Fundamentals of computational fluid dynamics*. 2nd ed. Oxford, United Kingdom, Butterworth-Heinemann. DOI: 10.1016/B978-0-7506-6594-0.X5037-1.

Holmes, B. J., Obara, C. J., Martin, G. L. & Domack, C. S. (1985) Manufacturing tolerances for natural laminar flow airframe surfaces. SAE Technical Paper 850863. DOI: 10.4271/850863.

Hosseini, S. M., Tempelmann, D., Hanifi, A. & Henningson, D. S. (2013) Stabilization of a swept-wing boundary layer by distributed roughness elements. *Journal of Fluid Mechanics*. 718. DOI: 10.1017/jfm.2013.33.

Hu, F. Q. (1996) On absorbing boundary conditions for linearized Euler equations by a perfectly matched layer. *Journal of Computational Physics*. 129 (1), 201–219. DOI: 10.1006/jcph.1996.0244.

Hu, F. Q. (2006) On the construction of PML absorbing boundary condition for the non-linear Euler equations. In: *44th AIAA Aerospace Sciences Meeting and Exhibit, 9–12 January 2006, Reno, NV*. AIAA Paper 2006-0798. DOI: 10.2514/6.2006-798.

Hu, F. Q., Li, X. D. & Lin, D. K. (2008) Absorbing boundary conditions for nonlinear Euler and Navier-Stokes equations based on the perfectly matched layer technique. *Journal of Computational Physics*. 227 (9), 4398–4424. DOI: 10.1016/j.jcp.2008.01.010.

Huerre, P. & Monkewitz, P. A. (1990) Local and global instabilities in spatially developing flows. *Annual Review of Fluid Mechanics*. 22, 473–537. DOI: 10.1146/annurev.fl.22.010190.002353.

Hultgren, L. S. & Håkan Gustavsson, L. (1981) Algebraic growth of disturbances in a laminar boundary layer. *Physics of Fluids*. 24 (6), 1000. DOI: 10.1063/1.863490.

International Energy Agency (2020) *Aviation*. International Energy Agency, Paris, France.

Israeli, M. & Orszag, S. A. (1981) Approximation of radiation boundary conditions. *Journal of Computational Physics*. 41 (1), 115–135. DOI: 10.1016/0021-9991(81)90082-6.

Itoh, N. (1986) The origin and subsequent development in space of Tollmien-Schlichting waves in a boundary layer. *Fluid Dynamics Research*. 1 (2), 119–130. DOI: 10.1016/0169-5983(86)90012-2.

Janke, E. & Balakumar, P. (1999) *On the stability of three-dimensional boundary layers. Part 1: linear and nonlinear stability*. National Aeronautics and Space Administration, Hampton, VA. Report number: NASA/CR-1999-209330.

Johnston, H. & Liu, J.-G. (2004) Accurate, stable and efficient Navier-Stokes solvers based on explicit treatment of the pressure term. *Journal of Computational Physics*. 199 (1), 221–259. DOI: 10.1016/j.jcp.2004.02.009.

Jordinson, R. (1971) Spectrum of eigenvalues of the Orr-Sommerfeld equation for Blasius flow. *Physics of Fluids*. 14 (11), 2535. DOI: 10.1063/1.1693363.

Joseph, D. D. (1976) *Stability of fluid motions I*. Springer Tracts in Natural Philosophy, 27. Berlin, Heidelberg, Germany, Springer. DOI: 10.1007/978-3-642-80991-0.

Joslin, R. D. (1998) Aircraft laminar flow control. *Annual Review of Fluid Mechanics*. 30, 1–29. DOI: 10.1146/annurev.fluid.30.1.1.

Kachanov, Y. S. & Levchenko, V. Y. (1984) The resonant interaction of disturbances at laminar-turbulent transition in a boundary layer. *Journal of Fluid Mechanics*. 138, 209–247. DOI: 10.1017/S0022112084000100.

Kerschen, E. (1989) Boundary layer receptivity. In: *AIAA 12th Aeroacoustic Conference, 10–12 April 1989, San Antonio, TX*. AIAA Paper 89-1109. DOI: 10.2514/6.1989-1109.

Kharina, A. & Rutherford, D. (2015) *Fuel efficiency trends for new commercial jet aircraft: 1960 to 2014*. International Council on Clean Transportation, Washington, DC.

Klebanoff, P. S., Tidstrom, K. D. & Sargent, L. M. (1962) The three-dimensional nature of boundary-layer instability. *Journal of Fluid Mechanics*. 12 (1), 1–34. DOI: 10.1017/s0022112062000014.

Kroll, N., Langer, S. & Schwöppe, A. (2014) The DLR flow solver TAU - status and recent algorithmic developments. In: *52nd Aerospace Sciences Meeting, 13–17 January 2014, National Harbor, MD*. AIAA Paper 2014-0080. DOI: 10.2514/6.2014-0080.

Kroo, I. (2001) Drag due to lift: concepts for prediction and reduction. *Annual Review of Fluid Mechanics*. 33, 587–617. DOI: 10.1146/annurev.fluid.33.1.587.

Kuzuoglu, M. & Mittra, R. (1996) Frequency dependence of the constitutive parameters of causal perfectly matched anisotropic absorbers. *IEEE Microwave and Guided Wave Letters*. 6 (12), 447–449. DOI: 10.1109/75.544545.

Landahl, M. T. (1975) Wave breakdown and turbulence. *SIAM Journal on Applied Mathematics*. 28 (4), 735–756. DOI: 10.1137/0128061.

Landahl, M. T. (1980) A note on an algebraic instability of inviscid parallel shear flows. *Journal of Fluid Mechanics*. 98 (2), 243–251. DOI: 10.1017/s0022112080000122.

Lee, D. S., Fahey, D. W., Forster, P. M., Newton, P. J., Wit, R. C. N., Lim, L. L., Owen, B. & Sausen, R. (2009) Aviation and global climate change in the 21st century. *Atmospheric Environment*. 43 (22-23), 3520–3537. DOI: 10.1016/j.atmosenv.2009.04.024.

Lele, S. K. (1992) Compact finite difference schemes with spectral-like resolution. *Journal of Computational Physics*. 103 (1), 16–42. DOI: 10.1016/0021-9991(92)90324-R.

Lessen, M. & Gangwani, S. T. (1976) Effect of small amplitude wall waviness upon the stability of the laminar boundary layer. *Physics of Fluids*. 19 (4), 510. DOI: 10.1063/1.861515.

LeVeque, R. J. (2007) *Finite difference methods for ordinary and partial differential equations: steady-state and time-dependent problems*. Other Titles in Applied Mathematics. Philadelphia, PA, Society for Industrial and Applied Mathematics. DOI: 10.1137/1.9780898717839.

Li, F. & Malik, M. R. (1995) Mathematical nature of parabolized stability equations. In: Kobayashi, R. (ed.), *Laminar-Turbulent Transition*. *IUTAM Symposium, 5–9 September 1994, Sendai, Japan*. Berlin, Germany, Springer, pp. 205–212. DOI: 10.1007/978-3-642-79765-1_24.

Lin, R.-S. & Malik, M. R. (1996) On the stability of attachment-line boundary layers. Part 1. The incompressible swept Hiemenz flow. *Journal of Fluid Mechanics*. 311, 239–255. DOI: 10.1017/S0022112096002583.

Liseikin, V. D. (2010) *Grid generation methods*. 2nd ed. Scientific Computation. Dordrecht, Netherlands, Springer. DOI: 10.1007/978-90-481-2912-6.

Löhner, R. (2019) Towards overcoming the LES crisis. *International Journal of Computational Fluid Dynamics*. 33 (3), 87–97. DOI: 10.1080/10618562.2019.1612052.

Mack, L. M. (1976) A numerical study of the temporal eigenvalue spectrum of the Blasius boundary layer. *Journal of Fluid Mechanics*. 73 (3), 497–520. DOI: 10.1017/S002211207600147X.

Mack, L. M. (1977) *Transition and laminar instability*. Jet Propulsion Laboratory, Pasadena, CA. Report number: NASA-CR-153203.

Mack, L. M. (1984) Boundary-layer linear stability theory. In: *Special Course on Stability and Transition of Laminar Flow*. Report number: AGARD-R-709.

Malik, M. R. (1990) Numerical methods for hypersonic boundary layer stability. *Journal of Computational Physics*. 86 (2), 376–413. DOI: 10.1016/0021-9991(90)90106-B.

Malik, M. R., Li, F. & Chang, C.-L. (1994) Crossflow disturbances in three-dimensional boundary layers: nonlinear development, wave interaction and secondary instability. *Journal of Fluid Mechanics*. 268, 1–36. DOI: 10.1017/s0022112094001242.

Malik, M. R., Li, F., Choudhari, M. M. & Chang, C.-L. (1999) Secondary instability of crossflow vortices and swept-wing boundary-layer transition. *Journal of Fluid Mechanics*. 399, 85–115. DOI: 10.1017/s0022112099006291.

Marec, J.-P. (2001) Drag reduction: a major task for research. In: Thiede, P. (ed.), *Aerodynamic Drag Reduction Technologies: Proceedings of the CEAS/DragNet European Drag Reduction Conference, 19–21 June 2000, Potsdam, Germany*. Notes on Numerical Fluid Mechanics, 76. Berlin, Heidelberg, Germany, Springer, pp. 17–27. DOI: 10.1007/978-3-540-45359-8_3.

Masad, J. A. & Iyer, V. (1994) Transition prediction and control in subsonic flow over a hump. *Physics of Fluids*. 6 (1), 313–327. DOI: 10.1063/1.868086.

McLean, D. (2012) *Understanding aerodynamics: arguing from the real physics*. Chichester, United Kingdom, John Wiley & Sons. DOI: 10.1002/9781118454190.

Menter, F. R., Langtry, R. & Völker, S. (2006) Transition modelling for general purpose CFD codes. *Flow, Turbulence and Combustion*. 77 (1-4), 277–303. DOI: 10.1007/s10494-006-9047-1.

Michel, R. (1951) *Étude de la transition sur les profils d'aile. Établissement d'un critère de détermination de point de transition et calcul de la traînée de profil incompressible [Study of transition on wing profiles. Establishment of a criterion to determine transition location and computation of incompressible profile drag]*. Office National d'Études et de Recherches Aérospatiales, France. Report number: 1/1578A.

Morkovin, M. V. (1969a) *Critical evaluation of transition from laminar to turbulent shear layers with emphasis on hypersonically traveling bodies*. Research Institute for Advanced Studies, Baltimore, MD. Report number: AFFDL-TR-68-149.

Morkovin, M. V. (1969b) On the many faces of transition. In: Wells, C. S. (ed.), *Viscous Drag Reduction: Proceedings of the Symposium on Viscous Drag Reduction held at the LTV Research Center, Dallas, Texas, September 24 and 25, 1968*. Boston, MA, Springer, pp. 1–31. DOI: 10.1007/978-1-4899-5579-1_1.

Morkovin, M. V., Reshotko, E. & Herbert, T. (1994) Transition in open flow systems - a reassessment. *Bulletin of the American Physical Society*. 39 (9), 1882.

Moulin, J., Jolivet, P. & Marquet, O. (2019) Augmented Lagrangian preconditioner for large-scale hydrodynamic stability analysis. *Computer Methods in Applied Mechanics and Engineering*. 351, 718–743. DOI: 10.1016/j.cma.2019.03.052.

Mughal, S. M. & Ashworth, R. (2013) Uncertainty quantification based receptivity modelling of crossflow instabilities induced by distributed surface roughness in swept wing boundary layers. In: *43rd Fluid Dynamics Conference, 24–27 June 2013, San Diego, CA*. AIAA Paper 2013-3106. DOI: 10.2514/6.2013-3106.

Nayfeh, A. H. (2004) *Perturbation methods*. Weinheim, Germany, Wiley-VCH. DOI: 10.1002/9783527617609.

Nayfeh, A. H., Ragab, S. A. & Al-Maaitah, A. A. (1988) Effect of bulges on the stability of boundary layers. *Physics of Fluids*. 31 (4), 796. DOI: 10.1063/1.866815.

Nenni, J. P. & Gluyas, G. L. (1966) Aerodynamic design and analysis on an LFC surface. *Astronautics & Aeronautics*. 4 (7), 52–57.

Ng, L. L. & Crouch, J. D. (1999) Roughness-induced receptivity to crossflow vortices on a swept wing. *Physics of Fluids*. 11 (2), 432–438. DOI: 10.1063/1.869860.

Niessen, S. (2017) *BiGlobal stability analysis: laminar shock-wave/boundary-layer interactions*. Unpublished. Master's thesis. University of Liège, Belgium.

Orr, W. M. F. (1907) The stability or instability of the steady motions of a perfect liquid and of a viscous liquid. Part I: a perfect liquid. *Proceedings of the Royal Irish Academy. Section A: Mathematical and Physical Sciences*. 27, 9–68.

Owen, P. R. & Randall, D. J. (1952) *Boundary layer transition on the swept wing*. Royal Aircraft Establishment, Farnborough, United Kingdom. Report number: 277.

Paredes, P., Hermanns, M., Le Clainche, S. & Theofilis, V. (2013) Order 10^4 speedup in global linear instability analysis using matrix formation. *Computer Methods in Applied Mechanics and Engineering*. 253, 287–304. DOI: 10.1016/j.cma.2012.09.014.

Park, D. & Park, S. O. (2013) Linear and non-linear stability analysis of incompressible boundary layer over a two-dimensional hump. *Computers & Fluids*. 73, 80–96. DOI: 10.1016/j.compfluid.2012.12.007.

Perraud, J. & Séraudie, A. (2000) Effects of steps and gaps on 2D and 3D transition. In: *European Congress on Computational Methods in Applied Science and Engineering, 11–14 September 2000, Barcelona, Spain*.

Pfenninger, W. (1965) Some results from the X-21A program. Part I. Flow phenomena at the leading edge of swept wings. In: *Recent Developments in Boundary Layer Research, Part IV*. AGARDograph 97.

Pfenninger, W. (1977) Laminar flow control, laminarization. In: *Special Course on Concepts for Drag Reduction*. Report number: AGARD-R-654.

Pfenninger, W. & Bacon, J. W. (1969) Amplified laminar boundary layer oscillations and transition at the front attachment line of a 45° swept flat-nosed wing with and without boundary layer suction. In: Wells, C. S. (ed.), *Viscous Drag Reduction: Proceedings of the Symposium on Viscous Drag Reduction held at the LTV Research Center, Dallas, Texas, September 24 and 25, 1968*. Boston, MA, Springer, pp. 85–105. DOI: 10.1007/978-1-4899-5579-1_4.

Pinna, F. (2012) *Numerical study of stability of flows from low to high Mach number*. PhD thesis. Sapienza University of Rome, Italy and von Karman Institute for Fluid Dynamics, Sint-Genesius-Rode, Belgium.

Pralits, J. O., Airiau, C., Hanifi, A. & Henningson, D. S. (2000) Sensitivity analysis using adjoint parabolized stability equations for compressible flows. *Flow, Turbulence and Combustion*. 65, 321–346. DOI: 10.1023/A:1011434805046.

Prandtl, L. (1905) Über Flüssigkeitsbewegung bei sehr kleiner Reibung [On the motion of fluids with very little friction]. In: Krazer, A. (ed.), *Verhandlungen des Dritten Internationalen Mathematiker-Kongresses [Proceedings of the Third International Congress of Mathematicians]. 8–13 August 1904, Heidelberg, Germany*. Leipzig, Germany, B. G. Teubner, pp. 484–491.

Reed, H. L. & Saric, W. S. (1989) Stability of three-dimensional boundary layers. *Annual Review of Fluid Mechanics*. 21, 235–284. DOI: 10.1146/annurev.fl.21.010189.001315.

Reed, H. L. & Saric, W. S. (2008) Transition mechanisms for transport aircraft. In: *38th Fluid Dynamics Conference and Exhibit, 23–26 June 2008, Seattle, WA*. AIAA Paper 2008-3743. DOI: 10.2514/6.2008-3743.

Rempfer, D. (2006) On boundary conditions for incompressible Navier-Stokes problems. *Applied Mechanics Reviews*. 59 (3), 107–125. DOI: 10.1115/1.2177683.

Reshotko, E. (2001) Transient growth: a factor in bypass transition. *Physics of Fluids*. 13 (5), 1067–1075. DOI: 10.1063/1.1358308.

Reynolds, O. (1883) An experimental investigation of the circumstances which determine whether the motion of water shall be direct or sinuous, and of the law of resistance in parallel channels. *Proceedings of the Royal Society of London*. 35 (224–226), 84–99. DOI: 10.1098/rspl.1883.0018.

Richtmyer, R. D. & Morton, K. W. (1967) *Difference methods for initial-value problems*. 2nd ed. Interscience Tracts In Pure and Applied Mathematics, 4. New York, NY, Interscience.

Rigas, G., Sipp, D. & Colonius, T. (2021) Nonlinear input/output analysis: application to boundary layer transition. *Journal of Fluid Mechanics*. 911. DOI: 10.1017/jfm.2020.982.

Rius Vidales, A. F., Kotsonis, M., Antunes, A. P. & Cosin, R. (2018) Effect of two-dimensional surface irregularities on swept wing transition: forward facing steps. In: *2018 AIAA Aviation Forum, Fluid Dynamics Conference, 25–29 June 2018, Atlanta, GA*. AIAA Paper 2018-3075. DOI: 10.2514/6.2018-3075.

Robitaillié-Montané, C. (2005) *Une approche non locale pour l'étude des instabilités linéaires. Application à l'écoulement de couche limite compressible le long d'une ligne de partage [A non-local approach for the analysis of linear instabilities. Application to the compressible, attachment-line boundary-layer flow]*. PhD thesis. École Nationale Supérieure de l'Aéronautique et de l'Espace, Toulouse, France.

Roden, J. A. & Gedney, S. D. (2000) Convolution PML (CPML): an efficient FDTD implementation of the CFS-PML for arbitrary media. *Microwave and Optical Technology Letters*. 27 (5), 334–339. DOI: 10.1002/1098-2760(20001205)27:5<334::AID-MOP14>3.0.CO;2-A.

Rodríguez, D., Gennaro, E. M. & Juniper, M. P. (2013) The two classes of primary modal instability in laminar separation bubbles. *Journal of Fluid Mechanics*. 734, R4. DOI: 10.1017/jfm.2013.504.

Rodríguez, D. & Theofilis, V. (2010) Structural changes of laminar separation bubbles induced by global linear instability. *Journal of Fluid Mechanics*. 655, 280–305. DOI: 10.1017/S0022112010000856.

Rosenhead, L. (ed.) (1963) *Laminar boundary layers: an account of the development, structure and stability of laminar boundary layers in incompressible fluids, together with a description of the associated experimental techniques*. Mineola, NY, Dover.

Saad, Y. (1980) Variations on Arnoldi's method for computing eigenelements of large unsymmetric matrices. *Linear Algebra and its Applications*. 34, 269–295. DOI: 10.1016/0024-3795(80)90169-x.

Saad, Y. & Schultz, M. H. (1986) GMRES: a generalized minimal residual algorithm for solving nonsymmetric linear systems. *SIAM Journal on Scientific and Statistical Computing*. 7 (3), 856–869. DOI: 10.1137/0907058.

Saeed, T. I., Mughal, M. S. & Morrison, J. (2016) The interaction of a swept-wing boundary layer with surface excrescences. In: *54th AIAA Aerospace Sciences Meeting, 4–8 January 2016, San Diego, CA*. AIAA Paper 2016-2065. DOI: 10.2514/6.2016-2065.

Salwen, H. & Grosch, C. E. (1981) The continuous spectrum of the Orr-Sommerfeld equation. Part 2. Eigenfunction expansions. *Journal of Fluid Mechanics*. 104, 445–465. DOI: 10.1017/s0022112081002991.

Saric, W. S. (1985) Boundary layer transition: T-S waves and crossflow mechanisms. In: *Aircraft Drag Prediction and Reduction*. Report number: AGARD-R-723.

Saric, W. S. (1994) Görtler vortices. *Annual Review of Fluid Mechanics*. 26, 379–409. DOI: 10.1146/annurev.fl.26.010194.002115.

Saric, W. S., Carrillo Jr., R. & Reibert, M. S. (1998) Leading-edge roughness as a transition control mechanism. In: *36th AIAA Aerospace Sciences Meeting and Exhibit, 12–15 January 1998, Reno, NV*. AIAA Paper 98-0781. DOI: 10.2514/6.1998-781.

Saric, W. S., Hoos, J. A. & Radeztsky, R. H. (1991) Boundary-layer receptivity of sound with roughness. In: Reda, D. C., Reed, H. L. & Kobayashi, R. (eds.), *Boundary Layer Stability and Transition to Turbulence*. *First ASME-JSME Fluids Engineering Conference*, *23–27 June 1991*, *Portland, OR*. Vol. 114, pp. 69–76.

Saric, W. S. & Nayfeh, A. H. (1975) Nonparallel stability of boundary-layer flows. *Physics of Fluids*. 18 (8), 945. DOI: 10.1063/1.861266.

Saric, W. S., Reed, H. L. & White, E. B. (2003) Stability and transition of three-dimensional boundary layers. *Annual Review of Fluid Mechanics*. 35, 413–440. DOI: 10.1146/annurev.fluid.35.101101.161045.

Schlatter, P., Brandt, L., de Lange, H. C. & Henningson, D. S. (2008) On streak breakdown in bypass transition. *Physics of Fluids*. 20 (10), 101505. DOI: 10.1063/1.3005836.

Schlichting, H. (1933) Zur Enstehung der Turbulenz bei der Plattenströmung [On the origins of turbulence in plate flow]. *Nachrichten von der Gesellschaft der Wissenschaften zu Göttingen, Mathematisch-Physikalische Klasse [Proceedings of the Society of Sciences of Göttingen, Mathematics-Physics Section]*. 181–208.

Schlichting, H. & Gersten, K. (2017) *Boundary-layer theory*. 9th ed. Berlin, Heidelberg, Germany, Springer. DOI: 10.1007/978-3-662-52919-5.

Schmid, P. J. (2007) Nonmodal stability theory. *Annual Review of Fluid Mechanics*. 39, 129–162. DOI: 10.1146/annurev.fluid.38.050304.092139.

Schmid, P. J. & Henningson, D. S. (2001) *Stability and transition in shear flows*. Applied Mathematical Sciences, 142. New York, NY, Springer. DOI: 10.1007/978-1-4613-0185-1.

Schmid, P. J., Lundbladh, A. & Henningson, D. S. (1994) Spatial evolution of disturbances in plane Poiseuille flow. In: Hussaini, M. Y., Gatski, T. B. & Jackson, T. L. (eds.), *Transition, Turbulence and Combustion*. Vol. 1. ICASE/LaRC Interdisciplinary Series in Science and Engineering, 2 & 3. Dordrecht, Netherlands, Springer, pp. 287–297. DOI: 10.1007/978-94-011-1032-7_28.

Schrauf, G. (1998) *COCO - a program to compute velocity and temperature profiles for local and nonlocal stability analysis of compressible, conical boundary layers with suction*. Zentrum für Angewandte Raumfahrtechnologie und Mikrogravitation, Bremen, Germany.

Schrauf, G. (2005) Status and perspectives of laminar flow. *The Aeronautical Journal*. 109 (1102), 639–644. DOI: 10.1017/s000192400000097x.

Schubauer, G. B. & Skramstad, H. K. (1947) Laminar boundary-layer oscillations and stability of laminar flow. *Journal of the Aeronautical Sciences*. 14 (2), 69–78. DOI: 10.2514/8.1267.

Shahinfar, S., Fransson, J. H. M., Sattarzadeh, S. S. & Talamelli, A. (2013) Scaling of streamwise boundary layer streaks and their ability to reduce skin-friction drag. *Journal of Fluid Mechanics*. 733, 1–32. DOI: 10.1017/jfm.2013.431.

Shirokoff, D. & Rosales, R. R. (2011) An efficient method for the incompressible Navier-Stokes equations on irregular domains with no-slip boundary conditions, high order up to the boundary. *Journal of Computational Physics*. 230 (23), 8619–8646. DOI: 10.1016/j.jcp.2011.08.011.

Shroff, G. M. & Keller, H. B. (1993) Stabilization of unstable procedures: the Recursive Projection Method. *SIAM Journal on Numerical Analysis*. 30 (4), 1099–1120. DOI: 10.1137/0730057.

Simen, M. (1992) Local and non-local stability theory of spatially varying flows. In: Hussaini, M. Y., Kumar, A. & Streett, C. L. (eds.), *Instability, Transition, and Turbulence*. ICASE NASA LaRC. New York, NY, Springer, pp. 181–201. DOI: 10.1007/978-1-4612-2956-8_18.

Slotnick, J., Khodadoust, A., Alonso, J., Darmofal, D., Gropp, W., Lurie, E. & Mavriplis, D. (2014) *CFD Vision 2030 study: a path to revolutionary computational aerosciences*. National Aeronautics and Space Administration, Washington, DC. Report number: NASA/CR-2014-218178.

Smagorinsky, J. (1963) General circulation experiments with the primitive equations. I. The basic experiment. *Monthly Weather Review*. 91 (3), 99–164. DOI: 10.1175/1520-0493(1963)091<0099:GCEWTP>2.3.CO;2.

Smith, A. M. O. & Gamberoni, N. (1956) *Transition, pressure gradient and stability theory*. Douglas Aircraft Company, El Segundo, CA. Report number: ES 26388.

Smith, F. T. (1982) On the high Reynolds number theory of laminar flows. *IMA Journal of Applied Mathematics*. 28 (3), 207–281. DOI: 10.1093/imamat/28.3.207.

Sommerfeld, A. (1909) Ein Beitrag zur hydrodynamischen Erklärung der turbulenten Flüssigkeitsbewegung [A contribution to the hydrodynamic explanation of turbulent fluid motion]. In: Castelnuovo, G. (ed.), *Atti del IV Congresso Internazionale dei Matematici [Proceedings of the Fourth International Congress of Mathematicians]. 6–11 April 1908, Roma, Germany*. Vol. 3. Roma, Germany, Reale Accademia dei Lincei, pp. 116–124.

Spalart, P. R. & Venkatakrishnan, V. (2016) On the role and challenges of CFD in the aerospace industry. *The Aeronautical Journal*. 120 (1223), 209–232. DOI: 10.1017/aer.2015.10.

Stewart, G. W. (2002) A Krylov-Schur algorithm for large eigenproblems. *SIAM Journal on Matrix Analysis and Applications*. 23 (3), 601–614. DOI: 10.1137/s0895479800371529.

Stock, H. W. & Degenhart, E. (1989) A simplified e^N method for transition prediction in two-dimensional, incompressible boundary layers. *Zeitschrift für Flugwissenschaften und Weltraumforschung [Journal of Aviation Science and Space Research]*. 13, 16–30.

Strand, B. (1994) Summation by parts for finite difference approximations for d/dx. *Journal of Computational Physics*. 110 (1), 47–67. DOI: 10.1006/jcph.1994.1005.

Strutt, J. W. (1880) On the stability, or instability, of certain fluid motions. *Proceedings of the London Mathematical Society*. 11, 57–72. DOI: 10.1112/plms/s1-11.1.57.

Strutt, J. W. (1917) On the dynamics of revolving fluids. *Proceedings of the Royal Society of London*. 93 (648), 148–154. DOI: 10.1098/rspa.1917.0010.

Succi, S. (2001) *The lattice Boltzmann equation: for fluid dynamics and beyond*. Numerical Mathematics and Scientific Computation. Oxford, United Kingdom, Clarendon Press.

Sunderland, R. & Sawyers, D. (2009) *Evaluation of AERAST large scale wind-tunnel test results*. Airbus. Report number: RP0905747.

Tam, C. K. W. & Webb, J. C. (1993) Dispersion-relation-preserving finite difference schemes for computational acoustics. *Journal of Computational Physics*. 107 (2), 262–281. DOI: 10.1006/jcph.1993.1142.

Tani, I., Hama, R. & Mituisi, S. (1940) *On the permissible roughness in the laminar boundary layer*. Aeronautical Research Institute, Tokyo Imperial University, Japan. Report number: 199.

Tao, T. (2016) Finite time blowup for an averaged three-dimensional Navier-Stokes equation. *Journal of the American Mathematical Society*. 29 (3), 601–674. DOI: 10.1090/jams/838.

Tempelmann, D., Schrader, L.-U., Hanifi, A., Brandt, L. & Henningson, D. S. (2012) Swept wing boundary-layer receptivity to localized surface roughness. *Journal of Fluid Mechanics*. 711, 516–544. DOI: 10.1017/jfm.2012.405.

Theofilis, V. (2003) Advances in global linear instability analysis of nonparallel and three-dimensional flows. *Progress in Aerospace Sciences*. 39 (4), 249–315. DOI: 10.1016/S0376-0421(02)00030-1.

Theofilis, V. (2011) Global linear instability. *Annual Review of Fluid Mechanics*. 43, 319–352. DOI: 10.1146/annurev-fluid-122109-160705.

Theofilis, V. (2017) The linearized pressure Poisson equation for global instability analysis of incompressible flows. *Theoretical and Computational Fluid Dynamics*. 31 (5), 623–642. DOI: 10.1007/s00162-017-0435-z.

Theofilis, V., Ferodov, A., Obrist, D. & Dallmann, U. (2003) The extended Görtler-Hämmerlin model for linear instability of three-dimensional incompressible swept attachment-line boundary layer flow. *Journal of Fluid Mechanics*. 487, 271–313. DOI: 10.1017/S0022112003004762.

Theofilis, V., Hein, S. & Dallmann, U. (2000) On the origins of unsteadiness and three-dimensionality in a laminar separation bubble. *Philosophical Transactions of the Royal Society of London. Series A: Mathematical, Physical and Engineering Sciences*. 358 (1777), 3229–3246. DOI: 10.1098/rsta.2000.0706.

Thomas, C., Mughal, S. & Ashworth, R. (2017) Development of Tollmien-Schlichting disturbances in the presence of laminar separation bubbles on an unswept infinite wavy wing. *Physical Review Fluids*. 2 (4). DOI: 10.1103/physrevfluids.2.043903.

Thomas, C., Mughal, S. M., Gipon, M., Ashworth, R. & Martinez-Cava, A. (2016) Stability of an infinite swept wing boundary layer with surface waviness. *AIAA Journal*. 54 (10), 3024–3038. DOI: 10.2514/1.j054755.

Thomas, C., Mughal, S. M., Roland, H., Ashworth, R. & Martinez-Cava, A. (2018) Effect of small surface deformations on the stability of Tollmien-Schlichting disturbances. *AIAA Journal*. 56 (6), 2157–2165. DOI: 10.2514/1.j056821.

Tollmien, W. (1929) Über die Entstehung der Turbulenz. 1. Mitteilung [On the origins of turbulence. 1st communication]. *Nachrichten von der Gesellschaft der Wissenschaften zu Göttingen, Mathematisch-Physikalische Klasse [Proceedings of the Society of Sciences of Göttingen, Mathematics-Physics Section]*. 21–44.

Trefethen, L. N., Trefethen, A. E., Reddy, S. C. & Driscoll, T. A. (1993) Hydrodynamic stability without eigenvalues. *Science*. 261 (5121), 578–584. DOI: 10.1126/science.261.5121.578.

Trottenberg, U., Oosterlee, C. W., Schüller, A., Brandt, A., Oswald, P. & Stüben, K. (2001) *Multigrid*. London, United Kingdom, Academic Press.

Tufts, M. W., Reed, H. L., Crawford, B. K., Duncan Jr., G. T. & Saric, W. S. (2017) Computational investigation of step excrescence sensitivity in a swept-wing boundary layer. *Journal of Aircraft*. 54 (2), 602–626. DOI: 10.2514/1.C033892.

Van Ingen, J. L. (1956) *A suggested semi-empirical method for the calculation of the boundary layer transition region*. Technological University of Delft, Netherlands. Report number: VTH-74.

Van Ingen, J. L. (2008) The e^N method for transition prediction. Historical review of work at TU Delft. In: *38th Fluid Dynamics Conference and Exhibit*, *23–26 June 2008*, *Seattle, WA*. AIAA Paper 2008-3830. DOI: 10.2514/6.2008-3830.

Wang, Y. X. & Gaster, M. (2005) Effect of surface steps on boundary layer transition. *Experiments in Fluids*. 39 (4), 679–686. DOI: 10.1007/s00348-005-1011-7.

Watmuff, J. H. (1999) Evolution of a wave packet into vortex loops in a laminar separation bubble. *Journal of Fluid Mechanics*. 397, 119–169. DOI: 10.1017/s0022112099006138.

Weickert, J. (1996) *Navier-Stokes equations as a differential algebraic system*. Chemnitz University of Technology, Germany. Report number: SFB393/96-08.

White, E. B. & Saric, W. S. (2005) Secondary instability of crossflow vortices. *Journal of Fluid Mechanics*. 525, 275–308. DOI: 10.1017/s002211200400268x.

White, F. M. (2006) *Viscous fluid flow*. 3rd ed. McGraw-Hill Series in Mechanical Engineering. New York, NY, McGraw-Hill.

Wie, Y.-S. & Malik, M. R. (1998) Effect of surface waviness on boundary-layer transition in two-dimensional flow. *Computers & Fluids*. 27 (2), 157–181. DOI: 10.1016/s0045-7930(97)00024-8.

Wörner, A., Rist, U. & Wagner, S. (2003) Humps/steps influence on stability characteristics of two-dimensional laminar boundary layer. *AIAA Journal*. 41 (2), 192–197. DOI: 10.2514/2.1960.

Wu, X. & Hogg, L. W. (2006) Acoustic radiation of Tollmien-Schlichting waves as they undergo rapid distortion. *Journal of Fluid Mechanics*. 550, 307–347. DOI: 10.1017/s0022112005008220.

Xu, H., Lombard, J.-E. W. & Sherwin, S. J. (2017a) Influence of localised smooth steps on the instability of a boundary layer. *Journal of Fluid Mechanics*. 817, 138–170. DOI: 10.1017/jfm.2017.113.

Xu, H., Mughal, S. M., Gowree, E. R., Atkin, C. J. & Sherwin, S. J. (2017b) Destabilisation and modification of Tollmien-Schlichting disturbances by a three-dimensional surface indentation. *Journal of Fluid Mechanics*. 819, 592–620. DOI: 10.1017/jfm.2017.193.

Zanus, L., Miró Miró, F. & Pinna, F. (2018) Nonlinear parabolized stability analysis of hypersonic flows in presence of curvature effects. In: *2018 AIAA Aerospace Sciences Meeting, 8–12 January 2018, Kissimmee, FL*. AIAA Paper 2018-2087. DOI: 10.2514/6.2018-2087.

Zanus, L. & Pinna, F. (2018) Stability analysis of hypersonic flows in local thermodynamic equilibrium conditions by means of nonlinear PSE. In: *2018 AIAA Aviation Forum, Fluid Dynamics Conference, 25–29 June 2018, Atlanta, GA*. AIAA Paper 2018-3696. DOI: 10.2514/6.2018-3696.

Appendix A

Body-fitted coordinates

Orthogonal body-fitted coordinates (x, y, z) are conveniently used to analyse curved wing geometries and to align the grid with the local flow direction within the realm of possibility. They can be seen as a particular case of generalised curvilinear coordinates. If (ξ, η, ζ) denotes Cartesian coordinates, the relation between the two coordinate systems can be written as

$$\begin{aligned} x &= x(\xi, \eta, \zeta) \\ y &= y(\xi, \eta, \zeta) \\ z &= z(\xi, \eta, \zeta). \end{aligned} \tag{A.1}$$

Knowing the elemental arc length in Cartesian coordinates is expressed as $(ds)^2 = (d\xi)^2 + (d\eta)^2 + (d\zeta)^2$, differentiating Eq. (A.1) gives

$$(ds)^2 = (h_x dx)^2 + (h_y dy)^2 + (h_z dz)^2 \tag{A.2}$$

where (h_x, h_y, h_z) are the Lamé coefficients of the transformation which appear in the expression of the gradient, divergence or Laplacian operators:

$$\nabla\phi = \left(\frac{1}{h_x}\frac{\partial\phi}{\partial x} \quad \frac{1}{h_y}\frac{\partial\phi}{\partial y} \quad \frac{1}{h_z}\frac{\partial\phi}{\partial z} \right)^T \tag{A.3}$$

$$\nabla \cdot \boldsymbol{\phi} = \frac{1}{h_x h_y h_z}\left(\frac{\partial h_y h_z \phi_x}{\partial x} + \frac{\partial h_x h_z \phi_y}{\partial y} + \frac{\partial h_x h_y \phi_z}{\partial z} \right) \tag{A.4}$$

$$\Delta\phi = \frac{1}{h_x h_y h_z}\left(\frac{\partial}{\partial x}\left(\frac{h_y h_z}{h_x}\frac{\partial\phi}{\partial x} \right) + \frac{\partial}{\partial y}\left(\frac{h_x h_z}{h_y}\frac{\partial\phi}{\partial y} \right) + \frac{\partial}{\partial z}\left(\frac{h_x h_y}{h_z}\frac{\partial\phi}{\partial z} \right) \right). \tag{A.5}$$

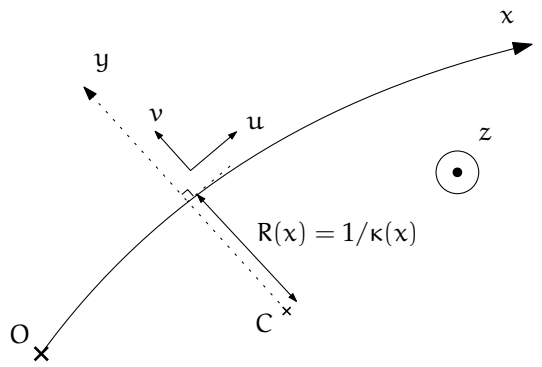

Figure A.1: Body-fitted orthogonal coordinates. R represents the local radius of the body contour, linked to the local body curvature $\kappa(x) = 1/R(x)$. The streamwise position of any point is measured by the distance along the body contour from the coordinate origin O. C is the local centre of curvature.

For body-fitted coordinates, the Lamé coefficients read

$$\begin{aligned} h_x &= 1 - \kappa(x)y \\ h_y &= 1 \\ h_z &= 1 \end{aligned} \tag{A.6}$$

where κ is the local body surface curvature. Figure A.1 represents a schematic view of the body-fitted coordinates. In this coordinate system, the wall-normal coordinate lines remain orthogonal to the surface and do not change orientation as the distance from the body increases to conform to the far-field upper boundary. However, important surface concavity would render the assumption invalid; wall-normal coordinate lines would cross, leading to an ill-posed body-fitted transformation. An example is a sharp indentation present on the body surface. Nonetheless, in this work surface irregularities are modelled via a distinct change of variables and not by the body-fitted coordinate system which alleviates any problems of that kind.

The 2.5D LHNS operator reads in body-fitted coordinates

$$\mathcal{L} = \begin{pmatrix} 0 & \chi\partial_x & \partial_y - \kappa\chi & i\beta \\ \chi\partial_x & \mathcal{D} + \chi\partial_x\bar{u} - \kappa\chi\bar{v} + \dfrac{\kappa^2\chi^2}{Re} & \partial_y\bar{u} - \kappa\chi\bar{u} + K + \dfrac{2\kappa\chi^2}{Re}\partial_x & 0 \\ \partial_y & \chi(2\kappa\bar{u} + \partial_x\bar{v}) - K - \dfrac{2\kappa\chi^2}{Re}\partial_x & \mathcal{D} + \partial_y\bar{v} + \dfrac{\kappa^2\chi^2}{Re} & 0 \\ i\beta & \chi\partial_x\bar{w} & \partial_y\bar{w} & \mathcal{D} \end{pmatrix} \tag{A.7}$$

where the operator $\mathcal{D}$ is

$$\begin{aligned}\mathcal{D} = \chi\left(\bar{u} - \frac{\partial_x\chi}{Re}\right)\frac{\partial}{\partial x} + \left(\bar{v} + \frac{\kappa\chi}{Re}\right)\frac{\partial}{\partial y} + i(\beta\bar{w} - \omega) \\ + \frac{\beta^2}{Re} - \frac{1}{Re}\left(\chi^2\frac{\partial^2}{\partial x^2} + \frac{\partial^2}{\partial y^2}\right).\end{aligned} \tag{A.8}$$

The parameter χ is defined as

$$\chi(x, y) = \frac{1}{h_x} = \frac{1}{1 - \kappa(x)y} \tag{A.9}$$

while K denotes the expression

$$K = \frac{\chi}{Re}\left(\chi\frac{\partial\kappa}{\partial x} + \kappa\frac{\partial\chi}{\partial x}\right). \tag{A.10}$$

The total resonant forcing reads

$$\mathcal{F}^{res} = \begin{pmatrix} 0 \\ -\chi\tilde{u}\partial_x\tilde{u} - \tilde{v}\partial_y\tilde{u} - \tilde{w}\partial_z\tilde{u} + \kappa\chi\tilde{u}\tilde{v} \\ -\chi\tilde{u}\partial_x\tilde{v} - \tilde{v}\partial_y\tilde{v} - \tilde{w}\partial_z\tilde{v} - \kappa\chi\tilde{u}^2 \\ -\chi\tilde{u}\partial_x\tilde{w} - \tilde{v}\partial_y\tilde{w} - \tilde{w}\partial_z\tilde{w} \end{pmatrix}. \tag{A.11}$$

The equations expressed in Cartesian coordinates are recovered in the large curvature limit, that is for $\kappa = 0$ and $\chi = 1$. Finally, the LPPE reads

$$\begin{aligned}\chi^2\frac{\partial^2\hat{p}}{\partial x^2} + \frac{\partial^2\hat{p}}{\partial y^2} + \chi\partial_x\chi\frac{\partial\hat{p}}{\partial x} - \kappa\chi\frac{\partial\hat{p}}{\partial y} - \beta^2\hat{p} + 2\chi^2(\partial_x\bar{u} - \kappa\bar{v})\frac{\partial\hat{u}}{\partial x} \\ + 2\chi(\partial_x\bar{v} + \kappa\bar{u})\frac{\partial\hat{u}}{\partial y} + 2\chi(i\beta\partial_x\bar{w} + \kappa\partial_y\bar{u})\hat{u} + 2\chi\partial_y\bar{u}\frac{\partial\hat{v}}{\partial x} \\ + 2\partial_y\bar{v}\frac{\partial\hat{v}}{\partial y} + 2(i\beta\partial_y\bar{w} + \kappa\chi^2(\kappa\bar{v} - \partial_x\bar{u}))\hat{v} = 0.\end{aligned} \tag{A.12}$$

Appendix B

Lagrange interpolant and matrix entries

The one-dimensional Lagrange interpolant in Eq. (4.3) is easily extended to two spatial dimensions. Evaluated at the grid node (x_i, y_j), the discrete value of the function ϕ reads

$$\phi(x_i, y_j) = \phi_{ij} = \sum_{k=s_{x,i}}^{s_{x,i}+q_x} \sum_{p=s_{y,j}}^{s_{y,j}+q_y} l_{x,ik}(x_i) l_{y,jp}(y_p) \phi_{kp}. \tag{B.1}$$

A degree of freedom corresponds to one variable $\phi \in (p, u, v, w)^T$ evaluated at one grid node (x_i, y_j) for $i \in [0, n_x]$ and $j \in [0, n_y]$. To prevent an underdetermined or overdetermined system of equations, it must be associated with one and only one equation among the governing PDEs, or the boundary condition if the degree of freedom is located at the boundary of the domain. At a continuous level, a governing linear equation may be written as

$$\begin{aligned} \sum_{r=1}^{n_\phi} \Bigg[& a_r(x,y) \frac{\partial^2 \phi_r}{\partial x^2} + b_r(x,y) \frac{\partial^2 \phi_r}{\partial y^2} + c_r(x,y) \frac{\partial^2 \phi_r}{\partial x \partial y} \\ & + d_r(x,y) \frac{\partial \phi_r}{\partial x} + e_r(x,y) \frac{\partial \phi_r}{\partial y} + f_r(x,y) \phi_r \Bigg] = 0 \end{aligned} \tag{B.2}$$

where n_ϕ is the number of independent variables and $(a_r, b_r, c_r, d_r, e_r)$ are the PDE coefficients which are in general functions of spatial coordinates. After mapping to the computational domain Ξ, Eq. (B.2) is transformed into

$$\sum_{r=1}^{n_\phi} \left[A_r \frac{\partial^2 \phi_r}{\partial \xi^2} + B_r \frac{\partial^2 \phi_r}{\partial \eta^2} + C_r \frac{\partial^2 \phi_r}{\partial \xi \partial \eta} + D_r \frac{\partial \phi_r}{\partial \xi} + E_r \frac{\partial \phi_r}{\partial \eta} + F_r \phi_r \right] = 0 \tag{B.3}$$

where $(A_r, B_r, C_r, D_r, E_r)$ are linear combinations of the original PDE coefficients multiplied by transformation metrics following Eqs. (4.7) and (4.8). If $\varpi_{x,ij} = l_{x,ij}(x_i)$ denotes the weights of the FD-q method that are node values of the Lagrange polynomials, Eq. (B.3) reads, after introducing the two-dimensional Lagrange interpolant defined in Eq. (B.1),

$$\begin{aligned}\sum_{r=1}^{n_\phi} \sum_{k=s_{x,i}}^{s_{x,i}+q_x} \sum_{p=s_{y,j}}^{s_{y,j}+q_y} \big[& A_{rij}\varpi''_{\xi,ik}\varpi_{\eta,jp} + B_{rij}\varpi_{\xi,ik}\varpi''_{\eta,jp} + C_{rij}\varpi'_{\xi,ik}\varpi'_{\eta,jp} \\ & + D_{rij}\varpi'_{\xi,ik}\varpi_{\eta,jp} + E_{rij}\varpi_{\xi,ik}\varpi'_{\eta,jp} + F_{rij}\varpi_{\xi,ik}\varpi_{\eta,jp} \big] \phi_{rkp} = 0\end{aligned} \tag{B.4}$$

which is evaluated at (x_i, y_j) or equivalently at the computational coordinates (ξ_i, η_j).

Equation (B.4) is filled with useful information. It pertains to one row of the finite-difference matrix whose location is completely determined by which specific grid node (x_i, y_j) and which specific variable of $\phi \in (p, u, v, w)^\intercal$ it is associated to. The triad (r, k, p) local to the summation determines a unique column of the matrix. The FD-q stencils $k \in [s_{x,i}, s_{x,i} + q_x]$ and $p \in [s_{y,j}, s_{y,j} + q_y]$ span the different columns and allow to determine the non-zero entries for the matrix preallocation and matrix assembly steps.